

THESIS

LINKS BETWEEN ATMOSPHERIC CLOUD RADIATIVE EFFECTS AND TROPICAL  
CIRCULATIONS

Submitted by

Michael R. Needham

Department of Atmospheric Science

In partial fulfillment of the requirements

For the Degree of Master of Science

Colorado State University

Fort Collins, Colorado

Spring 2021

Master's Committee:

Advisor: David A. Randall

James W. Hurrell

Xinfeng Gao

Copyright by Michael R. Needham 2021

All Rights Reserved

## ABSTRACT

### LINKS BETWEEN ATMOSPHERIC CLOUD RADIATIVE EFFECTS AND TROPICAL CIRCULATIONS

Atmospheric cloud radiative effects (ACRE) quantify the radiative heating or cooling due to clouds within the atmosphere. In this study, a framework is developed with which to analyze the ways that ACRE impact large-scale circulations in humid and dry regions of the tropics. The framework is applied to a set of simulations from a global atmospheric model configured with uniform tropical sea surface temperatures, following the protocol of the Radiative Convective Equilibrium Model Intercomparison Project. It is found that humid regions export energy and import moisture, and that ACRE in extremely humid regions are strong enough to change the sign of the net radiation tendency. This net heating drives a feedback in which large-scale ascent moistens the troposphere by lifting latent energy from near the surface. Moisture at these higher levels then forms clouds which in turn reinforce the ACRE, continuing the process. The relevance of this feedback to the germinal study of Riehl and Malkus (1958) is discussed.

Additionally, the analysis method reveals a simple relationship between cloud radiative effects and column relative humidity in the idealized model. The same relationship is also observed in cloud radiative effects calculated from satellite observations. This suggests a simple way to estimate the cloud radiative effect at the top of the atmosphere. The estimated cloud radiative effect may be useful in estimating the ACRE, which is harder to infer from measurements using previous methods. The estimation shows some skill at estimating the cloud radiative effect in humid regions across the tropics on time scales of one month or longer. The method is found to be extremely effective at estimating observed cloud radiative effects in the equatorial west Pacific. Weaknesses of the estimation method in relation to marine stratus clouds are discussed.

## ACKNOWLEDGEMENTS

I would like to thank Dr. David Randall for the guidance without which this thesis would not have been possible, as well as Dr. James Hurrell and Dr. Xinfeng Gao for their roles on my graduate committee. In addition, I would like to thank all of the Randall research group, and all of the students, faculty, and staff of the department of atmospheric science. Lastly, I would like to express my gratitude for the support I have received from my friends and family, especially from Kelsey, my wife, and Mary, my mother. This research was supported by the National Science Foundation.

## DEDICATION

*In memory of the late, great, one-of-a-kind Dan Needham*

## TABLE OF CONTENTS

ABSTRACT . . . . .	ii
ACKNOWLEDGEMENTS . . . . .	iii
DEDICATION . . . . .	iv
List of Tables . . . . .	viii
List of Figures . . . . .	ix
Chapter 1 Introduction . . . . .	1
1.1 Cloud Radiative Effect . . . . .	1
1.2 Convection in the Tropics . . . . .	3
1.2.1 The Earth’s Energy Balance . . . . .	3
1.2.2 Radiative Convective Equilibrium . . . . .	4
1.3 Convectively Coupled Tropical Dynamics . . . . .	6
1.3.1 Atmospheric Transports of Energy . . . . .	6
1.3.2 The Intertropical Convergence Zone . . . . .	7
1.3.3 Exports of Energy out of the ITCZ . . . . .	8
1.4 Temperature Dependence of High Clouds . . . . .	10
1.5 Outline . . . . .	14
Chapter 2 Methods . . . . .	16
2.1 Model Output, Reanalyses, and Observations . . . . .	16
2.1.1 Idealized Non-Rotating Tropical World . . . . .	16
2.1.2 Perpetual January Aquaplanet . . . . .	18
2.1.3 CERES Observations and ERA5 Reanalyses . . . . .	19
2.1.4 Oceanic Nino Index . . . . .	20
2.2 Column Relative Humidity Analysis . . . . .	21
2.2.1 Calculation of CRH . . . . .	21
2.2.2 Binning fields based on CRH . . . . .	22
Chapter 3 Cloud Radiative Effect and Column Relative Humidity . . . . .	24
3.1 The distribution of CRH and its dependence on SST . . . . .	25
3.2 The dependence of CRE at the boundaries on CRH . . . . .	26
3.3 CRE and CRH from observations and reanalyses . . . . .	30
3.4 Conclusions . . . . .	34
Chapter 4 Estimating the CRE using the CRH . . . . .	36
4.1 Using CRH to estimate the CRE at TOA . . . . .	36
4.2 Time Series Analysis . . . . .	42
4.3 Regional Subsets . . . . .	46
4.3.1 Annual Mean Values . . . . .	46
4.3.2 Regional Time Series . . . . .	47

4.4	Summary . . . . .	51
Chapter 5	Energy and Moisture Analysis as a function of CRH . . . . .	54
5.1	Moisture balance . . . . .	54
5.2	Energy balance . . . . .	58
5.3	Segue . . . . .	63
Chapter 6	A radiatively driven moisture feedback in extremely humid regions . . . . .	64
6.1	The vertical distribution of radiative tendencies and ACRE . . . . .	64
6.2	Dependence of static energies on CRH . . . . .	70
6.3	Vertical motions on large and convective scales . . . . .	74
6.4	Tropospheric moistening by vertical advection. . . . .	78
6.5	Conclusions . . . . .	85
Chapter 7	Riehl and Malkus, Revisited . . . . .	88
7.1	Climatology of AQPJAN Experiments . . . . .	89
7.2	CRH Analysis of AQPJAN Experiments . . . . .	95
7.2.1	Cloud Radiative Effect vs. Column Relative Humidity . . . . .	96
7.2.2	Energy and Moisture Balances . . . . .	97
7.2.3	Radiatively driven moisture feedback . . . . .	100
7.3	Summary of AQPJAN Results . . . . .	103
7.4	Conclusions . . . . .	104
7.4.1	Riehl and Malkus, Revisited . . . . .	104
7.4.2	Cloud Radiative Effect and Column Relative Humidity . . . . .	107
7.4.3	Future Work . . . . .	108
References . . . . .		110
Appendix A	FAT, PHAT, and FiTT . . . . .	118
A.1	The thermal expansion of the troposphere . . . . .	119
A.1.1	The radiatively driven divergence. . . . .	120
A.2	Thermodynamic dependance of upper-level clouds . . . . .	122
A.3	CRH Analysis for upper-level clouds . . . . .	125
A.4	Links between SST, CRH, and Anvil Clouds . . . . .	129
A.4.1	Temperature changes in the upper troposphere . . . . .	129
A.4.2	Changes in the TOA Brightness Temperature . . . . .	132
A.4.3	The Temperature of the Tropopause . . . . .	135
A.5	Conclusions . . . . .	136
Appendix B	Influence of ENSO on the CRE estimated from CRH . . . . .	138
B.1	East Pacific . . . . .	138
B.2	West Pacific . . . . .	140
B.3	Indian Ocean . . . . .	141
Appendix C	Comparison of latitude limits for AQPJAN experiments . . . . .	146
C.1	Cloud radiative effects versus column relative humidity . . . . .	147

C.2	Budgets of energy and moisture . . . . .	149
C.2.1	Moisture budget . . . . .	149
C.2.2	Energy budget . . . . .	150
C.3	The radiatively driven moisture feedback . . . . .	151

# List of Tables

3.1	Summary statistics for the distributions of CRH for each of the three experiments. The Mode is given as the center of the CRH bin with the largest probability density (the peak of the distributions shown in Fig. 3.2)	26
4.1	Time mean longwave CRE (first three columns) or shortwave CRE (last three columns) in each of the three tropical regions, as well as for the wider tropical belt. All values are in $Wm^{-2}$	46
6.1	Fraction of the domain, given as a percentage, with CRH below a given level. This is the area under the curves in Fig. 3.2 from 0% CRH to 70% or 80%.	86
7.1	Extension of summary statistics from Tbl. 3.1 for the distributions of CRH shown in Fig. 7.5. Statistics reflect each of the three AQPJAN experiments compared to each of the three RCEMIP experiments, as well as the ERA5 distribution. The Mode is given as the center of the CRH bin with the largest probability density (the peak of the distributions shown in Fig. 7.5)	95
7.2	Extension of Tbl. 6.1, showing the fraction of the domain with CRH below a given level for the AQPJAN and RCEMIP simulations, as well as the ERA5 reanalyses. This is the area under the curves in Fig. 7.5 from 0% CRH to 70% or 80%.	103
C.1	Summary statistics as in Tbl. 7.1, but also comparing the 10° and 30° latitude limits for both the AQPJAN experiments and for the ERA5 distribution.	146
C.2	Extension of Tbl. 6.1, showing the fraction of the domain with CRH below a given level for the AQPJAN simulations using both latitude limits the RCEMIP simulations, as well as the ERA5 reanalyses.	153

# List of Figures

1.1	Annual mean cloud radiative effect from CERES measurements for the period 2001 - 2011. Reproduced, from Fig. 7.7 of Boucher et al. (2013). ©World Meteorological Organization . . . . .	2
1.2	The heat balance of the earth and atmosphere, as it was understood in the early 20 <sup>th</sup> century. Reprinted from Dines (1917) . . . . .	4
1.3	A remarkably similar figure to Fig. 1.2, updated with 21 <sup>st</sup> century measurements. Reprinted from Trenberth et al. (2009). ©American Meteorological Society. Used with permission . . . . .	4
1.4	Equilibrium temperature profiles for simulations of radiative equilibrium with fixed relative humidity, with fixed absolute (specific) humidity, and radiative-convective equilibrium with fixed relative humidity. Reprinted from Manabe and Wetherald (1967)	5
1.5	12Z Temperature soundings on 25 January 2020 from three locations within the tropics: Lihue Airport Kaua’i, Hawai’i (159.34W, 21.99N), Saint Helena Island, United Kingdom (5.66W, 15.93S), and Singapore Changi Airport, Singapore, (103.98E, 1.36N)	5
1.6	Fig. 1 and Fig. 2 reproduced from Trenberth and Caron (2001). The left panel shows the annual mean TOA radiation balance from ERBE satellite observations. The solid line in the right panel shows the required atmosphere plus ocean northward energy transport required by the radiation balance. The two dashed lines show the atmospheric energy transport estimated from two reanalysis products. ©American Meteorological Society. Used with permission . . . . .	6
1.7	Annual mean precipitation climatology and de-seasonalized precipitation trend from GPCP, 1979 - 2017. Reproduced from Byrne et al. (2018) under Creative Commons CC BY license. . . . .	7
1.8	Vertical distribution of moist static energy in the ITCZ, reprinted from Riehl and Malkus (1958). “Ocean” refers to measurements taken over the ocean. . . . .	9

1.9	Schematic from Hartmann and Larson (2002) showing the principles of the FAT hypothesis. ©American Geophysical Union. Used under stated permissions policy. . . .	11
1.10	Profiles of cloud fraction for various SSTs using three independent GCMs. Reproduced from Bony et al. (2016). ©American Geophysical Union. Used under stated permissions policy. . . . .	12
1.11	Profiles of cloud fraction for various SSTs with temperature as the vertical coordinate. Reproduced from Seeley et al. (2019). ©American Geophysical Union. Used under stated permissions policy. . . . .	13
2.1	Cartoon showing the concept of super-parameterization. A two-dimensional cloud resolving model is embedded within a GCM grid cell to simulate sub-grid scale processes.	17
2.2	<b>Top</b> Comparison of 2 meter temperature from ER5 and SST from Aquaplanet experiments. <b>Bottom</b> Meridional distribution of surface temperature for the three AQPJAN experiments. . . . .	19
2.3	Oceanic Nino Index. El Niño (red) and La Niña (blue) are defined as the months where the magnitude of the index is greater than 0.5 K . . . . .	21
2.4	Fields of CRH from ERA5 and longwave CRE from CERES from an arbitrary date and time used to illustrate the CRH binning method used in further chapters. The CRH bin used is 70% to 90%, for illustrative purposes: binning in later chapters uses a much smaller bin width. . . . .	23
3.1	<b>Left</b> Contour plots of column relative humidity, and <b>Right</b> TOA brightness temperature for an arbitrary timestep from the 295 K RCEMIP simulation . . . . .	25
3.2	<b>Left</b> Area-weighted probability density function of column relative humidity for each of the three SST experiments. <b>Right</b> same as <b>Left</b> , but for the change in probability density function between experiments. Vertical line at 70% CRH is included for comparison with later plots in this chapter. . . . .	26

3.3	<b>Top Left</b> Longwave CRE at TOA as a function of column relative humidity for each of the three RCEMIP simulations calculated using the hourly mean history files. <b>Top Center</b> and <b>Top Right</b> same as <b>Top Left</b> , but for the shortwave CRE at TOA and net (LW + SW) CRE at TOA. <b>Center Row</b> and <b>Bottom Row</b> Same as <b>Top Row</b> , but for the CRE at the surface, and ACRE. . . . .	28
3.4	<b>Left</b> Longwave CRE at TOA calculated from CERES radiative fluxes for 19 October 2013. <b>Right</b> CRH calculated from ERA5 reanalysis on the same date. . . . .	31
3.5	Time-mean longwave CRE at TOA, with boxes showing the three subsets for analysis: Indian Ocean (INOC), Western Pacific (WPAC), and Eastern Pacific (EPAC). . . . .	31
3.6	Area-weighted probability density functions of CRH for the three regional subsets and the entire T-BELT region, for the 18-year period of investigation. . . . .	32
3.7	<b>Top Row</b> Longwave, shortwave, and net CRE at TOA calculated from CERES observations, binned by CRH calculated from ERA5 reanalysis. The three thick lines represent each of the three regional subsets, with the thin black line representing the whole T-BELT region. <b>Middle Row</b> and <b>Bottom Row</b> same as <b>Top Row</b> , but for surface CRE and ACRE, respectively. Compare with Fig. 3.3 . . . . .	33
4.1	Curves of T-BELT CRE as a function of CRE from Fig. 3.7 shown again for use in estimating CRE from CRH fields. . . . .	37
4.2	<b>Top</b> Annual mean longwave CRE at TOA calculated from daily-mean CERES observations from 2001-2019. <b>Middle</b> Annual mean longwave CRE at TOA estimated from daily mean ERA5 CRH over the same period. Description in text. <b>Bottom</b> Difference between <b>Top</b> and <b>Middle</b> . . . . .	38
4.3	Annual mean CRH in the T-BELT region from 2001-2019 calculated from ERA5 reanalysis. . . . .	39
4.4	Same as Fig. 4.2, but for the shortwave CRE. . . . .	40
4.5	Same as Fig. 4.2, but for the net CRE. . . . .	41

4.6	<b>Top</b> Time series showing the domain-mean longwave CRE estimated from ERA5 CRH fields (red line), and calculated from CERES satellite observations (black line). <b>Bottom</b> Same as <b>Top</b> , but for the shortwave CRE (blue line). . . . .	42
4.7	<b>Top</b> Pearson’s $R^2$ correlation between the monthly time series of estimated and actual longwave CRE at each location. <b>Bottom</b> Same as <b>Top</b> , but for the shortwave CRE. . .	43
4.8	Same as Fig. 4.6, but only for grid cells with CRH greater than 50%. . . . .	44
4.9	Pearson’s $R^2$ correlation between estimated and actual CRE when grid cells with CRH less than a particular threshold are excluded. . . . .	45
4.10	Same as Fig. 4.6, but for the EPAC region . . . . .	48
4.11	Scatter plot composite analysis comparing actual and estimated SW CRE in the EPAC region, for different ENSO phases or combinations of phases. Red dots show El Niño months, blue dots show La Niña, and white dots show the neutral phase. The diagonal line shows the idealized one-to-one correspondence. . . . .	49
4.12	Same as Fig. 4.6, but for the WPAC region. . . . .	51
4.13	Same as Fig. 4.6, but for the INOC region. . . . .	52
5.1	Seasonal mean plots of moisture convergence for JJA and DJF, calculated from ERA5 monthly mean reanalyses for the 21st century through 2018. . . . .	55
5.2	Fig. 3a from Bretherton et al. (2004), showing the precipitation rate across four ocean basins as a function of the column relative humidity, with the CRH given as a fraction. . . . .	56
5.3	Precipitation rate in the RCEMIP simulations, as a function of the CRH. Compare with Fig. 5.2 . . . . .	56
5.4	Precipitation, evaporation, and $P - E$ vs. CRH. . . . .	57
5.5	<b>Top</b> Annual mean moisture convergence calculated from ERA5 reanalyses, with the annual mean CRH contour of 70% superimposed in red. <b>Middle</b> and <b>Bottom</b> Same as <b>Top</b> , but for JJA and DJF. . . . .	59
5.6	Surface fluxes of moist static energy, radiation, and the net energy flux into the atmosphere from the surface. . . . .	60

5.7	Combined fluxes of radiation at the TOA and radiation plus moist static energy flux at the surface. Bottom panel shows the net TOA - SFC flux of energy. . . . .	61
6.1	<b>Top Left</b> Longwave heating rate profile as a function of column relative humidity for the 295 K experiment. <b>Top Center</b> and <b>Top Right</b> Same as <b>Top Left</b> , but for the 300 K and 305 K experiments. <b>Middle Row</b> and <b>Bottom Row</b> Same as <b>Top Row</b> , but for the shortwave and net radiative heating rates. Contours are spaced every 0.25 K Day <sup>-1</sup> . Red represents radiative heating, while blue represents radiative cooling. . . . .	65
6.2	Same as Fig. 6.1, but for the clear-sky radiation tendency. . . . .	67
6.3	Same as Fig. 6.1, but for ACRE. . . . .	69
6.4	<b>Top Row</b> Dry static energy profiles for each CRH bin. <b>Middle Row</b> and <b>Bottom Row</b> , same as <b>Top Row</b> , but for moist static energy and latent energy. The red contour on the plots in the middle and bottom rows shows the altitude of the mid-tropospheric minimum in moist static energy. . . . .	71
6.5	Vertical gradient of moist static energy for each CRH bin. The red line is the zero contour, and coincides with the level where the minimum in moist static energy occurs. . . . .	72
6.6	<b>Top Row</b> Updraft mass fluxes computed by the CRM for each CRH bin. <b>Bottom Row</b> Same as <b>Top Row</b> , but for downdrafts. . . . .	73
6.7	<b>Top Row</b> Net convective mass fluxes computed by the CRM for each CRH bin. <b>Middle Row</b> Large-scale vertical velocity for each CRH bin. . . . .	75
6.8	<b>Top Panel</b> vertically integrated $\bar{w}$ and <b>Bottom Panel</b> $\bar{w}$ across the 500 hPa surface for each of the three RCEMIP simulations, as a function of CRH. . . . .	76
6.9	Transport of moist static energy by the CRM. The nearly vertical red line shows the CRH bin where the largest transport occurs at each altitude. . . . .	77
6.10	Domain-average profiles of the Chikira parameter for each of the three RCEMIP simulations. . . . .	79
6.11	Contour plots of the Chikira parameter, for each CRH bin. The black and red lines show the contours where $\alpha$ equals one or zero, respectively. . . . .	81

6.12	Environmental moistening due to vertical motions induced by <b>Top Row</b> longwave, <b>Middle Row</b> shortwave, and <b>Bottom Row</b> longwave plus shortwave heating. . . . .	82
6.13	Same as Fig. 6.12, but for the moistening due to clear-sky radiative heating rates. . . . .	83
6.14	Same as Fig. 6.12, but for the moistening due to ACRE. . . . .	84
7.1	Reprint of bottom panel of Fig. 2.2. Meridional distribution of surface temperature for the three AQPJAN experiments. . . . .	89
7.2	Zonal mean zonal winds for each of the three AQPJAN simulations with white contours are spaced every $10 \text{ ms}^{-1}$ starting at $5 \text{ ms}^{-1}$ . The black lines show the zero contour. . . . .	90
7.3	<b>Left Column:</b> Zonal mean meridional streamfunction for each AQPJAN experiment. Contours are drawn every $3 \times 10^8 \text{ kg s}^{-1}$ . Red (blue) shading indicates clockwise (counter-clockwise) circulation. The black contours show where the streamfunction passes through zero. <b>Right Column:</b> Zonal mean precipitation (blue), evaporation (brown), and $P - E$ (light blue) for each of the AQPJAN simulations. Light gray vertical lines at 10S and 10N show the latitude limits used for analysis later in this chapter. . . . .	92
7.4	Integrated northward transports of energy (black) and moisture (blue) for the three AQPJAN simulations. . . . .	94
7.5	Probability density functions of CRH for the RCEMIP (black) and AQPJAN (Blue, Yellow, or Red) simulations ranging from $10^\circ\text{S}$ to $10^\circ\text{N}$ . <b>Bottom right</b> The three AQPJAN distributions compared to the ERA5 CRH distribution for $10^\circ\text{S}$ to $10^\circ\text{N}$ . . . . .	96
7.6	<b>Top Row</b> CRE at TOA, <b>Middle Row</b> CRE at Surface, and <b>Bottom Row</b> ACRE binned by CRH for each of the three AQPJAN simulations. Compare with Figs. 3.3, 3.7 . . .	98
7.7	<b>Top Row</b> Precipitation rate, evaporation rate, and $P - E$ as a function of CRH for the RCEMIP simulations, as presented previously in Chapter 5. <b>Bottom Row</b> Same as <b>Top Row</b> , but for the AQPJAN simulations. . . . .	99

7.8	<b>Top Row</b> Net fluxes of radiation and energy at the TOA, surface, and into the atmosphere as a function of CRH for the RCEMIP simulations, as presented previously in Chapter 5. <b>Bottom Row</b> Same as <b>Top Row</b> , but for the AQPJAN simulations. . . . .	100
7.9	Profiles of the moist static energy for the AQPJAN simulations, binned by the CRH as in Chapter 6. Compare with Fig. 6.4 . . . . .	101
7.10	Profiles of the CRM moist static energy flux for the AQPJAN simulations, binned by the CRH as in Chapter 6. Compare with Fig. 6.9 . . . . .	101
7.11	Profiles of the net radiation tendency for the AQPJAN simulations, binned by the CRH as in Chapter 6. Compare with the bottom row of Fig. 6.1 . . . . .	102
7.12	Profiles of the net radiatively-driven moistening for the AQPJAN simulations, binned by the CRH as in Chapter 6. Compare with Fig. 6.12 . . . . .	103
A.1	<b>Left</b> Temperature profiles for each of the RCEMIP simulations. Curved green lines are moist adiabats. <b>Right</b> Dry static stability profiles for each simulation. . . . .	120
A.2	<b>Left</b> Profiles of $D_R$ calculated from the full-sky longwave cooling rate. <b>Right</b> Profiles of cloud fraction. . . . .	122
A.3	<b>Panel A</b> Domain mean profiles of buoyancy flux computed on the CRM, with horizontal lines showing the altitude where the flux passes through zero aloft. <b>Panels B, C, and D</b> Full-sky longwave temperature tendency, Normalized cloud fraction, and $D_R$ normalized by the upper-level peak, respectively. Horizontal dotted lines show the level where the buoyancy flux passes through zero. <b>Panels E-H</b> , same as <b>Panels A-D</b> , but with temperature as the vertical coordinate, rather than altitude. . . . .	123
A.4	<b>Left</b> Domain average temperature of maximum cloud fraction and the level where the buoyancy flux passes through zero. <b>Center</b> Domain average temperature where $D_R$ is largest, and divergence-weighted temperature (defined in the text). <b>Right</b> Domain-average TOA brightness temperature. . . . .	124

A.5 **Top Row** Contours of cloud fraction binned by the CRH. Thin grey lines range from 0 to 0.2 with a spacing of 0.02, and the thick black line at a cloud fraction of 0.2. Shading ranges from 0 to 1 with a spacing of 0.1. The red line shows the level of maximum cloud fraction for each CRH bin. **Bottom Row** Contours of  $D_R$  computed with the full-sky longwave tendency with the black lines showing the zero contour and the red line showing the level of maximum  $D_R$ . . . . . 126

A.6 **Top Row** Contours of buoyancy flux binned by the CRH. The red line shows the level where the buoyancy flux passes through zero for each CRH bin. **Bottom Row** Contours of SPDT (defined in the text) computed by the CRM. In these plots the red line again shows the level where the buoyancy flux passes through zero for each CRH bin . . . . . 127

A.7 **Panel A** The temperature of the level of maximum cloud fraction in each CRH bin for each RCEMIP simulation. **Panel B** The change in temperature of the maximum cloud level for each set of simulations. **Panel C** Same as **Panel B**, but divided by the change in SST between simulations. **Panels D-F** and **G-I** same as **Panels A-C**, but for the temperature of the maximum of  $D_R$ , and the high cloud temperature (defined in the text), respectively. . . . . 131

A.8 Same as Fig. A.7, but for the **Top Row** full-sky emission temperature, **Middle Row** clear-sky emission temperature, and **Bottom Row** the CTE (defined in the text). . . . . 134

A.9 Same as Fig. A.7, but for the **Top Row** full-sky radiative tropopause, and **Bottom Row** the clear-sky radiative tropopause. . . . . 136

B.1 Scatter plot composite analysis comparing actual and estimated shortwave CRE in the EPAC region, for different ENSO states. Figure repeated from Fig. 4.11 . . . . . 139

B.2 Same as Fig. B.1, but for the longwave CRE in the EPAC region. . . . . 141

B.3 Correlation between actual and estimated shortwave CRE in the WPAC region, as in Fig. B.1 . . . . . 142

B.4 Same as Fig. B.2, but for the longwave CRE in the WPAC region. . . . . 143

B.5	Same as Fig. B.2, but for the shortwave CRE in the INOC region. . . . .	144
B.6	Same as Fig. B.2, but for the longwave CRE in the INOC region. . . . .	145
C.1	CRH distributions for each set of RCEMIP, AQPJAN10, and AQPJAN30 data. The bottom right panel compares the AQPJAN30 data to the ERA5 CRH distribution bounded by 30°S-30°N. . . . .	147
C.2	TOA and surface CRE and ACRE binned by CRH for each of the three AQPJAN simulations ranging from 30°S to 30°N. Compare with Figs. 3.3, 3.7, and 7.6. . . . .	148
C.3	Precipitation and Evaporation rates for the AQPJAN10 region and AQPJAN30 region. Compare with Fig. 7.7 . . . . .	149
C.4	TOA, surface, and net energy budget for the AQPJAN10 and AQPJAN30 regions. Compare with Fig. 7.8 . . . . .	150
C.5	Comparison of net ACRE for the AQPJAN10 and AQPJAN30 regions. Compare with Fig. 6.3 . . . . .	152
C.6	Comparison of tropospheric moistening by net radiation for the AQPJAN10 and AQPJAN30 regions. . . . .	154

# Chapter 1

## Introduction

### 1.1 Cloud Radiative Effect

In the earth-atmosphere system, photons can largely be separated into two groups determined by their origin. Solar energy is mostly in the form of visible light, which is composed of higher-energy photons with shorter wavelengths. The earth is cooled primarily by emitting radiation in the infrared range, which is composed of lower-energy photons with longer wavelengths. While radiation occurs over a continuum of wavelengths, separating it into these two longwave and shortwave domains aids in the conceptual understanding of radiative processes.

The radiative impact of clouds on the earth-atmosphere system is a delicate balance between competing longwave and shortwave effects. Broadly, clouds warm the planet in the longwave by absorbing emission from the surface and re-emitting to space at cooler temperatures. In the shortwave, clouds cool the planet by reflecting solar radiation, increasing the effective local albedo (Ramanathan et al., 1989). This cloud radiative effect (CRE) was quantified by Ramanathan (1987) as the difference between full-sky and clear-sky radiative fluxes at the top of the atmosphere (TOA). The CRE quantifies the impact of clouds on the TOA radiation balance, and in turn is important for calculating the magnitude of cloud feedbacks under a doubling of CO<sub>2</sub>, (Boucher et al., 2013).

Initial studies (Harrison et al., 1989; Ramanathan, 1987; Ramanathan et al., 1989) computed the CRE at TOA using satellite observations of Earth's radiation budget. Generally, the studies found a positive longwave CRE and a negative shortwave CRE. The properties of individual clouds determined whether the net CRE was positive or negative. For instance, low-level stratocumulus decks, like those commonly found off the coasts of California and Peru, emit to space at near-surface temperatures. This leads to a small longwave CRE. Those same clouds have a large shortwave CRE due to the increased reflection of solar radiation back to space (Harrison et al.,

1989). The strong shortwave effect overwhelms the weak longwave effect, so these clouds cool the system.

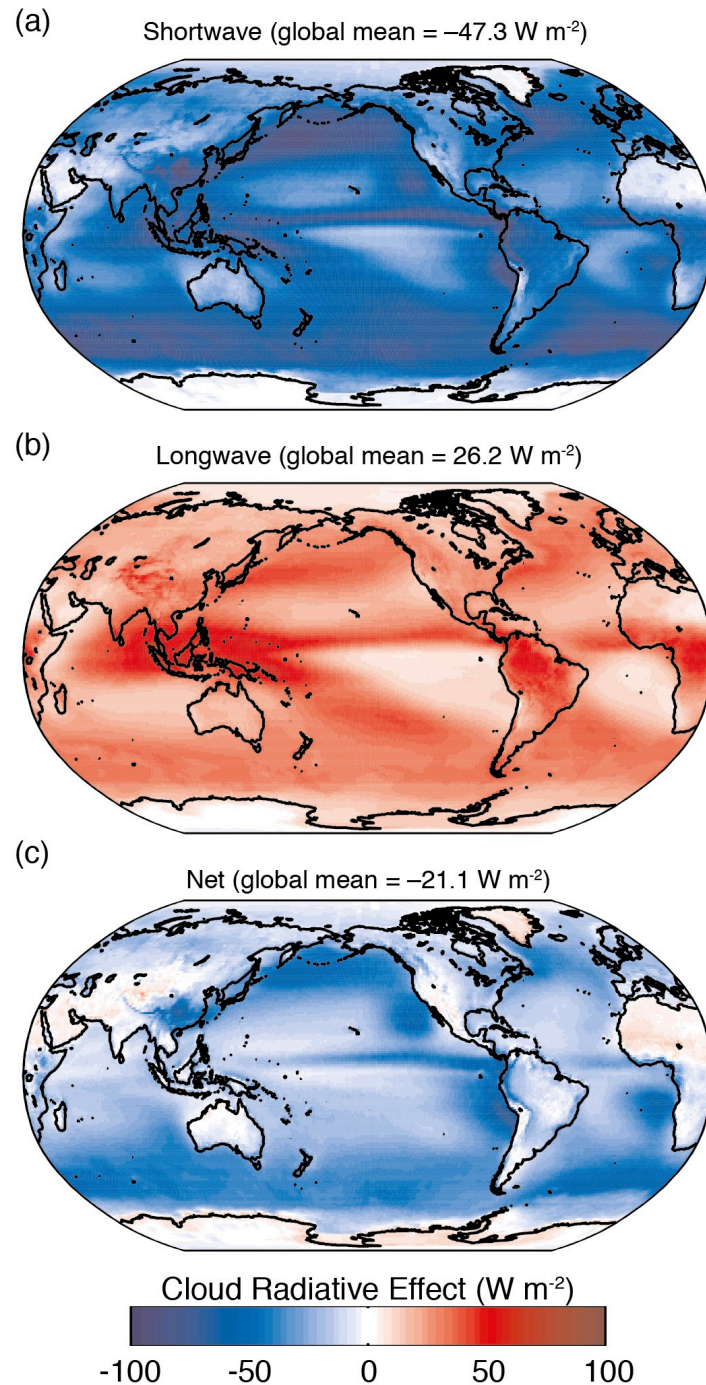


**Figure 1.1:** Annual mean cloud radiative effect from CERES measurements for the period 2001 - 2011. Reproduced, from Fig. 7.7 of Boucher et al. (2013). ©World Meteorological Organization

The total CRE is calculated as the difference between the longwave and shortwave terms which can both be large. Small changes in cloud properties such as cloud water content, depth, and altitude, can have a large effect on the CRE. This is especially important in the tropics where observations have shown that over large regions the longwave and shortwave effects may both be large, but the net CRE is very small (see, for example, Allan (2011) and panel (c) of Fig. 1.1).

Allan (2011) decomposed the CRE into surface and atmospheric components by combining satellite measurements with a surface radiation budget dataset. This analysis allowed for investigation into how clouds impact the radiative transfers of energy between the surface and atmosphere. Allan (2011) found that the small net CRE in the tropics was composed primarily of a large longwave heating in the atmosphere and a large shortwave cooling at the surface. The deep convective clouds in this region helped to redistribute energy upwards and make the atmospheric profile more stable. This indicates that in addition to transporting energy upwards to balance convective instability as predicted in early theories (Manabe and Strickler, 1964; Riehl and Malkus, 1958), deep tropical clouds also change the radiative properties of the atmosphere itself.

## **1.2 Convection in the Tropics**

### **1.2.1 The Earth's Energy Balance**

Radiation is the primary method of energy transfer between the earth and the rest of the universe. However, other methods of energy transfer are important within the earth system. Dines (1917) presented a simple schematic of the earth's energy balance that included an upward flux of non-radiative energy from the surface to the atmosphere (see Fig. 1.2). He separated this non-radiative energy into a moist component and a dry component. The dry component represented the motion of warm, near-surface air up to altitudes of about 5000 ft (1500 m). The moist component involved the loss of energy from the surface through the evaporation of water, and the gain of energy in the atmosphere when the water vapor later condensed. A modern analysis of the earth's energy budget (Trenberth et al., 2009) shows that the globally averaged energy transport by moist and dry convection is slightly less than  $100 \text{ Wm}^{-2}$ , mostly composed of the moist component.

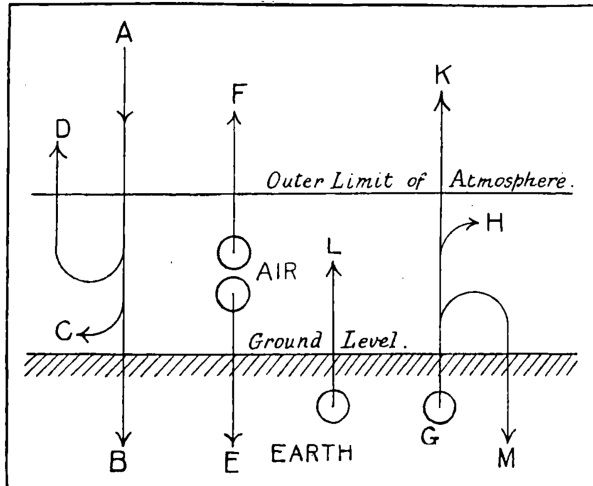


**Figure 1.2:** The heat balance of the earth and atmosphere, as it was understood in the early 20<sup>th</sup> century. Reprinted from Dines (1917)

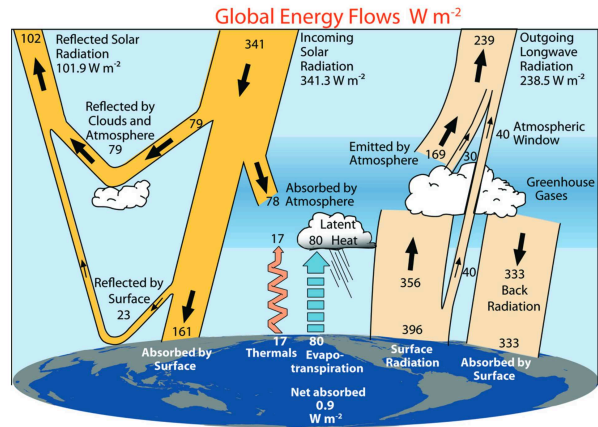


**Figure 1.3:** A remarkably similar figure to Fig. 1.2, updated with 21<sup>st</sup> century measurements. Reprinted from Trenberth et al. (2009). ©American Meteorological Society. Used with permission

This is about 28.4% of the average incoming solar radiation at the TOA. Dines (1917) estimated the value to be slightly lower, around 27.8% of the incoming solar radiation.

### 1.2.2 Radiative Convective Equilibrium

The inclusion of convection is vital to achieve realistic results in atmospheric models. Early single-column studies (Manabe and Strickler, 1964; Manabe and Wetherald, 1967) showed that the state of pure radiative equilibrium leads to a surface that is too warm, and a troposphere that is too cold. In addition, the lapse rate is unstable to dry convection. Radiative-convective equilibrium (RCE), where convective heating balances radiative cooling, is the simplest equilibrium state of the earth’s atmosphere (Wing et al., 2020). Manabe and Strickler (1964) and Manabe and Wetherald (1967) performed the first simulations of what we now call RCE using a simple one-dimensional model of the atmosphere. They showed that a physically realistic equilibrium temperature profile (see Fig. 1.4) could be found by using a method known as convective adjustment.

Convective adjustment is a simple algorithm for removing convective instability. It involves comparing the model lapse rate to the moist adiabatic lapse rate at every timestep. If the model lapse rate between two layers exceed this critical lapse rate, the profile is considered unstable to convection. The convective instability is removed by adjusting the model lapse rate to the

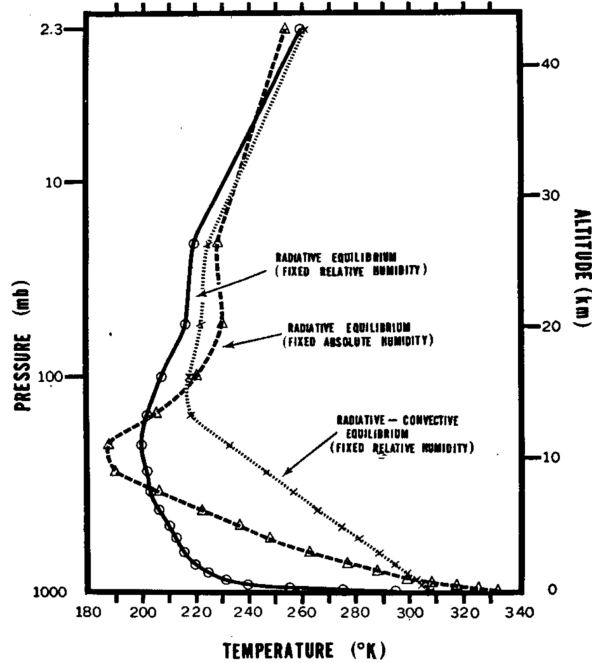


**Figure 1.4:** Equilibrium temperature profiles for simulations of radiative equilibrium with fixed relative humidity, with fixed absolute (specific) humidity, and radiative-convective equilibrium with fixed relative humidity. Reprinted from Manabe and Wetherald (1967) ©American Meteorological Society. Used with permission

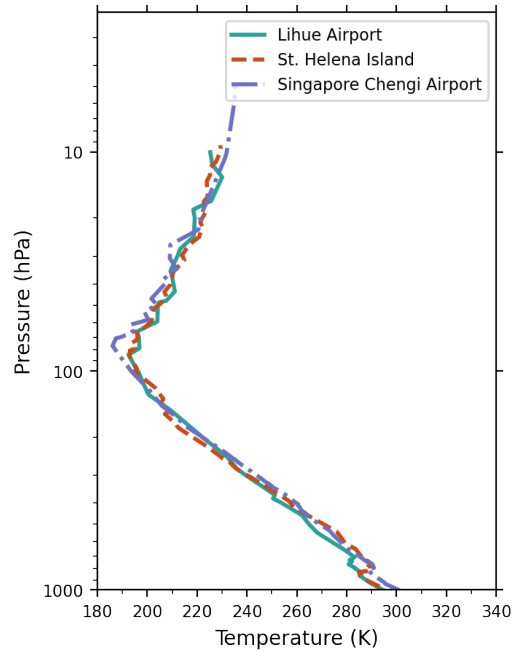


**Figure 1.5:** 12Z Temperature soundings on 25 January 2020 from three locations within the tropics: Lihue Airport Kaua'i, Hawai'i (159.34W, 21.99N), Saint Helena Island, United Kingdom (5.66W, 15.93S), and Singapore Changi Airport, Singapore, (103.98E, 1.36N)

critical lapse rate in a way that preserved static energy between the two layers. In practice, this results in a net upward flux of energy, mimicking the effects of convection. Using the method of convective adjustment, Manabe and Strickler (1964) calculated a temperature profile that is a reasonable approximation to a tropical temperature profile. Fig. 1.4 shows a temperature sounding from Manabe and Wetherald (1967), while 1.5 shows observational soundings taken from several tropical locations, for the purpose of comparison.

## 1.3 Convectively Coupled Tropical Dynamics

### 1.3.1 Atmospheric Transports of Energy

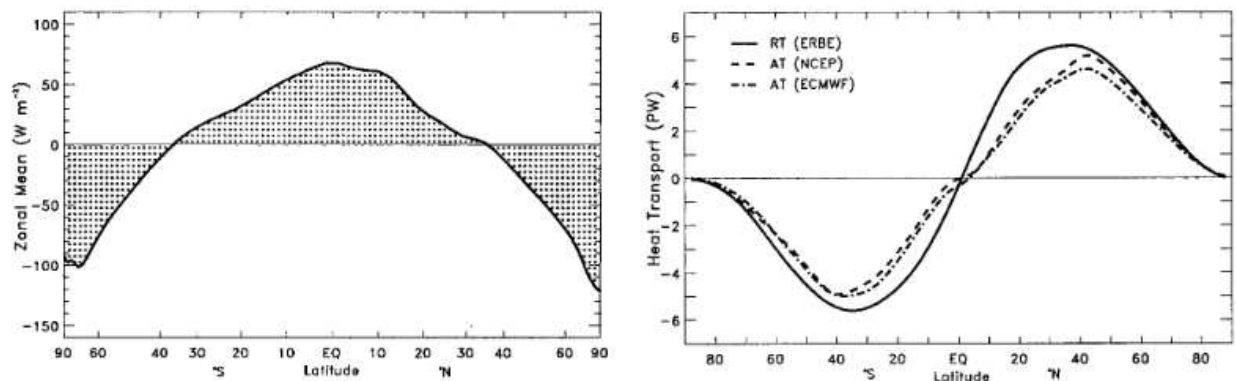


**Figure 1.6:** Fig. 1 and Fig. 2 reproduced from Trenberth and Caron (2001). The left panel shows the annual mean TOA radiation balance from ERBE satellite observations. The solid line in the right panel shows the required atmosphere plus ocean northward energy transport required by the radiation balance. The two dashed lines show the atmospheric energy transport estimated from two reanalysis products. ©American Meteorological Society. Used with permission

The energy budgets of Dines (1917) and Trenberth et al. (2009) account for the exchange of energy between the earth and atmosphere. This global mean perspective necessarily neglects the movements of energy within the atmosphere or the lower boundary (the oceans and the solid earth). Spatially resolved measurements of the TOA radiation budget reveal a convergence of radiation in the tropics and a divergence at the poles. This requires a net poleward flux of energy *within* the earth system from the tropics to higher latitudes.

Vonder Haar and Oort (1973) used satellite and radiosonde observations to calculate the poleward energy transport in the northern hemisphere oceans. They found that approximately 40% of the poleward transport occurs in the oceans, while 60% occurs in the atmosphere. Later work indicated that calculations using radiosonde measurements underestimated the atmospheric energy transports: Trenberth and Caron (2001) performed similar calculations with updated measurements and reanalyses and found that most of the transport in the northern hemisphere, and almost all of the transport in the southern hemisphere occurs in the atmosphere, with only a small fraction oc-

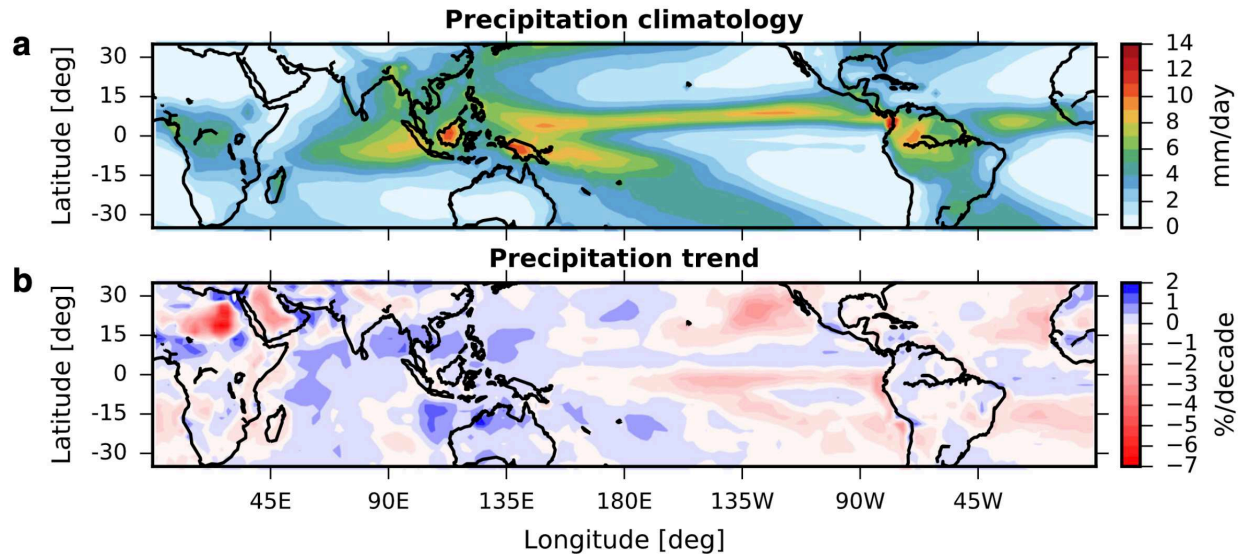


**Figure 1.7:** Annual mean precipitation climatology and de-seasonalized precipitation trend from GPCP, 1979 - 2017. Reproduced from Byrne et al. (2018) under Creative Commons CC BY license.

curing in the oceans. This can be seen in Fig. 1.6, which shows the energy transport by the atmosphere as presented in Trenberth and Caron (2001). In higher latitudes the energy transport is largely due to baroclinic eddies, while in the tropics the transport is largely due to the mean flow. A large part of our understanding of the energy export out of the tropics is due to the work of Riehl and Malkus (1958) on the energy balance of the intertropical convergence zone (ITCZ).

### 1.3.2 The Intertropical Convergence Zone

The ITCZ is a band of deep convective clouds that is closely related to the rising branch of the Hadley circulation. The ITCZ has long been understood as crucial to the redistribution of energy from the tropics to higher latitudes in the Hadley cells. (Neelin and Held, 1987; Riehl and Malkus, 1958). Nearly one third of the Earth’s annual precipitation falls within this tropical rain belt in the present climate (Kang et al., 2018). Recent work has led to a greater understanding of the processes that control the mean characteristics of the ITCZ in the present climate (Kang et al., 2018; Schneider et al., 2014), as well as expected changes in a warmer climate (Byrne et al., 2018).

Many state-of-the-art coupled climate models still fail to accurately represent the climatological distribution of tropical precipitation. In the present climate the ITCZ sits slightly north of the

equator (see panel a of Fig. 1.7). Models tend to predict a spurious second precipitation maximum in the southern hemisphere, a bias that has come to be known as the double ITCZ problem (Mehcho et al., 1995). This and other challenges indicate that the evolution of the ITCZ in a warmer climate remains an important question deserving of focused basic research (Bony et al., 2015).

### 1.3.3 Exports of Energy out of the ITCZ

In their germinal paper, Riehl and Malkus (1958) (hereafter RM58) performed an energy budget analysis of the “equatorial trough zone,” which we now call the ITCZ. RM58 performed their analysis of the transport of energy within the ITCZ by looking at the sum of enthalpy, potential energy, and latent energy. This combination is now known as the moist static energy,  $h$ , while the dry static energy,  $s$ , is the sum of enthalpy and potential energy. The static energies are useful quantities because they are approximately conserved following a parcel under dry adiabatic processes. In addition, the moist static energy is conserved during the condensation or evaporation of water vapor.

RM58 found that at low levels the net energy transport is into the ITCZ, with a net influx of latent energy by the mean flow. At upper levels, the net transport is out of the ITCZ, with a poleward flux of potential energy. Comparing the energy transport in the lower and upper levels, RM58 found that the ITCZ exports energy towards higher latitudes. This required a convergence of energy into the ITCZ from the surface. In order to balance the export of energy out of the ITCZ at upper levels, RM58 needed a mechanism to vertically transport latent and sensible heat from the moist, well-mixed boundary layer.

The dashed line in Fig. 1.8 shows the vertical distribution of  $h$  in the ITCZ, as calculated by RM58. RM58 found that  $h$  was well-mixed in the boundary layer, decreased up to a mid-tropospheric minimum, then began to increase with decreasing pressure. The mid-tropospheric minimum would come to be an important point in their work. They first suggested that the vertical transport may be accomplished by large-scale motions. However transport by the large-scale flow would weaken the moist static energy gradient because  $h$  is conserved following a parcel. The

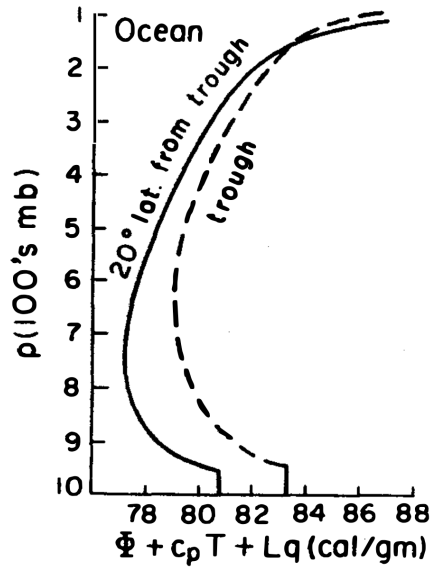


**Figure 1.8:** Vertical distribution of moist static energy in the ITCZ, reprinted from Riehl and Malkus (1958). “Ocean” refers to measurements taken over the ocean.

minimum in  $h$  observed in the mid-troposphere indicates that transport by the large-scale flow cannot account for the vertical transport of energy required in the ITCZ.

RM58 then suggested that the energy transport could be achieved by the “embedded central cores within in cumulonimbus clouds which are protected from mixing with the surroundings by the large cross section of the clouds.” In other words, deep convective clouds can act as protective tunnels around the central updrafts, allowing buoyant, moist air from the boundary layer to reach the highest levels of the troposphere without significantly mixing with the environment. They further estimated that only about “1500-5000 active undilute cloud towers around the globe” are needed to lift enough energy to balance the export of energy out of the ITCZ. The hypothesis of RM58 has been well supported in the subsequent decades, and remains critical to understanding the vertical and poleward energy transport within the tropical atmosphere.

Neelin and Held (1987) extended the analysis of RM58 by considering the vertically integrated budget of moist static energy. They presented a two-layer model of low-level convergence and upper-level divergence in the deep tropics. The difference in the divergence-weighted vertically integrated moist static energy at upper and lower levels, called the gross moist stability, was found

to be a useful quantity for simple models of tropical convergence. Developments regarding the gross moist stability and related quantities were reviewed by Raymond et al. (2009).

## 1.4 Temperature Dependence of High Clouds

Riehl and Malkus (1958) found that deep convective clouds within the ITCZ lift moist static energy from near the surface where it can then be transported poleward. Recent work has furthered our understanding of the thermodynamic constraints that regulate the behavior of these convective clouds, and of the important role played by radiation. Over the past two decades, it has been suggested that the temperature of anvil clouds should be independent of the surface temperature. The consequence of this would be a strong longwave CRE resulting from high anvil clouds emitting to space at the cold temperatures of the upper troposphere. This has come to be known as the fixed anvil temperature (FAT) hypotheses, first proposed by Hartmann and Larson (2002). The FAT hypothesis results from a series of thermodynamic arguments building upon one another.

The argument begins with horizontal gradients of temperature. In the midlatitudes, large-scale horizontal motions can be approximated by geostrophic flow, where the horizontal pressure-gradient force is balanced by the Coriolis effect in the equations of motion (Charney, 1963). In the tropics the Coriolis parameter is small, so horizontal differences in pressure are quickly reduced by the pressure-gradient force. This leads to the result, confirmed in observations, that horizontal pressure gradients in the tropics are small, compared to those of middle latitudes. Using hydrostatic balance, it can be shown that a weak horizontal pressure gradient at all levels requires a weak horizontal temperature gradient. This weak temperature gradient approximation (Charney, 1963; Sobel et al., 2001) simplifies the thermodynamic energy equation so that in clear regions of the tropics, the primary balance is between radiative cooling and subsidence warming.

The argument of Hartmann and Larson (2002) continues by noting that radiative cooling in the troposphere is primarily from longwave emission by water vapor, which is constrained by temperature. At the cold temperatures of the upper troposphere, the saturation vapor pressure limits the amount of water vapor, leading to weak longwave cooling. In addition, emission from the rota-

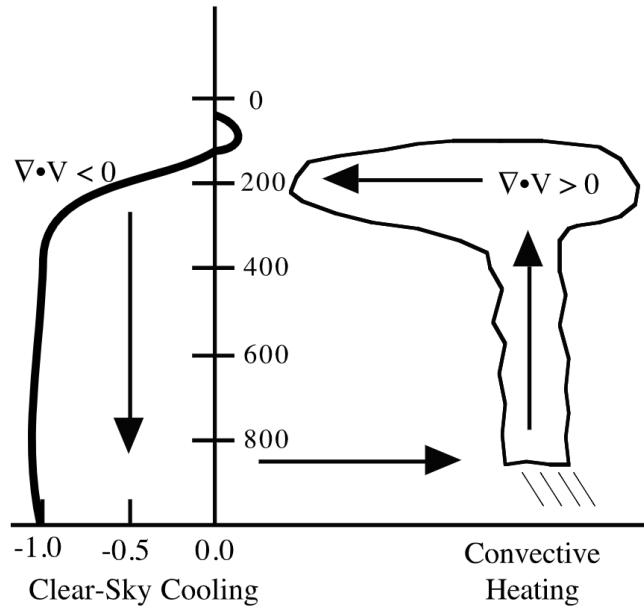


**Figure 1.9:** Schematic from Hartmann and Larson (2002) showing the principles of the FAT hypothesis. ©American Geophysical Union. Used under stated permissions policy.

tional band of water vapor shuts down at these cold temperatures. The inefficient longwave cooling causes a reduction in vertical motions which leads to a vertical divergence of the subsiding motion in clear regions. Through mass continuity, this vertical divergence must be balanced by horizontal convergence into clear regions. This in turn requires horizontal divergence out of cloudy regions, leading to the formation of anvil clouds (Bony et al., 2016; Seeley et al., 2019). Because the level where clear-sky longwave cooling becomes inefficient is determined only by the temperature, this places a thermodynamic constraint on the temperature of anvil clouds. A schematic of this process is shown in Fig. 1.9. There has been evidence for FAT in idealized modeling studies (Hartmann and Larson, 2002; Kuang and Hartmann, 2007). More realistic simulations (Zelinka and Hartmann, 2010) indicate that anvil temperatures increase with surface warming, although at a slower rate than the increase in surface temperature.

The CRE depends on the temperature of anvil clouds, but it also depends on the spatial extent of those same clouds. Lindzen et al. (2001) proposed that surface warming may lead to a reduction in the fractional area of tropical anvil clouds. This had the effect of linking the arguments of the FAT hypothesis with the iris effect. More clear skies would allow a greater fraction of longwave

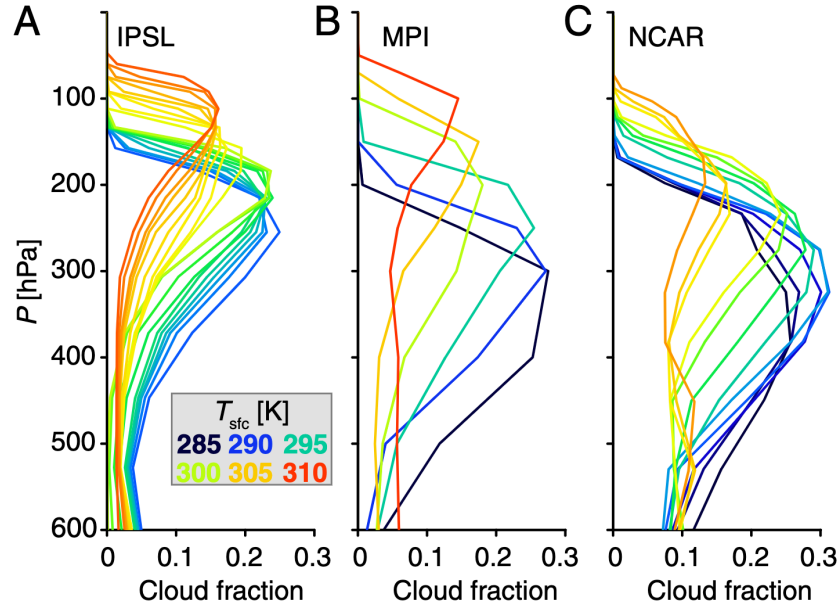


**Figure 1.10:** Profiles of cloud fraction for various SSTs using three independent GCMs. Reproduced from Bony et al. (2016). ©American Geophysical Union. Used under stated permissions policy.

radiation to escape to space, constituting a negative feedback on warming. This effect, termed the infrared iris, led to a spirited debate around the original paper (e.g. Hartmann and Michelsen (2002); Lindzen et al. (2002)). However, there has been observational evidence for an iris effect (Saint-Lu et al. (2020); Zelinka and Hartmann (2011)), as well as evidence from modeling studies (Bony et al. (2016); Mauritsen and Stevens (2015); Zelinka and Hartmann (2010)).

Bony et al. (2016) extended the thermodynamic arguments of the FAT hypothesis to argue for a thermodynamic control on the fractional area of high clouds. This had the effect of linking the arguments of the FAT hypothesis with the iris effect. Bony et al. (2016) proposed a mechanism linking the radiatively driven divergence from cloudy updrafts to changes in the static stability, in what can be called a stability iris effect. They note that for a given amount of radiative cooling, the magnitude of the vertical motion is inversely proportional to the static stability. For a warmer surface temperature, the stability at cloud top should be higher because it is calculated from a warmer moist adiabat. A more stable atmosphere would require less sinking motion to balance the same amount of radiative cooling, leading to a reduction in the radiatively driven horizontal divergence. This in turn would imply a reduction in the high cloud amount in a warmer climate.

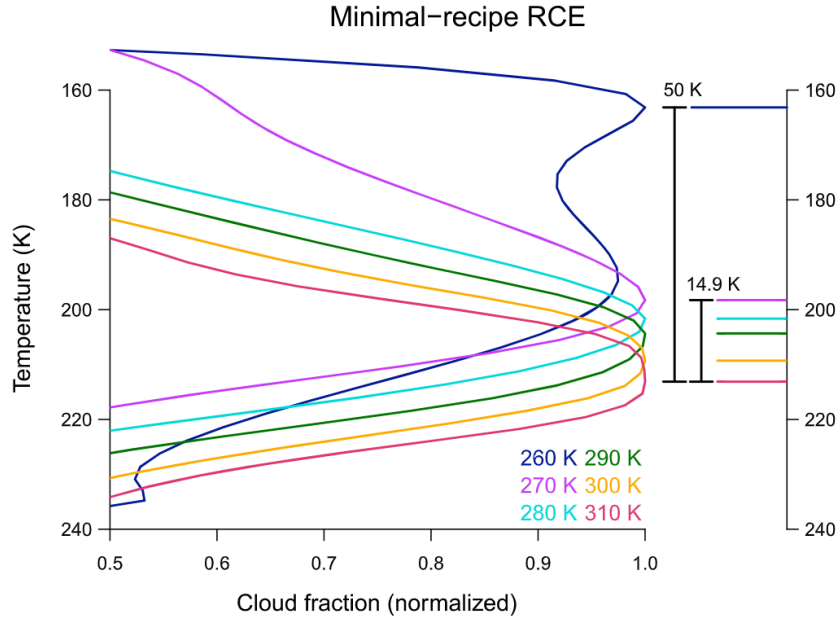


**Figure 1.11:** Profiles of cloud fraction for various SSTs with temperature as the vertical coordinate. Reproduced from Seeley et al. (2019). ©American Geophysical Union. Used under stated permissions policy.

They found broad support for their conclusions using three GCMs configured in RCE over tropical SSTs. Recent work by Saint-Lu et al. (2020) has found support for this stability iris using satellite and reanalysis data. The decrease in the longwave CRE associated with a decrease in the fractional coverage of high clouds would work in opposition to the increase predicted by a fixed anvil temperature, complicating the picture.

Seeley et al. (2019) presented a critique of the ideas that lead to FAT. They argued that the decline in longwave cooling at a specific temperature is valid only if water vapor is assumed to be a gray gas. In idealized simulations including only the “ingredients” used to predict FAT they found no evidence for a fixed anvil temperature (see Fig. 1.11). Instead, they found evidence for a fixed tropopause temperature (FiTT) at the level where the longwave cooling rate first passes through zero. It should be noted that the range of temperatures examined by Seeley et al. (2019) includes several SSTs that are much colder than those observed in the tropics (Hartmann et al., 2019).

Hartmann et al. (2019) responded to Seeley et al. (2019). They used tracer experiments from a cloud resolving model to show that the temperature where the buoyancy flux equals zero in

the upper troposphere changed very little when the surface temperature was increased. They also found that this level was near the level where the radiatively driven horizontal divergence peaked, showing evidence for a temperature control on the tops of convective updrafts. In the highest levels of the troposphere, there was a layer with a large negative buoyancy flux that coincided with large values of the tracer, indicating air that had recently been inside cloudy updrafts was overshooting the neutral buoyancy level to become negatively buoyant, before mixing with the environment. This overshooting of parcels from within cloudy updrafts can deposit small ice particles above the level of neutral buoyancy. Such particles have long lifetimes due to the extremely cold temperatures near the cold point.

## 1.5 Outline

Previous sections provided an overview of important developments for our understanding of the tropical atmosphere. This section provides an outline of this thesis, and discusses some of the major findings of the work. This thesis is organized as follows. Chapter 2 gives a brief description of the model simulations, observations, and reanalyses that will be used throughout. It also introduces a method for analyzing the cloud radiative effect and other fields using a quantity known as the column relative humidity (CRH, Bretherton et al. (2004)). This method will be used extensively throughout this thesis.

In Chapter 3, the method is applied to three non-rotating simulations of RCE with uniform SSTs to show that the CRE at TOA as a function of CRH is nearly independent of the SST. Calculations are then repeated using satellite observations and reanalyses, which show a broad agreement with the results from the model simulations. A CRH value of approximately 70% is found to be an important threshold for separating dry regions with low CRE from humid regions with high CRE.

It is then shown in Chapter 4 that the CRH can be used to estimate a CRE field that shows broad agreement with CRE from observations. The remainder of Chapter 4 investigates the accuracy of this estimation on different time-scales, and asks whether large-scale features of the climate such as ENSO impact the effectiveness of the method.

In Chapter 5, the moisture and energy budgets of the RCEMIP simulations are investigated within the CRH framework. The precipitation rate is found to be a universal function of the CRH, like the CRE, similar to results from the initial study that introduced the CRH (Bretherton et al., 2004). The difference between precipitation and evaporation changes sign at approximately the same CRH value in each RCEMIP experiment, and coincides with the 70% threshold that was identified in Chapter 3. This is then investigated using ERA5 reanalyses for the CRH and moisture convergence fields, and shows a broad agreement between the 70% threshold and the level where moisture convergence goes to zero. Analysis of the net energy flux finds that the curves also change sign near 70% CRH, although the CRH value increases slightly as the surface warms. Combined, these two balances show that energy is exported down the gradient out of the humid regions, while moisture is transported up the gradient into the humid regions (Neelin and Held, 1987).

In Chapter 6, the CRH analysis is expanded to investigate the vertically resolved radiative heating. The atmospheric cloud radiative effect is found to be strong enough to change the sign of the net radiation tendency in the most humid regions of the domain. This positive radiation tendency is found to induce large-scale rising motion in the same regions where convective-scale rising motion is diminished. It also plays a part in a radiatively driven moisture feedback in which large-scale rising motion lifts water vapor, which then condenses and leads to a stronger atmospheric cloud radiative effect.

In Chapter 7, several key calculations from previous Chapters are repeated using a more realistic rotating aquaplanet forced by a meridionally varying SST distribution. These are included to show that the results of earlier chapters are robust and can be qualitatively reproduced using simulations that are more realistic than the RCEMIP experiments. Conclusions are then summarized, and an explicit link is drawn from the work of this thesis to the germinal work of Riehl and Malkus (1958), along with a discussion of the direction of future work.

# Chapter 2

## Methods

### 2.1 Model Output, Reanalyses, and Observations

Analyses discussed in the following chapters will utilize data from a number of sources. Much of the analysis will be focused on output from idealized simulations using a state-of-the-art global circulation model (GCM), the NCAR Community Atmosphere Model (CAM). There are two sets of simulations. The first is an extremely idealized simulation forced by a non-rotating aquaplanet with a uniform SST, following the RCEMIP protocol of Wing et al. (2018). The second introduces rotation, and utilizes a zonally symmetric SST distribution inspired by the AquaPlanet Experiment of Neale and Hoskins (2000). Results from calculations with the model outputs are compared to ECMWF ERA5 reanalyses, to CERES satellite observations, and to an index of ENSO. Full descriptions of the data used are given in the following sections.

#### 2.1.1 Idealized Non-Rotating Tropical World

Global atmospheric models forced by idealized sea surface temperatures (SSTs) provide an intermediate level of complexity between simple single-column models and fully coupled earth system models. Atmospheric models configured in radiative-convective equilibrium (RCE) allow for a convenient sandbox in which to investigate fundamental physical processes in the absence of complications due to land surfaces, rotation, meridional gradients in temperature, and other asymmetries. The response to warming of CRE, large-scale circulations, anvil temperature, and other processes can be investigated by simply increasing the SSTs that force the model. Interesting results can then be brought out of the simple model and tested using more complicated models, reanalyses, and observations.

The Radiative-Convective Equilibrium Model Intercomparison Project (RCEMIP, described by Wing et al. (2018)) provides a standardized experimental protocol that can be used to compare the tropical response to surface warming across different models. RCEMIP specifies models to be

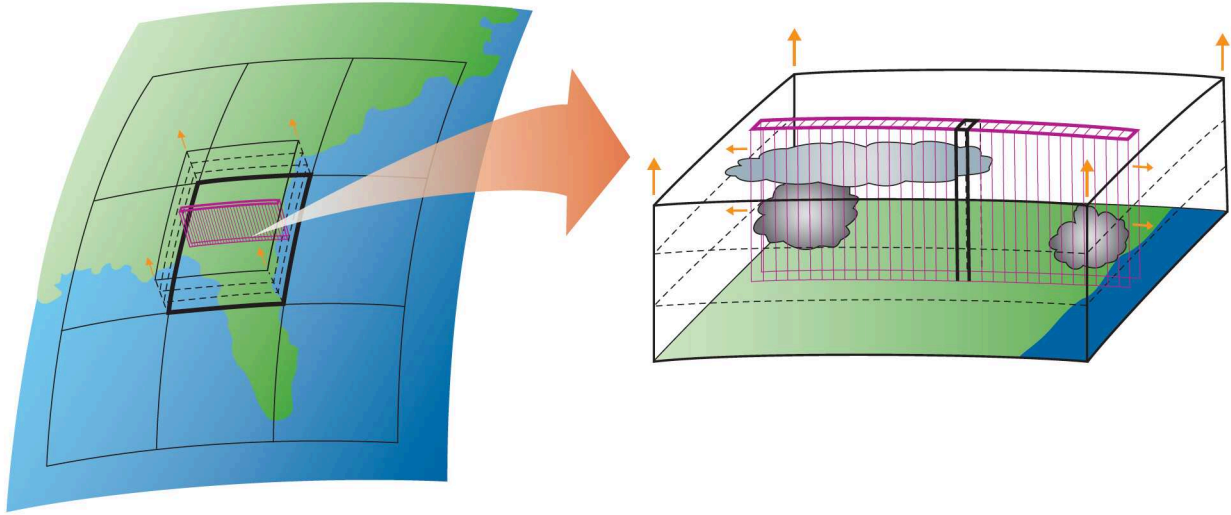


**Figure 2.1:** Cartoon showing the concept of super-parameterization. A two-dimensional cloud resolving model is embedded within a GCM grid cell to simulate sub-grid scale processes.

run over uniform SSTs of 295 K, 300 K, and 305 K (22°C, 27°C, and 32°C) to approximate the warm SSTs found near the equator. The simulations prescribe uniform insolation at all latitudes without a diurnal cycle to achieve homogeneous boundary conditions, so the shortwave effect may be somewhat larger than is expected in the real tropics. 720 timesteps of hourly-mean data, corresponding to 30 days, are used in the following analysis. An extensive analysis of more than 30 models following the RCEMIP protocol is presented by Wing et al. (2020).

The majority of results in this thesis come from three simulations using the super-parameterized version of the Community Atmosphere Model (SP-CAM) in radiative-convective equilibrium. The model was configured as a non-rotating aquaplanet with uniform SSTs, following the RCEMIP protocol. The horizontal grid used a uniform lat-lon grid spacing of 1.25° longitude by 0.92° latitude leading to larger grid cells near the equator and smaller grid cells near the poles. Domain-averaged values take this variable grid area into account by weighting means against the cosine of latitude. The model uses a hybrid sigma-pressure vertical coordinate with 26 layers that were then projected onto isobars for analysis.

The super-parameterized version of CAM embeds a two-dimensional cloud-resolving model (CRM) within each GCM grid cell. The CRM is the System for Atmospheric Modeling, originally

documented in Khairoutdinov and Randall (2003) (See Fig. 2.1 for a cartoon of this configuration). Using the CRM allows the explicit simulation of sub-grid scale processes. The CRM solves the equations of motion on a grid with a horizontal grid spacing of 4 km that shares the bottom 24 layers of the GCM. Updraft mass fluxes are calculated as

$$M_u = \rho \sigma_u w_u, \quad (2.1)$$

where  $\rho$  is the air density of the layer,  $w_u$  is the vertical velocity inside updrafts, and  $\sigma_u$  is the fractional area covered by the updrafts. A similar equation yields the CRM downdraft mass fluxes. Only velocities with absolute values that exceed a given threshold are included in calculating the updraft and downdraft mass fluxes, with a threshold of  $2 \text{ ms}^{-1}$  used in these simulations. Jenney et al. (2020) analyzed these same experiments, and included a discussion of sensitivity to the threshold for these updrafts and downdrafts. The CRM also computed the mixing ratios of precipitating (liquid rain, snow, and graupel) and non-precipitating (liquid, ice) cloud water at each model level using SAM’s single-moment microphysics scheme.

The CRM fields were then averaged over the GCM grid cell and saved as part of the history files. The time-mean fields computed by the model were saved at hourly, daily, and monthly intervals, and each of the three experiments was run for at least three years. Unless otherwise specified, the analysis used thirty days of hourly-mean data from an extension of the original experiment. For a more detailed discussion of super-parameterization, see Randall et al. (2016).

### 2.1.2 Perpetual January Aquaplanet

In addition to the idealized experiments described in §2.1.1, three additional simulations were performed using a more realistic experimental setup. These experiments, referred to as “AQPJAN,” were calculated on a rotating version of SP-CAM. Insolation was held constant in time at an angle corresponding to 15 January, and the model was forced by a simplified SST distribution drawn from ERA5 two-meter temperatures for the month of January. A plot showing the three SST

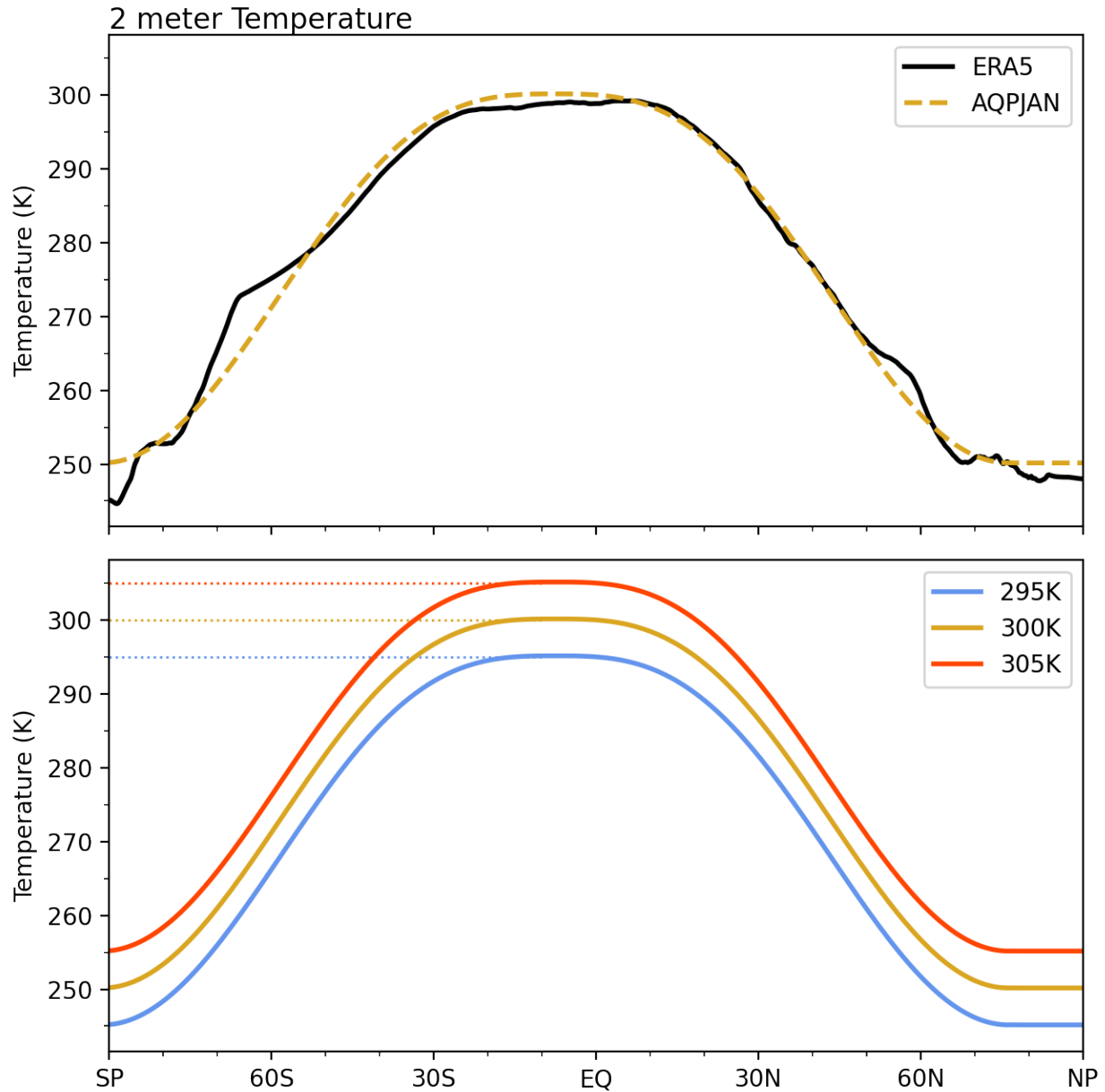


**Figure 2.2:** **Top** Comparison of 2 meter temperature from ERA5 and SST from Aquaplanet experiments. **Bottom** Meridional distribution of surface temperature for the three AQPJAN experiments.

distributions is included in Fig. 2.2. The tropical temperatures were selected to roughly correspond with the 295K, 300K, and 305K surface temperatures from the RCEMIP experiments.

### 2.1.3 CERES Observations and ERA5 Reanalyses

Chapters 3, 4, and 6 focus extensively on the relationship between the column relative humidity (CRH, defined in §2.2) and the cloud radiative effect. CRE can be easily computed from

satellite observations of TOA radiative fluxes as the difference between clear sky and full sky fluxes (Doelling et al., 2016; Ramanathan, 1987). Satellite observations come from the Clouds and the Earths Radiant Energy System (CERES) SYN1deg product (Doelling et al., 2016). The SYN1deg product provides observations of full-sky radiative fluxes, and estimates of clear-sky fluxes on synoptic time-scales at a 1-degree spatial resolution. Analyses in Chapters 3 and 4 utilize daily mean radiative fluxes from January 1, 2001 to December 31, 2019, focusing on the region between 30°S and 30°N.

Calculation of CRH requires vertically resolved fields of temperature and specific humidity, which were retrieved from the European Centre for Medium-Range Weather Forecasts (ECMWF) ERA5 reanalysis (Hersbach et al., 2020). The reanalyses were retrieved on a 1-degree grid at 6-hourly intervals, from which daily-mean values were computed. The data cover the same time-span as the CERES observations. In Chapter 5, the CRH fields are compared to seasonal mean and annual mean plots of the moisture convergence. The fields are computed from monthly mean ERA5 fields of the large scale precipitation rate and surface latent heat fluxes covering the same period from January 2001 to December 2019.

#### **2.1.4 Oceanic Nino Index**

In Chapter 4, as well as in Appendix B, the CRE is estimated from CRH using a method developed later in the text. As part of the evaluation of the method, the accuracy of the estimation is considered during different phases of the El Niño–Southern Oscillation (ENSO). There are several different indices used to designate ENSO (Barnston, 2015; Trenberth, 1997), but for simplicity, the Oceanic Niño Index (ONI) is used here, as it is the operational index used by the National Oceanic and Atmospheric Administration (NOAA). The ONI is a three month running mean of SST anomalies relative to a 30-year climatology, averaged over the Niño 3.4 region (5°S–5°N, 120°–170°W) (National Weather Service, 2020). An El Niño is defined as a period where the ONI is greater than 0.5 K, while a La Niña is defined as a period where the ONI is less than -0.5 K (Dahlman, 2016). Fig. 2.3 shows a time series of the ONI from January 2001 to December 2019.

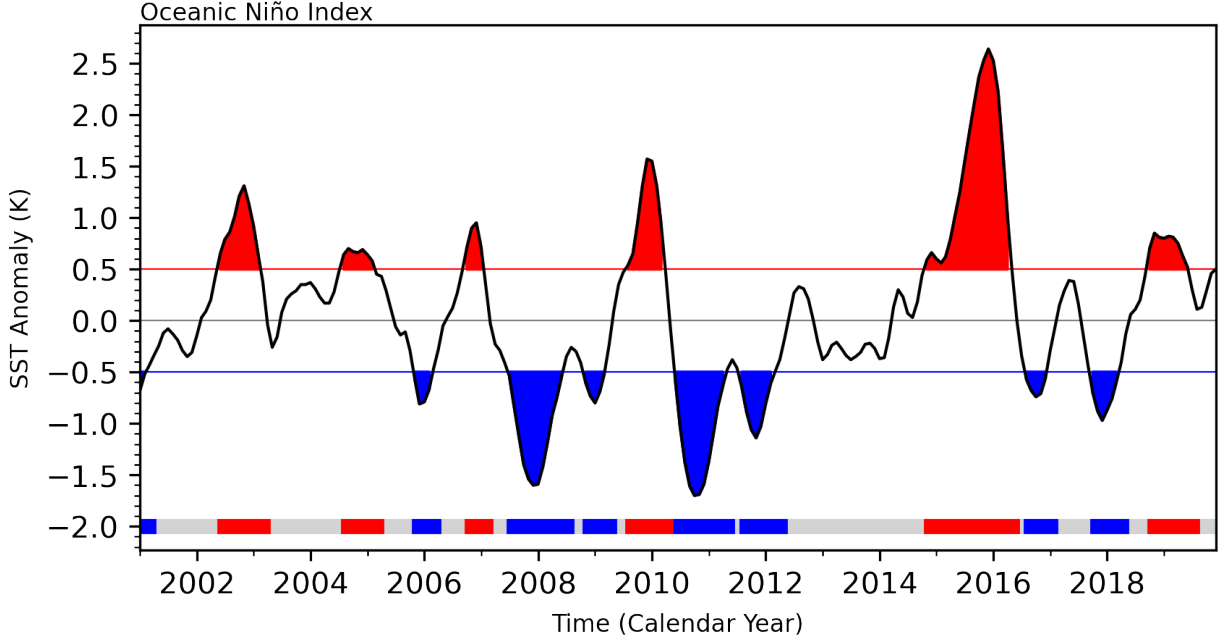


**Figure 2.3:** Oceanic Niño Index. El Niño (red) and La Niña (blue) are defined as the months where the magnitude of the index is greater than 0.5 K

## 2.2 Column Relative Humidity Analysis

### 2.2.1 Calculation of CRH

The column relative humidity is an integrated measure of the degree of saturation of an atmospheric column. It is defined (Bretherton et al., 2004, 2005) as the ratio between the vertically integrated actual and saturation specific humidity. The saturation specific humidity,  $q^*$ , is related to the saturation mixing ratio,  $r^*$ , through

$$q^* = \frac{r^*}{1 + r^*}. \quad (2.2)$$

In turn,  $r^*$ , can be calculated at a given pressure using the saturation vapor pressure,  $e_s$ , through

$$r^* = \frac{0.622e_s}{p - e_s}. \quad (2.3)$$

Lastly,  $e_s$  can be found through the Clausius-Clapeyron relation, and is approximated using the August-Roche-Magnus formula as

$$e_s(T) \approx 6.1094 \exp\left(\frac{17.625T}{243.04 + T}\right), \quad (2.4)$$

where  $T$  is the temperature in Celsius and  $e_s$  is in hPa. Combining these equations in turn gives an expression for the saturation specific humidity, which can be integrated to give the column relative humidity as

$$\text{CRH} = \frac{\int_0^{p_s} q dp}{\int_0^{p_s} q^* dp}, \quad (2.5)$$

where the gravitational constant  $g$  has canceled in the numerator and denominator. This gives a CRH value between zero and one. The value is then multiplied by one hundred to give a percentage.

### 2.2.2 Binning fields based on CRH

In later chapters, a relatively simple method will be used to bin various fields based on a CRH threshold. First, a CRH range will be chosen. Every grid cell with a CRH value within that threshold will be collected. Then the chosen grid cells are used to collect values from a secondary field, such as the CRE. These values are then combined in an area-weighted average to give a single value for the CRH bin. Fig. 2.4 illustrates this method. A similar process yields binned vertical profiles, rather than single values for each bin.

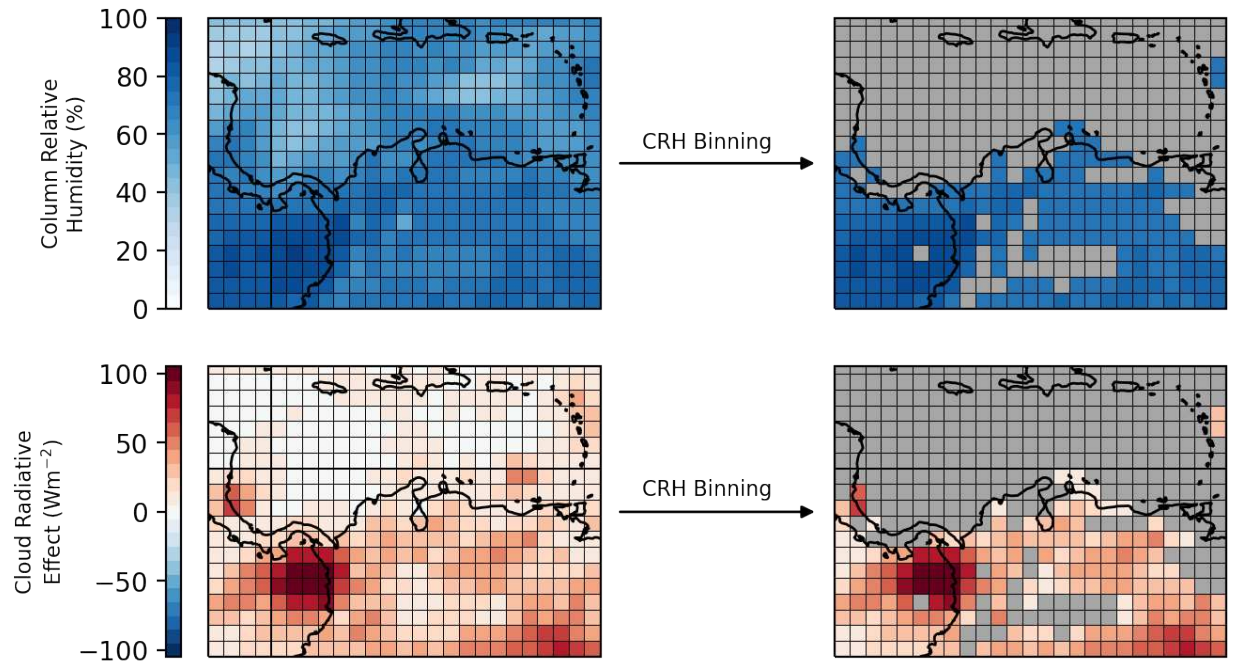


**Figure 2.4:** Fields of CRH from ERA5 and longwave CRE from CERES from an arbitrary date and time used to illustrate the CRH binning method used in further chapters. The CRH bin used is 70% to 90%, for illustrative purposes: binning in later chapters uses a much smaller bin width.

## Chapter 3

# Cloud Radiative Effect and Column Relative

## Humidity

We begin with the analysis of three aquaplanet experiments performed using a super-paramaterized version of the Community Atmosphere Model (SP-CAM) following the protocol of the Radiative-Convective Equilibrium Model Intercomparison Project (RCEMIP). Each simulation is performed for a non-rotating aquaplanet with uniform SSTs of 295 K, 300 K, and 305 K under perpetual equinox conditions. A full description of these simulations, including the methods for calculating model diagnostics, can be found in §2.1.1. The RCEMIP protocol is described fully in Wing et al. (2018), and preliminary results from the RCEMIP project for a large ensemble of models are discussed in a recent paper by Wing et al. (2020).

To compliment previous studies on the cloud radiative effect (CRE, see §1.1), here we investigate how the CRE depends on the column relative humidity (CRH). The CRH is a normalized measure of the total water vapor of a column, calculated as the ratio of the column integrated water vapor path to the column integrated saturation water vapor path, following Bretherton et al. (2004). There are a few reasons that CRH is an attractive metric for describing the range of clear and cloudy regions in the data compared to, say, the precipitation rate or the optical depth. CRH is constrained to fall between zero and one (or zero and one-hundred percent), which makes it easy to compare results across simulations. Another advantage of the CRH is that the total water in the column is known to be important to the attenuation of radiation.

A characteristic plot of CRH for an arbitrary timestep from the 295 K experiment is shown in the left panel of Fig. 3.1. For comparison, a plot of the brightness temperature at the same timestep is also included. The CRH captures the general structure of cloudy and clear regions as seen in the brightness temperature, but the change from clear to cloudy regions is more gradual.

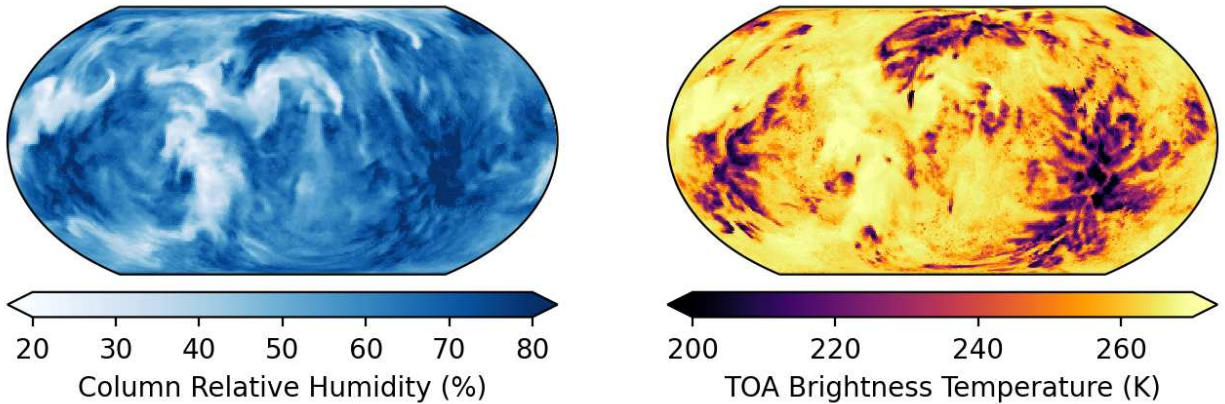


**Figure 3.1:** **Left** Contour plots of column relative humidity, and **Right** TOA brightness temperature for an arbitrary timestep from the 295 K RCEMIP simulation

For example, the dark region of low brightness temperatures in the lower right-hand portion of the domain corresponds to the dark region of high CRH in the same location.

### 3.1 The distribution of CRH and its dependence on SST

Probability density functions for the CRH for each of the three RCEMIP experiments are shown in the left panel of Fig. 3.2, while the change in the PDFs between experiments is shown in the right panel. The PDFs are calculated from data that is weighted by the cosine of latitude to account for the decrease in the area of grid cells near the poles. The bin width for the PDFs is 0.5%, for a total of 200 bins ranging from 0% to 100% CRH. Tbl. 3.1 provides summary statistics for the distribution of CRH for each of the RCEMIP experiments.

As the surface temperature is increased, the domain becomes less humid, as evidenced by the decrease in the mean CRH. This decrease is accomplished by an increase in the frequency of regions with CRH less than 50%, and a decrease in the frequency of regions with CRH in ranging from 50% to 70%. There is an increase in the frequency for humid regions with CRH greater than 70%, but this is not enough to overcome the increased frequency of regions with low CRH. The standard deviation increases from the 295 K to the 300 K and 305 K simulations. Each of the distributions has a negative skewness, indicating a longer tail in the dry regions, but the magnitude

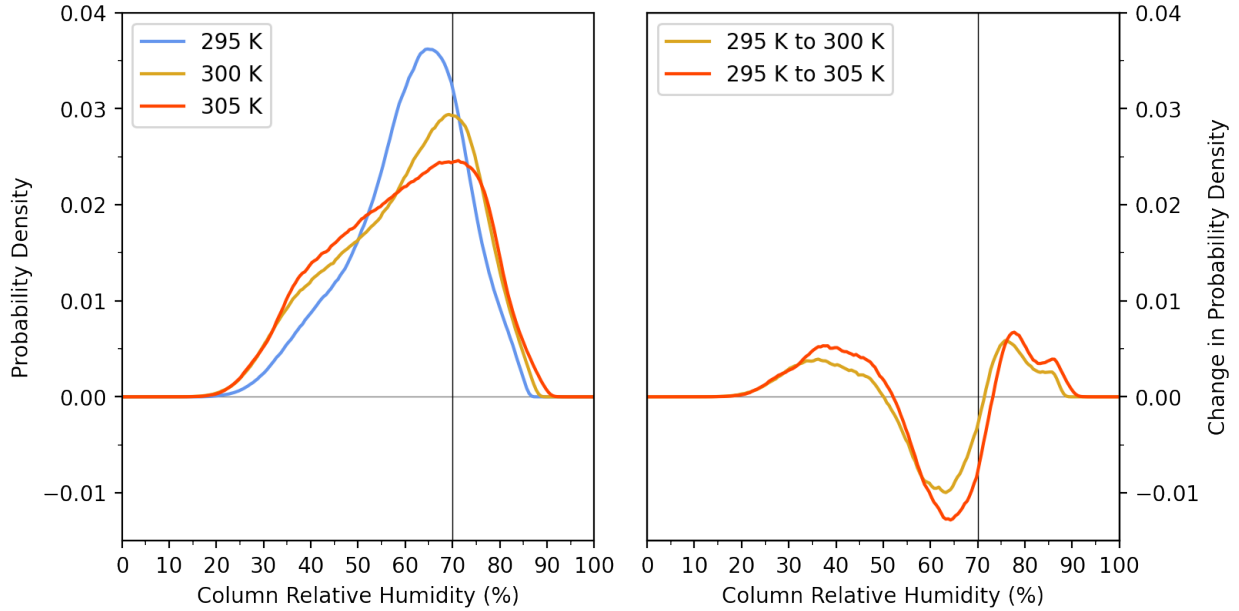


**Figure 3.2:** **Left** Area-weighted probability density function of column relative humidity for each of the three SST experiments. **Right** same as **Left**, but for the change in probability density function between experiments. Vertical line at 70% CRH is included for comparison with later plots in this chapter.

of the skewness decreases as the surface temperature increases. While the mean CRH decreases across the simulations, the mode increases with increasing SST.

As will be discussed in the next section there is a relatively simple connection between the CRH and the CRE. The changes in the distribution of CRH discussed in this section are directly relevant to the change in CRE across the simulations.

### 3.2 The dependence of CRE at the boundaries on CRH

The longwave, shortwave, and combined CRE at the TOA and at the surface were found for a range of CRH values. The CRE was calculated as the difference between clear-sky and full-sky

**Table 3.1:** Summary statistics for the distributions of CRH for each of the three experiments. The Mode is given as the center of the CRH bin with the largest probability density (the peak of the distributions shown in Fig. 3.2)

	Mean	Standard Deviation	Skewness	Mode
<b>295 K</b>	60.76%	11.95	-0.49	64.75%
<b>300 K</b>	59.91%	15.08	-0.45	69.25%
<b>305 K</b>	59.38%	15.13	-0.26	71.25%

radiative fluxes for all of the grid cells with CRH within a 5% range (for example, between 60% and 65%). The atmospheric cloud radiative effect (ACRE) was found as the difference between the TOA and surface CRE and represents the enhanced radiative heating or cooling of the atmosphere as a result of clouds. It should be noted that the uniform insolation and lack of a diurnal cycle may lead to shortwave effects that are larger than would otherwise be expected. CRE at TOA, at surface, and ACRE are shown as a function of CRH in Fig. 3.3. A brief glance at the figure shows one of the major conclusions of this thesis: the mean CRE appears to be a nearly universal function of the CRH, with only slight variations due to differences in the SSTs of the simulations.

The top row of Fig. 3.3 shows the CRE at TOA for these CRH bins, and is characterized by a clear relationship between the CRH and the CRE. In the longwave, shown in panel A, regions of low CRH correspond to regions of low CRE. The low humidity does not support the formation of many clouds, so the full-sky radiation flux is very close to the clear-sky flux. As the CRH is increased up to about 70%, the CRE increases slowly. The curves then show a “kink” near 70% CRH, where a vertical line has been added. This 70% value marks a rough boundary between regions with small and large CRE. Large longwave CRE are generally associated with high-level clouds that emit to space at a much colder temperature than the surface. The large CRE in these regions suggest that the 70% threshold can also be interpreted as a boundary separating regions of no clouds or low-level clouds from regions of high-level clouds. This will be discussed later in the text in Chapter 5. Additionally, the large longwave CRE at high CRH is directly relevant to the FAT hypothesis as discussed in §1.4, and is included in the analysis of Appendix A.

The shortwave CRE at the TOA shown in panel B is also small for regions of low CRH. It begins to slowly increase in magnitude with CRH from about 30% to the kink at 70%. Here, the increase in magnitude is due to a higher effective albedo for clouds than for the surface, as well as increased absorption of shortwave radiation. Like the longwave component, the magnitude of the shortwave CRE increases rapidly with CRH above the 70% boundary. The negative shortwave effect is larger than the positive longwave effect so that the net CRE is negative at the top of the atmosphere, as shown in panel C. While the net CRE is large for regions above the 70% boundary,

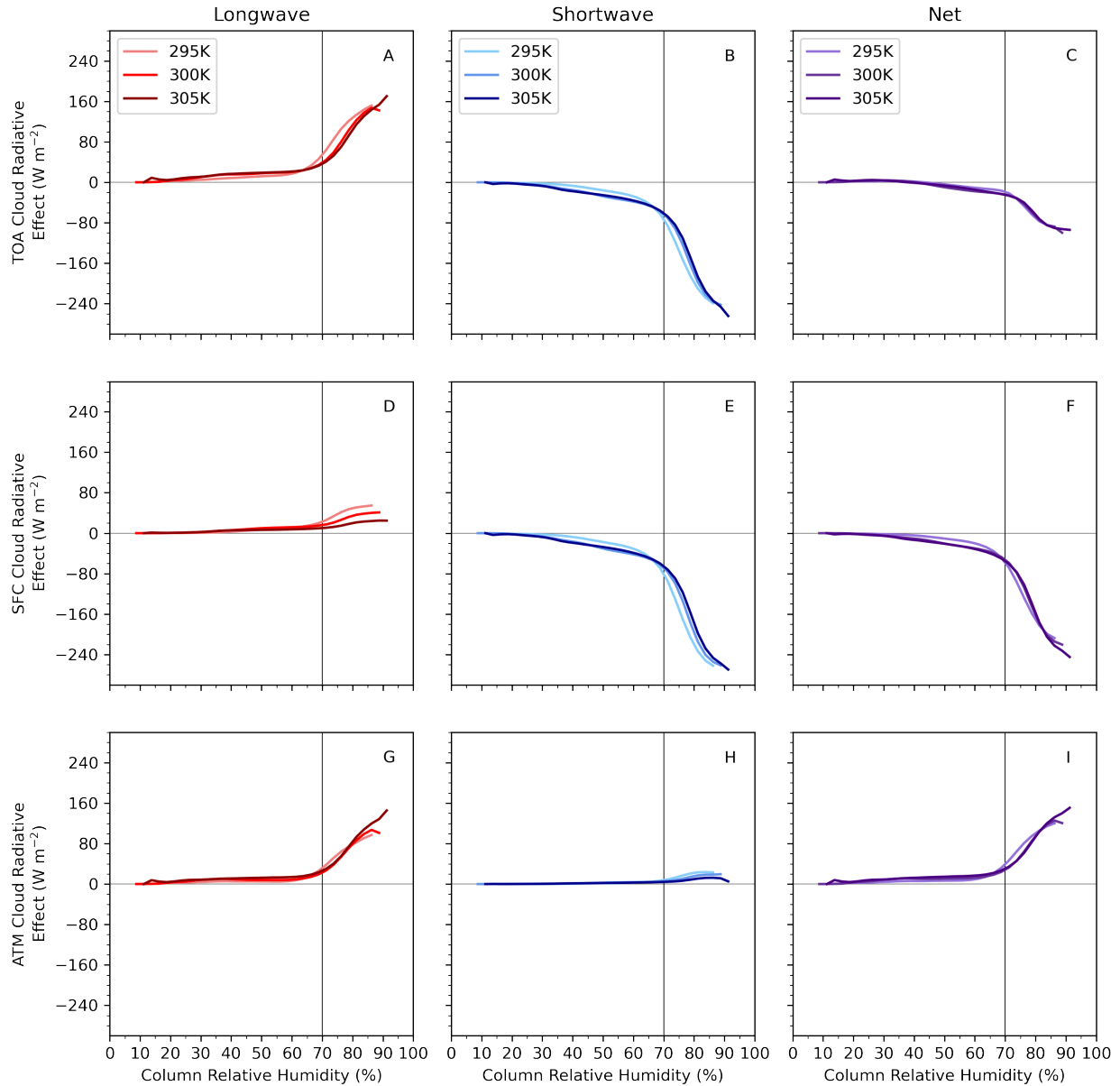


**Figure 3.3:** **Top Left** Longwave CRE at TOA as a function of column relative humidity for each of the three RCEMIP simulations calculated using the hourly mean history files. **Top Center** and **Top Right** same as **Top Left**, but for the shortwave CRE at TOA and net (LW + SW) CRE at TOA. **Center Row** and **Bottom Row** Same as **Top Row**, but for the CRE at the surface, and ACRE.

this region encompasses about 10 - 15% of the entire domain, so that the domain-mean CRE is small, as predicted by previous studies (see §1.1).

The middle row of Fig. 3.3 shows the CRE at the surface. The longwave CRE is smaller in magnitude at the surface than at the TOA. The positive values likely represent the increase in downwelling longwave radiation associated with emission to the surface from the base of clouds.

For regions of high CRH the longwave effect at the surface decreases with increasing SST, in contrast with several of the other curves which change little as the SST increases. To determine why this is the case, it is helpful to revisit how the CRE has been defined. The CRE is given as the difference in clear-sky and full-sky radiative fluxes. The clear-sky fluxes are computed using the same temperature and humidity profiles as the full-sky fluxes, but with the cloud fraction set to zero. Then, the CRE is due entirely to absorption by clouds and not due to any effects of the humidity profile.

With this in mind, the decrease in the longwave CRE at the surface as the SST increases indicates that the difference in temperature between the surface and cloud base is smaller in the warmer experiments. This may be a result of the increased stability of the temperature profile as the surface warms (Bony et al., 2016). The existence of clouds in a column reduces the amount of insolation to reach the surface so that the shortwave CRE at the surface is nearly identical to the shortwave effect at the TOA. Then, the net CRE at the surface is strongly negative because the shortwave effect is so much stronger.

The ACRE can be found by taking the difference between the CRE at the TOA and the surface, and is shown in the bottom row of Fig. 3.3. Consistent with the TOA and surface CRE, the effect is small for regions of low CRH. The longwave CRE effect is larger at the TOA than at the surface so that the longwave ACRE is strongly positive above the 70% boundary. Similarly, the shortwave ACRE is very close to zero below the 70% boundary. The small shortwave ACRE suggests that the shortwave effect of clouds is almost entirely due to an increase in cloud albedo and not due to increased absorption. This is consistent with the common approximation that the atmosphere is transparent to shortwave radiation. Above the 70% threshold, the positive shortwave ACRE is evidence for a small amount of shortwave absorption by clouds. When the longwave and shortwave effects are combined, the net ACRE is positive everywhere. Where the CRH is small, the ACRE is small, and where the CRH is large, the ACRE becomes large and positive. The ACRE in humid regions is a central component of the analysis of Chapter 6, where it is strong enough to induce large-scale ascent.

Comparing the net CRE at the TOA, surface, and atmosphere (the right column of Fig. 3.3), we can investigate how clouds impact the transfers of radiative energy between the surface, atmosphere, and space. The net CRE is nearly zero for regions with CRH less than 50%, and is negative for all other regions. The net CRE at the surface is negative, while the net ACRE is positive. This implies that the effect of clouds is to reduce the amount of radiation that reaches the surface, while increasing the amount that is absorbed in the atmosphere. Because the net CRE is negative above 50% CRH, it appears that the cooling associated with clouds in the shortwave is more important for determining the net CRE than the heating associated with clouds in the longwave for these RCEMIP simulations. However, the shortwave effects likely are larger than would otherwise be expected due to the uniform insolation of these experiments. This could potentially lead to a different sign for the net CRE.

When looking at Fig. 3.3, there are a few minor ways that the increase in SST changes the CRE. The main effect of SST seems to be to shift the CRH value where the transition between small and large CRE occurs, but this effect is only present in some of the panels and not in others. Another effect of increasing SST is to change the magnitude of the emission of longwave radiation from cloud base to the surface (Fig. 3.3D), although it is unclear why this occurs.

These minor instances aside, it appears that the CRE is broadly independent of the SST and instead is determined by the CRH. It is natural to ask whether this same result holds outside of the idealized conditions of the RCEMIP simulations. To answer that question, the calculations with CRH and CRE are repeated in the following section using satellite observations and atmospheric reanalyses.

### **3.3 CRE and CRH from observations and reanalyses**

Daily clear-sky and full-sky radiative fluxes measured by the CERES satellite were used to compute the longwave and shortwave CRE at TOA and surface, and ACRE for the period from January 1, 2001 to December 31, 2019. The CRH field for the same period of time was calculated following the method discussed in Chapter 2 using three-dimensional fields of temperature and

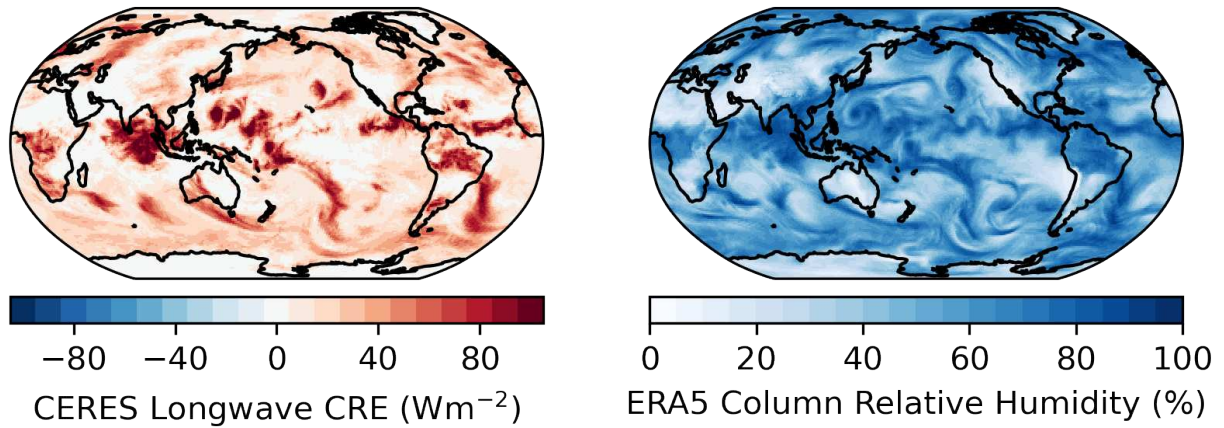


**Figure 3.4:** **Left** Longwave CRE at TOA calculated from CERES radiative fluxes for 19 October 2013. **Right** CRH calculated from ERA5 reanalysis on the same date.

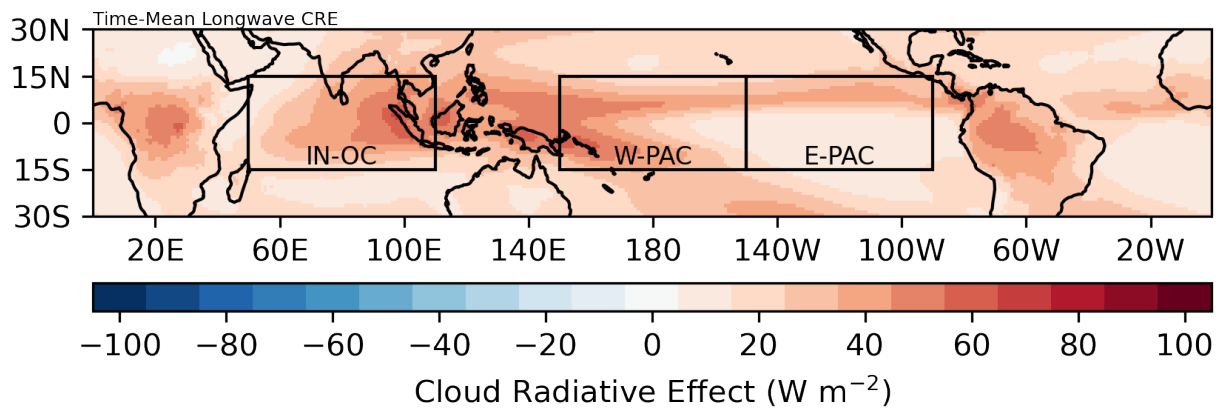


**Figure 3.5:** Time-mean longwave CRE at TOA, with boxes showing the three subsets for analysis: Indian Ocean (INOC), Western Pacific (WPAC), and Eastern Pacific (EPAC).

specific humidity from ERA5 reanalyses. Fig. 3.4 shows plots of the longwave CRE at TOA and the CRH for the same arbitrary date and time. The figure shows that the CRH broadly captures many of the features that are evident in the CRE field. These include a Typhoon south of Japan, MJO activity in the Indian Ocean, and cloudiness along the ITCZ, among other features.

To compare with the RCEMIP results, three tropical subsets of the CERES and ERA5 datasets were used, ranging from 15°S to 15°N. The subsets represent the Indian Ocean (INOC, 50°E-110°E), west Pacific (WPAC, 150°E-150°W), and east Pacific (EPAC 150°W-90°W). Each of the regions is mostly over ocean with some landmasses included, especially in the INOC region. In addition to these three regions, the analysis was repeated for the entire belt from 30°S to 30°N

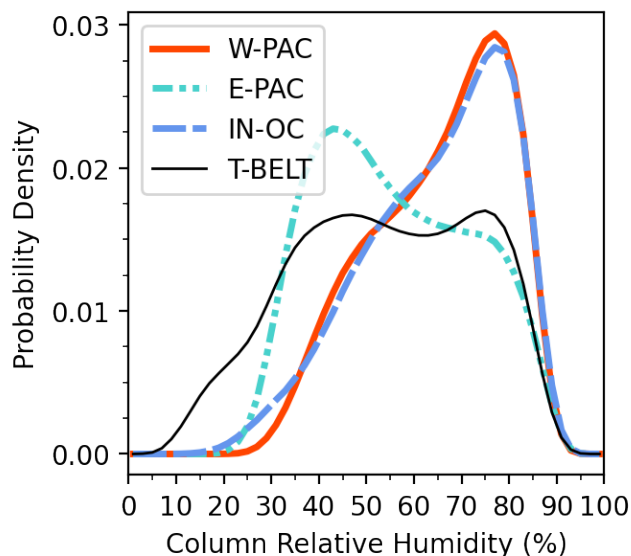


**Figure 3.6:** Area-weighted probability density functions of CRH for the three regional subsets and the entire T-BELT region, for the 18-year period of investigation.

(T-BELT). Fig. 3.5 shows the annual-mean longwave CRE at TOA from CERES with these three subset regions highlighted on the map.

The time-mean view shows some of the range of conditions represented in each subset. The INOC region encompasses an area associated with the south asian monsoon, the WPAC region includes areas of deep convection associated with the intertropical and south Pacific convergence zones, and the EPAC region contains some areas of deep convection along the ITCZ, but also areas of suppressed convection over the cold tongue. While smaller boxes could have been drawn to focus on the cloudiest regions, the larger boxes were chosen to include a wide range of SSTs and CRH values.

Probability distributions of the CRH for the three regions, as well as for the wider T-BELT are shown in Fig. 3.6. The distributions for the three regions range from approximately 20% to 90% CRH, but the peaks in the distributions occur at different CRH values. Both the WPAC and INOC regions are much more humid than the EPAC region, and peak near 80% CRH compared to 40% for the EPAC. This is to be expected, as the WPAC and INOC regions are associated with a large amount of precipitation while the EPAC region is associated with much less precipitation, as shown in Fig. 1.7 of §1.3.2. The distribution for the larger T-BELT is wider and ranges from 10%

up to 90% CRH. The small values of CRH are absent in the subset regions, and likely represent dry conditions over deserts. The T-BELT distribution is bimodal, with two peaks that correspond to the peaks from the subset regions.

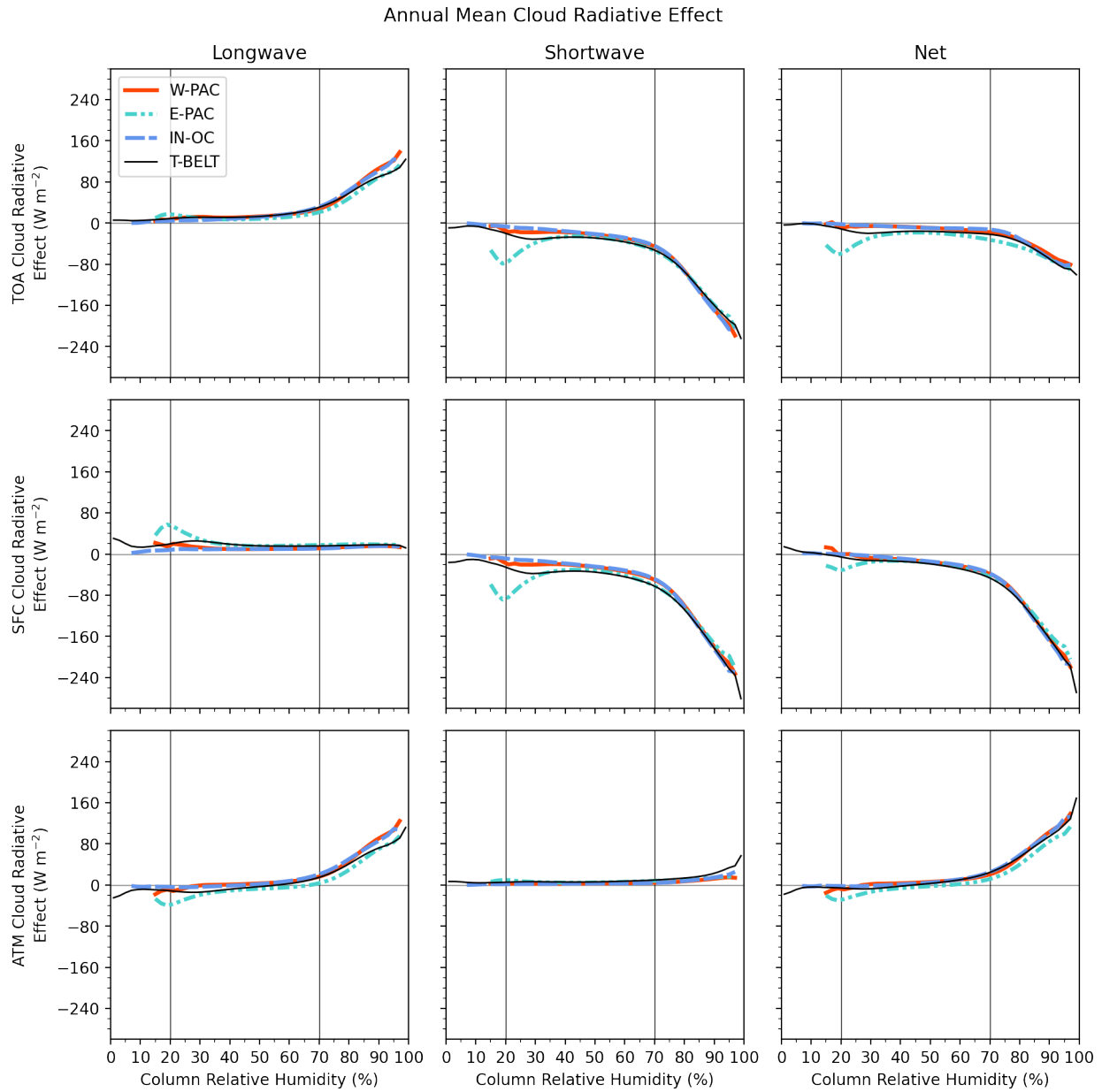


**Figure 3.7:** **Top Row** Longwave, shortwave, and net CRE at TOA calculated from CERES observations, binned by CRH calculated from ERA5 reanalysis. The three thick lines represent each of the three regional subsets, with the thin black line representing the whole T-BELT region. **Middle Row** and **Bottom Row** same as **Top Row**, but for surface CRE and ACRE, respectively. Compare with Fig. 3.3

The CRH analysis of the previous section was repeated for the CERES and ERA5 data. Fields of longwave, shortwave, and net CRE from CERES observations in each region were separated into bins by the corresponding CRH calculated from ERA5. The mean CRE value within each bin was found, and is shown in Fig. 3.7 as a function of the CRH.

The similarity between Fig. 3.7 and Fig. 3.3 is striking. Like the RCEMIP data, the CRE from CERES show a strong dependence on the CRH, across a wide variety of conditions. The CRE is small for small CRH values, and begins to increase in magnitude when the CRH exceeds approximately 70%. This relationship holds for the regional subsets as well as for the wider T-BELT region, showing that the inclusion of land or areas further from the equator does not significantly change the conclusion.

A notable deviation from the RCEMIP data is evident for the EPAC curves. At approximately 20% CRH, the EPAC curves show a secondary peak in CRE in the longwave and shortwave, with a stronger effect in the shortwave. This may represent the effect of low-level stratus decks or trade-wind cumuli which reflect a large amount of sunlight, but emit to space at near-surface temperatures. This difference from the RCEMIP data was not obvious before the analysis was performed, but is unsurprising as there is no place in the RCEMIP simulations that can emulate the cold tongue and cloud decks that characterize the EPAC region.

The robust relationship between the CRH and CRE in both idealized and observational data suggests that the distribution of CRH may be used to estimate the distribution of CRE, at least in some mean sense. This possibility is explored further in the following chapter.

## 3.4 Conclusions

The relationship between cloud radiative effects and column relative humidity in idealized simulations was investigated. When the CRE was binned by CRH, it was found to be a nearly universal function of the CRH. The CRE was small for small values of CRH, and was large for large values of CRH. A threshold of approximately 70% CRH was found to be an important inflection point, separating regions where the CRE was small from regions where it became large.

The calculations leading to these results were then repeated using CRE from eighteen years of CERES satellite observations and CRH calculated from ERA5 reanalyses. The same universal curves of CRE versus CRH were found in three tropical subsets of the domain, as well as in a much larger belt ranging from 30°S to 30°N. The universal relationship in both the RCEMIP simulations, as well as when satellite observations were combined with reanalyses was intriguing, and suggests that the CRH may be used to estimate the CRE, at least in some general way. Chapter 4 is spent investigating this possibility.

The results discussed in this chapter have focused on how the CRH can be used to order the domain into more or less humid regions. Chapter 5 continues this theme by investigating the energy and moisture budgets of the domain in terms of the CRH. The 70% threshold that has appeared throughout this chapter remains a constant feature. The net TOA minus surface energy flux and the net precipitation minus evaporation as a function of CRH both change sign near 70%. An analogy is then drawn between the heat balance of the saturated regions and that of the ITCZ as first discussed by Riehl and Malkus (1958). Further connections are made to the work of Riehl and Malkus (1958) in Chapters 6 and 7, where the CRH is used to separate vertically resolved fields of longwave and shortwave heating rates. These vertically resolved fields prove to be important to furthering the understanding of the transport of moist static energy by the convective and environmental scales.

## Chapter 4

### Estimating the CRE using the CRH

A key result of the previous chapter was that the mean cloud radiative effect binned by the column relative humidity is largely insensitive to the surface temperature. This was found in idealized aquaplanet simulations following the RCEMIP protocol (§2.1.1), and was also found when reanalyses were combined with satellite observations (§2.1.3). This chapter is motivated by two simple questions. First, can the CRH be used to estimate the CRE? And if so, on what time scales? The short answer is that the universal curves of CRE versus CRH from Fig. 3.7 do appear to show some skill in estimating longwave and shortwave CRE when the CRH is large, on time-scales of a month or longer.

In this chapter, fields of the CRH from reanalyses are combined with curves of CRE as a function of CRH to give an estimate of the CRE. The estimate is able to generally represent the large scale annual mean spatial structure of the longwave and shortwave CRE. On shorter time scales the estimate is less accurate, but still shows promise. A domain-mean time-series of the estimated CRE compared to the actual CRE shows reasonable agreement when regions of low CRH are excluded. Regional-mean time-series plots comparing the estimated CRE to the actual CRE over the west Pacific show a strong correlation in both the longwave and shortwave. Over the east Pacific the correlation is larger in the longwave than in the west Pacific, but it is somewhat lower in the shortwave. A simple composite analysis shows evidence that errors in the shortwave CRE in the EPAC region may be related to the El Niño-Southern Oscillation (ENSO). Over the Indian Ocean there is a moderate correlation between the estimated and actual CRE, but it is found to be lower than the WPAC or EPAC regions.

#### 4.1 Using CRH to estimate the CRE at TOA

The TOA longwave and shortwave CRE as a function of CRH from Fig. 3.7 are shown again in the left panel of Fig. 4.1 for the entire region ranging from 30°S to 30°N. The right panel of

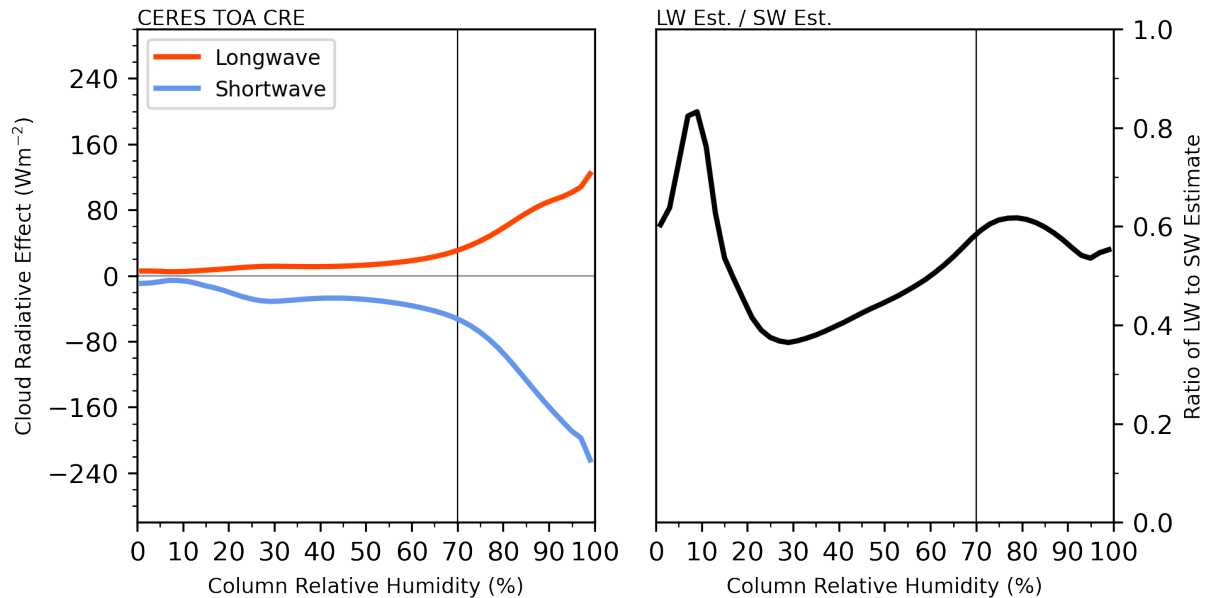


**Figure 4.1:** Curves of T-BELT CRE as a function of CRE from Fig. 3.7 shown again for use in estimating CRE from CRH fields.

the same figure shows the ratio of the longwave to the shortwave curves. The ratio is smallest between 25% to 30%. This is near the CRH value where a secondary peak was observed for the EPAC region in Fig. 3.7, although that peak was closer to 20% CRH. It was suggested in Chapter 3 that the secondary peak was associated with stratus clouds. The minimum in the right panel of Fig. 4.1 would support that suggestion, as low level stratus clouds are associated with very large shortwave CRE and much smaller longwave effects. If the CRE for this CRH was only due to low level stratus clouds, the magnitude of the minimum would presumably be much closer to zero. Then, the CRE near 30% is likely due to a combination of low-level stratus clouds as well as other clouds in relatively dry regions where the longwave and shortwave CRE are of similar magnitude. Through most of the domain, the ratio is between 0.4 to 0.6, indicating that longwave CRE tend to be weaker than shortwave effects at a given CRH, consistent with Fig. 1.1.

The two curves in the left panel were then used to estimate the CRE at each grid cell within the tropical belt using CRH calculated from reanalyses. The CRE was estimated by mapping the CRH at each grid cell to the corresponding CRE value. This was done at each time step, and then the resulting field of estimated CRE was averaged temporally. In Fig. 4.2, the top panel shows

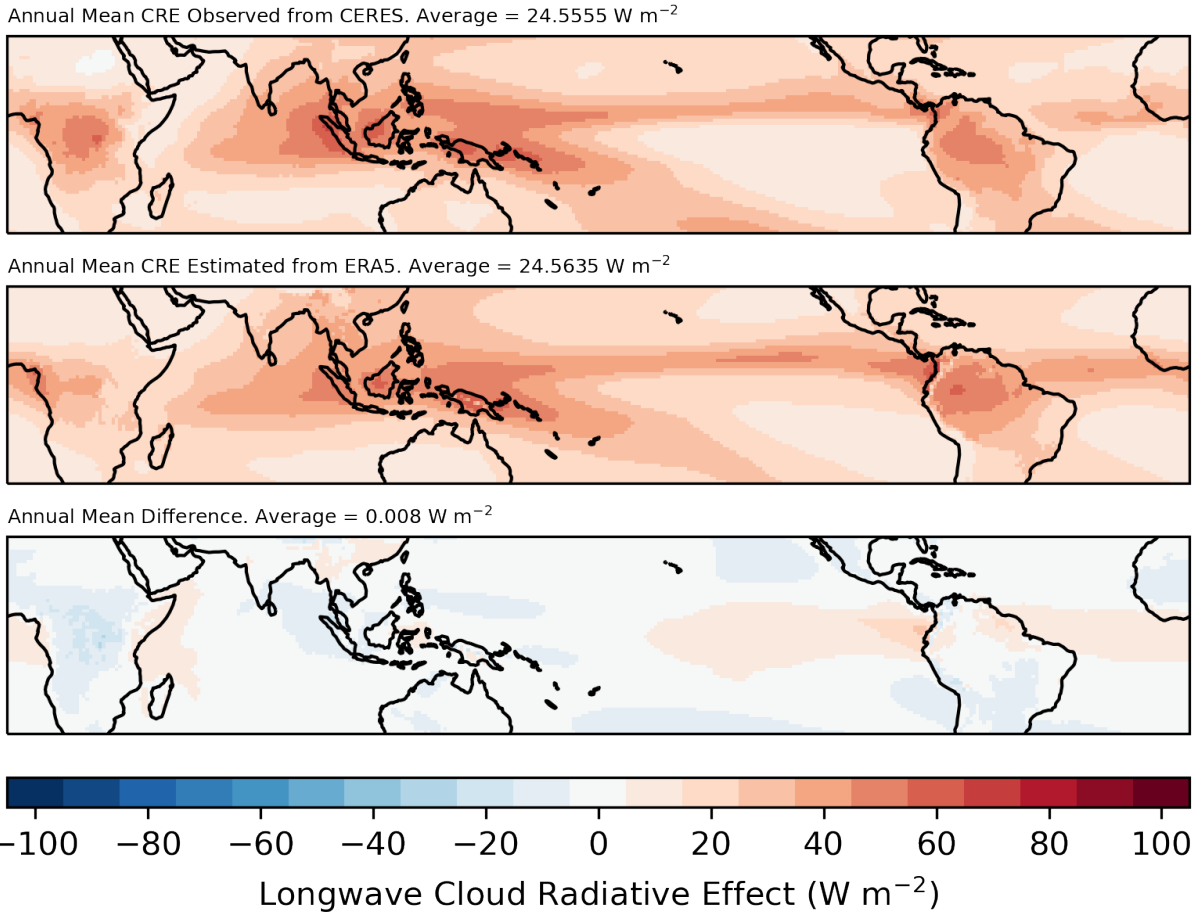


**Figure 4.2:** **Top** Annual mean longwave CRE at TOA calculated from daily-mean CERES observations from 2001-2019. **Middle** Annual mean longwave CRE at TOA estimated from daily mean ERA5 CRH over the same period. Description in text. **Bottom** Difference between **Top** and **Middle**.

the annual mean longwave CRE at TOA from CERES observations averaged over the period from 2001 through 2019. The middle panel of the figure shows the annual mean longwave CRE at TOA estimated using the CRH from ERA5 reanalysis. The bottom panel shows the difference between the two. Figs. 4.4, and 4.5 show the same for the shortwave CRE and the net CRE calculated as the sum of longwave and shortwave effects.

Fig. 4.2 shows that the observed and estimated longwave CRE are very similar in the annual mean. The estimation is able to reproduce many of the features of the observed CRE, including the large CRE over rain forests as well as over the south Pacific and intertropical convergence zones. In most regions of the bottom panel of the figure, the lack of shading indicates a difference of less

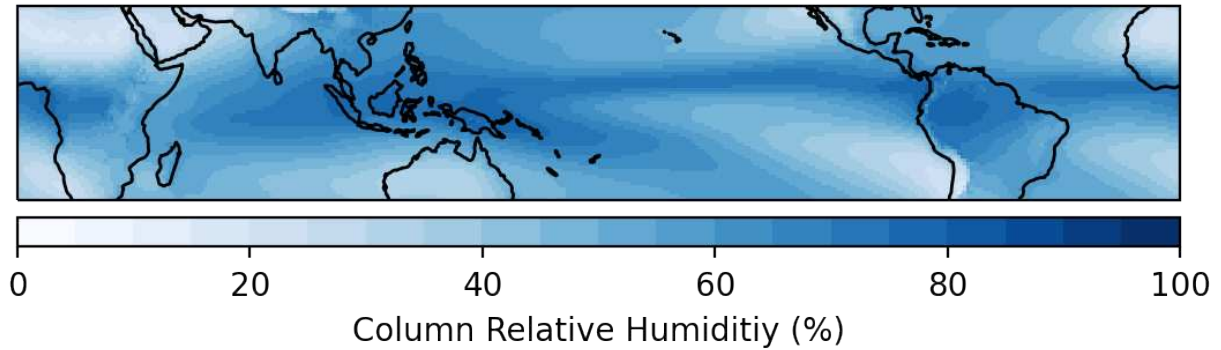


**Figure 4.3:** Annual mean CRH in the T-BELT region from 2001-2019 calculated from ERA5 reanalysis.

than  $5 \text{ Wm}^{-2}$ , which is a good agreement for a quantity that can exceed  $100 \text{ Wm}^{-2}$  in some places. There are physical interpretations for the regions where the difference is larger.

First, the CRH method underestimates the CRE over equatorial Africa and overestimates the CRE over the ocean directly east or west of the continent. The reasons for this can be inferred by looking at the annual-mean CRH from reanalyses shown in Fig. 4.3. The CRH fails to represent the sharp land-sea contrast over this region which is important to the development of clouds.

Another obvious error exists over the cold tongue regions of the Atlantic and Pacific. Here, the cooler SSTs suppress convection, leading to fewer high clouds than would be expected based on the CRH alone, leading to an overestimation of the CRE. This suggests that this method of estimating CRE may be more accurate during El Niño than La Niña. As will be discussed at the end of this chapter, this appears to be true. The blue regions off of the western coasts of Chile and Mexico are associated with low-level stratus clouds. The error associated with these regions is discussed below in reference to the shortwave CRE in Fig. 4.4, where the error is more pronounced. As shown in the figure, the difference between the two plots, averaged over the entire domain from  $30^\circ\text{S}$  to  $30^\circ\text{N}$  is very close to zero.

Next, the annual mean shortwave CRE is shown in Fig. 4.4. As in Fig. 4.2, the top panel shows the CRE observed from CERES, the middle panel shows the CRE estimated from the CRH, and the bottom panel shows the difference between the two. Again, there is broad agreement in the behavior, although the CRH method fails to recognize the effects of stratocumulus decks off

Annual Mean CRE Observed from CERES. Average =  $-46.1963 \text{ W m}^{-2}$



Annual Mean CRE Estimated from ERA5. Average =  $-46.2126 \text{ W m}^{-2}$



Annual Mean Difference. Average =  $-0.0163 \text{ W m}^{-2}$

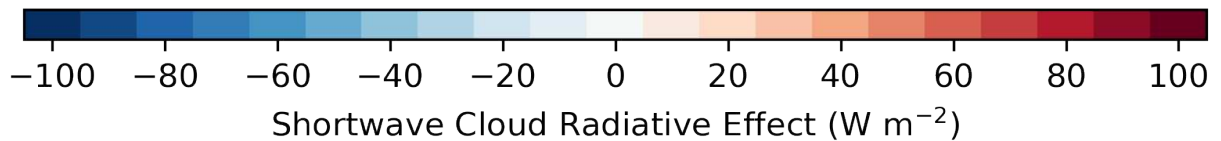


**Figure 4.4:** Same as Fig. 4.2, but for the shortwave CRE.

the west coasts of Chile, Mexico, southern Africa, and Australia. Here, the subsiding branches of the Hadley Cells dry the troposphere above the shallow boundary layer, leading to small CRH values, as shown in Fig. 4.3. At the same time, the enhanced evaporation in these regions leads to a large amount of water vapor in the boundary layer, which forms the low-level stratus clouds that characterize the regions. These clouds reflect a large amount of sunlight, leading to a strong shortwave CRE.

The CRH model fails to represent these low-level clouds because the CRH is a vertically-integrated measure of the amount of water vapor in the column, and contains no information about the vertical structure of water vapor. It is possible that some method that combines the CRH with the liquid or ice water path may be able to better represent these stratocumulus regions, but that is beyond the scope of this Chapter.

Annual Mean CRE Observed from CERES. Average =  $-21.6408 \text{ W m}^{-2}$



Annual Mean CRE Estimated from ERA5. Average =  $-21.6491 \text{ W m}^{-2}$



Annual Mean Difference. Average =  $-0.0083 \text{ W m}^{-2}$

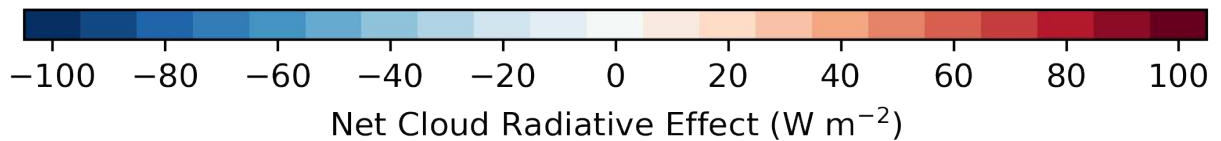
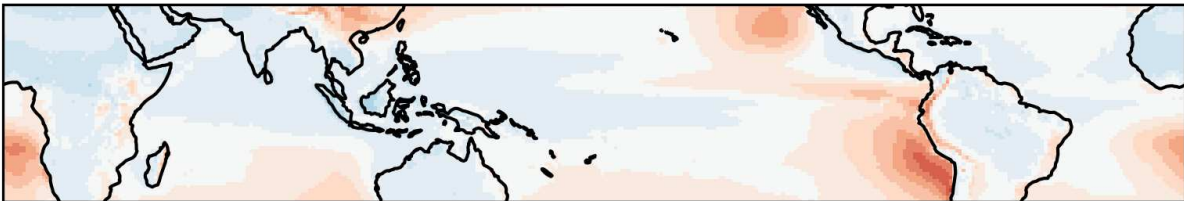


**Figure 4.5:** Same as Fig. 4.2, but for the net CRE.

In addition to the differences associated with the stratus regions, there are also large differences over the Andes mountains, parts of east Asia, and parts of equatorial Africa. While this appears to suggest that the CRH method of estimating CRE works better over oceans than over land, evidence from the later in this chapter suggests instead that this may be the result of a systematic overestimation of the CRE over land compared to over oceans.

Lastly, Fig. 4.5 shows the net longwave plus shortwave CRE. The net CRE was calculated by adding together the longwave and shortwave fields rather than by using the curve for the net CRE in Fig. 3.7. The CRH estimates the net CRE to be negative everywhere, which appears to be correct over all oceanic regions, but misses a small region of positive CRE along the Sahel region of northern Africa. The effect of the ITCZ is still visible, although the features are much

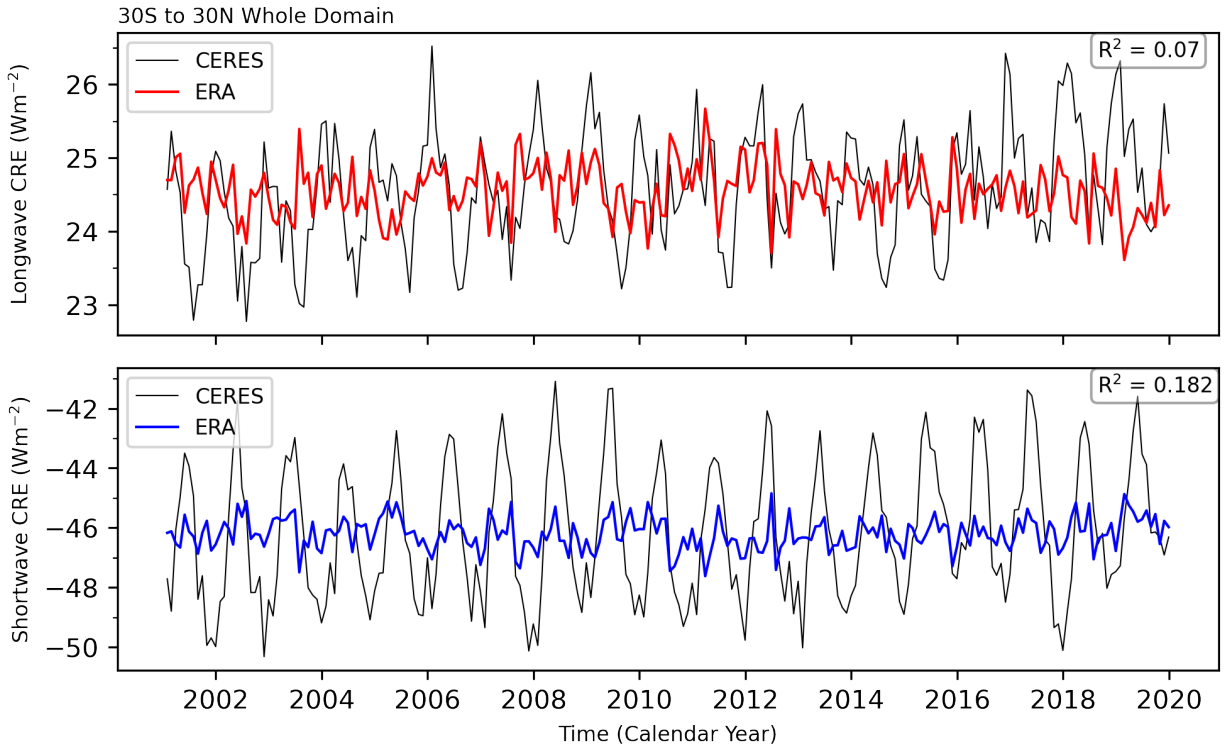


**Figure 4.6: Top** Time series showing the domain-mean longwave CRE estimated from ERA5 CRH fields (red line), and calculated from CERES satellite observations (black line). **Bottom** Same as **Top**, but for the shortwave CRE (blue line).

less defined than for the individual longwave and shortwave cases. The average difference over the region is again quite small.

## 4.2 Time Series Analysis

The estimated CRE and the actual CRE were further compared by looking at time-series plots of the monthly mean CRE over the entire  $30^{\circ}\text{S}$  to  $30^{\circ}\text{N}$  region. First, the daily-mean fields of the CRE and CRH over the 19 year period were averaged into monthly means at each grid cell. Then the area-weighted average of the spatial data was found for each month.

Monthly time series plots comparing the estimated to the actual longwave CRE are shown in the top panel of Fig. 4.6, where the estimated values have been shifted so that both series have the same mean. The magnitude of this shift is shown later, in Tbl. 4.1. Pearson's  $R^2$  correlation between the two is nearly zero, showing poor linear agreement. The  $R^2$  for the shortwave is

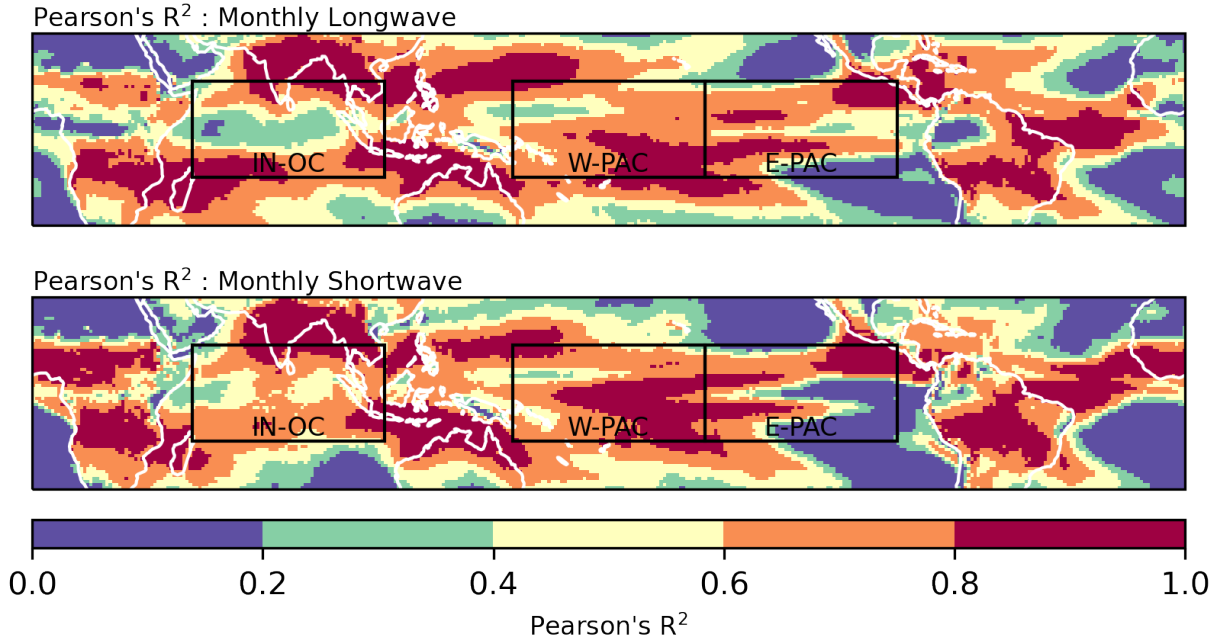


**Figure 4.7:** **Top** Pearson's  $R^2$  correlation between the monthly time series of estimated and actual longwave CRE at each location. **Bottom** Same as **Top**, but for the shortwave CRE.

somewhat better, but still does not show a strong correlation between the estimated and actual CRE. This poor result is surprising given that the maps in Figs. 4.2 and 4.4 show such a good agreement over the domain. The difference plots shown in the bottom panels of Figs. 4.2, 4.4, and 4.5 may provide an explanation for the small correlation shown in Fig. 4.6. The regions with the largest error between the actual and estimated CRE coincided with marine stratus regions where the CRH was small but the CRE was large.

Fig. 4.7 shows Pearson's  $R^2$  correlation between the estimated and actual CRE for each grid cell. The correlation here is again between the monthly mean values, but is calculated at each location rather than averaged over the entire domain. The color bar is split into quintiles ranging from zero to one. From the plots, it is clear that the regions with the worst correlation (shown in blue) are associated with the stratus decks discussed previously, as well as some desert regions. Conversely, there are many regions where the correlation is greater than 0.6 or even 0.8 (shown in orange and red). These are associated with the ITCZ, rain forests in South America and Africa, the monsoon region of south Asia, among other regions.

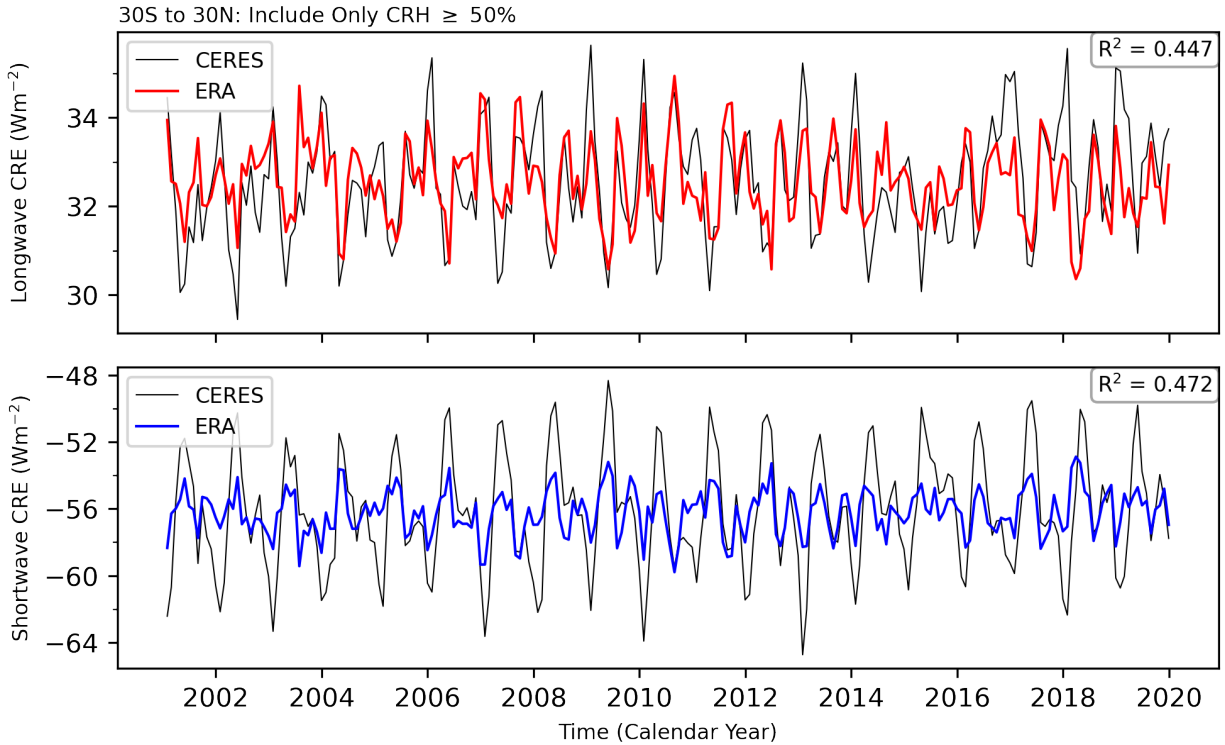


**Figure 4.8:** Same as Fig. 4.6, but only for grid cells with CRH greater than 50%.

Informed by the Fig. 4.7, as well as Figs. 4.2 - 4.5 showing contours of the annual mean CRE, we notice that regions where the estimated CRE agrees poorly with the actual CRE are associated with low stratus clouds off the west coasts of the continents. From Fig. 4.3 these regions are also associated with relatively low values of CRH. We then hypothesize that the CRE method is unable to estimate the CRE in regions of low CRH because it is unable to account for the low level stratus clouds there which contribute strongly to the CRE. In addition, desert regions also appear problematic for estimating the CRE, although the physical reason for this remains unclear.

Fig. 4.8 shows a second time-series comparison between the estimated and actual CRE, where only grid cells with a CRH greater than 50% have been included. The agreement here is much better than for the entire tropical region, with  $R^2$  values greater than 0.4. As in Fig. 4.6, the estimated values have been shifted so that both series have the same mean. The estimated longwave CRE captures much of the variation of the actual CRE, and the variability is of approximately the right magnitude. The shortwave CRE also captures much of the variation, but the magnitudes of

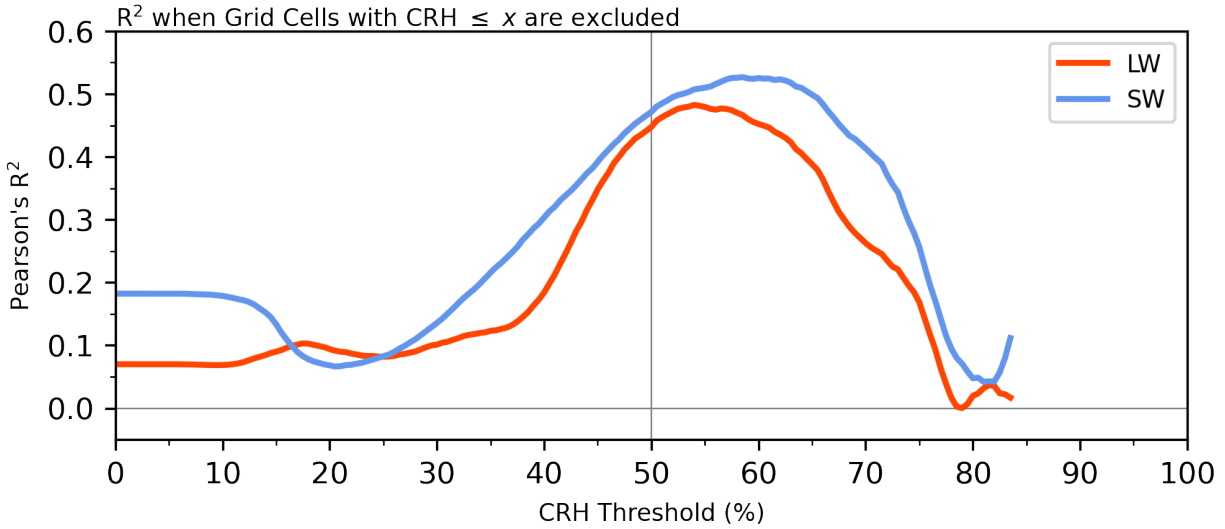


**Figure 4.9:** Pearson's  $R^2$  correlation between estimated and actual CRE when grid cells with CRH less than a particular threshold are excluded.

the changes are smaller. This supports the suggestion that the estimation method works better in regions of large CRH.

While excluding all grid cells with  $CRH \leq 50\%$  improved the correlation between the two time series, the choice of a 50% threshold was ultimately an arbitrary one. To see how the correlation changes when different thresholds are used, the  $R^2$  correlation was found for a range of CRH values. The procedure was to select a CRH threshold, find the domain-mean time series of estimated and actual CRE for all grid cells where the CRH exceeded the threshold, and then find the  $R^2$  correlation between the two. This calculation again utilized the monthly-mean data used in the previous time-series plots, and the result is shown in Fig. 4.9.

From the figure, it is clear that excluding grid cells with low CRH does in fact increase the correlation between the time series. The 50% threshold used in Fig. 4.8 gave one of the larger  $R^2$  values, and the largest  $R^2$  was found by excluding all CRH less than about 55% for the longwave, and about 60% for the shortwave. Excluding grid cells with CRH values larger than this led to a drop in the  $R^2$  correlation. This is to be expected, as the previous chapter emphasized the importance of regions of high CRH for determining the CRE. It is not immediately obvious why the peak in the  $R^2$  should occur at different CRH values for the longwave and shortwave curves,

but it is interesting that both peaks occur near 55% to 60%, showing that excluding regions of low CRH leads to a better estimation of the CRE.

## 4.3 Regional Subsets

### 4.3.1 Annual Mean Values

The previous section focused on evaluating the CRE over the entire region. Now, we turn our attention to the regional subsets first discussed in Chapter 3. The first three columns of Tbl. 4.1 show the annual mean longwave CRE computed from satellite observations, estimated from CRH, and the difference between the two for the three regional subsets used in Chapter 3, for the entire belt from 30°S to 30°N, as well as for land only and ocean only subsets.

In the annual mean, the difference between the domain-average longwave CRE estimated from CRH is on the order of  $0.01 \text{ Wm}^{-2}$ . The differences for the regional subsets, by contrast, have larger magnitudes. The largest difference is found in the EPAC region where the CRH method overestimates the CRE by nearly  $6 \text{ Wm}^{-2}$ . This is consistent with the difference plot from Fig. 4.2, which showed a broad region where the estimated CRE was larger than the actual CRE over the east Pacific. In other words, using the same CRE curve at every location may introduce unavoidable biases in regions such as the east Pacific, where the characteristics of clouds are qualitatively different than in other regions. This agrees with the work of Kubar et al. (2007), who found that clouds in the east Pacific were warmer than clouds in the west Pacific by about 5 K. This would then lead to a smaller CRE for a given cloud type in the east Pacific compared to the west Pacific.

**Table 4.1:** Time mean longwave CRE (first three columns) or shortwave CRE (last three columns) in each of the three tropical regions, as well as for the wider tropical belt. All values are in  $\text{Wm}^{-2}$

	<b>CERES</b>	<b>ERA5</b>	<b><math>\Delta</math> LW</b>	<b>CERES</b>	<b>ERA5</b>	<b><math>\Delta</math> SW</b>
<b>30°S-30°N</b>	24.5553	24.5635	<b>0.0082</b>	-46.1961	-46.2126	<b>-0.0165</b>
<b>WPAC</b>	33.7544	33.3536	<b>-0.4008</b>	-53.5233	-58.8012	<b>-5.278</b>
<b>EPAC</b>	18.2203	24.1013	<b>5.881</b>	-45.9694	-45.8732	<b>0.0962</b>
<b>INOC</b>	34.6229	33.1616	<b>-1.4613</b>	-52.5946	-58.6439	<b>-6.0493</b>
<b>Land Only</b>	26.1866	23.9607	<b>-2.2259</b>	-40.3925	-44.7797	<b>-4.3871</b>
<b>Ocean Only</b>	23.9951	24.7705	<b>0.7754</b>	-48.19	-46.7048	<b>1.4852</b>

The final three columns of Tbl. 4.1 shows the difference in the estimated and actual CRE for the shortwave effects. The difference in shortwave CRE over the whole domain is again on the order of  $0.01 \text{ Wm}^{-2}$ , although it is slightly larger than the difference in the longwave CRE. For the regional subsets, the largest differences are found over the WPAC and INOC regions, with errors greater than  $5 \text{ Wm}^{-2}$ . Although the sign in both cases is negative, these errors show that the CRH method has overestimated the magnitude of the CRE in these regions. In contrast to the longwave error in the EPAC region, there is no obvious physical explanation for these errors. However it is possible that it is a result of including the entire domain in the calculation that lead to the curves in Fig. 4.1. From Fig. 3.7, the shortwave CRE at TOA for the entire domain is close to the curve for the EPAC region, and is larger in magnitude than either the WPAC or INOC regions. In other words, there may be better agreement in the EPAC and INOC regions if the stratus regions were excluded from the calculations that led to the curve in Fig. 4.1. However this would certainly lead to a larger error for the entire tropical belt.

The bottom two rows of Tbl. 4.1 show the difference in the longwave or shortwave CRE when only land or only ocean grid cells are included. For both the longwave and the shortwave, the CRH method is more accurate over the ocean than over land. The CRH method underestimates the magnitude of the CRE over land, which can be seen in the blue shading over Africa and parts of South America in Fig. 4.2. In the shortwave, the CRH method *overestimates* the magnitude of the CRE over land. This is visible in Fig. 4.4 where there are again blue regions over the continents, although in this case they represent larger negative values. The difference over oceans is smaller in magnitude than the difference over land, and is of opposite sign. Over oceans, the CRH method overestimates the CRE in the longwave, and underestimates it in the shortwave.

### 4.3.2 Regional Time Series

Next, time-series plots for the actual and estimated CRE were found for three regional subsets corresponding to the west Pacific, east Pacific, and Indian Ocean, following the method of the previous section. As in Figs. 4.6 and 4.8, each of the estimations have been shifted to have the same mean as the time series of the actual CRE. The magnitude of the shift corresponds approximately

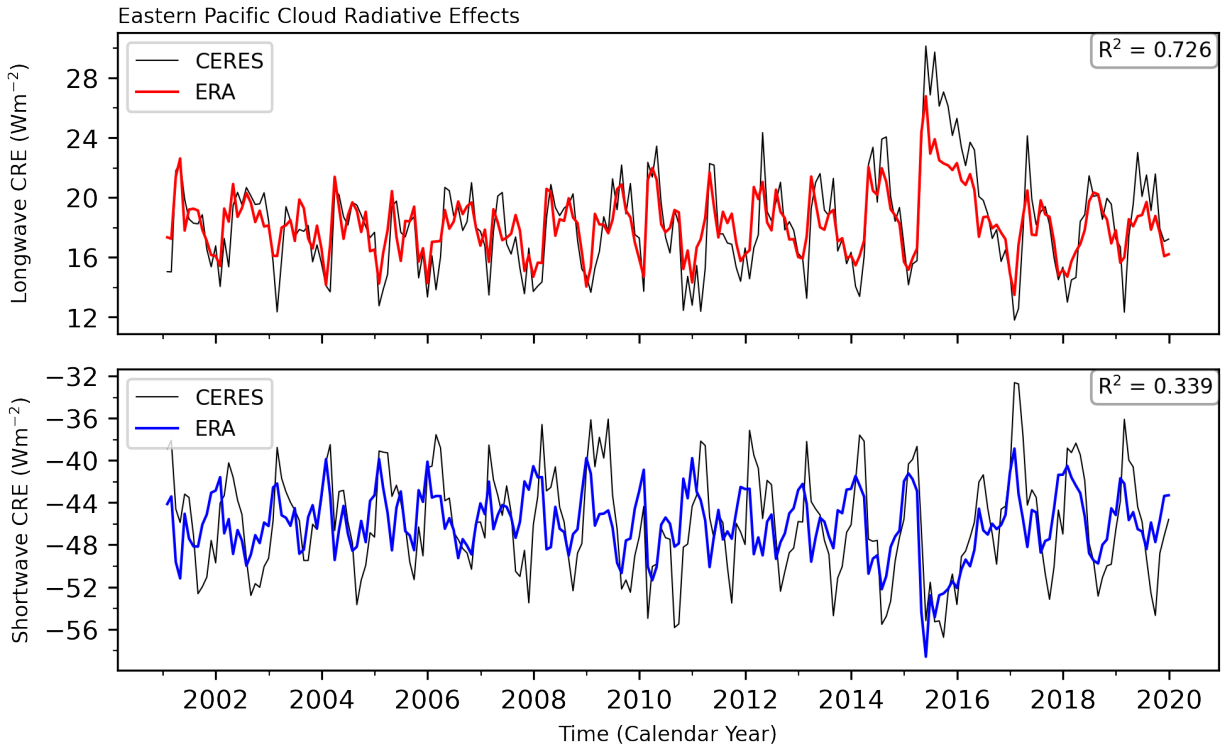


**Figure 4.10:** Same as Fig. 4.6, but for the EPAC region

to the difference column from Tbl. 4.1, although the actual size will be slightly different as the values from the tables were calculated from the 6-hourly data rather than from the monthly-mean data.

Figs. 4.10, 4.12, and 4.13 show time series and correlations for each of the three regional subsets. In the EPAC region, the estimated longwave CRE does a very good job of reproducing the variability of the actual CRE, with a  $R^2$  value above 0.7. The agreement between the estimated and actual longwave CRE shown in Fig. 4.10 is after the shift of about  $6 \text{ Wm}^{-2}$ , indicating that the CRH method systematically overestimates the longwave CRE in this region, as discussed previously. In the shortwave, there is some agreement between the two series, but the correlation is markedly lower. An obvious question is whether the disagreement between the two methods is in any way tied to ENSO, the largest source of variability in the east Pacific.

To answer this question, a simple composite analysis was performed on the two time series showing the estimated and actual shortwave CRE in the EPAC region. First, each month repre-

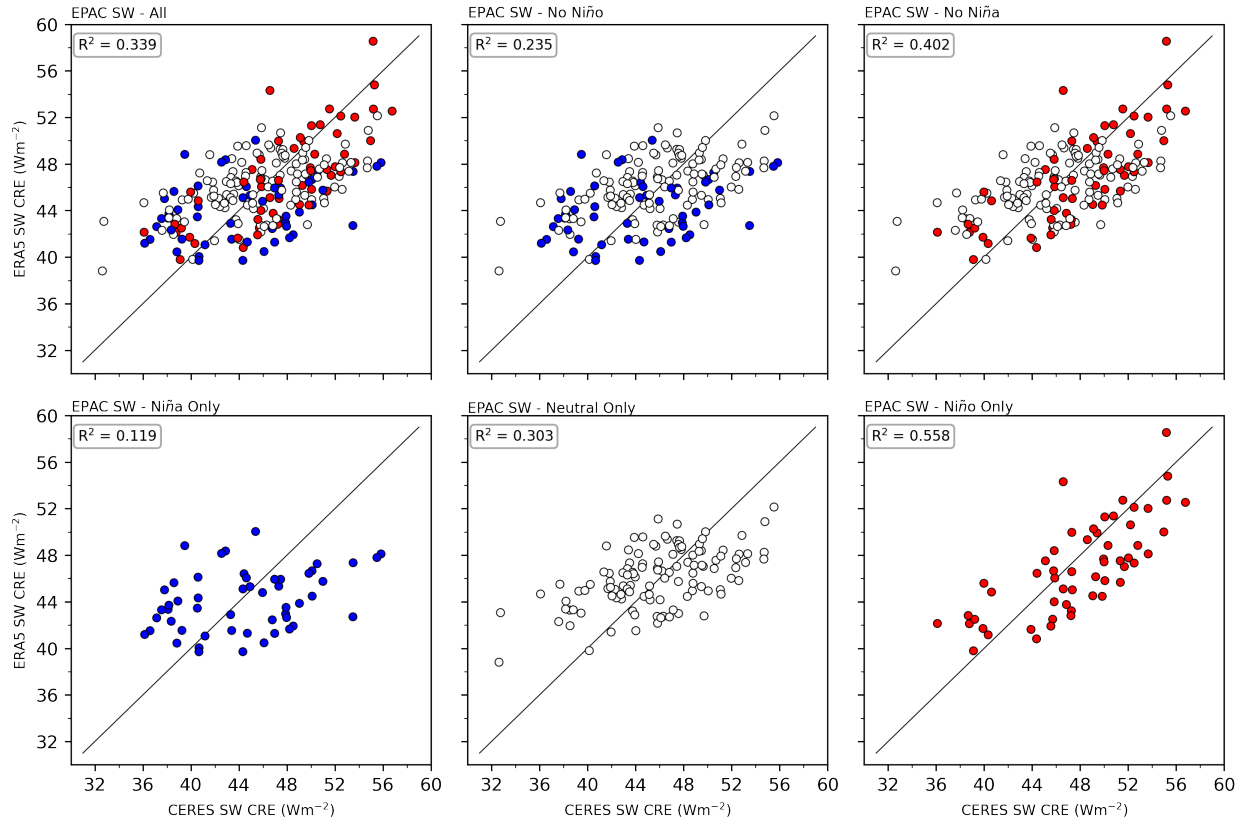


**Figure 4.11:** Scatter plot composite analysis comparing actual and estimated SW CRE in the EPAC region, for different ENSO phases or combinations of phases. Red dots show El Niño months, blue dots show La Niña, and white dots show the neutral phase. The diagonal line shows the idealized one-to-one correspondence.

sented in Fig. 4.10 was mapped to the corresponding value of the Oceanic Niño Index (ONI, see §2.1.4). For example, January 2016 was tagged as an El Niño month because the ONI for DJF 2016 exceeded the 0.5 K threshold. Note that the ONI is computed using a centered three month running mean, which is why the CRE data for January 2016 was mapped to the DJF data point rather than to the NDJ data point. Then, subsets were taken from the time series data to collect only the values that occurred during a particular ENSO phase, or combination of phases. A total of six subsets were investigated: the entire record, two subsets that combined the neutral and Niño or neutral and Niña phases, and then each of the three phases alone (Niña, neutral, and Niño). After the desired subset was selected, the correlation coefficient between the estimated and actual CRE was found.

The results of these calculations are shown in Fig. 4.11, where the points have been shaded red for the Niño phase, white for the neutral phase, and blue for the Niña phase. The top left panel shows data for the entire nineteen year period of analysis, without removing any subsets. This corresponds to the two time series plots in the bottom panel of Fig. 4.10, and shows the same  $R^2$  correlation. The top middle and top right panels show the same data as the top left panel, but after removing months corresponding to either El Niño or La Niña, respectively. The bottom three panels show the months corresponding to either the La Niña, neutral, or El Niño phase.

The highest correlation occurs when only the Niño months are included in the analysis (bottom right panel), and the lowest occurs when only the Niña months are included. The higher correlation during El Niño can be explained physically by considering the warmer ocean temperatures and more active convection in the east Pacific associated with an El Niño. These features would lead to a reduction in the low stratus clouds that are problematic for the CRH method. From Figs. 4.2 and 4.4, the stratus decks cause the largest problem in estimating the shortwave CRE, and only cause minor errors in estimating the longwave. This would explain why the correlation in the EPAC region is much higher for the longwave than for the shortwave CRE. Further links between the estimated CRE and ENSO are discussed in Appendix B, in particular those in relation to the west Pacific.

Next, Fig. 4.12 shows a comparison of actual and estimated CRE in the west Pacific. In the WPAC region the estimated CRE in both the longwave and shortwave are largely able to reproduce the variability of the actual CRE, with the exception of a few extreme peaks. These peaks coincide with strong El Niño events, which lead to a larger magnitude of the actual CRE that the estimated CRE is unable to reproduce. As will be discussed in Appendix B, the accuracy of the estimation method is impacted in both the EPAC and WPAC regions, although in opposite ways. In the EPAC the accuracy is increased during El Niño, while in the WPAC the accuracy is diminished.

Lastly, Fig. 4.13 compares the time series over the Indian Ocean. As a whole, the INOC region shows the worst agreement between the actual and estimated CRE. And unlike the EPAC and WPAC regions, the disagreement cannot be tied to ENSO (see Appendix B). Other factors

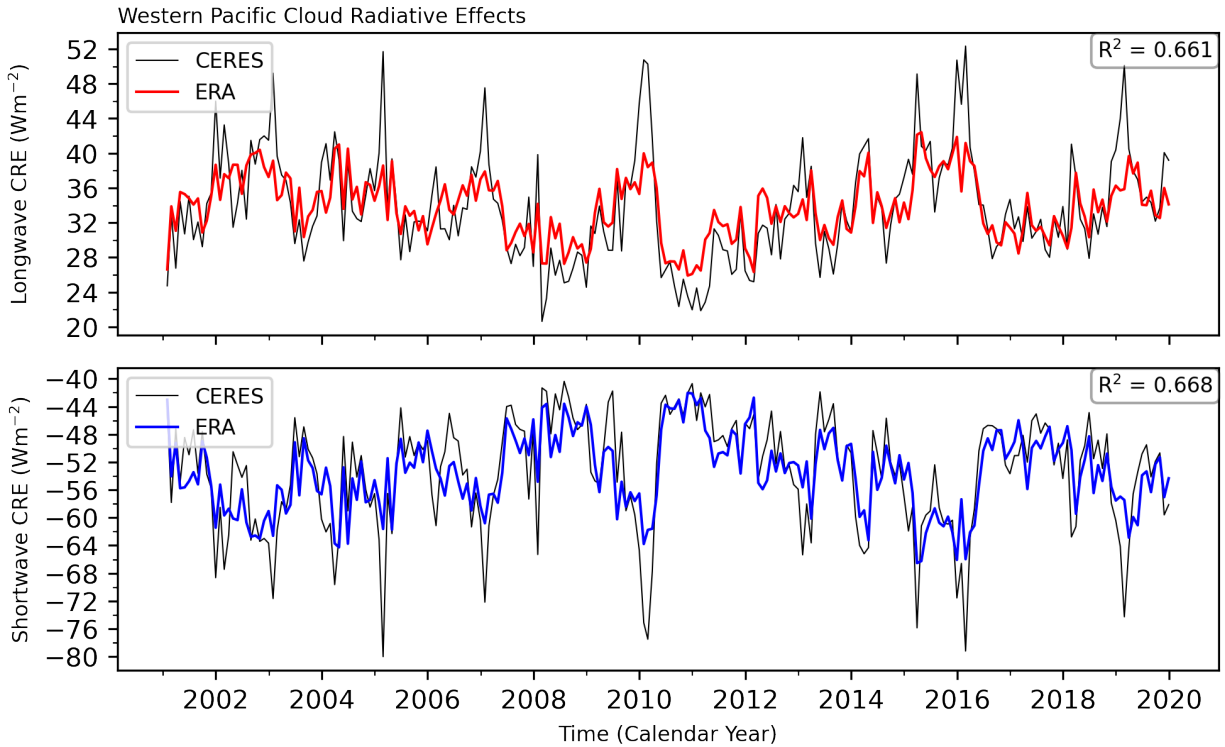


**Figure 4.12:** Same as Fig. 4.6, but for the WPAC region.

such as the Madden-Julian Oscillation or the South Asian Monsoon may be to blame here, but the ultimate cause of the error is left to future work.

## 4.4 Summary

In Chapter 3, the relationship between the CRH and the CRE was found to be nearly independent of the SST in idealized simulations of RCE, as well as in calculations involving satellite observations and reanalyses. These results motivated the work of this chapter, where the CRH calculated from reanalyses was used to estimate the CRE. This estimated CRE was then compared to the actual CRE calculated from satellite observations.

The CRH method was able to reproduce many of the large-scale features of the longwave and shortwave CRE fields. In particular, it showed features associated with the intertropical and south Pacific convergence zones and tropical rain forests over equatorial Africa and South America. The largest differences between the actual and estimated CRE were found to be associated with regions

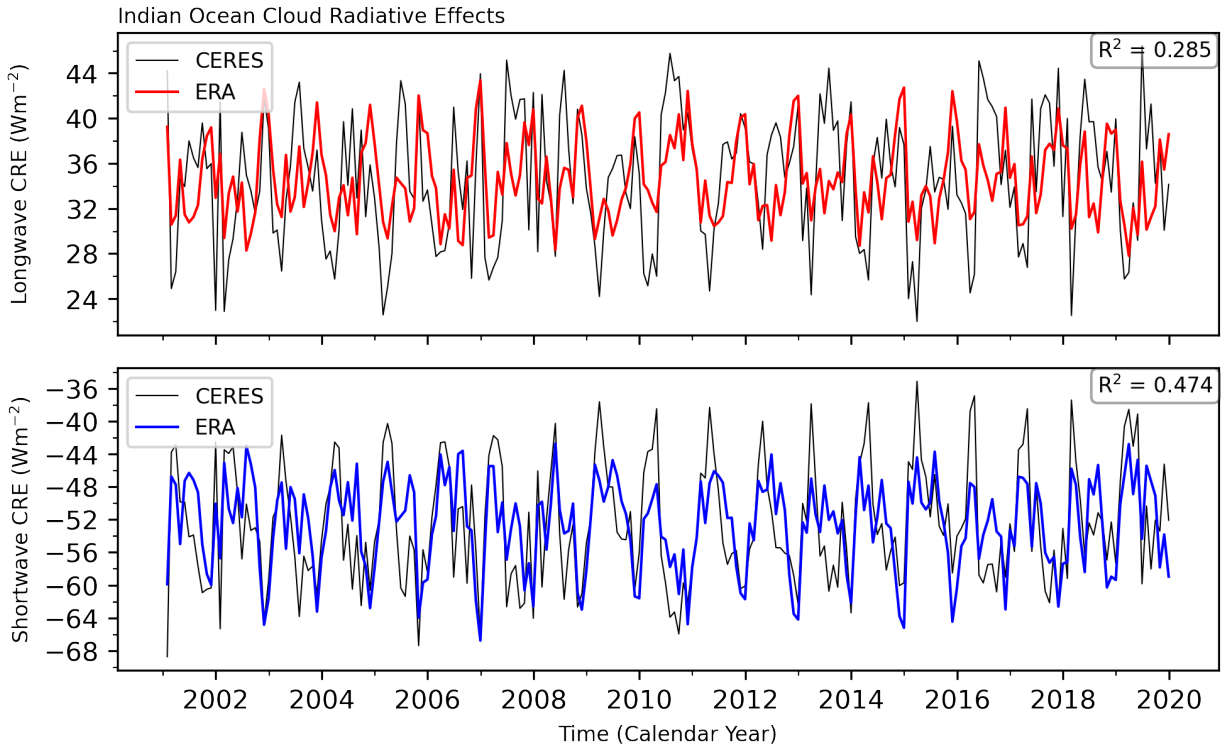


**Figure 4.13:** Same as Fig. 4.6, but for the INOC region.

of low-level stratus clouds found off the west coasts of the continents. These stratus clouds have a weak CRE in the longwave, but a strong CRE in the shortwave. The shortwave error associated with these low clouds helps to explain why the CRH method was generally worse at estimating the shortwave CRE compared to the longwave.

The CRH method was then investigated in terms of the temporal accuracy. Averaged over the entire domain, the CRE estimated from the CRH was a poor predictor of the actual CRE. However when the driest grid cells were excluded (where  $CRH \leq 50\%$ ), the agreement was much better. Lastly, the temporal analysis was repeated for the same three regional subsets used in Chapter 3. The best overall agreement between the two methods was found in the west Pacific. In the east Pacific, the influence of the stratus clouds likely contributed to errors in estimating the shortwave CRE. When a simple composite analysis was used to compare the accuracy of the shortwave estimation in different ENSO phases, the correlation in the EPAC was found to be largest during El Niño and smallest during La Niña. Errors in the Indian Ocean region were left

unexplored in this chapter, but in Appendix B it is shown that the errors are not explained by variability associated with ENSO.

The next chapter continues to use the CRH analysis framework of previous chapters, but no longer as it relates to cloud radiative effects. Instead, Chapter 5 investigates the moisture and energy budgets in terms of the CRH, for the RCEMIP experiments and in reanalyses.

## Chapter 5

### Energy and Moisture Analysis as a function of CRH

In Chapter 3, the CRE was found to be a nearly universal function of the CRH for the RCEMIP simulations, and showed only minor changes as the surface warmed. A CRH value of approximately 70% was found to be an inflection point separating regions of large CRE from regions with small CRE (see Fig. 3.3). Calculations performed using satellite observations and reanalyses were consistent with these model-based findings (Fig. 3.7), and again showed a qualitative change at 70% CRH.

In this chapter, an analysis is made of the energy and moisture budgets of the RCEMIP simulations, binned by the CRH. The calculations are performed by direct analogy to studies that have looked at the meridional transports of energy and moisture in the real atmosphere (e.g. Vonder Haar and Oort (1973), Trenberth and Caron (2001)). The CRH value of 70% is found to be a useful threshold for separating regions where moisture converges from regions where it diverges. It is also found to generally separate regions where radiation converges into the atmosphere, in agreement with the discussion of atmospheric cloud radiative effects from Chapter 3. Taken together, it is found that moisture flows against the gradient from the dry to humid regions, while energy flows down the gradient from the humid to dry regions. This conclusion is then connected to the work of Riehl and Malkus (1958).

#### 5.1 Moisture balance

The time-averaged horizontal transport of water vapor within the atmosphere can be calculated in terms of the vertically-integrated convergence of water vapor, as

$$\int_0^{\infty} -\nabla_H \cdot (\rho \mathbf{V}q) dz = P - E, \quad (5.1)$$

where  $q$  is the water vapor.  $P$  and  $E$  are rates of precipitation and evaporation, and represent the local sources and sinks of moisture. In locations where  $P - E$  is positive, the atmosphere is losing

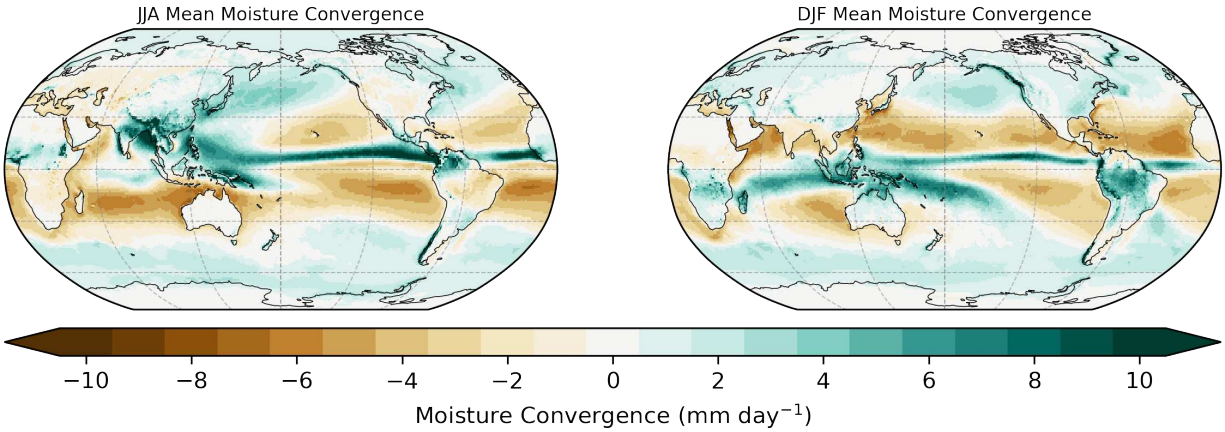


**Figure 5.1:** Seasonal mean plots of moisture convergence for JJA and DJF, calculated from ERA5 monthly mean reanalyses for the 21st century through 2018.

more water to precipitation than it is gaining through evaporation. The opposite is true when  $P - E$  is negative. It is known that the time-mean, domain-mean  $P - E$  is small, so Eq. 5.1 represents a simple water cycle in which moisture enters the atmosphere in one location through evaporation, is transported through dynamical and cloud processes, and then exits the atmosphere in another location through precipitation.

Seasonal mean plots of Eq. 5.1 for June, July, and August (JJA), and December, January, and February (DJF) are shown in Fig. 5.1. The moisture flux convergence was calculated using monthly mean precipitation rates and latent heat fluxes from ERA5 reanalyses. The plots show a divergence of moisture in the subtropics along with a strong convergence of moisture into the intertropical and south Pacific convergence zones. There is also a smaller convergence of moisture into higher latitudes. These plots indicate that evaporation of ocean water in the subtropics is the primary source of moisture for the atmosphere.

In contrast to the real world, the RCEMIP simulations contain no land masses or meridional gradients in temperature (see §2.1.1). This means that there are no regions in the RCEMIP simulations where  $P - E$  is different from zero in a time mean sense. However, certain regions can be a source or sink for moisture on shorter time-scales. The study of Bretherton et al. (2004) suggests that the CRH may be a useful metric for separating the domain into regions that are sources or sinks of moisture. Fig. 5.2 shows the relationship between CRH and observations of the precipitation

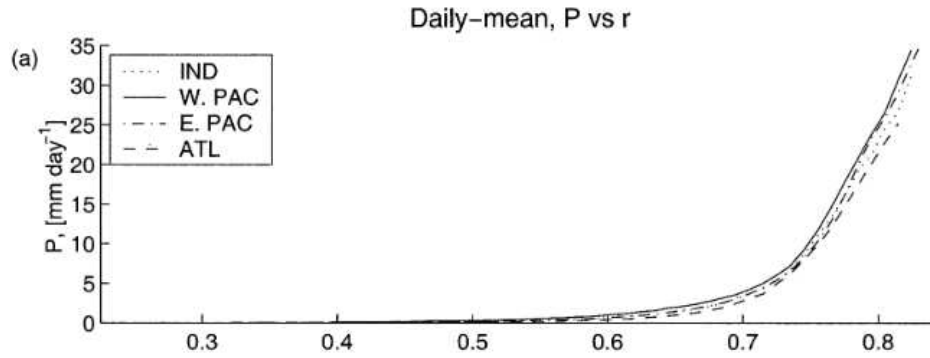


**Figure 5.2:** Fig. 3a from Bretherton et al. (2004), showing the precipitation rate across four ocean basins as a function of the column relative humidity, with the CRH given as a fraction.

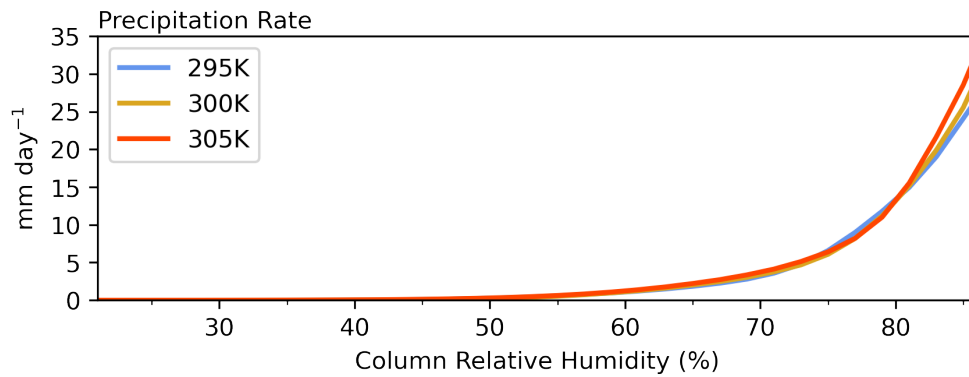


**Figure 5.3:** Precipitation rate in the RCEMIP simulations, as a function of the CRH. Compare with Fig. 5.2 rate across four ocean basins as presented in Bretherton et al. (2004). The ocean basins encompass a wide range of SSTs and cloud conditions, but the precipitation rate at a particular CRH shows little difference between the regions.

The precipitation rate as a function of CRH for the RCEMIP simulations is shown in Fig. 5.3, with the y-axis scaled to show the same range as Fig. 5.2. Like the curves from Bretherton et al. (2004), the RCEMIP precipitation curves appear to be a nearly universal function of the CRH. Both show a rapid increase in the precipitation rate as the CRH becomes greater than 60%, although the RCEMIP curves show a smaller precipitation rate at a given CRH. There also appears to be little difference in the precipitation rate at a given CRH value across the three SSTs.

The precipitation rate as a function of CRH is shown again in the top panel of Fig. 5.4, with a different scaling on the y-axis. The scaling is chosen to coincide with the middle and bottom

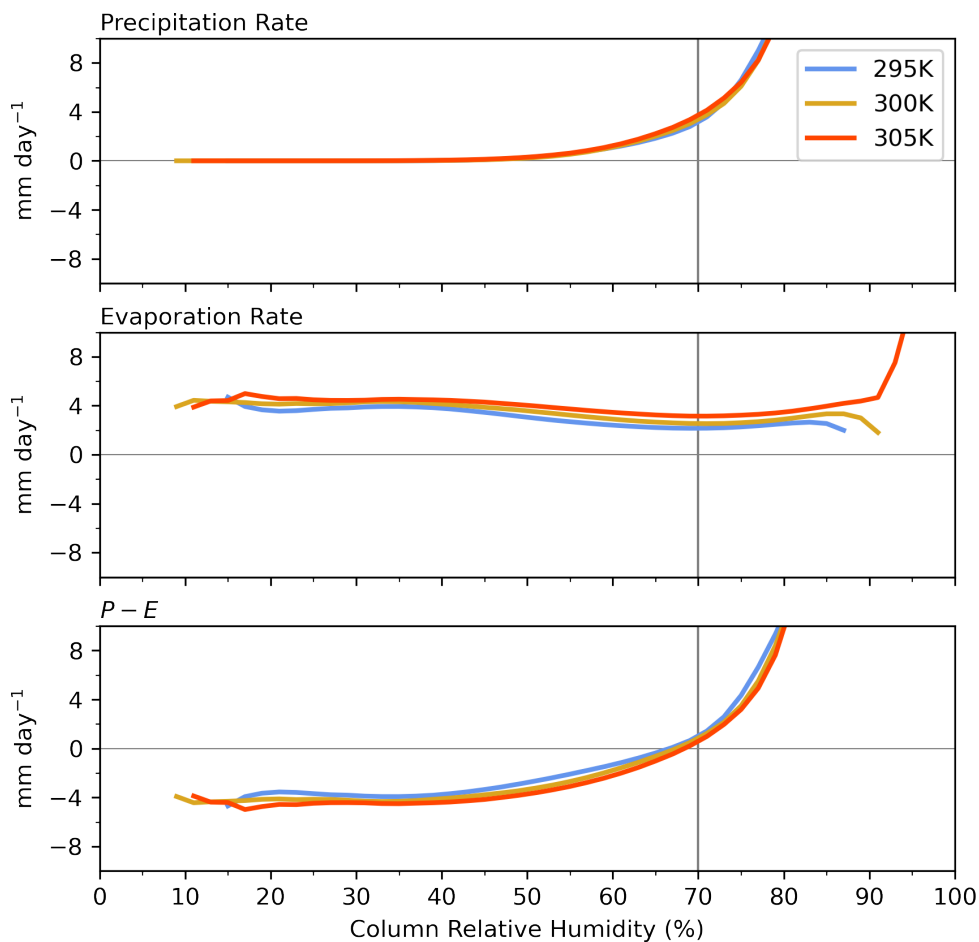


**Figure 5.4:** Precipitation, evaporation, and  $P - E$  vs. CRH.

panels of the figure. The middle panel of Fig. 5.4 shows the evaporation rate as a function of the CRH, calculated from the latent heat flux. The evaporation rate shows little if any dependence on the CRH, and increases slightly as the surface warms.

The bottom panel of Fig. 5.4 shows the moisture flux convergence calculated using Eq. 5.1 as the difference between the top and middle panels. Like the precipitation rate, these curves are largely independent of the SST. Moreover, they pass through zero between 65% - 70% CRH; the same value that was identified in Chapter 3 in both the RCEMIP simulations, as well as in CERES and ERA5 analysis. For CRH greater than 70% the positive  $P - E$  indicates that local precipitation is a larger sink to moisture than local evaporation is a source. This requires an upgradient transport

of moisture into regions of high CRH from regions of low CRH. Fig. 5.4 confirms that this is possible, as the curve for  $P - E$  is negative for CRH less than 70%.

Does the CRH value of 70% have relevance to  $P - E$  in the real atmosphere? Fig. 5.5 shows contours of the annual-mean, JJA-mean, and DJF-mean moisture convergence calculated from monthly-mean ERA5 reanalyses. The plots show the belt ranging from 30°S to 30°N where the relationship found in the RCEMIP simulations can be best expected to hold. Also included in red are contours showing the annual-mean or seasonal-mean 70% CRH contour, using the data calculated in Chapter 3.

The 70% contour does a good of outlining regions of moisture convergence in places where the gradient is sharp. There are some places where the agreement is worse, such as along the southeastern edge of the south Pacific convergence zone. Broadly, however, the 70% CRH contour appears to be a useful threshold for separating the domain into dry regions with low CRE that are a source of moisture, and humid regions with high CRH that are a sink for moisture.

## 5.2 Energy balance

In a way similar to Eq. 5.1, the time-mean energy balance of an atmospheric column can be written in terms of the convergence of moist static energy as

$$-\int_0^{\infty} \nabla_H \cdot (\rho \mathbf{V} h) dz = \nabla \cdot (\mathbf{R} + \mathbf{F}_h). \quad (5.2)$$

Here,  $\mathbf{R}$  and  $\mathbf{F}_h$  represent the flux of radiation and moist static energy into the column, from the surface and TOA. Eq. 5.2 can be rewritten as

$$F = SW_{\text{Toa}} + LW_{\text{Toa}} + SW_{\text{Sfc}} + LW_{\text{Sfc}} + SH + LE \quad (5.3)$$

where the terms on the right hand side represent the net fluxes of shortwave and longwave radiation, sensible heat, and latent energy into the column.

The terms representing the surface energy budget are shown in Fig. 5.6, where they have been binned by the CRH. The sign convention used is that positive values represent a flux of energy

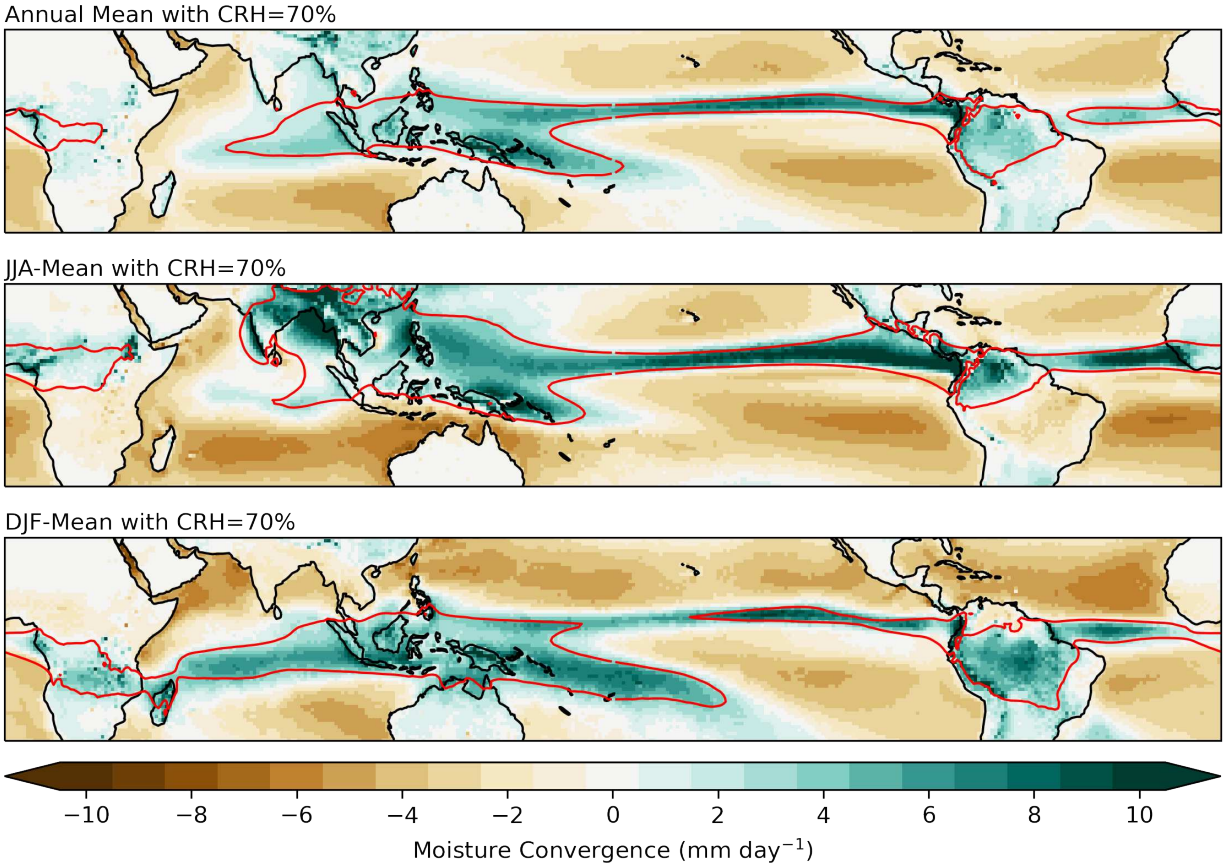


**Figure 5.5:** **Top** Annual mean moisture convergence calculated from ERA5 reanalyses, with the annual mean CRH contour of 70% superimposed in red. **Middle** and **Bottom** Same as **Top**, but for JJA and DJF.

or radiation into the atmosphere from the surface, and each of the terms is shown using the same scale on the y-axis. The surface sensible and latent heat fluxes are combined to give the surface flux of moist static energy, which is shown in the top panel of Fig. 5.6. The moist static energy flux is positive everywhere and does not change much for different CRH bins. It does show a slight dependence on the surface temperature, and increases in magnitude as the surface warms.

In contrast to the flux of moist static energy, the surface radiation fluxes show a clear dependence on CRH. The net shortwave radiation is directed into the surface while longwave radiation is directed out of the surface. In most of the domain, the shortwave component dominates, leading to a net radiation flux into the surface. In the humid region, the increased cloudiness prevents shortwave radiation from reaching the surface so that the net radiation flux goes to zero. This is an effect of the enhanced ACRE in humid regions, as discussed in Chapter 3. As will be seen below,

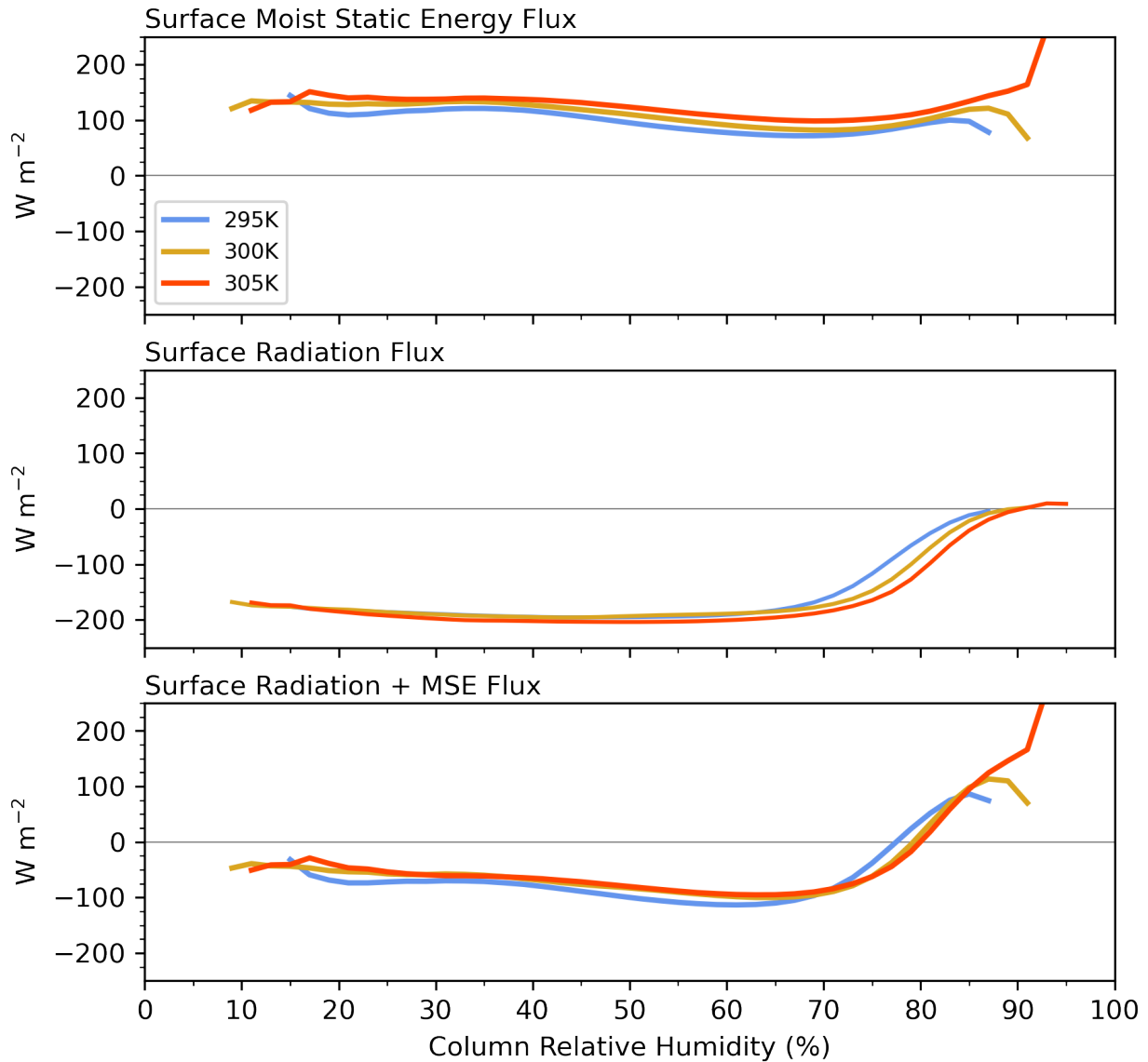


**Figure 5.6:** Surface fluxes of moist static energy, radiation, and the net energy flux into the atmosphere from the surface.

the disappearance of the surface radiation flux contributes to a strong net flux of energy into the atmosphere in humid regions.

Combining the surface heat and radiation fluxes leads to the curves in the bottom panel of Fig. 5.6. In most of the domain the net flux is into the surface, driven by the large shortwave fluxes. In the humid region, the curves become small and eventually change sign, representing a net flux of energy from the surface into the atmosphere. Following Neelin and Held (1987), the flux of energy

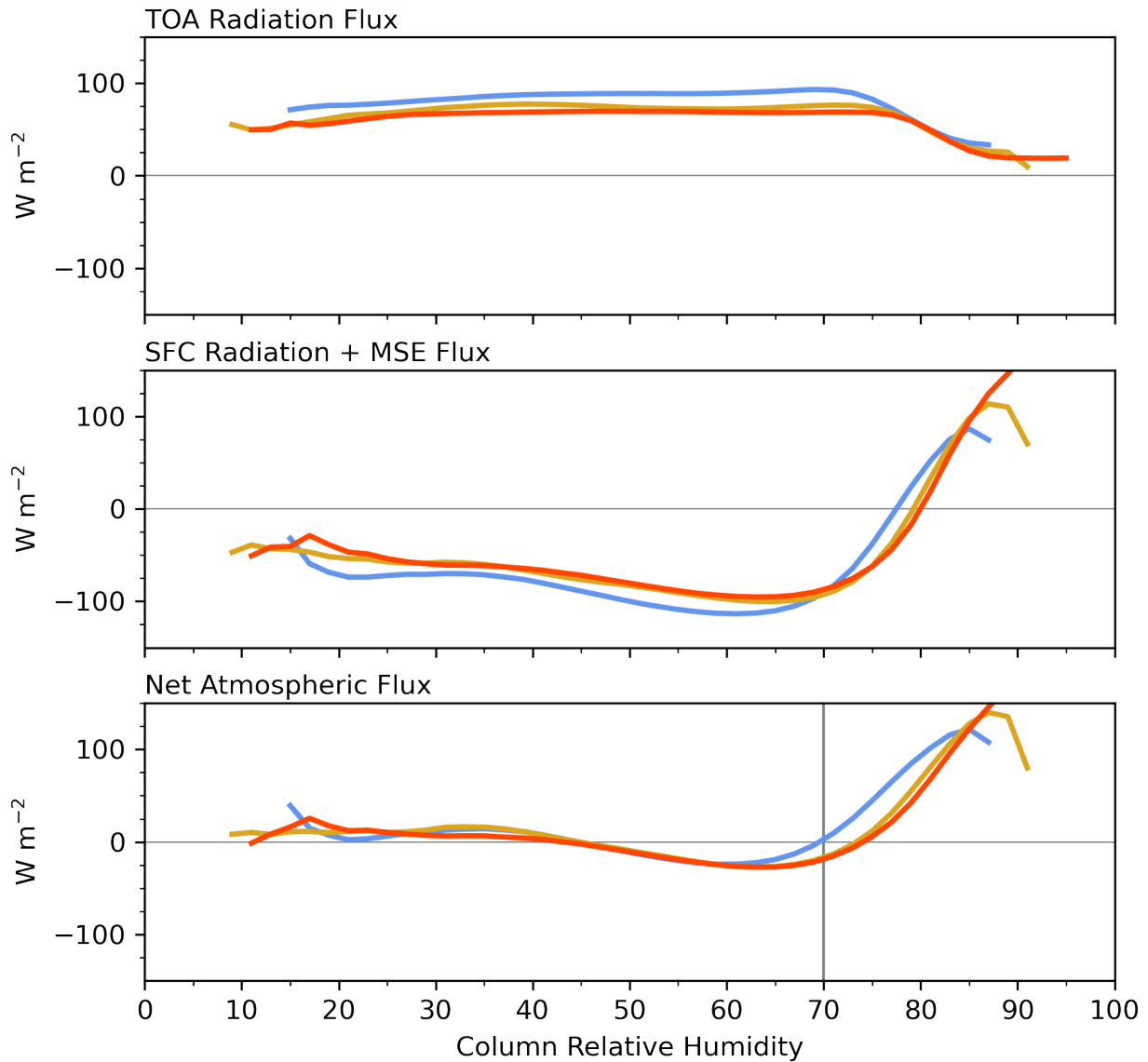


**Figure 5.7:** Combined fluxes of radiation at the TOA and radiation plus moist static energy flux at the surface. Bottom panel shows the net TOA - SFC flux of energy.

into the atmosphere leads to a strong convergence in the humid regions. This helps to explain the convergence of moisture shown in the bottom panel of Fig. 5.4.

Next, the combined TOA radiative fluxes from Eq. 5.2 are shown in the top panel of Fig. 5.7. The flux is positive everywhere in the domain, and the sign convention once again is that a flux into the atmosphere is positive. As discussed in §2.1.1 and in Chapter 3, the RCEMIP protocol employs an extremely strong shortwave forcing, so the TOA radiation flux would not be uniformly positive in the real atmosphere. However, the atmosphere is largely transparent to shortwave radiation, so a

reduction in the insolation would likely not change the energy flux convergence all that much. With this in mind, the bottom panel shows the TOA radiation flux combined with the surface radiation and moist static energy fluxes.

For CRH less than 50%, the net atmospheric flux is near zero, implying the convergence of the winds is near zero (Neelin and Held, 1987). The atmospheric flux becomes slightly negative between 50% to about 70% CRH implying divergence. In the humid region the net atmospheric flux becomes positive and large, implying convergence. From Fig. 5.6 it is clear that this positive flux is due to a change in the radiation flux, rather than in the moist static energy flux. The curve for the 295 K simulation passes through zero near 70% CRH, while the 300 K and 305 K simulations pass through zero closer to 75%. Then, for most of the humid domain, there is a net vertical convergence of energy into the atmosphere, due largely to changes in the radiative fluxes. This is complimentary to the results of Chapter 3, where it was found that humid regions were associated with a large atmospheric cloud radiative effect.

Using the same reasoning as in the previous section, a surplus of energy in the humid region combined with an energy deficit from 45% to 70% CRH would require a net flux of energy from the humid region to the dry region. In contrast to the up-gradient transport of moisture from dry to humid regions, this indicates a down-gradient transport of energy from humid to dry region, implying positive gross moist stability (Neelin and Held, 1987; Raymond et al., 2009).

When combined with the result from Fig. 5.3, we are left with the image of a dry region and a humid region separated by a threshold of 70% CRH, in which evaporation of ocean water in the dry region is transported into the humid region where it is lost through precipitation. At the same time, the humid region is an energy source for the atmosphere due primarily to atmospheric cloud radiative effects, rather than to an increased flux of moist static energy from the surface. This conceptual model is analogous to the model of the ITCZ presented by Riehl and Malkus (1958), in which latent energy converges into the deep tropics at the same time as potential energy and enthalpy are exported to higher latitudes.

## 5.3 Segue

This chapter has analyzed the moisture and energy budgets of the RCEMIP simulations in terms of the column relative humidity. A CRH of 70% was again found to be an important threshold between regions of small and large CRE. The net precipitation minus evaporation changed sign at approximately 70%, indicating a boundary between dry regions characterized by evaporation and humid regions characterized by precipitation. The ERA5 reanalyses shows that the 70% CRH value aligned with the location where the moisture convergence vanishes in some places, including along the ITCZ. However the CRH contour deviated from the location where  $P - E$  equals zero in other places.

An energy budget analysis showed that the humid region is a source of energy for the atmosphere, in addition to being a sink for moisture. A comparison was then drawn between the humid region and the ITCZ as discussed by Riehl and Malkus (1958). In future chapters, this link to Riehl and Malkus (1958) will be made more explicit, beginning in Chapter 6 with a discussion of a feedback between moisture and radiation in the humid region.

## Chapter 6

# A radiatively driven moisture feedback in extremely humid regions

Chapter 3 was focused on the cloud radiative effect at the TOA, at the surface, and the atmospheric cloud radiative effect. The column relative humidity proved to be a powerful metric for estimating CRE, and a CRH of 70% was found to be an important threshold for separating regions of small and large CRE. In Chapter 5, that 70% value was found to separate dry regions associated with evaporation from humid regions associated with precipitation. In addition, the humid region was found to be a source of energy for the atmosphere, in a way that suggests it may be analogous to the ITCZ.

In this chapter, the CRH is used to bin vertical profiles of radiative heating rates, static energies, and other fields. This analysis is used to investigate the relationship between radiative heating rates and the drying (moistening) caused by large-scale subsiding (rising) motion. We show that in humid regions the extremely large longwave and shortwave ACRE is able to change the sign of the net radiation tendency through a layer that spans most of the troposphere. This leads to a radiatively driven moisture feedback where strong ACRE in the humid region causes rising motion that lifts moisture. The moisture then increases the amount of cloudiness in turn increases the ACRE, continuing the process. The relevance of this feedback to the vertical transport of energy as studied by Riehl and Malkus (1958) is discussed.

### 6.1 The vertical distribution of radiative tendencies and ACRE

The three RCEMIP simulations described in §2.1.1 provide vertically resolved full-sky and clear-sky radiative tendencies. Profiles of the longwave, shortwave, and net radiative tendency were found as a function of CRH. The procedure here is identical to that used in §3.2, except that a vertical profile was calculated for each CRH bin rather than a vertical integral.

Contour plots of the radiative tendency profiles are shown in Fig. 6.1. On each plot, the horizontal shows the column relative humidity and the vertical axis shows the altitude. Also included are vertical lines at 70% CRH, corresponding to the threshold between dry and humid regions as discussed in Chapter 5. In the figures to follow, the 295 K and 300 K contours are very similar, while there are qualitative differences between these and the contours for the 305 K simulation.

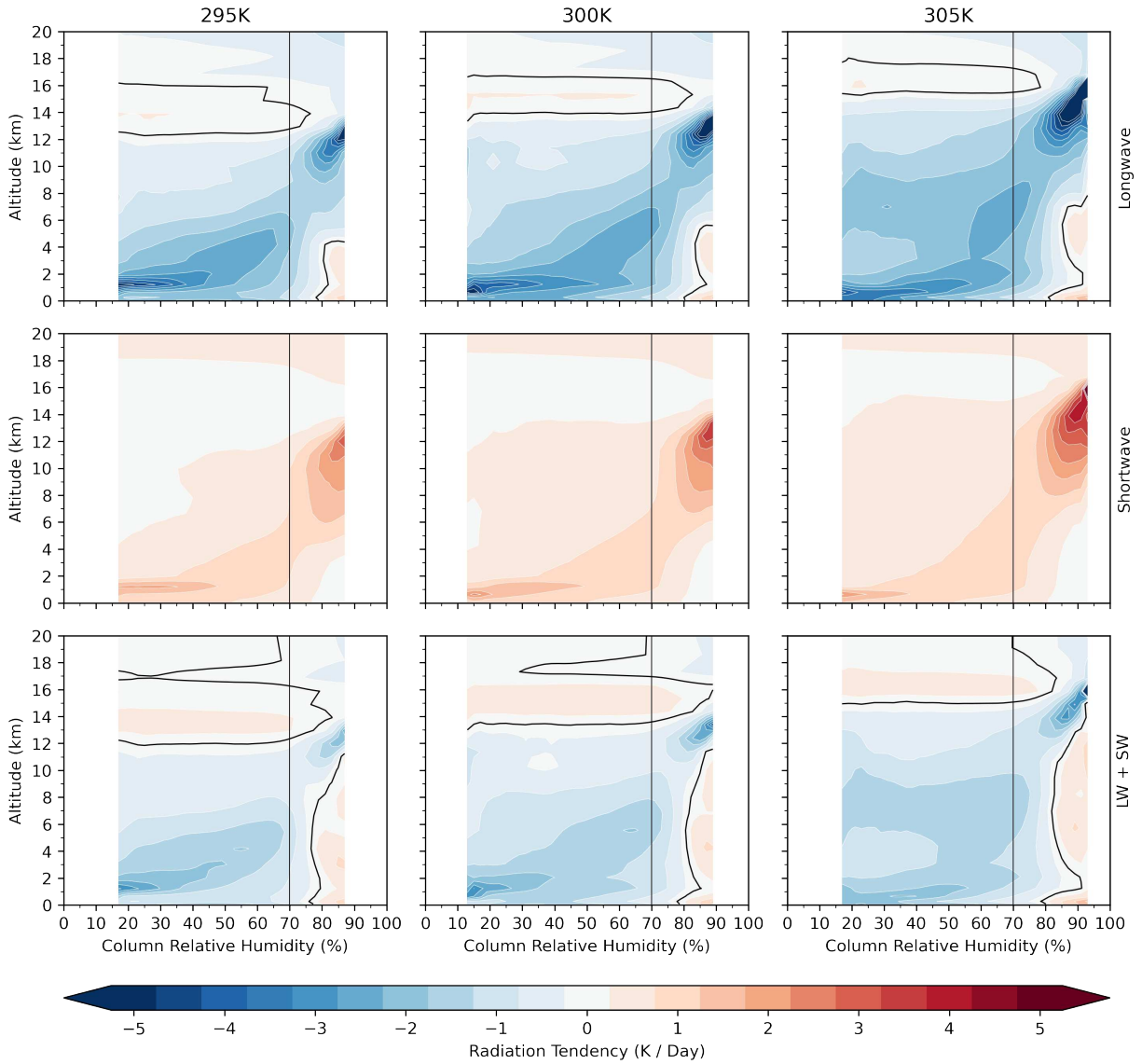


**Figure 6.1:** **Top Left** Longwave heating rate profile as a function of column relative humidity for the 295 K experiment. **Top Center** and **Top Right** Same as **Top Left**, but for the 300 K and 305 K experiments. **Middle Row** and **Bottom Row** Same as **Top Row**, but for the shortwave and net radiative heating rates. Contours are spaced every  $0.25 \text{ K Day}^{-1}$ . Red represents radiative heating, while blue represents radiative cooling.

The top row of Fig. 6.1 shows the longwave radiative tendency profile for each CRH bin. In regions of low CRH the majority of the cooling occurs from water vapor in the boundary layer. Even in the dry regions, there is a significant amount of low-level water vapor because the lower boundary in the RCEMIP simulations is ocean. At higher altitudes in the dry regions, the tendency represents a small cooling that decreases in magnitude up to the radiative tropopause. The exception is the 305 K simulation, which has a secondary maximum in longwave cooling near 5 to 7 km in the dry regions.

As the CRH increases from 50% to 70%, the cooling begins to shift to higher altitudes, and above 70% CRH the longwave tendencies become very strongly negative aloft. In the most humid regions of the domain, the longwave tendency becomes weakly positive from the surface to an altitude of 4 - 7 km, depending on the simulation. This positive longwave tendency was unexpected, and later plots will show that the sign change is due to strong ACRE in these regions.

The structure of the shortwave tendency is more simple than the longwave, with heating at all altitudes in every part of the domain. Similar to the longwave tendency, the maximum in heating shifts from the boundary layer in dry regions to the higher altitudes in humid regions. The 305 K simulation shows some evidence of a secondary maximum of the shortwave tendency in the dry regions, but it is not as distinct as for the longwave tendency.

The net radiative tendency is negative in most regions of the troposphere from the boundary layer up to the radiative tropopause. This indicates that the longwave component tends to dominate. However, in the most humid regions, the net radiative tendency is positive throughout the depth of the troposphere. Comparing the longwave, shortwave, and net tendencies, the longwave heating contributes to this heating up to the middle of the troposphere, but the powerful shortwave heating is responsible for the net positive values aloft. The importance of this radiative heating will be discussed later.

The vertical line at 70% CRH roughly divides the radiative tendencies into two distinct regions, corresponding to the dry and humid regions that were the subject of Chapter 5. The radiative heating in dry region is concentrated in the moist boundary layer. Emission to space at these near-surface temperatures corresponds to the small longwave CRE shown in Fig. 3.3. An absence of

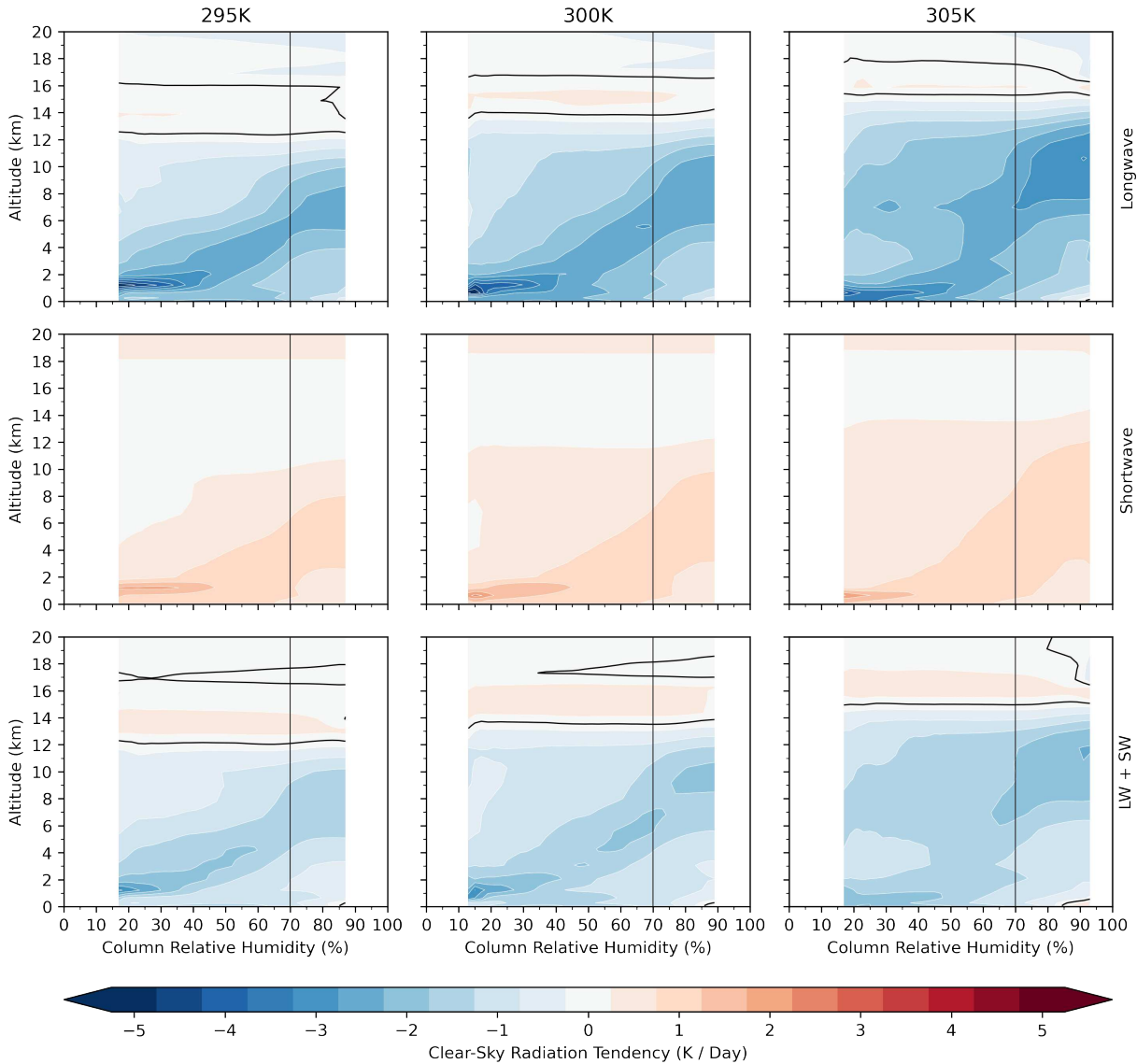


**Figure 6.2:** Same as Fig. 6.1, but for the clear-sky radiation tendency.

many clouds in the dry region would lead to an effective albedo that is very close to the surface albedo, corresponding to the small shortwave CRE. There was no noticeable difference between the CRE for the 305 K simulation from the other two in the dry region, so the secondary maximum observed near 7 km for this experiment appears to have little effect on the TOA or surface radiation balance. The radiative effects in the humid region are better explained by comparing the full-sky and clear-sky radiation tendencies.

Fig. 6.2 shows the same calculation as Fig. 6.1, but substituting the clear-sky for the full-sky radiation tendency. While the clear-sky radiation calculations omit any interactions with clouds, they still include interactions with water vapor. Similarities and differences between these two figures can help to indicate whether a particular phenomenon is due to water vapor, or due to cloud effects. Notably, the clear-sky tendencies shift upwards as the CRH increases, showing that the shift to higher altitudes is due to water vapor, not absorption by clouds. In addition, the 305 K simulation still has a secondary maximum in the dry region, indicating that it too is a result of water vapor and not clouds. A major difference between these plots is found in extremely humid regions, where the full-sky and clear-sky tendencies have opposite signs. This implies that the net radiative heating found in regions with high CRH is due to the absorption of longwave and shortwave radiation by clouds, and not from absorption by water vapor.

Fig. 6.3 shows the difference between the clear-sky and full-sky radiation tendencies for each CRH bin. This figure shows the absorption, emission and scattering of radiation by clouds alone. The contours in Fig. 6.3 can be interpreted as the vertically resolved ACRE. The most obvious feature of these plots is the strong ACRE found in regions with CRH greater than 70%. The longwave ACRE shows strong positive values from the surface through most of the troposphere, with a strong negative ACRE near the tropopause. Deep cloud layers in the humid regions appear to absorb a large amount of longwave radiation, leading to a significant heating that is absent in dry regions. Above this level the negative values indicate increased emission from the tops of clouds to space. The strong cooling from cloud top rather than from near the surface corresponds to the large TOA longwave CRE in humid regions, consistent with the results of Chapter 3. The shortwave plots show a similar structure to the longwave, but of opposite sign. There appears to be a large amount of absorption of solar radiation near the tops of the clouds, preventing absorption that would otherwise have occurred below.

The strong positive net ACRE in moist regions confirms the qualitative difference in the clear-sky and full-sky radiation tendencies. In the extremely humid regions, clouds absorb a large amount of longwave and shortwave radiation, leading to a net heating throughout the troposphere that is larger than the cooling associated with water vapor.

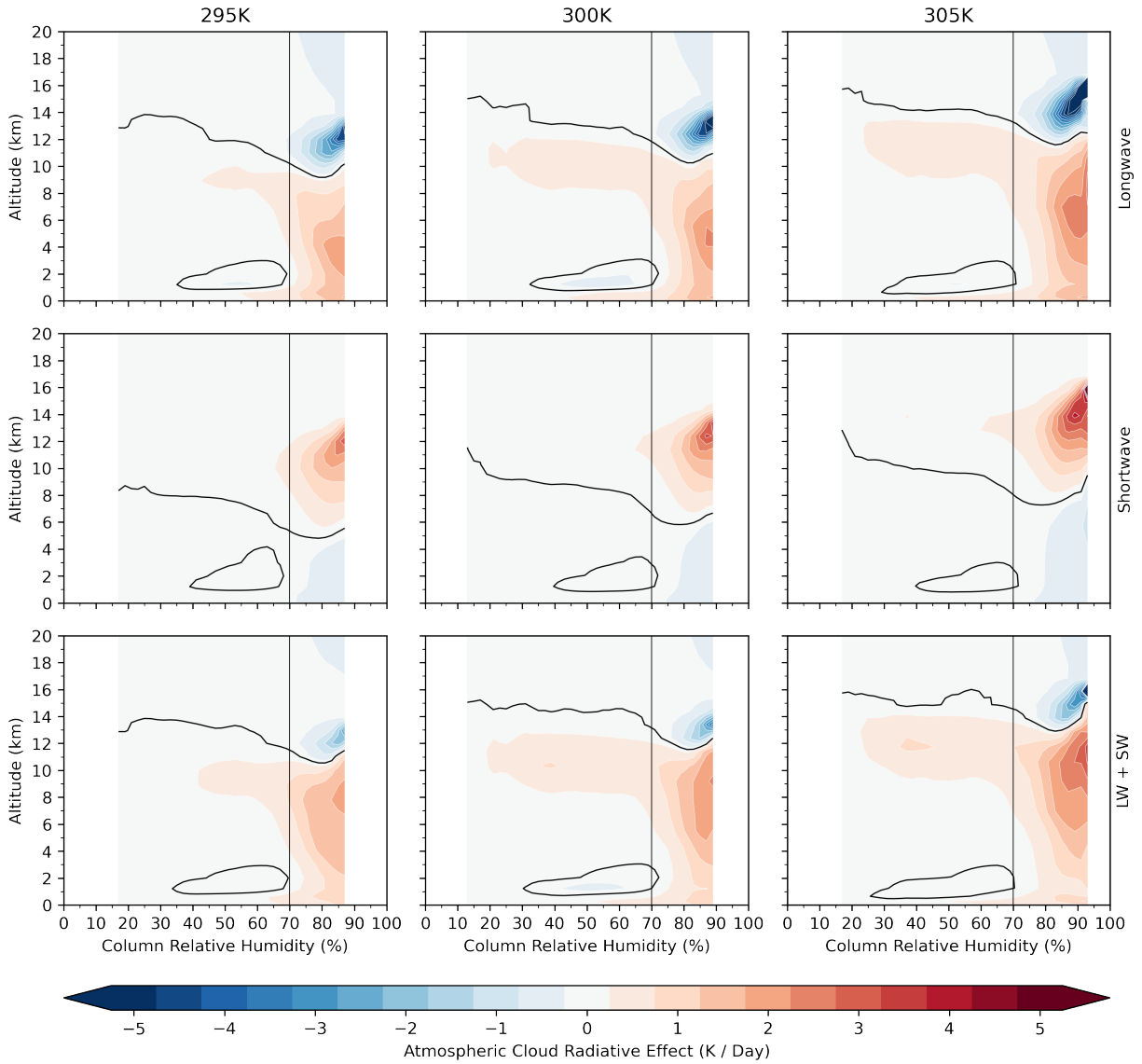


**Figure 6.3:** Same as Fig. 6.1, but for ACRE.

Also seen extending out from the moist regions are “peninsulas” of positive ACRE that become larger and stronger as the surface temperature increases. While binning by CRH does not show any true spatial structure, these features appear similar to the cirrus clouds that typically flow out from deep convective anvils. Like cirrus clouds, these peninsulas cover a much larger area than is covered by the humid regions. There are also small pockets of ACRE with opposite sign in the lowest altitudes of the dry regions. In the same way that the peninsulas resemble cirrus clouds,

these pockets resemble low-level stratus decks with increased longwave cooling near cloud top and increased heating below.

## 6.2 Dependence of static energies on CRH

As discussed in §1.3.1, Riehl and Malkus (1958) (hereafter RM58) investigated the vertical transport of static energies within the ITCZ. This vertical transport was necessary to account for the net export of energy out of the ITCZ by the Hadley circulation. The dry static energy is defined as

$$s \equiv c_p T + gz, \quad (6.1)$$

while the moist static energy is defined as

$$h \equiv s + L_v q \quad (6.2)$$

The static energies are useful quantities because they are conserved under adiabatic processes, and  $h$  is also conserved under the condensation or evaporation of water vapor.

Fig. 6.4 shows vertical profiles of each of the terms in Eq. 6.2, binned by the CRH as the previous figures of this chapter. Also included are the vertical lines at 50% and 70% CRH for direct comparison with the figures from that chapter. For CRH less than 70% the dry static energy is nearly independent of CRH. In the tropics, the small Coriolis parameter leads to small horizontal gradients of temperature (see §1.4). It is therefore not surprising that the combination of potential energy and enthalpy at a given altitude does not depend strongly on the CRH. Above 70% CRH there is some CRH dependence in the dry static energy profiles aloft (e.g. near 14 km for the 305 K simulation), but these are minor. As the surface temperature increases, the contours in the upper-troposphere become closer together, indicating that the soundings have become more stable.

The moist static energy profiles are more interesting. The red lines show the level of the moist static energy minimum, a quantity that was central to the vertical transport of energy in the tropics as discussed by RM58. For the driest regions with CRH less than 50%, the profiles show the

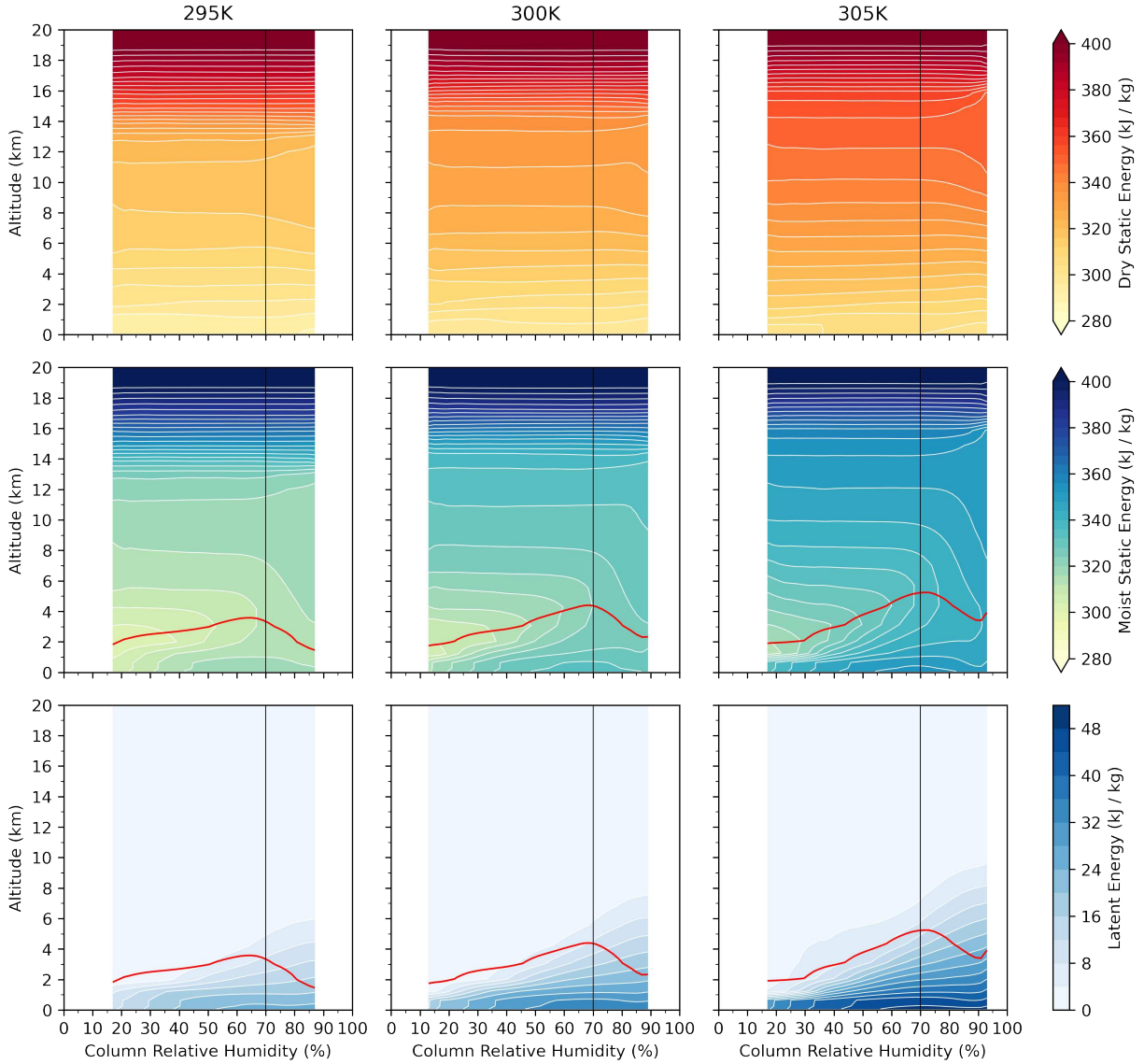


**Figure 6.4:** **Top Row** Dry static energy profiles for each CRH bin. **Middle Row** and **Bottom Row**, same as **Top Row**, but for moist static energy and latent energy. The red contour on the plots in the middle and bottom rows shows the altitude of the mid-tropospheric minimum in moist static energy.

characteristic mid-tropospheric minimum in  $h$  seen in Fig. 1.8. However as the CRH is increased, this minimum becomes less distinct. For the most humid regions, above 70%, the minimum nearly disappears altogether. This behavior can be seen in a similar plot for the frozen moist static energy in Bretherton et al. (2005).

The latent energy, calculated as the difference between moist and dry static energies, shows the clearest dependence on the CRH. This dependence is unsurprising because the CRH is calculated

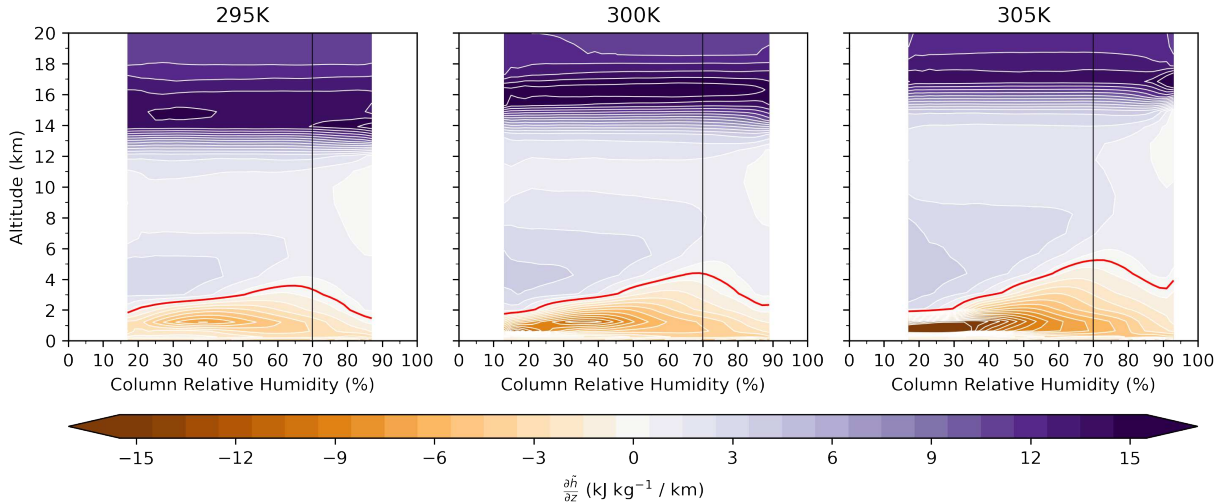


**Figure 6.5:** Vertical gradient of moist static energy for each CRH bin. The red line is the zero contour, and coincides with the level where the minimum in moist static energy occurs.

using the specific humidity, which is proportional to the latent energy. The contours of latent energy are helpful for understanding the reduction in the minimum of moist static energy. As the CRH increases, the altitude of a particular latent energy contour rises steadily. In the most humid regions, the water vapor contours are no longer parallel to the minimum in  $h$ , and there is a large amount of water vapor present above the minimum.

The red contour itself also shows an interesting dependence on CRH. For regions with CRH less than 70%, the minimum in moist static energy steadily moves to higher altitudes as the CRH increases. The moist static energy minimum roughly follows a contour of constant latent energy. However for CRH greater than 70%, the altitude of the minimum begins to decrease with increasing CRH, and the minimum begins to cross contours of constant latent energy.

To further show the dependence of moist static energy on CRH, Fig. 6.5 shows a plot of the vertical gradient of  $h$ , calculated as  $\frac{\partial \tilde{h}}{\partial z}$ . In dry regions, contours show large values of the gradient above and below the minimum, showing that the minimum is very distinct. As the CRH increases, the magnitude of the gradient above and below the red contour decreases. In regions of large CRH, the contours of the moist static energy gradient reach their smallest values above the minimum, showing the weakening of the moist static energy minimum in humid regions.

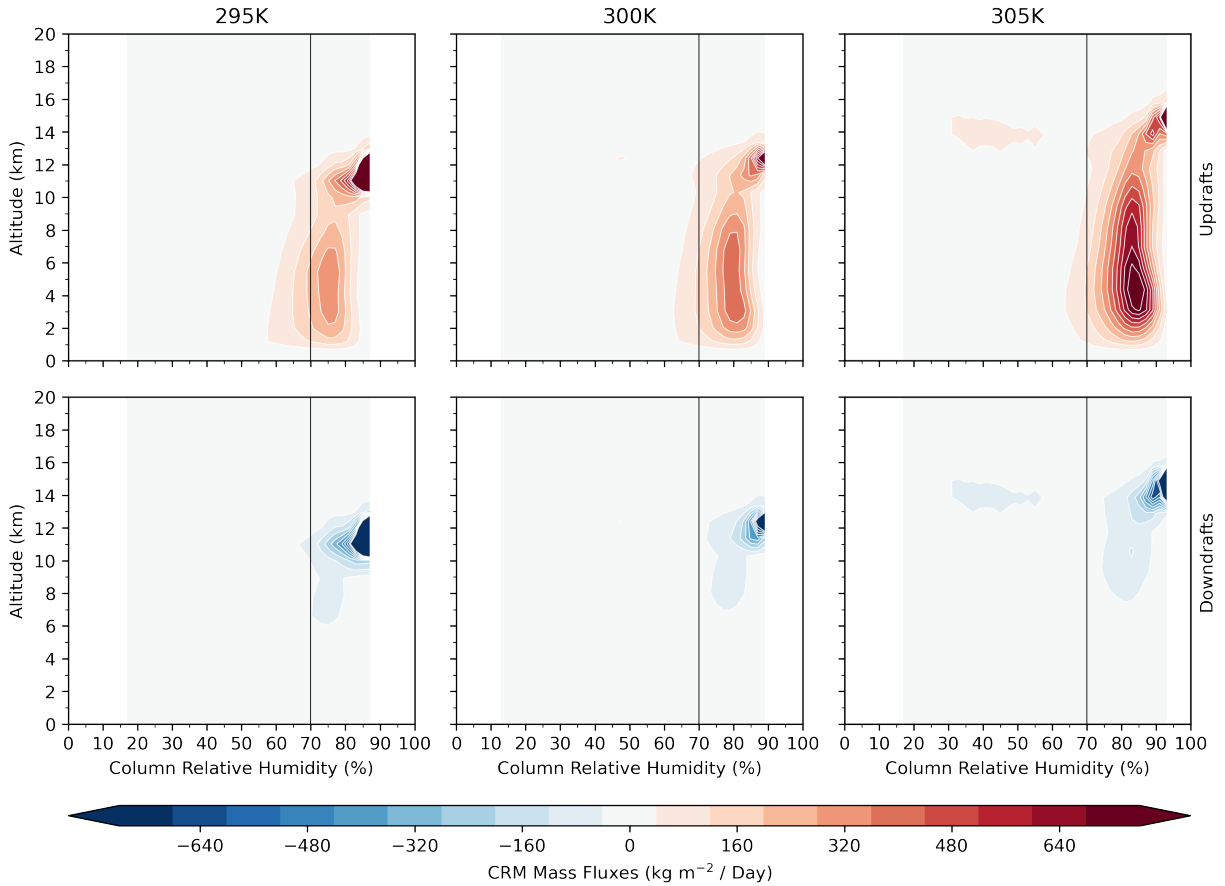


**Figure 6.6:** **Top Row** Updraft mass fluxes computed by the CRM for each CRH bin. **Bottom Row** Same as **Top Row**, but for downdrafts.

What causes the minimum of moist static energy to weaken in regions of high CRH? Or, equivalently, what causes the vertical transport of latent energy into the middle and upper-troposphere? The remainder of this chapter will be dedicated to answering this question. One clue to the answer comes from the original paper of RM58. They noticed that compared to the mean sounding, the minimum in moist static energy was weaker in “areas of ascent connected with synoptic disturbances.” This motivates us to look at differences in vertical motions on large and convective scales.

### 6.3 Vertical motions on large and convective scales

The convective updraft and downdraft mass fluxes calculated by the cloud resolving model are shown in Fig. 6.6 as functions of the CRH, as discussed in §2.1.1. Updraft mass fluxes are calculated as

$$M_u = \rho \sigma_u w_u, \quad (6.3)$$

where  $\rho$  is the air density,  $w_u$  is the mean velocity of the ascending grid cells from the CRM, and  $\sigma_u$  is the area of the ascending grid cells. Only velocities greater than  $2 \text{ ms}^{-1}$  are included in the calculation, to isolate the most intense convection. Downdraft mass fluxes are calculated in a similar way, using the area and velocity in grid cells where the velocity points downward. The  $2 \text{ ms}^{-1}$  threshold corresponds to “intense” convection as described in Jenney et al. (2020), who tested different velocity thresholds for computing the CRM mass fluxes.

The vast majority of convective vertical motion below about 10 km is associated with updrafts rather than downdrafts. The downdrafts mainly serve to balance the updrafts in the upper troposphere, likely to balance convection that overshoots the level of neutral buoyancy aloft. In dry regions, there is very little motion on the sub-grid scale. As the CRH increases, the updrafts begin to increase in strength. The maximum in the updrafts occurs around 5 to 7 km and at about 75% CRH. However the updrafts weaken in the extremely humid parts of the domain.

Net vertical motions from the convective-scale and large-scale flow are shown in Fig. 6.7 as functions of the CRH. Following Arakawa and Schubert (1974), the environmental mass flux is calculated as

$$\widetilde{M} = \overline{M} - M_c, \quad (6.4)$$

where  $\overline{M}$  and  $M_c$  are the mass fluxes at the grid-scale and convective-scale, respectively. In these simulations, the grid-scale mass flux much larger than the convective-scale flux, so that  $\widetilde{M}$  is very

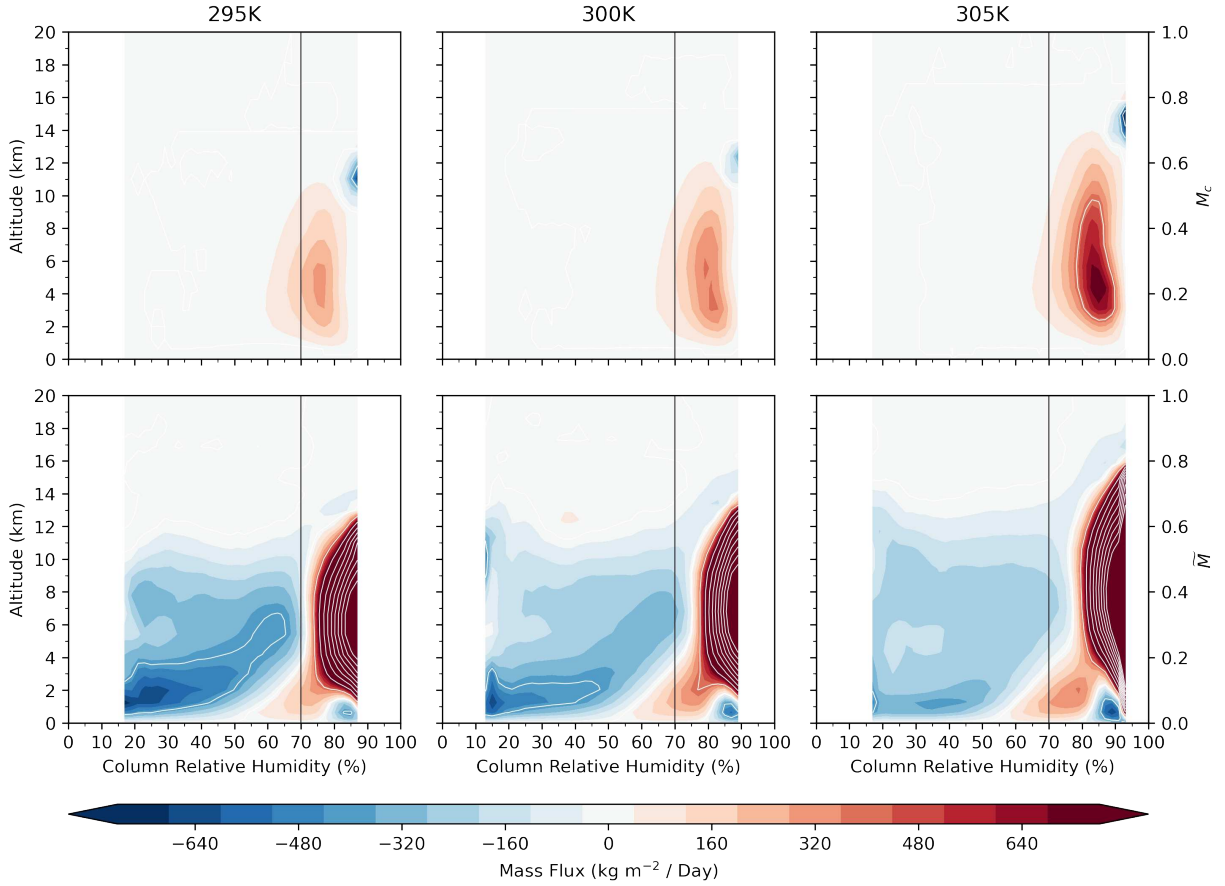


**Figure 6.7:** **Top Row** Net convective mass fluxes computed by the CRM for each CRH bin. **Middle Row** Large-scale vertical velocity for each CRH bin.

similar to  $\overline{M}$ . This is likely due to the  $2 \text{ ms}^{-1}$  vertical velocity threshold used by the CRM to calculate mass fluxes.

In the dry region,  $M_c$  is weak, while the large-scale flow shows sinking motion. In the region between 50% and 70% CRH there is weak large-scale rising motion in the boundary layer underneath a region of subsidence. In humid regions, there is a trade-off between rising motion on convective and large scales. As previously mentioned, the convective-scale updrafts weaken and go to zero for regions of extremely high CRH. The large-scale motion, however, maximizes for these extremely humid regions. This shows a shift from convective-scale updrafts to large scale rising motion  $\overline{M}$  in the most humid parts of the domain, consistent with Jenney et al. (2020). This rising motion on the large scale lifts latent energy from the boundary layer to higher levels in the troposphere.

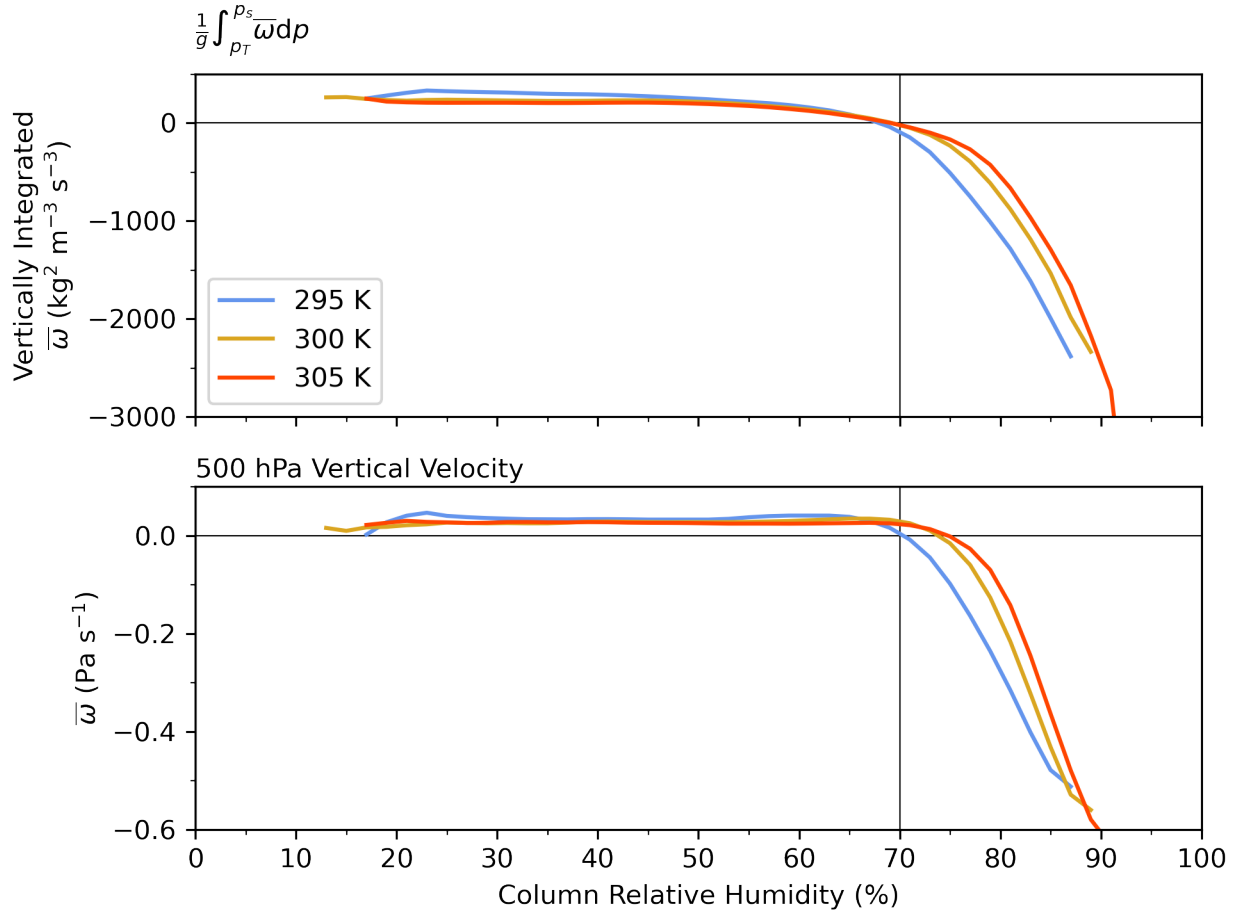


**Figure 6.8:** **Top Panel** vertically integrated  $\bar{\omega}$  and **Bottom Panel**  $\bar{\omega}$  across the 500 hPa surface for each of the three RCEMIP simulations, as a function of CRH.

To show the shift to large-scale rising motion in the humid region, Fig. 6.8 shows two measures of the large scale vertical velocity as a function of the CRH. The first is the vertically integrated  $\bar{\omega}$ , calculated as

$$\text{Vertically Integrated } \bar{\omega} = \frac{1}{g} \int_{p_T}^{p_s} \bar{\omega} dp. \quad (6.5)$$

The second is the vertical velocity across the 500 hPa surface. Both measures show qualitatively similar results, with weak subsiding motion throughout most of the domain, as well as strong rising motion in the extremely humid regions. Interestingly, both quantities shift from subsiding to ascending motion near the 70% CRH threshold, although the 500 hPa  $\omega$  changes sign across a

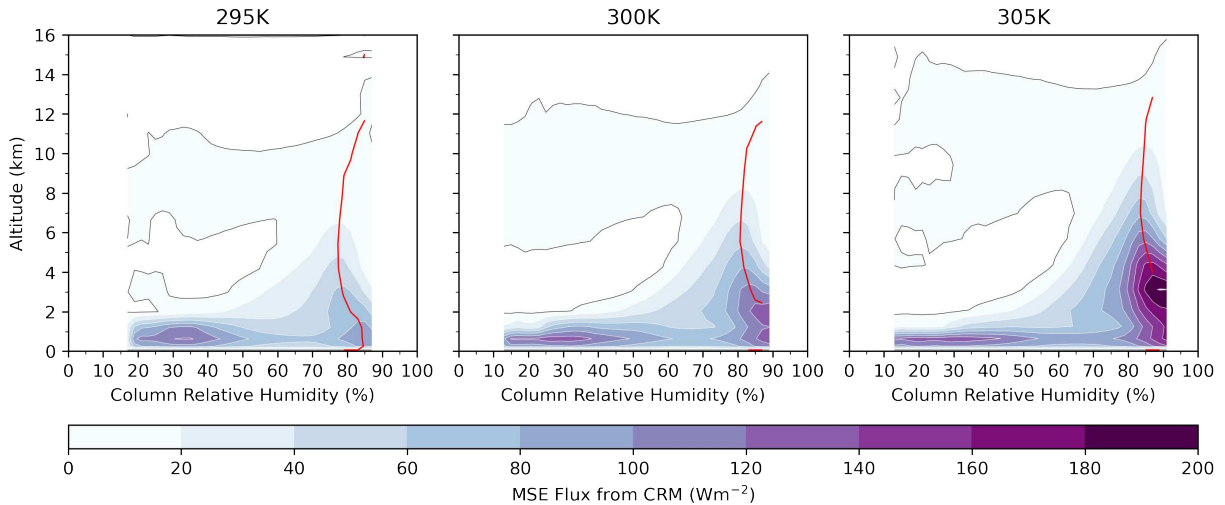


**Figure 6.9:** Transport of moist static energy by the CRM. The nearly vertical red line shows the CRH bin where the largest transport occurs at each altitude.

wider range of CRH values. The consequences of this shift to large scale motion can be seen by looking at the transport of moist static energy by the CRM.

Fig. 6.9 shows contours of the moist static energy flux by the CRM. In contrast to the mass fluxes which are calculated using a threshold of  $2 \text{ ms}^{-1}$ , the flux of  $h$  is calculated using all vertical velocities. The transport of  $h$  is small in the dry region above about 2 km. It is only in the humid region where there is a large transport of  $h$  into the upper troposphere, coinciding with the CRM mass flux contours in Fig. 6.7. Like the mass flux contours, the maximum in moist static energy flux at a given altitude occurs near 80% CRH, and decreases as the CRH increases beyond this level. This is shown in the red lines in Fig. 6.9.

The sharp upward decrease of the MSE flux in Fig. 6.9 implies a convergence of the moist static energy flux in extremely humid regions in the middle troposphere, near 4 to 6 km. The location of the convergence coincides with the minimum in the moist static energy profiles seen in Fig. 6.4. This suggests that the a convergence of moist static energy on convective scales is responsible for weakening the moist static energy minimum in humid regions.

RM58 hypothesized that undilute convective updrafts were necessary to bypass the minimum in moist static energy. The results of this chapter support that conclusion for the vast majority of the domain. However in extremely humid regions, the situation appears more complicated.

There, the convective mass flux goes to zero and there is a convergence of moist static energy in the mid troposphere. This is in contrast to the picture of RM58, where strong convective towers transport mass and moist static energy from lower to upper levels, bypassing the mid troposphere. At the same time, the large-scale mass flux reaches its largest values in the extremely humid region. Instead of convective-scale transport as in Fig. 6.9 which bypasses the minimum in  $h$ , the strong large-scale ascent may be responsible for the vertical transport of energy for humid parts of the domain.

## 6.4 Tropospheric moistening by vertical advection.

But what causes the large-scale rising motion? Rising motion on convective scales is a buoyancy-driven instability in which a parcel that is warmer than its environment feels a force displacing it upward. The parcel then rises until it comes into equilibrium with its surroundings and is no longer positively buoyant. Rising motion on large scales requires a process to heat the broader environment, rather than to heat individual parcels. The heating then drives large scale ascent, in contrast to ascent on the scale of individual updrafts. The rising environment will transport properties of low-level air to higher levels in the troposphere. In particular, large-scale ascent will tend to transport water vapor upwards.

Chikira (2014) derived a form of the specific humidity equation,

$$\left(\frac{\partial q}{\partial t}\right) \simeq (\alpha - 1)(\tilde{C} - \tilde{E}) + \frac{\alpha}{L_v}(Q_r + \tilde{Q}_i + Q_{df}) + D_q + S_{df} + S_{hf}, \quad (6.6)$$

to investigate how the processes that control environmental-scale rising motion contribute to moistening or drying of the atmosphere by transporting moisture. In Eq. 6.6,  $\tilde{C} - \tilde{E}$  is the net rate of condensation minus re-evaporation of precipitation.  $Q_r$ ,  $\tilde{Q}_i$ , and  $Q_{df}$  represent heating due to radiation, liquid-ice transition, and vertical diffusion.  $D_q$  is the moisture tendency from detrainment, and  $S_{df}$  and  $S_{hf}$  are moisture source terms from diffusion and high-frequency waves, respectively. The non-dimensional parameter  $\alpha$ , defined as

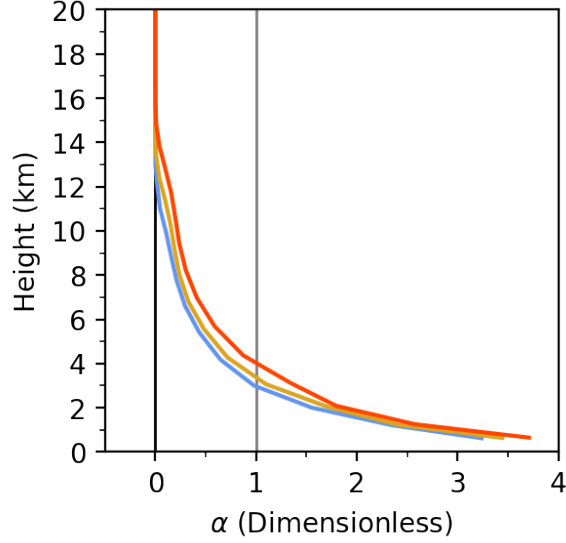


**Figure 6.10:** Domain-average profiles of the Chikira parameter for each of the three RCEMIP simulations.

$$\alpha \equiv -\frac{L_v}{c_p \pi} \left( \frac{\partial \langle q \rangle}{\partial p} \right) \left( \frac{\partial \langle \theta \rangle}{\partial p} \right)^{-1} = -\left( \frac{\partial \langle q \rangle}{\partial z} \right) \left( \frac{\partial \langle s \rangle}{\partial z} \right)^{-1} = 1 - \left( \frac{\partial \langle h \rangle}{\partial z} \right) \left( \frac{\partial \langle s \rangle}{\partial z} \right)^{-1}, \quad (6.7)$$

measures how efficient a particular process is at moistening (drying) the environment by inducing rising (sinking) motion. The vertical gradient of  $s$  is always positive, so the sign of  $\alpha$  is determined by the vertical gradient of  $h$ . Net condensation, on its own, will tend to dry the environment because it converts water vapor to liquid water. However if  $\alpha$  is greater than one, the upward motion associated with the heating from condensation will tend to moisten the atmosphere even considering the water vapor lost to condensation. Other heating rates act more simply. For example, if  $\alpha$  is greater than zero, then radiative heating (cooling) will tend to moisten (dry) the environment by inducing rising (sinking) motion. The vertical distribution of  $\alpha$  can give insight into which processes tend to moisten the environment at different altitudes.

Domain-averaged vertical profiles of  $\alpha$  are shown in fig. 6.10 for each of the RCEMIP experiments. At low altitudes  $\alpha$  is greater than one. Here, rising motion due to heating from condensation, as well as radiation will tend to moisten the environment. Above about 4 km,  $\alpha$  becomes less than one, so condensation can no longer moisten the environment by inducing upward motion,

although heating from sources such as radiation still may be able to moisten. Put another way,  $\alpha$  is greater than zero almost everywhere, so rising motion alone will always tend to moisten the environment, but above 4 km the loss of water vapor to condensation is larger than the gain due to rising motion. As the surface temperature warms, the profiles of  $\alpha$  shift to higher altitudes. This is a consequence of the warmer temperature profile adjusting to a more stable adiabat, as  $T$  is used in the calculation of  $h$  and  $s$ . The change in tropospheric stability in a warmer climate is discussed in Appendix A.

Fig. 6.11 shows contours of  $\alpha$  binned by the CRH, similar to other figures in this chapter. The thick black contour shows the level where  $\alpha$  equals one, while the red contour shows where  $\alpha$  equals zero. The contours of  $\alpha$  are greater than zero in most of the troposphere, indicating that any heating will tend to increase the moist static energy of the environment by inducing rising motion, notwithstanding any sinks due to net condensation. The black contour is identical to the level of the minimum in moist static energy. This is not a coincidence, but results from the role of the vertical gradient of  $h$  in the definition of  $\alpha$  as seen in Eq. 6.7. Another consequence of the connection between  $h$  and  $\alpha$  is that the vertical gradient of  $\alpha$  is small above the level of minimum MSE in regions of high CRH.

As mentioned previously, the black contour at  $\alpha$  equal to one marks an important level. Above this level, moistening due to the heating associated with condensation is no longer effective because the condensation itself is a greater sink for water vapor. In other words, the heating from condensation is able to moisten the environment up to level of the minimum in moist static energy. The contours of the moist static energy gradient in Fig. 6.5 show that the gradient weakens both above and below the minimum. Condensation heating, then, may be relevant to lowering the altitude of the moist static energy minimum, but not in weakening the moist static gradient above the minimum.

As condensation heating cannot account for the moistening of the troposphere above the minimum in moist static energy, radiation is the next obvious heat source to consider. From Eq. 6.6, the moistening of the environment due to radiation can be calculated as

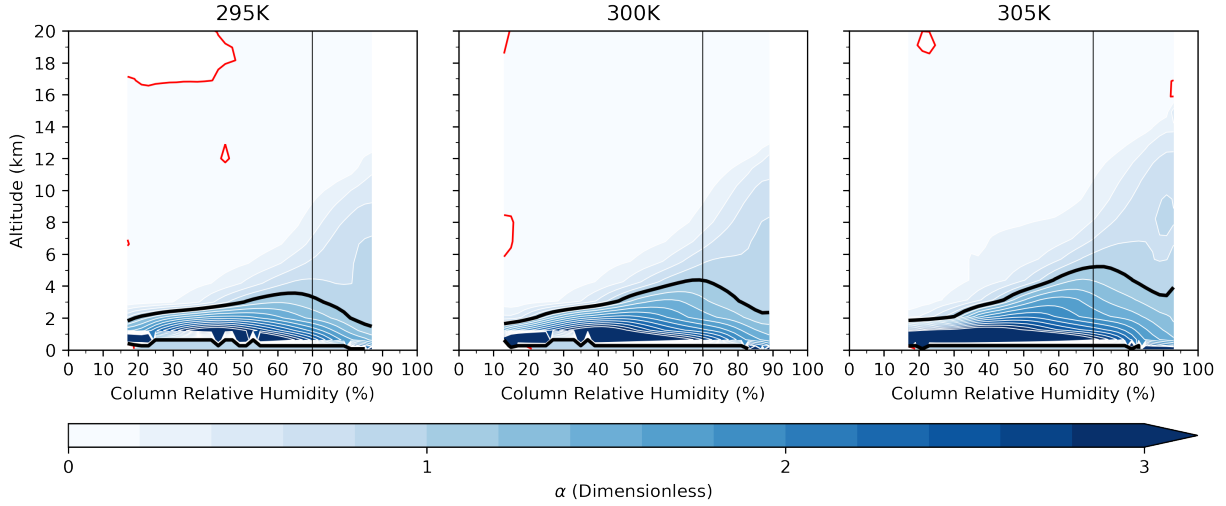


**Figure 6.11:** Contour plots of the Chikira parameter, for each CRH bin. The black and red lines show the contours where  $\alpha$  equals one or zero, respectively.

$$\left(\frac{\partial \tilde{q}}{\partial t}\right)_r = \frac{\alpha}{L_v} (Q_{rl} + Q_{rs}), \quad (6.8)$$

where  $Q_{rl}$  and  $Q_{rs}$  are the longwave and shortwave heating rates. Plots of the moistening due to radiation for the CRH bins are shown in Fig. 6.12. The moistening is separated into contributions from longwave, shortwave, and net radiation, with values shown on a logarithmic scale. As can be inferred from Eq. 6.8, the sign of the moistening is almost always determined by the sign of the radiation, because  $\alpha$  is greater than zero almost everywhere.

As discussed in §6.1, the longwave tendency is negative throughout most of the domain throughout the troposphere. The exception is for regions of high CRH below about 5 km. This is reflected in the top row of Fig. 6.12, which shows that the longwave cooling dries most of the domain by inducing sinking motion. For regions of high CRH, net longwave heating induces rising motion which moistens the domain up to this 5 km level. Shortwave radiation heats the domain at all levels, which tend to moisten the domain. The combination of longwave and shortwave effects is negative throughout most of the domain reflecting that longwave cooling tends to be stronger than shortwave heating in the troposphere. For regions of high CRH, the opposite is found. The net ra-

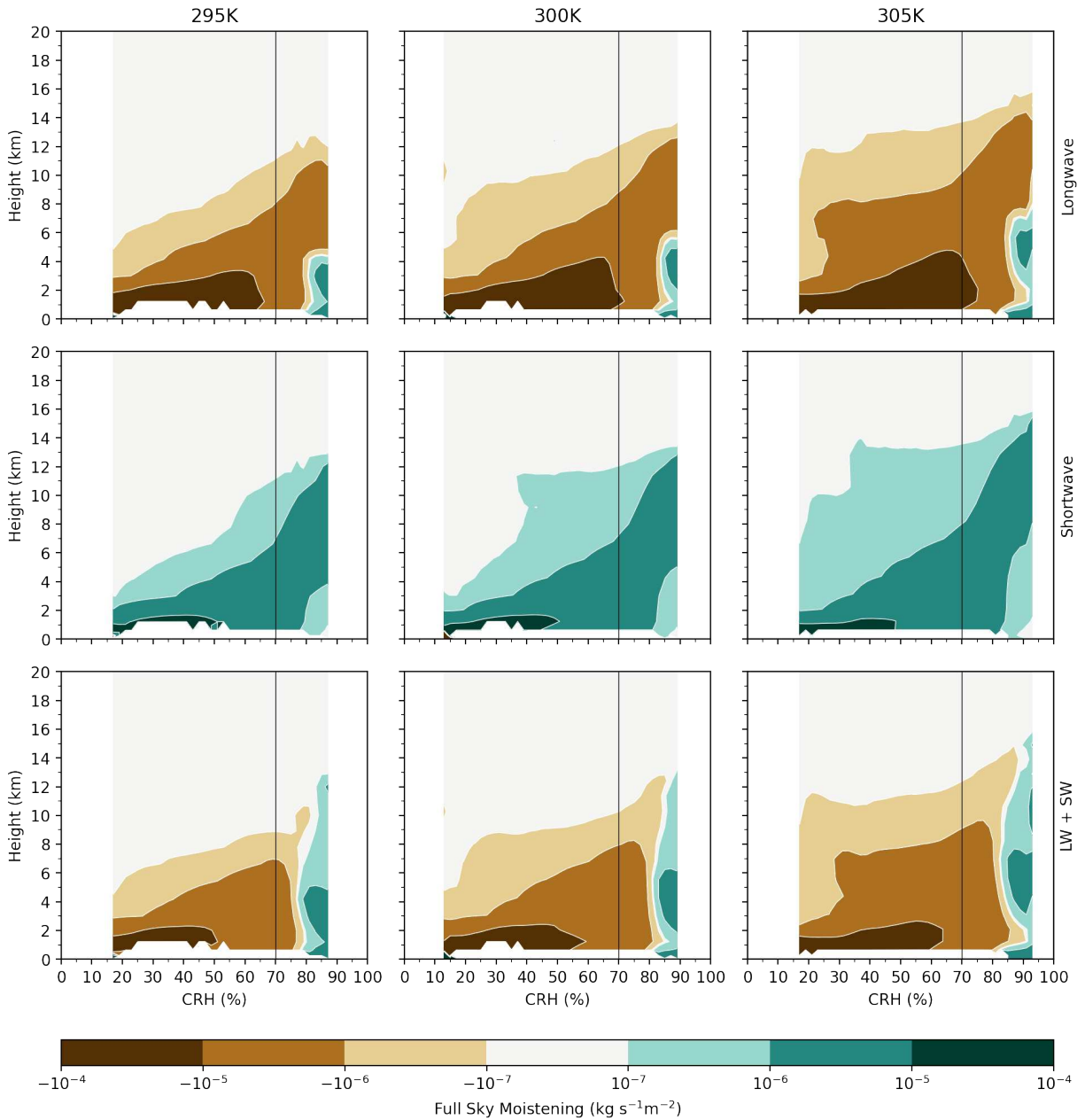


**Figure 6.12:** Environmental moistening due to vertical motions induced by **Top Row** longwave, **Middle Row** shortwave, and **Bottom Row** longwave plus shortwave heating.

diation tendency in these extremely humid regions is positive throughout most of the troposphere, leading to rising motion that moistens the domain.

This radiatively driven rising motion tends to reduce the gradient in moist static energy through the vertical transport of latent energy. The longwave and shortwave effects work together to drive

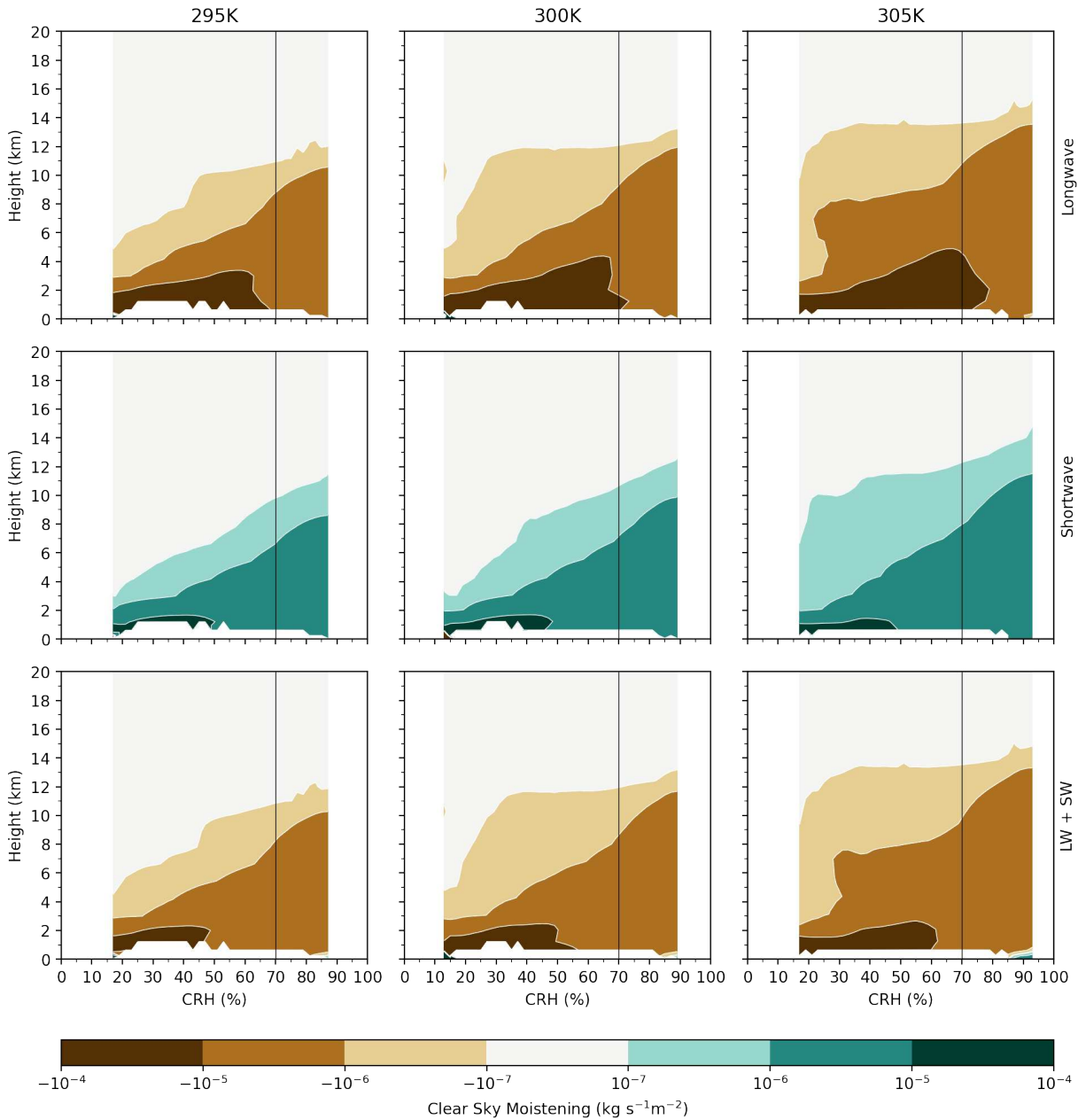


**Figure 6.13:** Same as Fig. 6.12, but for the moistening due to clear-sky radiative heating rates.

the vertical motion up to the altitude where the longwave tendency changes sign. Above this level the shortwave heating wins out and drives rising motion through the depth of the troposphere.

In a similar way to the calculations in §6.1, the full-sky and clear-sky heating rates can be used to investigate whether the moistening comes from absorption by water vapor or from absorption by clouds. Fig. 6.13 shows the moistening calculated from the clear-sky radiation tendencies.

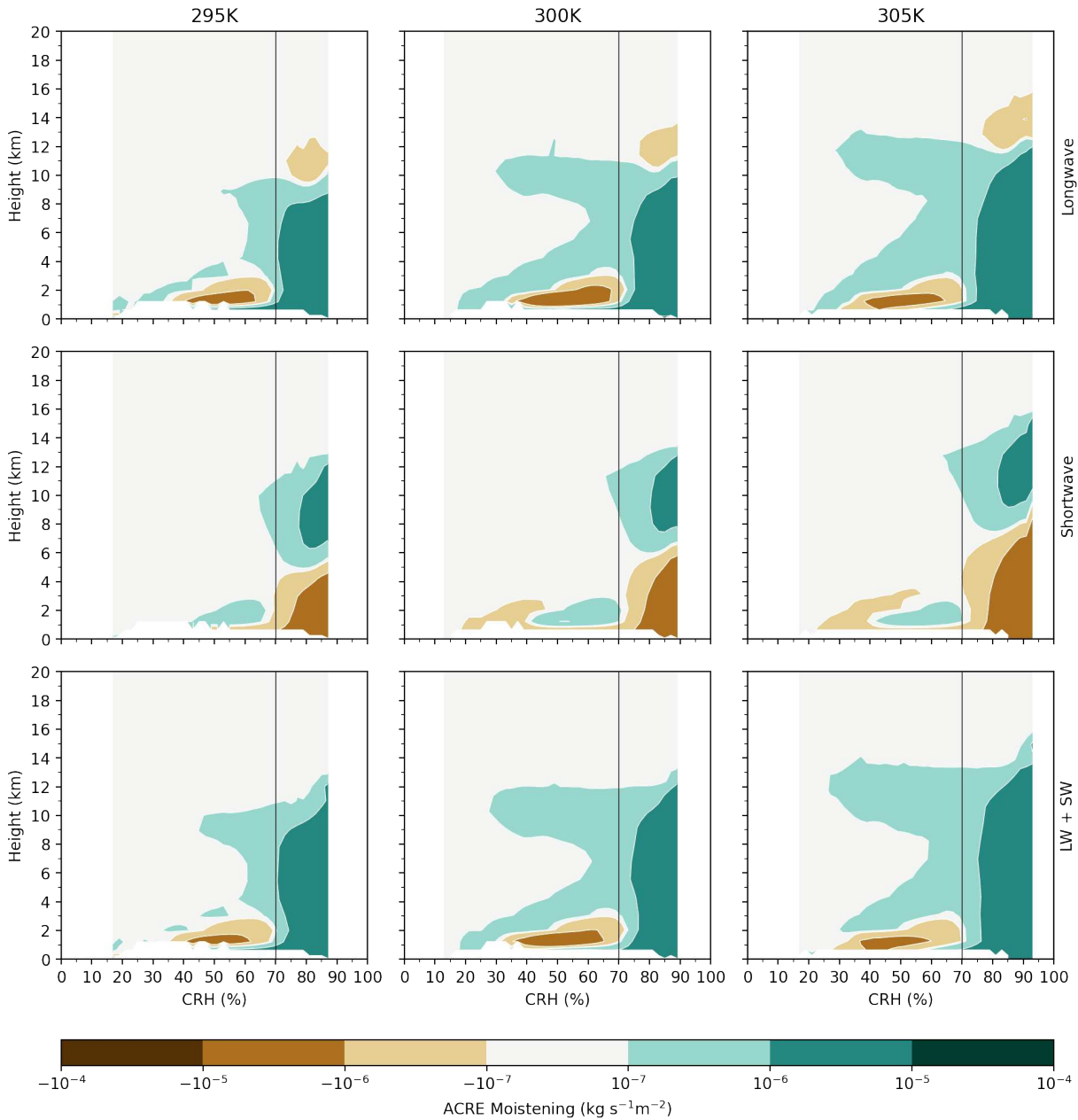


**Figure 6.14:** Same as Fig. 6.12, but for the moistening due to ACRE.

The clear-sky plots are similar to the full-sky plots for regions of the domain with CRH less than 70%. From Fig. 6.2, the clear-sky longwave tendency is negative throughout the entire domain, regardless of the CRH. This cooling results in drying due to the clear-sky longwave tendency in regions of high CRH. The moistening in the most saturated parts of the domain must then be caused by the absorption of radiation by clouds. This is a key result of this thesis, and is illustrated in Fig.

6.14, which shows strong moistening through the depth of the troposphere for CRH larger than 70% due to ACRE.

## 6.5 Conclusions

RM58 hypothesized that a few thousand convective updrafts throughout the tropics are enough to balance the energy budget of the ITCZ. The convective updrafts were required for the energy transport in order to “tunnel through” the observed minimum in the moist static energy. In our idealized simulations of RCE, the minimum in  $h$  becomes weaker in the most humid parts of the domain. Due to the lack of rotation, horizontal temperature gradients are weak in these experiments, so the change in the moist static energy must be caused by the transport of latent energy from the moist boundary layer to the level of the minimum in  $h$ . Contours of the moist static energy flux by the CRM indicated a large flux convergence in the extremely humid regions at the same level where the minimum in  $h$  occurred. This suggests that the mid tropospheric minimum in  $h$  is weakened in the humid regions by convective scale transport of  $h$  from low levels to the mid troposphere.

In addition to a weaker minimum in  $h$  in the humid regions, the vertical gradient of  $h$  also decreases in the humid regions above the minimum, indicating a transport of latent energy from lower levels. The transport could not occur on small scales because the convective scale mass flux is small in the humid region. However, the large-scale mass flux is large in these regions, consistent with a shift from convective to environmental rising motion in humid regions that has been discussed in previous work (Jenney et al., 2020).

Using the moisture tendency equation in terms of the  $\alpha$  parameter of Chikira (2014), we showed that heating due to condensation is unable to account for the weakening of the moist static energy gradient above the minimum. Instead, heating by radiation is the most likely cause. Averaged over the entire domain, the longwave emission from water vapor leads to a net negative radiation tendency. In terms of Eq. 6.6, the radiative cooling would tend to dry the atmosphere, rather than moisten it. However in extremely humid regions, clouds absorb longwave radiation in a deep layer

that extends from the surface up to 10 or 11 km. This heating is enough to overcome the longwave cooling by water vapor, but only up to 5 or 6 km. Above this altitude, the absorption of shortwave radiation by water vapor and clouds is large enough to overcome the longwave cooling so that the net radiation tendency from the surface up to 10 or 12 km is positive. Using the equation for the moisture tendency due to radiation (Eq. 6.8), this net heating would lead to a vertical transport of moisture from near the surface.

This relationship between rising motion and moisture transport is synergistic. The deep cloud layers found in regions of high CRH absorb a large amount of longwave radiation, driving vertical moisture transport in regions that are already quite humid. This moisture transport then causes more cloud condensate to absorb radiation, leading to a radiatively driven moisture feedback. This mechanism also provides an explanation for the shift from convective-scale rising motion as explained by RM58 to environmental motion in regions of extremely high CRH, as discussed in Jenney et al. (2020).

In addition, longwave and moisture feedbacks have been identified as important mechanisms with relevance to the onset and continuation of convective self-aggregation (Wing and Emanuel, 2014; Wing et al., 2017). While self-aggregation is not a main focus of this thesis, it would be interesting to see how this radiatively driven moisture feedback, which works to shift motion from convective to large scales, would impact the self-aggregation of convection.

A few caveats should be mentioned at this point. The first is that this region of moistening by large-scale ascent is only found in regions of CRH greater than about 80%. The PDFs of CRH from Fig. 3.2 show that this only a small fraction of the domain, so transport on the convective scale following RM58 is still the primary method for the vertical transport of energy Tbl. 6.1 shows

**Table 6.1:** Fraction of the domain, given as a percentage, with CRH below a given level. This is the area under the curves in Fig. 3.2 from 0% CRH to 70% or 80%.

	CRH $\leq$ 70%	CRH $\leq$ 80%
<b>295 K</b>	78.98%	97.35%
<b>300 K</b>	71.92%	94.82%
<b>305 K</b>	74.94%	94.78%

that this is between 2.5% to 5% of the domain, depending on the simulation. Secondly, the data analyzed come from simulations performed without a diurnal cycle and with uniform isolation at all latitudes, following the RCEMIP protocol of Wing et al. (2018). This may have led to shortwave tendencies that were larger than would be otherwise expected in the tropical atmosphere. Part of Chapter 7 repeats this analysis using a more realistic set of simulations, to show that the results are not overly sensitive to the model configuration.

# Chapter 7

## Riehl and Malkus, Revisited

The RECMIP simulations used in previous chapters are highly idealized representations of the tropical atmosphere. While they are a helpful starting point, it is important to recognize their limitations. As discussed in §2.1.1, the RCEMIP simulations utilize a non-rotating aquaplanet with uniform SSTs. The lack of rotation prevents the development of a large-scale circulation and leads to much weaker horizontal winds than are observed in the real atmosphere. Because of these uniform conditions, water vapor is more or less evenly distributed in space in a time average sense. This is in contrast to the real atmosphere where certain regions are typically wet, while other regions are typically dry, as discussed in Chapter 5. In addition, the simulations use uniform insolation and neglect the diurnal cycle, leading to artificially enhanced shortwave heating.

In order to test whether the results from previous chapters are robust to different experimental setups, several key calculations from Chapters 3, 5 and 6 are repeated in this chapter using a more realistic set of simulations. The experimental setup used in this chapter represents a rotating aquaplanet under perpetual January conditions, and is designated AQPJAN. The simulations utilize the same super-parameterized version of the community atmosphere model as the RCEMIP experiments. A diurnal cycle is included, and insolation is set at a fixed angle corresponding to January 15. The model is forced by prescribed SSTs drawn from ERA5 2-meter temperatures for the month of January. Additional SST distributions are found by uniformly increasing or decreasing the smoothed distribution by 5 K. a graphical representation of the three SST distributions is shown in Fig. 7.1.

Unless otherwise specified, analysis in this chapter uses 200 days of daily mean model output covering the region from 10°S to 10°N. As discussed in Appendix C, very similar results are found using 30°S to 30°N as latitude limits, although there are some key differences which are noted as they arise. A full description of these experiments is given in §2.1.2.

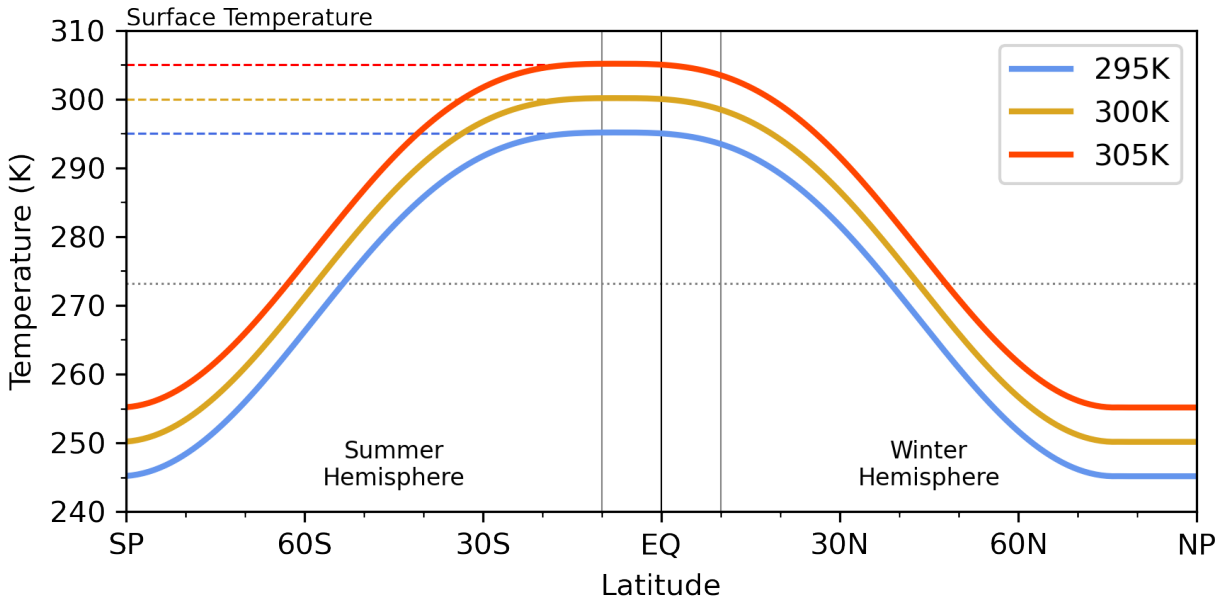


**Figure 7.1:** Reprint of bottom panel of Fig. 2.2. Meridional distribution of surface temperature for the three AQPJAN experiments.

## 7.1 Climatology of AQPJAN Experiments

Before repeating the CRH analysis of earlier chapters, the first section of this chapter is devoted to evaluating the AQPJAN simulations to make sure that they represent a reasonable approximation to the earth system. The AQPJAN simulations utilize a zonal-mean SST distribution, and any other zonal asymmetries that would result from including a land surface are absent. Then, the simulations are assessed in terms of the zonal-mean characteristics.

Plots of the zonal mean zonal wind are shown in Fig. 7.2. The winds show subtropical jets in both hemispheres near 200hPa, with a stronger jet in the winter hemisphere. There is also a strong polar night jet in the northern hemisphere, surface westerlies in the mid-latitudes and surface easterlies at the equator. These characteristics are all consistent with the observed terrestrial winds during the month of January. Each of the simulations also shows weak stratospheric westerlies over the summer poles where there are easterlies in the real atmosphere. While this is a notable deviation from the winds of the real atmosphere, it is likely of little practical importance for the following analysis of the tropical troposphere.

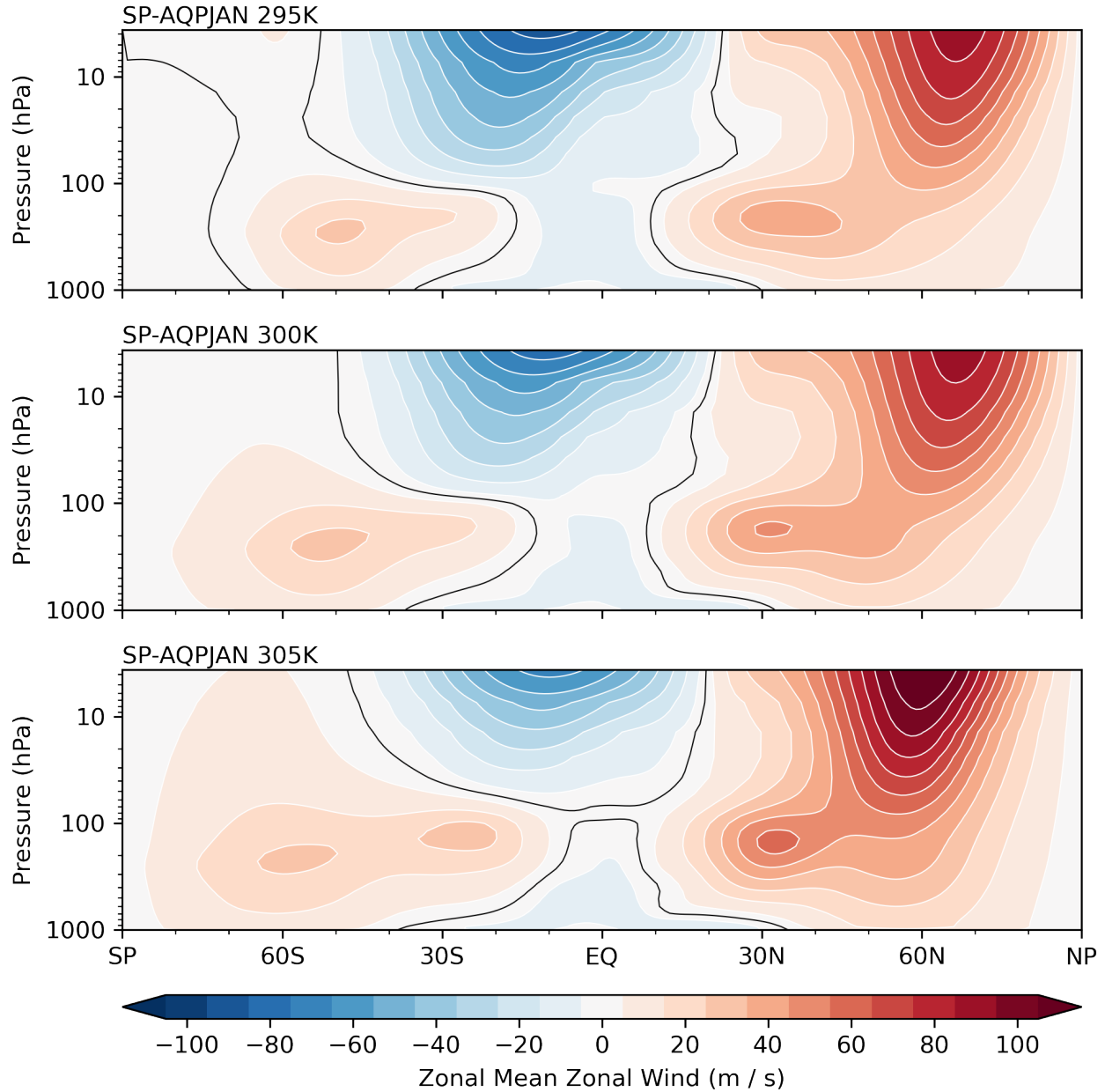


**Figure 7.2:** Zonal mean zonal winds for each of the three AQPJAN simulations with white contours are spaced every  $10 \text{ ms}^{-1}$  starting at  $5 \text{ ms}^{-1}$ . The black lines show the zero contour.

The plots of the zonal winds in Fig. 7.2 show that the tropical troposphere of the AQPJAN simulations is found within a dynamical environment that resembles the real Earth. As this thesis is concerned with transports of moisture and energy between dry and humid regions, the mean meridional circulation is assessed next. The zonal-mean meridional and vertical winds can be used to define a streamfunction,  $\psi$ , according to

$$\bar{v}^\lambda 2\pi a \cos \varphi \equiv g \frac{\partial \psi}{\partial p}, \quad (7.1)$$

and

$$\bar{\omega}^\lambda 2\pi a^2 \cos \varphi \equiv -g \frac{\partial \psi}{\partial \varphi}. \quad (7.2)$$

Contours of the streamfunction show the direction of the large-scale flow in the latitude-pressure plane. The streamfunction was then found by vertically integrating Eq. 7.1 as

$$\bar{\psi}^\lambda = \frac{2\pi a \cos \varphi}{g} \int_p^{p_0} \bar{v}^\lambda dp', \quad (7.3)$$

with the top of atmosphere boundary condition that  $\psi = 0$  at  $p = p_0$ . Plots of the streamfunction for each of the three AQPJAN simulations are shown in the left column of Fig. 7.3. Inspection of the streamfunction plots shows a strong Hadley cell in the northern hemisphere accompanied by a somewhat weaker cell in the southern hemisphere, consistent with terrestrial conditions for the month of January. Much like the real atmosphere, the two cells drive equatorial flow at the surface, and poleward flow aloft.

The effects of these circulations can be seen in the right column of Fig. 7.3, which shows the zonal mean precipitation, evaporation, and the difference between the two. The subsiding branches of the Hadley cells suppress precipitation and are associated with increased evaporation, so that the zonal-mean  $P - E$  is negative in the subtropics. The low-level flow transports the recently-evaporated water towards the equator, leading to a convergence of moisture. This can be seen in Fig. 7.3 where the zonal-mean  $P - E$  shows a sharp, positive spike just north of the equator. Each experiment demonstrates a single ITCZ, marked by a peak in precipitation that is co-located with the maximum in moisture convergence. The zonal-mean precipitation rate here is on the order of  $10 \text{ mm day}^{-1}$ .

As the surface temperature increases, the subtropical maxima in evaporation increase in magnitude, leading to an increase in the divergence of moisture from these latitudes. As this moisture is transported towards the equator by the mean flow, the equatorial maxima in moisture conver-

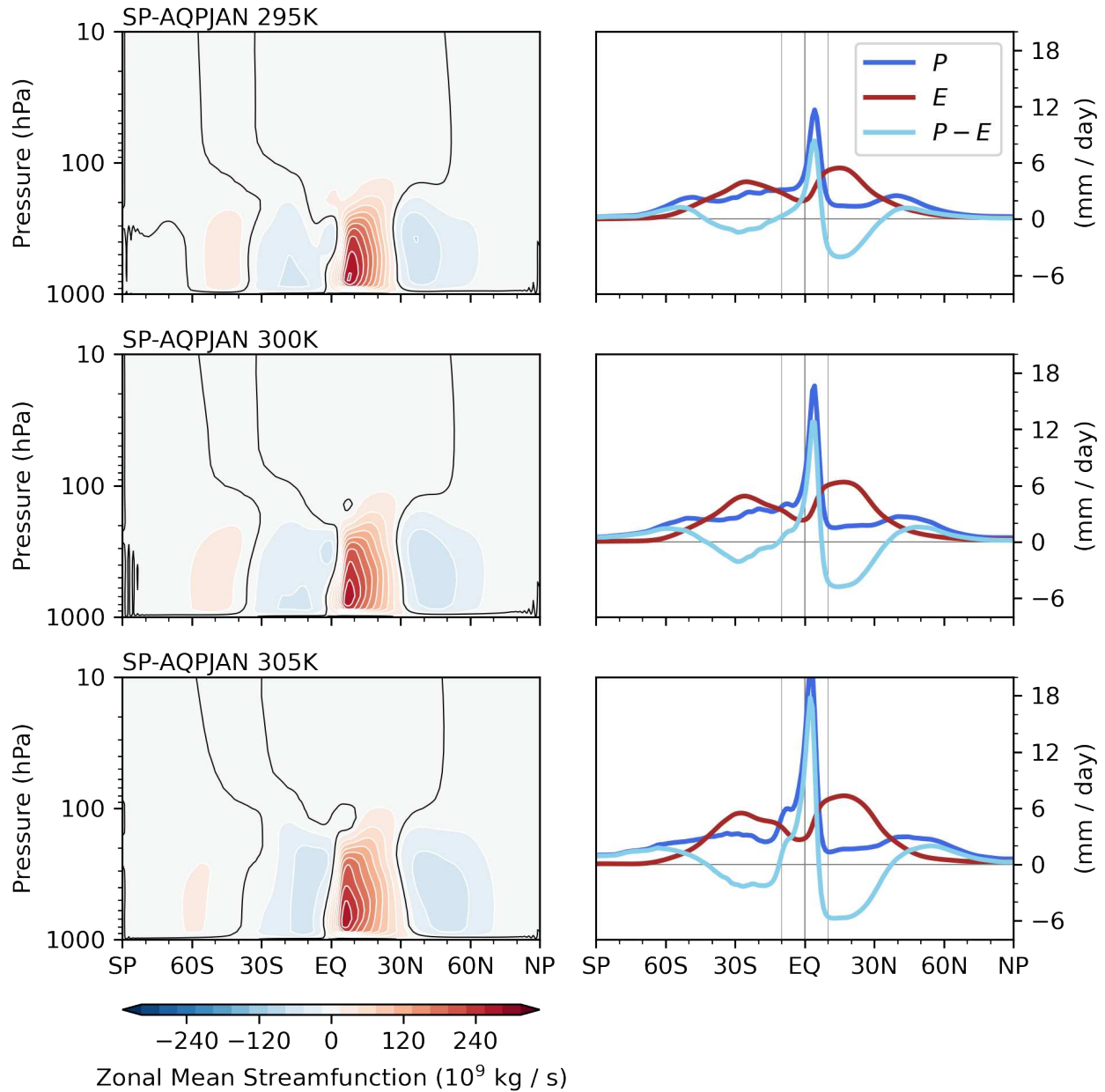


**Figure 7.3: Left Column:** Zonal mean meridional streamfunction for each AQPJAN experiment. Contours are drawn every  $3 \times 10^8 \text{ kg s}^{-1}$ . Red (blue) shading indicates clockwise (counter-clockwise) circulation. The black contours show where the streamfunction passes through zero. **Right Column:** Zonal mean precipitation (blue), evaporation (brown), and  $P - E$  (light blue) for each of the AQPJAN simulations. Light gray vertical lines at 10S and 10N show the latitude limits used for analysis later in this chapter.

gence and precipitation also increase in magnitude. This is consistent with studies of the ITCZ under climate change (e.g., Su et al. (2017)) which predict an increase in tropical precipitation in a warmer climate.

To quantify the magnitude of the transport of moisture by the mean flow, as well as the transport of energy, the integrated northward transports across an arbitrary latitude  $\varphi$  were calculated using

$$\overline{\Theta^{\lambda,t}}(\varphi) = 2\pi a^2 \int_{-\pi/2}^{\varphi} \overline{N^{\lambda,t}} \cos \varphi' d\varphi'. \quad (7.4)$$

Here  $a$  is the radius of the earth, and  $N^{\lambda,t}$  represents the zonal-mean, time-mean net flux of energy or moisture into the column from the surface or TOA. In the case of moisture,  $N^{\lambda,t}$  was calculated using the difference in precipitation and evaporation rates. In the case of energy,  $N^{\lambda,t}$  was calculated using the net flux of longwave and shortwave radiation into the column from the surface and TOA, as well as the net fluxes of latent and sensible heat into the atmosphere from the surface. In calculating the transports using Eq. 7.4, a slight correction was made by subtracting the global-mean, time-mean value of  $N$  from  $N^{\lambda,t}$ . This is a result of our physical theories, which assume that globally, over over long time periods, the Earth is in energy balance with the rest of the universe, and that the difference between precipitation and evaporation is zero. In model output this is nearly, but not exactly, true. By subtracting the long-term mean we ensure it. Then, the transports go to zero at the North Pole in addition to the South pole. For these calculations, the correction was on the order of  $1 \text{ Wm}^{-2}$  for the energy transport, and on the order of  $0.01 \text{ mm day}^{-1}$  for the moisture transport.

Fig. 7.4 shows the integrated northward transports of energy and moisture as a function of latitude. Beginning with energy, the transport is southward in most of the southern hemisphere, and northward in most of the northern hemisphere. Then, the tropics as a whole are exporting energy to higher latitudes in the AQPJAN simulations. This is consistent with the real atmosphere, as satellite observations of the Earth's radiation budget show a net flux of radiation into the tropics from the TOA, and a net flux of energy out of higher latitudes, requiring a poleward transport of energy within the atmosphere (Trenberth and Caron, 2001; Vonder Haar and Oort, 1973). In Fig. 7.4 transport in the northern hemisphere is larger than in the southern hemisphere, as the meridional temperature gradient is larger between the tropics and the winter pole. The maximum in northern hemisphere energy transport occurs just above near  $30^\circ\text{N}$ , a latitude where the streamfunction

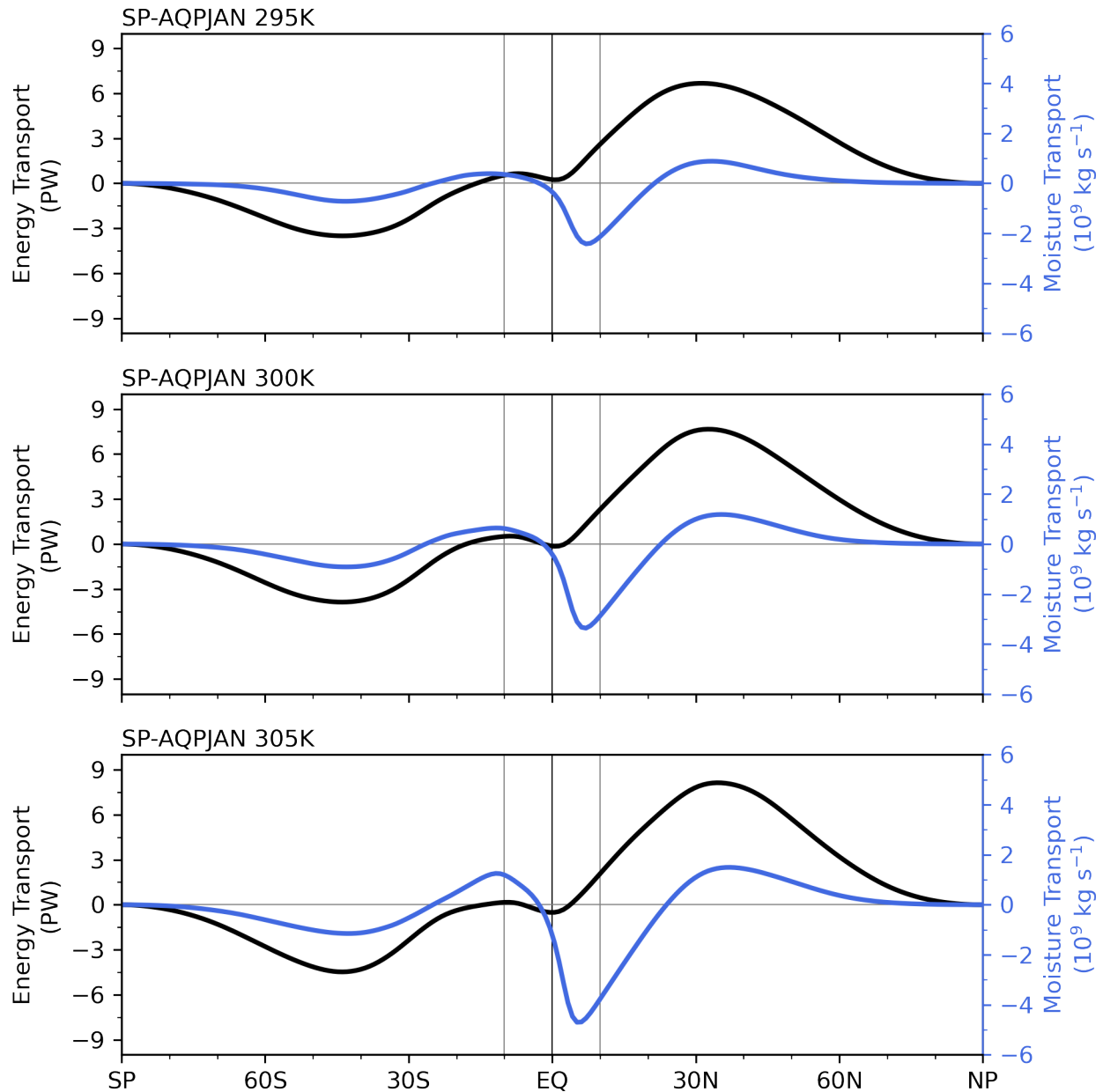


**Figure 7.4:** Integrated northward transports of energy (black) and moisture (blue) for the three AQPJAN simulations.

plots in Fig. 7.3 go to zero. Then, most of the energy transport for latitudes greater than  $30^\circ$  is accomplished not by the mean flow, but by eddies. In the tropics the transport is nearly zero, indicating that there is very little energy transport across the equator.

The moisture transport in Fig. 7.4 is similar to the energy transport. In the mid latitudes the moisture transport is poleward in both hemispheres, and coincides with the poleward transport of

energy. This is the result of the mid-latitude storm tracks, where extra-tropical cyclones transport energy and moisture from the mid-latitudes toward the poles. However, the energy and moisture transports are in the opposite direction in the region from 10°S to 30°N. In the tropics the transport of energy is poleward, while the transport of moisture is equatorward. This can be explained by the study of Riehl and Malkus (1958), who found that the ITCZ was a location of low-level moisture convergence, and upper-level energy divergence. These plots again show that the AQPJAN simulations do a reasonable job of providing an idealized version of the real atmosphere, without including any of the zonal asymmetries.

## 7.2 CRH Analysis of AQPJAN Experiments

Next, the subset of the domain ranging from 10°S to 10°N was used to calculate fields of CRH for the AQPJAN experiments following the method discussed in Chapter 3. Probability distributions of the CRH are shown in Fig. 7.5, along with the PDF from the corresponding RCEMIP simulation. For each AQPJAN simulation, the peak in the distribution occurs at a higher CRH than for the RCEMIP experiment. This is the result of the boundary conditions of the RCEMIP simulations which are homogeneous and isotropic along the surface. The AQPJAN simulations, however, include regions where there is a time-mean convergence of moisture, leading to higher values of the CRH.

**Table 7.1:** Extension of summary statistics from Tbl. 3.1 for the distributions of CRH shown in Fig. 7.5. Statistics reflect each of the three AQPJAN experiments compared to each of the three RCEMIP experiments, as well as the ERA5 distribution. The Mode is given as the center of the CRH bin with the largest probability density (the peak of the distributions shown in Fig. 7.5)

	Mean	Standard Deviation	Skewness	Mode
<b>295 K AQPJAN</b>	70.58%	8.64	-0.63	74.25%
<b>295 K RCEMIP</b>	60.75%	11.95	-0.49	64.75%
<b>300 K AQPJAN</b>	71.92%	9.08	-0.63	75.25%
<b>300 K RCEMIP</b>	59.91%	15.08	-0.45	69.25%
<b>305 K AQPJAN</b>	73.36%	10.04	-0.71	77.75%
<b>305 K RCEMIP</b>	59.38%	15.13	-0.26	71.25%
<b>ERA5</b>	65.03%	14.96	-0.56	76.75%

The bottom-right panel shows the CRH distributions for the AQPJAN simulations, as well as the distribution of the CRH calculated from ERA5 reanalyses from 10°S to 10°N. As the surface warms the peak in the distribution shifts to higher CRH, perhaps as a result of the increased tropical moisture convergence shown earlier in Fig. 7.3. The peak in the ERA5 distribution is smaller, but is located at a similar CRH as the 300K AQPJAN simulation. The ERA5 distribution shows many more locations with CRH less than 60% than the AQPJAN simulations. This may be a result of the inclusion of CRH values over land, which are generally less humid than over ocean.

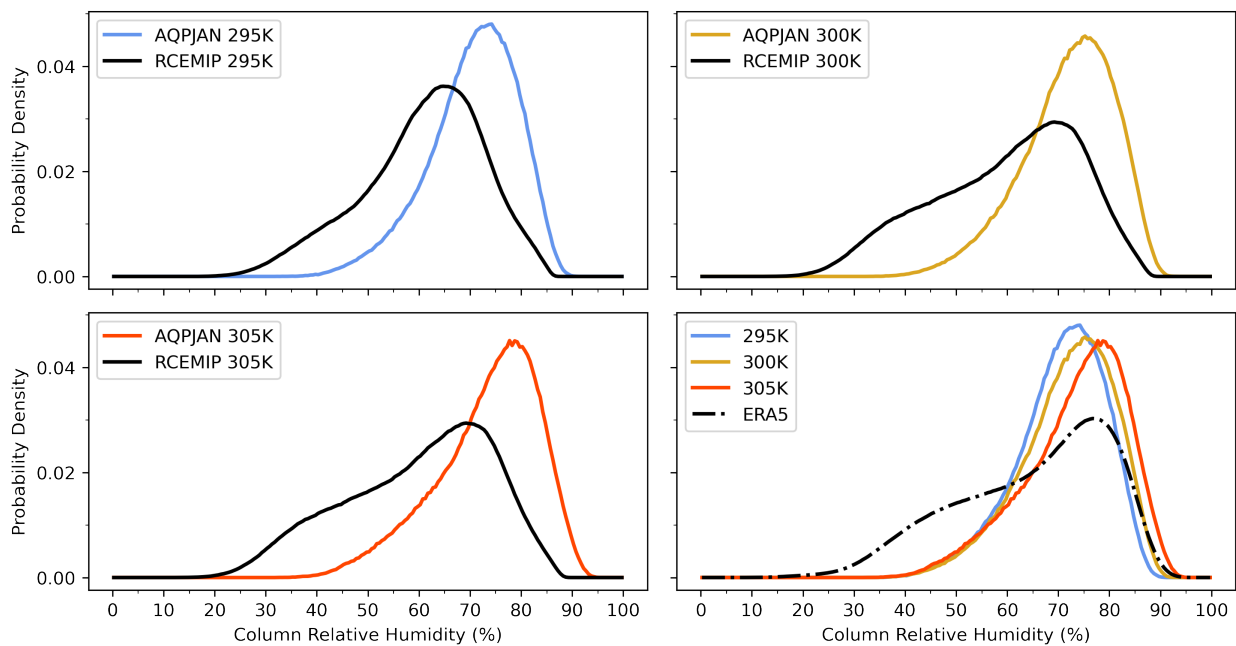


**Figure 7.5:** Probability density functions of CRH for the RCEMIP (black) and AQPJAN (Blue, Yellow, or Red) simulations ranging from 10°S to 10°N. **Bottom right** The three AQPJAN distributions compared to the ERA5 CRH distribution for 10°S to 10°N.

### 7.2.1 Cloud Radiative Effect vs. Column Relative Humidity

Following the method of §3.2, the longwave, shortwave, and net CRE at the TOA and surface were found for the AQPJAN experiments between 10°S and 10°N. These curves were then used to calculate the ACRE as a function of CRH. The CRE was binned by the CRH, and is shown in Fig. 7.6. Like the CRE in the RCEMIP simulations (Fig. 3.3), and the CRE calculated from satellite

observations (Fig. 3.7), the CRE as a function of CRH is largely independent of the SST in the AQPJAN simulations. The CRE curves in Fig. 7.6 again show a small CRE in the dry region with CRH lower than 70%, and large CRE in humid regions.

A key difference between the AQPJAN curves and the curves for the RCEMIP simulations and CERES observations is found in the dry region. In the RCEMIP and CERES data, the curves for the longwave and shortwave CRE go to zero as the CRH becomes small. In the AQPJAN simulations the mean longwave and shortwave CRE at the TOA is nonzero in the dry region, although the net CRE does go to zero in the dry region. When the calculation is repeated for the AQPJAN simulations after expanding the latitude limits from 10°S to 10°N to 30°S to 30°N, the longwave and shortwave CRE at TOA go to zero for small CRH, consistent with the RCEMIP and CERES data. This and other differences between the AQPJAN simulations when the latitude limits are expanded are discussed further in Appendix C.

## 7.2.2 Energy and Moisture Balances

The energy and moisture balances as a function of CRH were then found for the AQPJAN simulations. This was done using the same method as was used for the RCEMIP simulations in Chapter 5. Fig. 7.7 shows the precipitation rate, evaporation rate, and the difference between the two as a function of CRH for both the RCEMIP and AQPJAN simulations. The precipitation rate is again a nearly universal function of the CRH, consistent with findings from previous studies (Bretherton et al. (2004), figure shown in Fig. 5.2) and with the RCEMIP simulations (Fig. 5.3).

The largest difference between the RCEMIP and AQPJAN simulations can be seen in the evaporation rates. The AQPJAN simulations show a much stronger difference in evaporation between the dry and humid regions. This may be the result of both dynamical and hydrological factors. As discussed in previous chapters, the lack of rotation or any meridional gradients in temperature prevent the formation of any sort of large-scale circulation in the RCEMIP simulation like the circulations found in Figs. 7.2 and 7.3. The circulations lead to strong surface winds, as well as to subtropical regions with strong gradients in moisture between the ocean surface and the atmosphere. As the evaporation rate is calculated using a bulk aerodynamic formula that is proportional

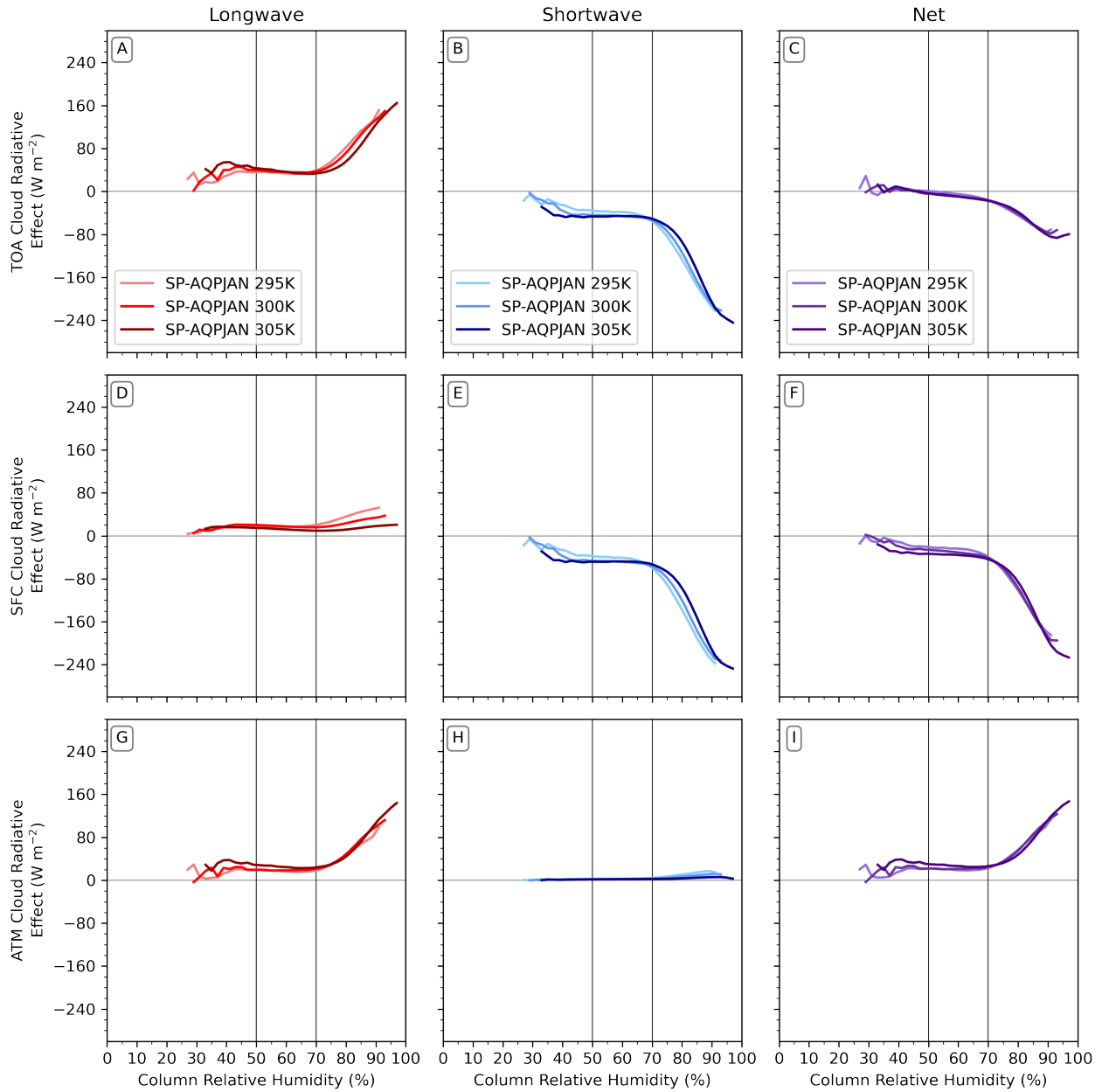


**Figure 7.6: Top Row CRE at TOA, Middle Row CRE at Surface, and Bottom Row ACRE binned by CRH for each of the three AQPJAN simulations. Compare with Figs. 3.3, 3.7**

to both the magnitude of the surface winds and the near-surface vertical moisture gradient, the dynamical and hydrological forcings likely contribute to the increased evaporation seen in regions of low CRH in the AQPJAN simulations. When the full subtropics are included by expanding the latitude limits, the evaporation rate in the dry regions increases further (Fig. C.3).

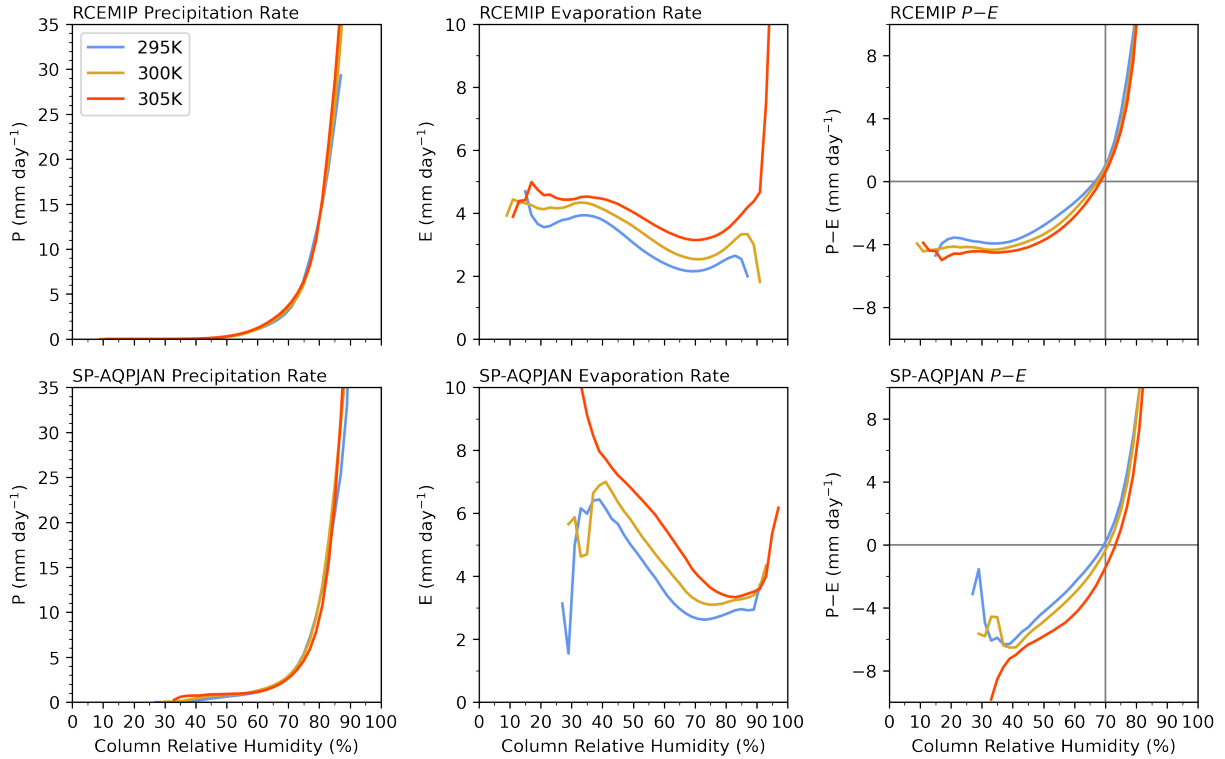


**Figure 7.7: Top Row** Precipitation rate, evaporation rate, and  $P - E$  as a function of CRH for the RCEMIP simulations, as presented previously in Chapter 5. **Bottom Row** Same as **Top Row**, but for the AQPJAN simulations.

The right-hand column of Fig. 7.7 shows the difference in precipitation and evaporation for the RCEMIP and AQPJAN simulations. Unlike the RCEMIP simulations, there is a slight increase in the CRH value where the curves pass through zero for the AQPJAN simulations, although this value is still very close to 70%. This supports our previous conclusion that the humid region, marked by a CRH threshold of approximately 70% serves as a location of moisture convergence, while the dry region serves as a source of moisture by facilitating the evaporation of ocean water into the atmosphere.

In addition to the moisture budget, Fig. 7.8 shows the energy budget of the AQPJAN simulations binned by the CRH, and compared to that of the RCEMIP simulations. There is a key difference in the budget as calculated for the AQPJAN and RCEMIP experiments. The RCEMIP budget is calculated over the entire planet, and represents a closed system where the only sources or sinks of energy occur at the lower or upper boundaries. The AQPJAN simulations, in contrast,

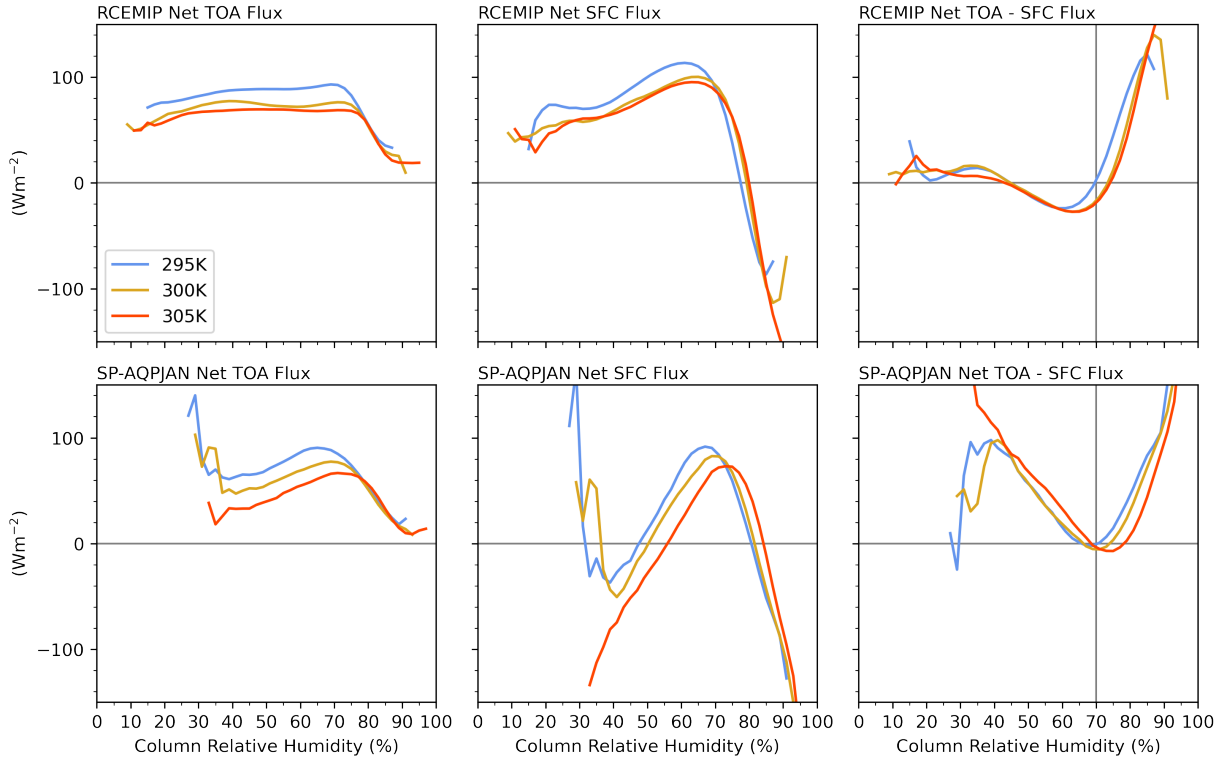
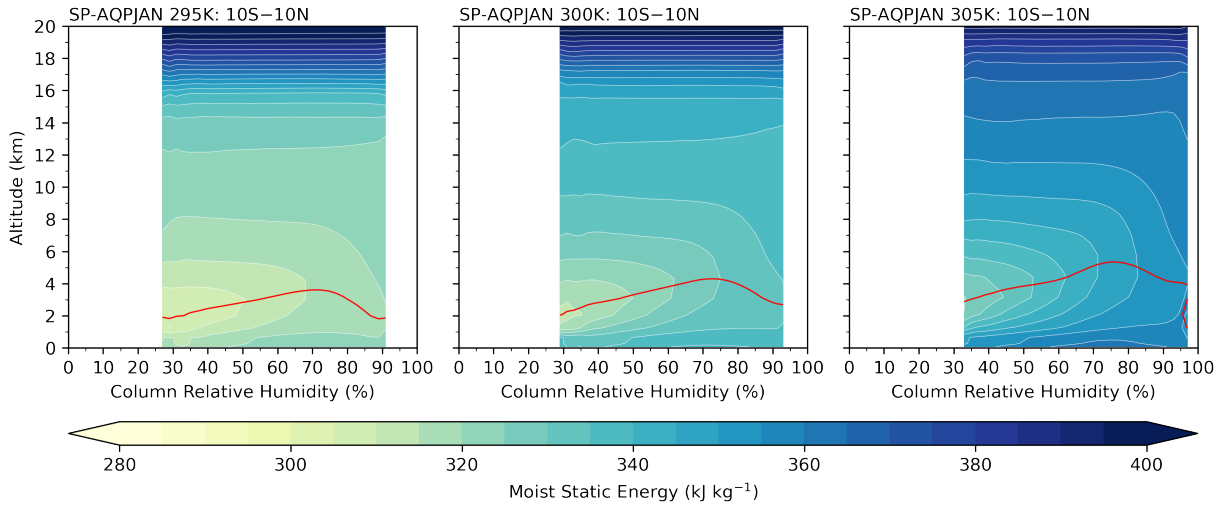


**Figure 7.8: Top Row** Net fluxes of radiation and energy at the TOA, surface, and into the atmosphere as a function of CRH for the RCEMIP simulations, as presented previously in Chapter 5. **Bottom Row** Same as **Top Row**, but for the AQPJAN simulations.

range from  $10^{\circ}\text{N}$  to  $10^{\circ}\text{N}$ , and there is a significant amount of energy transport out of the tropics and to mid-latitudes, as is shown in Fig. 7.4. However, the curves of the net flux of energy still go to zero near 70% CRH for the AQPJAN simulations, marking a clear boundary between the two regions, even if the flux remains positive in the dry region.

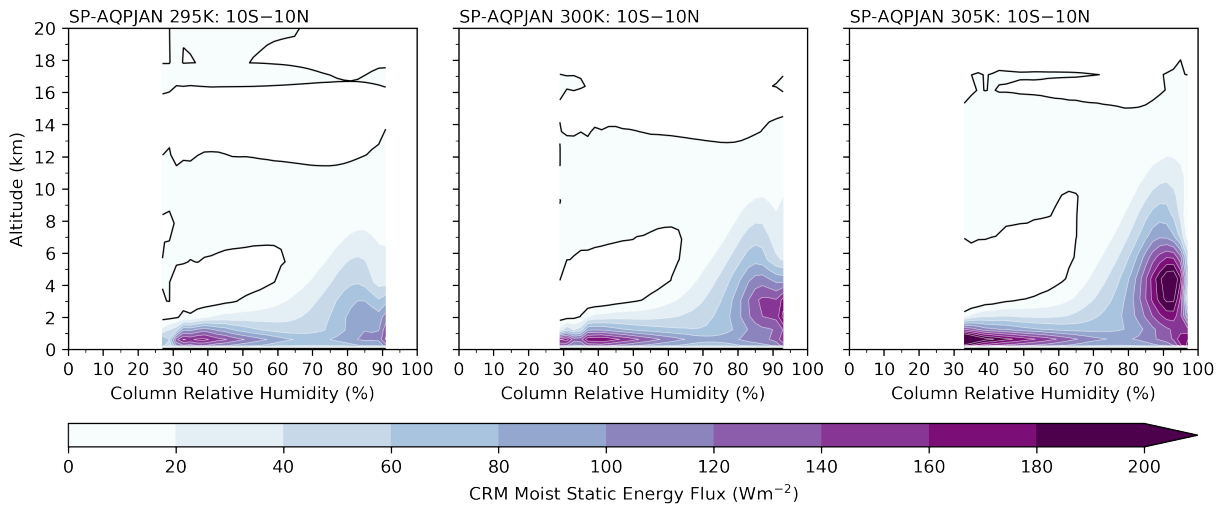
### 7.2.3 Radiatively driven moisture feedback

Next, an analysis is made of the vertical structure of the AQPJAN simulations, binned by the CRH. While the entire analysis was performed following the method of Chapter 6, only key plots are included here for the sake of brevity. Fig. 7.9 shows the profiles of moist static energy binned by the CRH for the AQPJAN simulations. Like the corresponding plots from the RCEMIP simulations, the mid-tropospheric minimum in  $h$  is present, and becomes weaker in the humid region. The minimum also occurs at the highest altitude near 70% CRH, shown by the red curve.



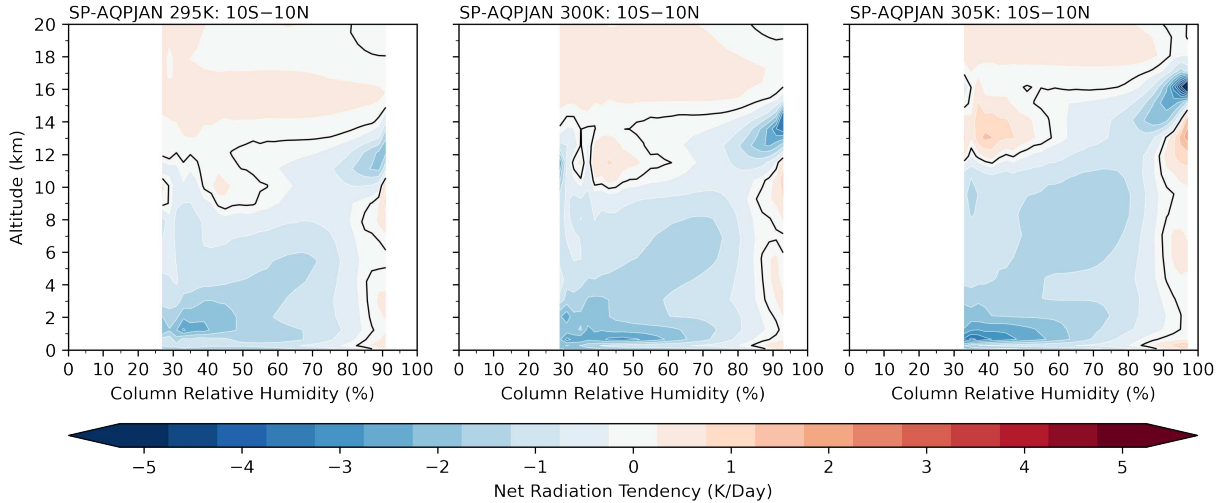
**Figure 7.9:** Profiles of the moist static energy for the AQPJAN simulations, binned by the CRH as in Chapter 6. Compare with Fig. 6.4

Fig. 7.9 confirms that the moist static energy minimum becomes weaker in humid regions of the AQPJAN simulations, consistent with results from the RCEMIP simulations.



**Figure 7.10:** Profiles of the CRM moist static energy flux for the AQPJAN simulations, binned by the CRH as in Chapter 6. Compare with Fig. 6.9

Plots of the flux of  $h$  by the CRM are shown in Fig. 7.10. Like the corresponding figures for the RCEMIP simulations, the MSE flux increases in magnitude as the surface warms, and the contours reach higher altitudes. The contours also reach a maximum with regard to CRH in the middle of



**Figure 7.11:** Profiles of the net radiation tendency for the AQPJAN simulations, binned by the CRH as in Chapter 6. Compare with the bottom row of Fig. 6.1

the humid region, before declining as the CRH becomes very large. This indicates that the shift from convective-scale energy transport to large-scale energy transport is present in the AQPJAN simulations as well as in the RCEMIP simulations.

The net longwave plus shortwave radiation tendency binned by CRH is shown in Fig. 7.11 for each of the AQPJAN simulations. These contours share many of the same characteristics that were found in the RCEMIP simulations. These include maxima in radiative cooling in the boundary layer of the dry regions, and maxima in the upper troposphere of the humid regions. More importantly for the radiatively driven feedback discussed in Chapter 6, the net radiation tendency becomes positive through a deep layer of the troposphere in the extremely humid region, consistent with results from the RCEMIP simulations. In addition, a difference is seen in the upper-troposphere for CRH near 40%, where there is a lobe of positive heating that extends from the stratosphere down into the troposphere. This lobe does not appear in when the latitude limits are expanded to 30°, as is discussed in Appendix C.

Lastly, Fig. 7.12 shows contours of the net radiatively driven moistening, as calculated using Eq. 6.6, Chikira’s equation for the water vapor tendency. Like the corresponding plots in Chapter 6, radiation acts to dry the atmosphere throughout most of the domain in the AQPJAN simulations.

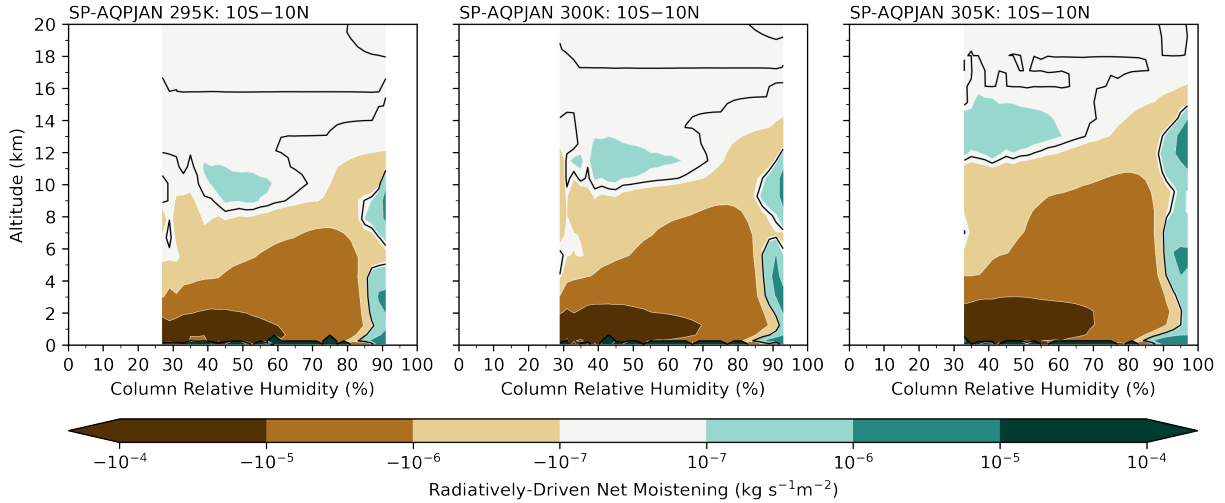


**Figure 7.12:** Profiles of the net radiatively-driven moistening for the AQPJAN simulations, binned by the CRH as in Chapter 6. Compare with Fig. 6.12

However in the extremely humid region, the net radiation tendency becomes positive, leading to rising motion which tends to moisten the domain.

### 7.3 Summary of AQPJAN Results

In this Chapter, important calculations from Chapters 3, 5, and 6 were repeated to investigate whether the results of previous chapters, calculated using output from the idealized RCEMIP simulations, could be reproduced using a more realistic experimental setup. The calculations were repeated using a set of experiments designated “AQPJAN,” which used a super-parameterized version of the community atmosphere model configured over a rotating aquaplanet with a meridional

**Table 7.2:** Extension of Tbl. 6.1, showing the fraction of the domain with CRH below a given level for the AQPJAN and RCEMIP simulations, as well as the ERA5 reanalyses. This is the area under the curves in Fig. 7.5 from 0% CRH to 70% or 80%.

	CRH $\leq$ 70%	CRH $\leq$ 80%
<b>295 K AQPJAN</b>	42.81%	87.08%
<b>300 K AQPJAN</b>	37.41%	80.51%
<b>305 K AQPJAN</b>	32.05%	71.49%
<b>295 K RCEMIP</b>	78.99%	97.35%
<b>300 K RCEMIP</b>	71.94%	94.83%
<b>305 K RCEMIP</b>	74.95%	94.79%
<b>ERA5</b>	54.93%	83.55%

SST distribution and a realistic solar cycle with a zenith angle corresponding to the 15th of January. The AQPJAN simulations were found to give a realistic approximation to the real atmosphere, including realistic distributions of zonal winds, and a large-scale circulation. Calculations showed that the simulations included a single ITCZ just north of the equator, subtropical maxima in evaporation, and realistic meridional transports of moisture and energy.

In the AQPJAN simulations, the CRE as a function of the CRH (Fig. 7.6) was found to be largely independent of the SST, and showed broad agreement with previous calculations (Figs. 3.3, 3.7), including a threshold of 70% CRH to separate dry regions with small CRE from humid regions with large CRE. This 70% threshold was also found to mark the CRH value where the difference between precipitation and evaporation changed signs, marking the boundary between humid and dry regions. The AQPJAN simulations also showed evidence of the radiatively driven moisture feedback discussed in Chapter 6, as the net radiation tendency became positive for extremely humid regions. This radiative heating induced rising motion, which led to a moistening of the troposphere as moisture was lifted to higher altitudes by the large-scale flow.

Broadly, analysis of the AQPJAN simulations agreed with the analysis of the RCEMIP simulations, and the differences between the two were minor. As mentioned a few times through this chapter, the choice of the 10°S to 10°N was ultimately an arbitrary one. Appendix C repeats some of the analysis of this chapter in the same simulations but with the latitude limits extended to range from 30°S to 30°N, with a general agreement found.

This chapter marks the last chapter of analysis in this thesis. The next section serves as a final conclusion, where the most important results of each of the previous chapters are summarized, and a brief discussion of the direction of future work is included.

## **7.4 Conclusions**

### **7.4.1 Riehl and Malkus, Revisited**

The work of Riehl and Malkus (1958) (RM58) has been a cornerstone of our understanding of the tropical atmosphere for more than six decades. RM58 used vertically coarse radiosonde

observations from about seventy stations to estimate the heat balance of deep tropics, what we would call the energy budget. They correctly inferred that latent energy is transported into the ITCZ at lower levels against the moisture gradient, while dry static energy is transported out of the ITCZ at upper levels along the energy gradient. In this way, the ITCZ acts as a source of energy for the rest of the atmosphere due to strong ACRE, at the same time as it is a sink for moisture. Furthermore, they correctly identified convective transport as the mechanism by which energy is transported vertically within the ITCZ.

RM58 were restricted to using estimates of the zonal-mean, monthly mean radiation excess in the northern hemisphere alone to construct their radiation balance for the summer and winter hemispheres. Sensible heat fluxes were calculated as a residual from radiation and latent heat fluxes, rather than being independently computed. And a moving coordinate system that followed the seasonal path of the ITCZ was used in order to maximize the utility of the relatively small number of radiosonde observations. Indeed, a sizable portion of their study is devoted to the laborious task of collecting and compiling disparate sources of data.

Now, more than sixty years later, we have many more tools at our disposal with which to further our understanding of the energy and moisture balances within the tropics. These tools allow us to approach the problem in ways that were not possible when RM58 published their germinal study. Perhaps most importantly, we possess decades of finely resolved satellite observations of radiative fluxes, as well as estimates of surface sensible and latent heat fluxes from observations and reanalyses. We are able to reconstruct the atmospheric energy and moisture balances at any moment at any location, within the spatial and temporal resolution of our data. In addition, we have access to many years of simulated data in the form of high resolution global circulation model output. Balances of energy and moisture can be computed with this model output to compare with observations and reanalyses. In addition, the model output allows for investigation of the vertically resolved fields such as temperature, humidity, and radiative heating rates as an extension to the radiosonde observations used by RM58

An important finding of this thesis is the the assumptions of RM58 were very good. For example, the assumption that "no heat flow takes place through the equatorial trough," is largely

supported by Fig. 7.4, which shows that the integrated poleward transport of energy is near zero at the equator and on the summer side of the ITCZ in the three AQPJAN simulations. Similar results have been shown for energy transports in the real atmosphere (Trenberth and Caron, 2001; Vonder Haar and Oort, 1973). This assumption justified the use by RM58 of a coordinate system that migrated seasonally with the ITCZ, which allowed them to use data from a given station twice in calculating data for the winter and summer seasons.

The analysis in this thesis shows that the first main conclusion of RM58, that the ITCZ is an energy source and moisture sink, extends to humid regions more generally. Chapter 5 showed that the humid regions of the RCEMIP simulations were characterized by an up-gradient transport of moisture and a down-gradient transport of energy (Neelin and Held, 1987). In addition, the boundary between humid and dry regions of approximately 70% CRH corresponded roughly with the CRH value that outlines convergence zones in the real tropics.

This thesis also supports the second main conclusion of RM58, that energy transport on convective scales is the primary method of vertical transport in the tropics. Here the word primary is important, as Chapter 6 emphasized the importance of moisture transport on large scales in the extremely humid regions. These regions represented less than 5% of the domain for the RCEMIP simulations, but were a much larger fraction for the AQPJAN simulations within  $10^\circ$  of the equator (Tbl. 7.2).

This shift to large scale motion in extremely humid regions has been discussed in the recent work of Jenney et al. (2020). A possible mechanism for the shift was suggested at the end of Chapter 6, in the form of a radiatively driven moisture feedback. In extremely humid regions, the high degree of cloudiness leads to a powerful atmospheric cloud radiative effect. The ACRE is strong enough to change the sign of the net radiation tendency, which is negative in most of the tropical troposphere. The positive tendency leads to rising motion on the environmental scale. The rising motion alone cannot account for the vertical transport of moisture, but when the moisture tendency equation is written following Chikira (2014), it is clear that the positive radiation tendency induces a moistening of the troposphere.

## 7.4.2 Cloud Radiative Effect and Column Relative Humidity

In Chapter 3 the longwave, shortwave, and net CRE at a given CRH were found to be independent of the SST for a set of three simulations following the RCEMIP protocol (Jenney et al., 2020; Wing et al., 2018). Each of the simulations showed a “kink” in the curve of CRE versus CRH, with a rapid increase in CRE with CRH for CRH values greater than about 70%. These calculations were then repeated using satellite observations for the CRE, and reanalyses for the CRH. The curves of CRE versus CRH from observations and reanalyses showed essentially the same results as the RCEMIP simulations, and were a nearly universal function of CRH, regardless of the surface conditions.

The nearly universal curves of CRE versus CRH suggested that the CRH could be used to estimate the CRE. This was investigated in Chapter 4, where a method was developed to estimate the CRE based on the CRH. The method was able to reproduce the annual mean map of longwave and shortwave CRE with only small errors in most places. The exception was over regions of marine stratus clouds off of the west coasts of continents. Then, the CRH estimation method was evaluated in a monthly mean sense. A time series of longwave and shortwave CRE estimated from CRH was able to reproduce the CRE when only CRH greater than 50% were included, a heuristic which effectively removed the troublesome stratus regions from the calculation while preserving important regions such as the ITCZ.

The estimation method was then evaluated for three oceanic regions. The monthly correlation was found to be very good over the west Pacific in the longwave and shortwave, and over the east Pacific in the longwave ( $R^2 \simeq 0.7$ ). The correlation was somewhat worse over the east Pacific in the shortwave, and over the Indian Ocean in both the longwave and shortwave ( $0.2 \leq R^2 \leq 0.5$ ). A simple composite analysis showed that the correlation of the shortwave CRE over the east Pacific was lowest during La Niña months ( $R^2 = 0.119$ ) and highest during El Niño months ( $R^2 = 0.558$ ), compared to the entire record over the east Pacific ( $R^2 = 0.339$ ). Further links between the accuracy of the estimation method and ENSO are discussed in Appendix B.

### 7.4.3 Future Work

There are several ways in which to extend the work of this thesis. These can broadly be organized into three categories. The first relates to the direct link between CRH and CRE from Chapter 3. The second relates to the method of estimating the CRE from the CRH as discussed in Chapter 4. And the third relates to the radiatively driven moisture feedback of Chapter 6.

In Chapter 3, the RCEMIP simulations represent tropical conditions, and the satellite observations were restricted to a latitude belt within  $30^\circ$  of the equator. Then, does the CRE follow the same universal function of the CRH at higher latitudes and over cooler SSTs? If not, does the CRE follow some other function of the CRH, or does it behave in an entirely different way? A key conclusion of Chapter 3 was that the curves of CRE versus CRH are independent of the surface conditions in simulations, satellite observations, and reanalyses. How does this link between CRH, CRE, and SST relate to the fixed anvil temperature and related hypotheses (Bony et al., 2016; Hartmann and Larson, 2002; Seeley et al., 2019; Zelinka and Hartmann, 2010)? This link is discussed briefly in Appendix A, where it is shown that the 70% threshold may be helpful in separating regions where the principles of the FAT hypothesis can be expected to hold.

Secondly, the method of Chapter 4 skillfully estimates large CRE when the CRH is large, but struggles to estimate the CRE when the CRH is small. This was attributed to the effect of stratus regions off the west coasts of continents. Then, can the CRH estimation method be improved by removing the effects of the stratus regions in some way? This could possibly be achieved by altering the curves used to estimate the CRH (Fig. 4.1) when the CRH is small. Another possibility is that including another field such as the liquid or ice water path could be used in conjunction with the CRH to estimate the CRE. This may allow for more easily discriminating between desert and marine stratus regions, which are both dry in terms of the CRH, but are otherwise quite different. Another question is to what extent the CRH can be used to estimate the precipitation rate, following the universal curves precipitation presented in Bretherton et al. (2004) and in Chapter 5.

In addition, the estimation method was applied only at the CRE at TOA, while Chapter 4 showed nearly universal curves of surface CRE and ACRE versus CRH as well. The TOA CRE

is easy to observe from satellite observations, while observations of the surface and atmospheric effects are more difficult. Can a similar method be developed to estimate either of those effects from the CRH? Lastly, the high degree of skill achieved by modeling the CRE using the simple curves in Fig. 4.1 suggests that a machine learning method such as a neural network (Gentine et al., 2018; Rasp et al., 2018) may be able to estimate the CRE with a high degree of accuracy using only a few variables.

Finally, the moisture feedback. The feedback describes a process in which the clouds associated with extremely humid regions play an active role in moistening the local atmosphere, thus contributing to their own longevity. This may be relevant to the persistence of convective self-aggregation (Bretherton et al., 2005; Held et al., 1993; Wing and Emanuel, 2014; Wing et al., 2017). A link to self-aggregation has been suggested before in this thesis, but this work still needs to be done in earnest.

# References

- Richard P Allan. Combining satellite data and models to estimate cloud radiative effect at the surface and in the atmosphere. *Met. Apps*, 18(3):324–333, September 2011.
- Akio Arakawa and Wayne Howard Schubert. Interaction of a cumulus cloud ensemble with the Large-Scale environment, part I. *J. Atmos. Sci.*, 31(3):674–701, April 1974.
- Anthony Barnston. Why are there so many ENSO indexes, instead of just one? <https://www.climate.gov/news-features/blogs/enso/why-are-there-so-many-enso-indexes-instead-just-one>, January 2015. Accessed: 2020-12-22.
- Sandrine Bony, Bjorn Stevens, Dargan M W Frierson, Christian Jakob, Masa Kageyama, Robert Pincus, Theodore G Shepherd, Steven C Sherwood, A Pier Siebesma, Adam H Sobel, Masahiro Watanabe, and Mark J Webb. Clouds, circulation and climate sensitivity. *Nat. Geosci.*, 8:261, March 2015.
- Sandrine Bony, Bjorn Stevens, David Coppin, Tobias Becker, Kevin A Reed, Aiko Voigt, and Brian Medeiros. Thermodynamic control of anvil cloud amount. *Proc. Natl. Acad. Sci. U. S. A.*, 113(32):8927–8932, August 2016.
- O Boucher, D Randall, P Artaxo, C Bretherton, G Feingold, P Forster, V-M Kerminen, Y Kondo, H Liao, U Lohmann, P Rasch, S K Satheesh, S Sherwood, B Steven, and X Y Zhang. Clouds and aerosols. In T F Stocker, D Qin, G-K Plattner, M Tignor, S K Allen, J Boschung, A Nauels, Y Xia, V Bex, and P M Midgley, editors, *Climate Change 2013: The Physical Science Basis. Contribution of Working Group I to the Fifth Assessment Report of the Intergovernmental Panel on Climate Change*, pages '571–657'. Cambridge University Press, Cambridge, United Kingdom and New York, NY, USA, 2013.
- Christopher S Bretherton, Matthew E Peters, and Larissa E Back. Relationships between water vapor path and precipitation over the tropical oceans. *J. Clim.*, 17(7):1517–1528, 2004.

- Christopher S Bretherton, Peter N Blossey, and Marat Khairoutdinov. An Energy-Balance analysis of deep convective Self-Aggregation above uniform SST. *J. Atmos. Sci.*, 62(12):4273–4292, December 2005.
- Michael P Byrne, Angeline G Pendergrass, Anita D Rapp, and Kyle R Wodzicki. Response of the intertropical convergence zone to climate change: Location, width, and strength. *Curr Clim Change Rep*, 4(4):355–370, August 2018.
- Jung Hyo Chae and Steven C Sherwood. Insights into Cloud-Top height and dynamics from the seasonal cycle of Cloud-Top heights observed by MISR in the west pacific region. *J. Atmos. Sci.*, 67(1):248–261, January 2010.
- Jule G Charney. A note on Large-Scale motions in the tropics. *J. Atmos. Sci.*, 20(6):607–609, November 1963.
- Minoru Chikira. Eastward-Propagating intraseasonal oscillation represented by Chikira–Sugiyama cumulus parameterization. part II: Understanding moisture variation under weak temperature gradient balance. *J. Atmos. Sci.*, 71(2):615–639, February 2014.
- Lu Ann Dahlman. Climate variability: Oceanic niño index. <https://www.climate.gov/news-features/understanding-climate/climate-variability-oceanic-ni%C3%B1o-index>, August 2016. Accessed: 2020-12-22.
- W H Dines. The heat balance of the atmosphere. *Q.J.R. Meteorol. Soc.*, 43(182):151–158, February 1917.
- David R Doelling, Moguo Sun, Le Trang Nguyen, Michele L Nordeen, Conor O Haney, Dennis F Keyes, and Pamela E Mlynczak. Advances in geostationary-derived longwave fluxes for the ceres synoptic (syn1deg) product. *J. Atmos. Ocean. Technol.*, 33(3):503–521, March 2016.
- Zachary A Eitzen, Kuan-Man Xu, and Takmeng Wong. Cloud and radiative characteristics of tropical deep convective systems in extended cloud objects from CERES observations. *J. Clim.*, 22(22):5983–6000, November 2009.

- P Gentine, M Pritchard, S Rasp, G Reinaudi, and G Yacalis. Could machine learning break the convection parameterization deadlock? *Geophys. Res. Lett.*, 45(11):5742–5751, June 2018.
- Edwin F Harrison, Patrick Minnis, B R Barkstrom, V Ramanathan, and G G Gibson. Seasonal variation of cloud radiative forcing derived from the earth radiation budget experiment. *J. Geophys. Res.*, 95(D11), February 1989.
- Bryce E Harrop and Dennis L Hartmann. Testing the role of radiation in determining tropical cloud-top temperature. *J. Clim.*, 25(17):5731–5747, September 2012.
- Dennis L Hartmann and Kristin Larson. An important constraint on tropical cloud - climate feedback. *Geophys. Res. Lett.*, 29(20):12–1–12–4, October 2002.
- Dennis L Hartmann and Marc L Michelsen. NO EVIDENCE FOR IRIS. *Bull. Am. Meteorol. Soc.*, 83(2):249–254, February 2002.
- Dennis L Hartmann, Peter N Blossey, and Brittany D Dygert. Convection and climate: What have we learned from simple models and simplified settings? *Current Climate Change Reports*, June 2019.
- Isaac M Held, Richard S Hemler, and V Ramaswamy. Radiative-Convective equilibrium with explicit Two-Dimensional moist convection. *J. Atmos. Sci.*, 50(23):3909–3927, December 1993.
- Hans Hersbach, Bill Bell, Paul Berrisford, Shoji Hirahara, András Horányi, Joaquín Muñoz-Sabater, Julien Nicolas, Carole Peubey, Raluca Radu, Dinand Schepers, Adrian Simmons, Cornel Soci, Saleh Abdalla, Xavier Abellan, Gianpaolo Balsamo, Peter Bechtold, Gionata Biavati, Jean Bidlot, Massimo Bonavita, Giovanna Chiara, Per Dahlgren, Dick Dee, Michail Diamantakis, Rossana Dragani, Johannes Flemming, Richard Forbes, Manuel Fuentes, Alan Geer, Leo Haimberger, Sean Healy, Robin J Hogan, Elías Hólm, Marta Janisková, Sarah Keeley, Patrick Laloyaux, Philippe Lopez, Cristina Lupu, Gabor Radnoti, Patricia Rosnay, Iryna Rozum, Freja Vamborg, Sebastien Villaume, and Jeannoël Thépaut. The ERA5 global reanalysis. *Q.J.R. Meteorol. Soc.*, 146(730):1999–2049, July 2020.

- Nadir Jeevanjee and Stephan Fueglistaler. Simple spectral models for atmospheric radiative cooling. *J. Atmos. Sci.*, 77(2):479–497, February 2020.
- A M Jenney, D A Randall, and M D Branson. Understanding the response of tropical ascent to warming using an energy balance framework. *J. Adv. Model. Earth Syst.*, May 2020.
- Sarah M Kang, Yechul Shin, and Shang-Ping Xie. Extratropical forcing and tropical rainfall distribution: energetics framework and ocean ekman advection. *npj Climate and Atmospheric Science*, 1(1):20172, January 2018.
- Marat F Khairoutdinov and David A Randall. Cloud resolving modeling of the ARM summer 1997 IOP: Model formulation, results, uncertainties, and sensitivities. *J. Atmos. Sci.*, 60(4):607–625, February 2003.
- Zhiming Kuang and Christopher S Bretherton. Convective influence on the heat balance of the tropical tropopause layer: A Cloud-Resolving model study. *J. Atmos. Sci.*, 61(23):2919–2927, December 2004.
- Zhiming Kuang and Dennis L Hartmann. Testing the fixed anvil temperature hypothesis in a Cloud-Resolving model. *J. Clim.*, 20(10):2051–2057, May 2007.
- Terence L Kubar, Dennis L Hartmann, and Robert Wood. Radiative and convective driving of tropical high clouds. *J. Clim.*, 20(22):5510–5526, November 2007.
- Richard S Lindzen, Ming-Dah Chou, and Arthur Y Hou. Does the earth have an adaptive infrared iris?, 2001.
- Richard S Lindzen, Ming-Dah Chou, and Arthur Y Hou. Comment on “no evidence for iris”. *Bull. Am. Meteorol. Soc.*, 83(9):1345–1349, 2002.
- Roland A Madden and Paul R Julian. Detection of a 40–50 day oscillation in the zonal wind in the tropical pacific. *Journal of Atmospheric Sciences*, 28(5):702–708, July 1971.

- Syukuro Manabe and Robert F Strickler. Thermal equilibrium of the atmosphere with a convective adjustment. *J. Atmos. Sci.*, 21(4):361–385, July 1964.
- Syukuro Manabe and Richard T Wetherald. Thermal equilibrium of the atmosphere with a given distribution of relative humidity. *J. Atmos. Sci.*, 24(3):241–259, May 1967.
- Thorsten Mauritsen and Bjorn Stevens. Missing iris effect as a possible cause of muted hydrological change and high climate sensitivity in models. *Nat. Geosci.*, 8:346, April 2015.
- C R Mechoso, A W Robertson, N Barth, M K Davey, P Delecluse, P R Gent, S Ineson, B Kirtman, M Latif, H Le Treut, T Nagai, J D Neelin, S G H Philander, J Polcher, P S Schopf, T Stockdale, M J Suarez, L Terray, O Thual, and J J Tribbia. The seasonal cycle over the tropical pacific in coupled Ocean-Atmosphere general circulation models. *Mon. Weather Rev.*, 123(9):2825–2838, September 1995.
- National Weather Service. Cold & warm episodes by season. [https://origin.cpc.ncep.noaa.gov/products/analysis\\_monitoring/ensostuff/ONI\\_v5.php](https://origin.cpc.ncep.noaa.gov/products/analysis_monitoring/ensostuff/ONI_v5.php), December 2020. Accessed: 2020-12-22.
- R B Neale and B J Hoskins. A standard test for agcms including their physical parametrizations: I: The proposal. *Atmos. Sci. Lett.*, 1(2):101–107, July 2000.
- J David Neelin and Isaac M Held. Modeling tropical convergence based on the moist static energy budget. *Mon. Weather Rev.*, 115(1):3–12, 1987.
- V Ramanathan. The role of earth radiation budget studies in climate and general circulation research. *J. Geophys. Res.*, 92(D4):4075, 1987.
- V Ramanathan, R D Cess, E F Harrison, P Minnis, B R Barkstrom, E Ahmad, and D L Hartmann. Cloud-Radiative forcing and climate: Results from the earth radiation budget experiment. *Science*, 243(4887):57–63, January 1989.

- David Randall, Charlotte DeMott, Cristiana Stan, Marat Khairoutdinov, James Benedict, Rachel McCrary, Katherine Thayer-Calder, and Mark Branson. Simulations of the tropical general circulation with a multiscale global model. *Meteorol. Monogr.*, 56:15.1–15.15, April 2016.
- Stephan Rasp, Michael S Pritchard, and Pierre Gentine. Deep learning to represent subgrid processes in climate models. *Proc. Natl. Acad. Sci. U. S. A.*, 115(39):9684–9689, September 2018.
- David J Raymond, Sharon L Sessions, Adam H Sobel, and Željka Fuchs. The mechanics of gross moist stability. *J. Adv. Model. Earth Syst.*, 1(3), March 2009.
- Herbert Riehl and Joanne S Malkus. On the heat balance in the equatorial trough zone. *Geophysica*, 6, 1958.
- Marion Saint-Lu, Sandrine Bony, and Jean-louis Dufresne. Observational evidence for a stability iris effect in the tropics. *Geophys. Res. Lett.*, 47(14):17, July 2020.
- Tapio Schneider, Tobias Bischoff, and Gerald H Haug. Migrations and dynamics of the intertropical convergence zone. *Nature*, 513(7516):45–53, September 2014.
- Jacob T Seeley, Nadir Jeevanjee, and David M Romps. Fat or fitt: Are anvil clouds or the tropopause temperature invariant? *Geophys. Res. Lett.*, 46(3):1842–1850, February 2019.
- Adam H Sobel, Johan Nilsson, and Lorenzo M Polvani. The weak temperature gradient approximation and balanced tropical moisture waves. *J. Atmos. Sci.*, 58(23):3650–3665, December 2001.
- Hui Su, Jonathan H Jiang, J David Neelin, T Janice Shen, Chengxing Zhai, Qing Yue, Zhien Wang, Lei Huang, Yong-Sang Choi, Graeme L Stephens, and Yuk L Yung. Tightening of tropical ascent and high clouds key to precipitation change in a warmer climate. *Nat. Commun.*, 8:15771, June 2017.
- Kevin E Trenberth. The definition of el niño. *Bull. Am. Meteorol. Soc.*, 78(12):2771–2778, December 1997.

- Kevin E Trenberth and Julie M Caron. Estimates of meridional atmosphere and ocean heat transports. *J. Clim.*, 14(16):3433–3443, August 2001.
- Kevin E Trenberth, John T Fasullo, and Jeffrey Kiehl. Earth’s global energy budget. *Bull. Am. Meteorol. Soc.*, 90(3):311–324, March 2009.
- Thomas H Vonder Haar and Abraham H Oort. New estimate of annual poleward energy transport by northern hemisphere oceans. *J. Phys. Oceanogr.*, 3(2):169–172, April 1973.
- Allison A Wing and Kerry Andrew Emanuel. Physical mechanisms controlling self-aggregation of convection in idealized numerical modeling simulations. *Journal of Advances in Modeling Earth Systems*, 6(1), March 2014.
- Allison A Wing, Kerry Emanuel, Christopher E Holloway, and Caroline Muller. Convective Self-Aggregation in numerical simulations: A review. *Surv. Geophys.*, 38(6):1173–1197, November 2017.
- Allison A Wing, Kevin A Reed, Masaki Satoh, Bjorn Stevens, Sandrine Bony, and Tomoki Ohno. Radiative–convective equilibrium model intercomparison project. *Geoscientific Model Development*, 11(2):793–813, March 2018.
- Allison A Wing, Catherine L Stauffer, Tobias Becker, Kevin A Reed, Min-Seop Ahn, Nathan P Arnold, Sandrine Bony, Mark Branson, George H Bryan, Jean-Pierre Chaboureau, Stephan R Roode, Kulkarni Gayatri, Cathy Hohenegger, I-Kuan Hu, Fredrik Jansson, Todd R Jones, Marat Khairoutdinov, Daehyun Kim, Zane K Martin, Shuhei Matsugishi, Brian Medeiros, Hiroaki Miura, Yumin Moon, Sebastian K Mueller, Tomoki Ohno, Max Popp, Thara Prabhakaran, David Randall, Rosimar Rios-Berrios, Nicolas Rochetin, Romain Roehrig, David M Romps, James H Ruppert, Jr., Masaki Satoh, Levi G Silvers, Martin S Singh, Bjorn Stevens, Lorenzo Tomassini, Chiel C Heerwaarden, Shuguang Wang, and Ming Zhao. Clouds and convective self-aggregation in a multi-model ensemble of radiative-convective equilibrium simulations. *J. Adv. Model. Earth Syst.*, July 2020.

Kuan-Man Xu, Takmeng Wong, Bruce A Wielicki, Lindsay Parker, Bing Lin, Zachary A Eitzen, and Mark Branson. Statistical analyses of satellite cloud object data from CERES. part II: Tropical convective cloud objects during 1998 el niño and evidence for supporting the fixed anvil temperature hypothesis. *J. Clim.*, 20(5):819–842, March 2007.

Mark D Zelinka and Dennis L Hartmann. Why is longwave cloud feedback positive? *J. Geophys. Res.*, 115(D16):1606, August 2010.

Mark D Zelinka and Dennis L Hartmann. The observed sensitivity of high clouds to mean surface temperature anomalies in the tropics. *J. Geophys. Res.*, 116(D23), December 2011.

# Appendix A

## FAT, PHAT, and FiTT

A main conclusion of Chapter 3 was that the cloud radiative effect as a function of the column relative humidity was largely, but not entirely, independent of the SST. This appendix will investigate how the CRH analysis framework developed in the main text can be applied to the relationship between upper-level clouds and the cloud radiative effect at the top of the atmosphere. The theoretical foundation for this analysis rests on the fixed anvil temperature (FAT) hypothesis of Hartmann and Larson (2002) which was discussed in §1.4. Briefly, the FAT hypothesis suggests that the tops of tropical anvil clouds remain at the same temperature, regardless of the surface temperature. The reason given is that clear-sky longwave cooling in the troposphere decreases rapidly with height near 220K, and because longwave cooling balances subsidence warming, this should lead to a vertical divergence in mass in clear regions. Below that level, radiative cooling must be balanced by convective heating.

This appendix begins with a discussion of the thermal expansion of the troposphere in a warmer climate, followed by a brief derivation of the radiatively driven divergence (Kuang and Hartmann, 2007), a quantity central to the FAT hypothesis. Then, following in the tradition of modeling and observational studies of the FAT hypothesis (including Hartmann and Larson (2002), Kubar et al. (2007), Kuang and Hartmann (2007), Xu et al. (2007), Eitzen et al. (2009), Chae and Sherwood (2010), Zelinka and Hartmann (2010, 2011), Harrop and Hartmann (2012), and Seeley et al. (2019) among others), the validity of the FAT hypothesis is assessed in a domain-mean sense for the three RCEMIP simulations. Next, the CRH analysis framework is applied to the FAT hypothesis to investigate how the temperature of the maximum in cloud fraction depends on the CRH. Finally, the link between the temperature of high clouds and the effective brightness temperature at the TOA is considered, along with a brief discussion of the fixed tropopause temperature (FiTT) hypothesis of Seeley et al. (2019).

The domain-average analysis finds that the temperature at the level of maximum cloud fraction increases by approximately 30% of the increase in surface temperature, providing support for a proportionally higher anvil temperature (PHAT, Zelinka and Hartmann (2010)), rather than a FAT. In addition, the temperature where the domain-mean buoyancy flux profile passes through zero changes by approximately 2 K in response to a 10 K increase in surface temperature. This is in general agreement with recent work by Hartmann et al. (2019).

The CRH analysis finds qualitative differences in the behavior of the dry and humid parts of the domain, when the 70% threshold of previous chapters is used to separate the regions. In the dry region, the temperature of the level of maximum cloud fraction increases by about 20% from the 295 K to 300 K simulation, and by about 30% between the 295 K to 305 K simulation, with a larger increase between the 300 K and 305 K simulations. However in the saturated region, the relative increase in the temperature of the maximum cloud fraction is much larger. Similar results are found for the TOA brightness temperature, a field which is of central importance to the radiative balance of the atmosphere, as well as for other fields.

## **A.1 The thermal expansion of the troposphere**

As a starting point, Fig. A.1 shows temperature profiles for the three RCEMIP simulations on a Skew-T diagram. Above the turbulent boundary layer, the temperature profiles largely follow a line of moist adiabatic ascent from 900 to 200 hPa. This is in agreement with two theoretical arguments. The first is that in the absence of Coriolis effects (like these simulations without rotation), horizontal temperature gradients are weak (Charney (1963), Sobel et al. (2001)). The second is that the ascent of a moist parcel of air is approximately moist-adiabatic. Combining these two, the temperature profile of deep convective storms necessarily sets the large-scale temperature profile to that of a moist adiabat ascending from around 900 hPa.

As the surface temperature increases in these simulations, the mean temperature profile shifts to a warmer moist adiabat. In addition to being warmer, the temperature profile is also more stable to vertical motions. This can be seen in the right panel of Fig. A.1 which shows vertical profiles

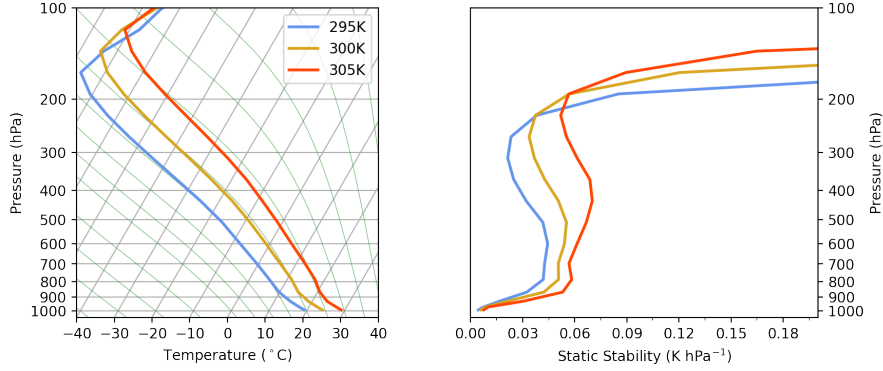


**Figure A.1:** **Left** Temperature profiles for each of the RCEMIP simulations. Curved green lines are moist adiabats. **Right** Dry static stability profiles for each simulation.

of the dry static stability. The static stability can be defined (Zelinka and Hartmann, 2010, 2011) in several ways including

$$S = \frac{\kappa T}{p} - \frac{\partial T}{\partial p} = \frac{-1}{c_p} \frac{\partial s}{\partial p}, \quad (\text{A.1})$$

where the ideal gas law and hydrostatic relation have been used to convert between the first and second forms. In Eq. A.1,  $s$  is the dry static energy, defined in Eq. 6.1. This increased stability throughout the troposphere has been identified as an important factor in determining the altitude, temperature, and amount of high clouds. For example, Chae and Sherwood (2010) found that seasonal differences in the stability profile could explain seasonal differences in cloud-top temperature observed in the west pacific, and Bony et al. (2016) suggested that the higher stability associated with a warmer adiabat could help to account for the reduction in upper-level clouds that has been found in model simulations of a warmer climate. In addition, the increase in stability aloft was a central issue in the work of Zelinka and Hartmann (2010), which is discussed in detail below.

### A.1.1 The radiatively driven divergence.

Using the weak temperature gradient balance (Charney, 1963; Sobel et al., 2001), and the area-averaged dry static energy budget (e.g. Bony et al. (2016); Jenney et al. (2020); Zelinka and Hartmann (2010) among others), the environmental-scale vertical velocity can be written as

$$\bar{\omega} = -\frac{1}{S}(\bar{R} + \bar{C}). \quad (\text{A.2})$$

In Eq. A.2,  $\bar{R}$  is the radiative temperature tendency, and  $\bar{C}$  represents the temperature tendency from cloud processes. In regions where convection is not active,  $\bar{C}$  is negligible, and the vertical motions associated with radiative cooling can be approximated by

$$\bar{\omega} \simeq -\frac{1}{S}\bar{R}. \quad (\text{A.3})$$

The sign of  $\bar{R}$  determines the sign of  $\bar{\omega}$  because  $S$  is positive everywhere.

As previous studies have shown, (Kuang and Hartmann (2007), Zelinka and Hartmann (2010), Bony et al. (2016)), the horizontal divergence from cloudy regions can be calculated using mass continuity in terms of the radiatively driven vertical divergence in clear regions. This can be shown as

$$\nabla \cdot \mathbf{V}_H = -\frac{\partial \bar{\omega}}{\partial p} \simeq \frac{\partial}{\partial p} \left( \frac{1}{S} \bar{R} \right) \equiv D_R. \quad (\text{A.4})$$

$D_R$  represents the radiatively driven divergence from cloudy regions, or equivalently, the radiatively driven convergence into clear regions.

Fig. A.2 shows domain-averaged profiles of  $D_R$  calculated with the full-sky longwave cooling rate for each of the RCEMIP simulations, as well as the cloud fraction. As the SST increases, the larger static stability leads to a decrease in the upper-level peak in  $D_R$ . The upper-level peak in cloud fraction does not noticeably change from the 295K to 300K simulation, but decreases from the 300K to 305K simulation. These results are in general agreement with Bony et al. (2016), who found that a more stable profile lead to a reduction in  $D_R$  and a reduction in upper-level cloud fraction. This appendix is not directly concerned with changes in the magnitude of  $D_R$  or the magnitude of the cloud fraction with surface warming, so later figures will normalize both  $D_R$  and the cloud fraction by the upper-level maximum.

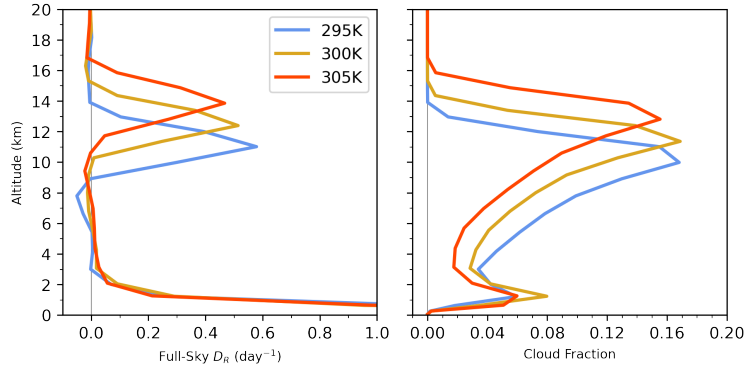


**Figure A.2:** **Left** Profiles of  $D_R$  calculated from the full-sky longwave cooling rate. **Right** Profiles of cloud fraction.

In addition to  $D_R$  and the cloud fraction, the buoyancy flux has been identified as an important quantity controlling the temperature of the top of tropical anvil clouds (Hartmann et al., 2019). The next section links the buoyancy flux, the cloud fraction, and  $D_R$ , and investigates how they change as the surface warms as a way to evaluate the FAT hypothesis.

## A.2 Thermodynamic dependance of upper-level clouds

The buoyancy flux is the vertical flux of virtual potential temperature scaled by the buoyancy (Hartmann et al., 2019; Kuang and Bretherton, 2004), and represents the flux of energy associated with turbulent, convective processes. A positive flux indicates that convection is working with buoyancy to generate convective kinetic energy, while a negative flux indicates that convection is working against buoyancy.

Panel A of Fig. A.3 shows profiles of the buoyancy flux computed from the CRM for each of the RCEMIP simulations. In the boundary layer, the buoyancy flux reaches its largest values as turbulent eddies transport energy away from the warm surface. The buoyancy flux becomes briefly negative around 2 km, representing the influence of convective inhibition. Above this level, the buoyancy flux is relatively constant through most of the troposphere, before decreasing with height and ultimately passing through zero. The level where the buoyancy flux passes through zero occurs at a higher altitude in warmer simulations, following the expansion of the troposphere as discussed previously.

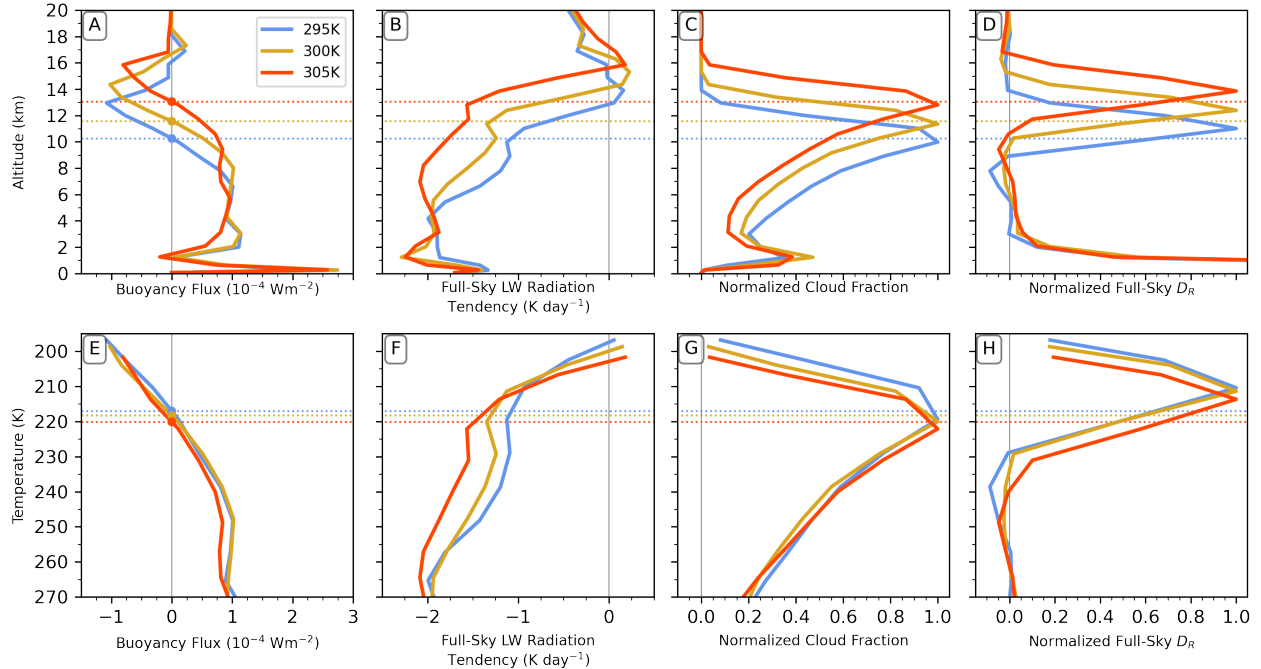


**Figure A.3:** Panel A Domain mean profiles of buoyancy flux computed on the CRM, with horizontal lines showing the altitude where the flux passes through zero aloft. Panels B, C, and D Full-sky longwave temperature tendency, Normalized cloud fraction, and  $D_R$  normalized by the upper-level peak, respectively. Horizontal dotted lines show the level where the buoyancy flux passes through zero. Panels E-H, same as Panels A-D, but with temperature as the vertical coordinate, rather than altitude.

Panels B, C, and D show profiles of the longwave cooling rate, normalized cloud fraction, and normalized  $D_R$ , with horizontal dotted lines showing the altitude where the buoyancy flux passes through zero. The zero level appears to coincide with the “kink” in the longwave cooling rate (Jeevanjee and Fueglistaler, 2020). The zero level also coincides with the level where the cloud fraction is largest, and is slightly below the peak in  $D_R$ . When altitude is the vertical coordinate, each of the profiles expands upwards as the SST increases, following the thermal expansion of the troposphere. Near the surface, the profiles sit nearly on top of one-another, with the expansion beginning to be noticeable near 3 to 4 km.

Panels E, F, G and H show the same profiles as panels A-D using temperature as the vertical coordinate, rather than altitude. In Panel E, the horizontal dotted lines mark the temperature where the buoyancy flux passes through zero. They show that this level occurs at approximately 220 K, consistent with the findings of Hartmann et al. (2019). In addition, the three buoyancy flux profiles

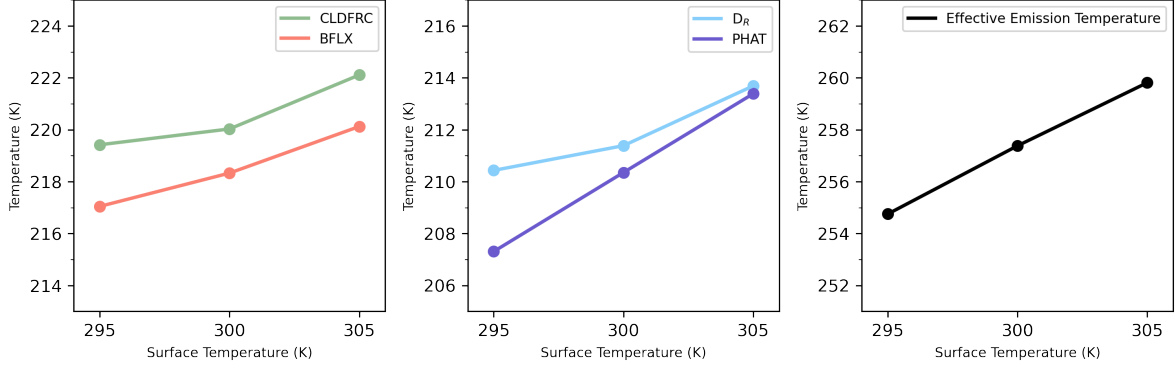


**Figure A.4:** **Left** Domain average temperature of maximum cloud fraction and the level where the buoyancy flux passes through zero. **Center** Domain average temperature where  $D_R$  is largest, and divergence-weighted temperature (defined in the text). **Right** Domain-average TOA brightness temperature.

sit nearly on top of one-another in temperature space, indicating that the buoyancy flux at a given atmospheric temperature changes by very little as the SST increases.

Using temperature as a vertical coordinate shows that as the atmosphere adjusts to a warmer adiabat, certain profiles expand to reach higher altitudes, but in such a way as to remain at approximately the same temperature. The profiles are not perfectly isothermal, but shift to slightly warmer temperatures, showing support for PHAT. This can be seen in the buoyancy flux, normalized cloud fraction, and normalized  $D_R$ . It can also be seen to a lesser degree in the radiative tendency, which shows a change in magnitude as the SST increases, changing the shape of the profile.

To evaluate the FAT and PHAT hypotheses, Fig. A.4 shows the change in temperature of several metrics as the SST increases. These include the maximum in cloud fraction, the maximum in  $D_R$ , and the level where the buoyancy flux passes through zero, all of which were discussed previously. Also included are the effective emission temperature at the top of the atmosphere, calculated using the Stefan-Boltzmann relation, and the divergence-weighted high cloud temperature, calculated as

$$T_{hc} = \frac{\sum_{T=270K}^{T=T_{min}} T \times D_R}{\sum_{T=270K}^{T=T_{min}} D_R}, \quad (\text{A.5})$$

following Zelinka and Hartmann (2010). In each of the panels in Fig. A.4, the horizontal and vertical axes are scaled to cover a range of 10 K.

For each of the quantities in Fig. A.4, the increase in temperature is smaller in magnitude than the increase in surface temperature, in line with the principles of the FAT hypothesis. However for certain quantities the increase in temperature approaches 50% of the increase in SST. This which would show support for PHAT over FAT. With these results in mind, a few important caveats should be mentioned.

The first is that the actual temperature of an anvil cloud is difficult to define. The definition implicitly used above is the temperature at the level where cloud fraction peaks, but the upper-level peak in cloud fraction is spread out in temperature space (see Fig. A.2). The top of the cloud fraction profile, with temperatures below 220K shifts to slightly warmer temperatures as the SST increases. This behavior is also seen in the profile of  $D_R$ , and is more consistent with PHAT than FAT.

The second caveat relates to the specific experimental setup used here. The vertical grid spacing is on the order of 1 km in the region of interest because of the high computational cost of performing simulations over an entire globe. Due to the dry conditions near the tropopause, the temperature lapse rate aloft approaches the dry adiabatic lapse rate of  $9.8 \text{ K km}^{-1}$ . This means that the accuracy of the values in Fig. A.4 is limited by the model resolution.

It is important to note that the upper-tropospheric quantities occur at temperatures ranging from 205 K to 225 K, while the effective TOA emission temperature occurs at a much warmer temperature near 255 K to 260 K. This is due to the fact that the cloud fraction is not unity. Even in regions of relatively high cloud fraction, a significant portion of radiation from lower levels escapes to space. This shows the limits of considering the effect of clouds on the domain as a whole, rather than on clear and cloud regions separately. The next section applies the column relative humidity analysis of previous chapters to the effects of upper-level clouds.

### **A.3 CRH Analysis for upper-level clouds**

Following the method of §2.2, the top row of Fig. A.5 shows contours of cloud fraction binned by the CRH, with temperature as the vertical coordinate. Each of the plots shows a local maximum

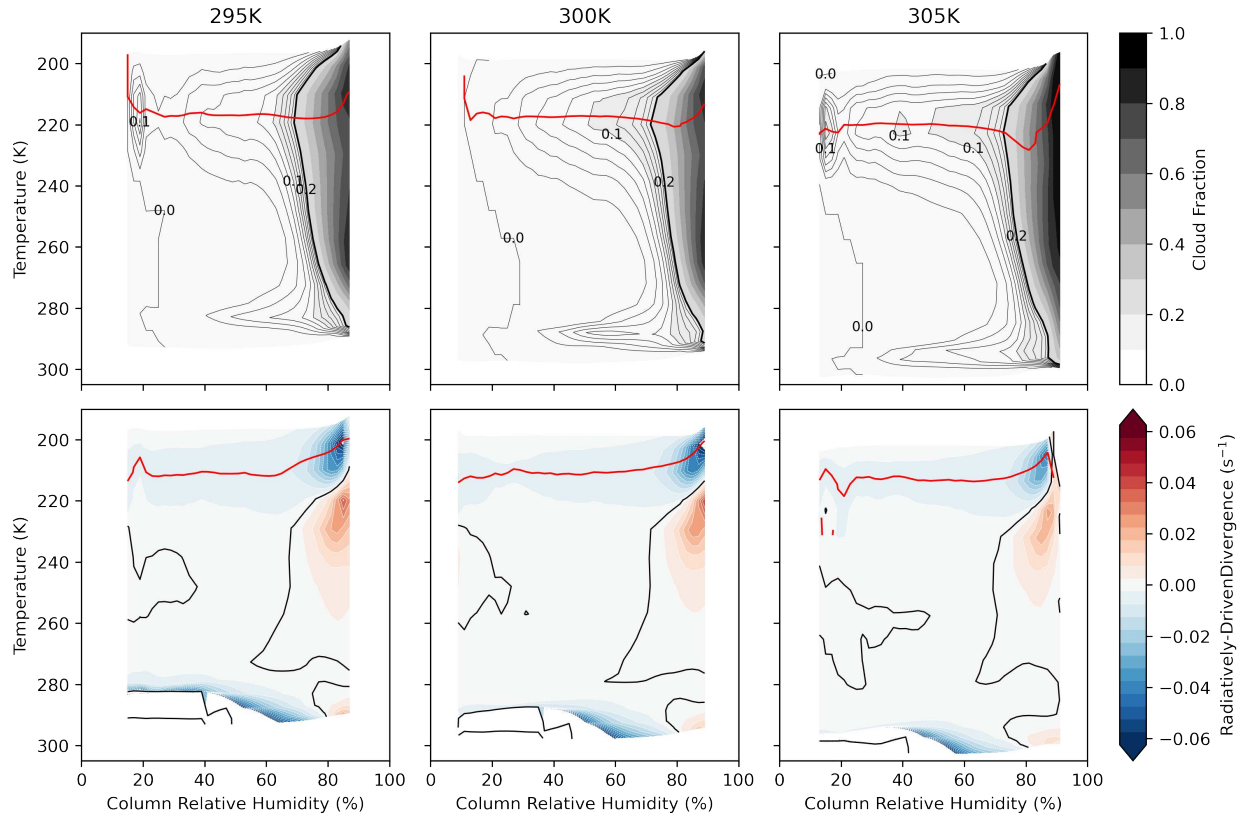


**Figure A.5: Top Row** Contours of cloud fraction binned by the CRH. Thin grey lines range from 0 to 0.2 with a spacing of 0.02, and the thick black line at a cloud fraction of 0.2. Shading ranges from 0 to 1 with a spacing of 0.1. The red line shows the level of maximum cloud fraction for each CRH bin. **Bottom Row** Contours of  $D_R$  computed with the full-sky longwave tendency with the black lines showing the zero contour and the red line showing the level of maximum  $D_R$ .

in the lower troposphere that shifts to warmer temperatures as the SST increases. The lower maximum can be interpreted as low-level stratus decks, or shallow cumuli that fail to break through a layer of convective inhibition. Each panel also shows a second, larger peak in the upper troposphere. The upper maximum, shown as the horizontal red line, is at approximately 220 K for each of the three simulations, consistent with the temperatures shown in Fig. A.4. This seems to show support for the principles of the FAT hypothesis. The panels also indicate, however, that the upper-level peak is not at a single level, but instead spans 10s of Kelvin in temperature space. In the most humid regions, the cloud fraction becomes larger and much more uniform with height. Each of the simulations still shows a maximum in the vicinity of 220 K, but this maximum is much less defined.

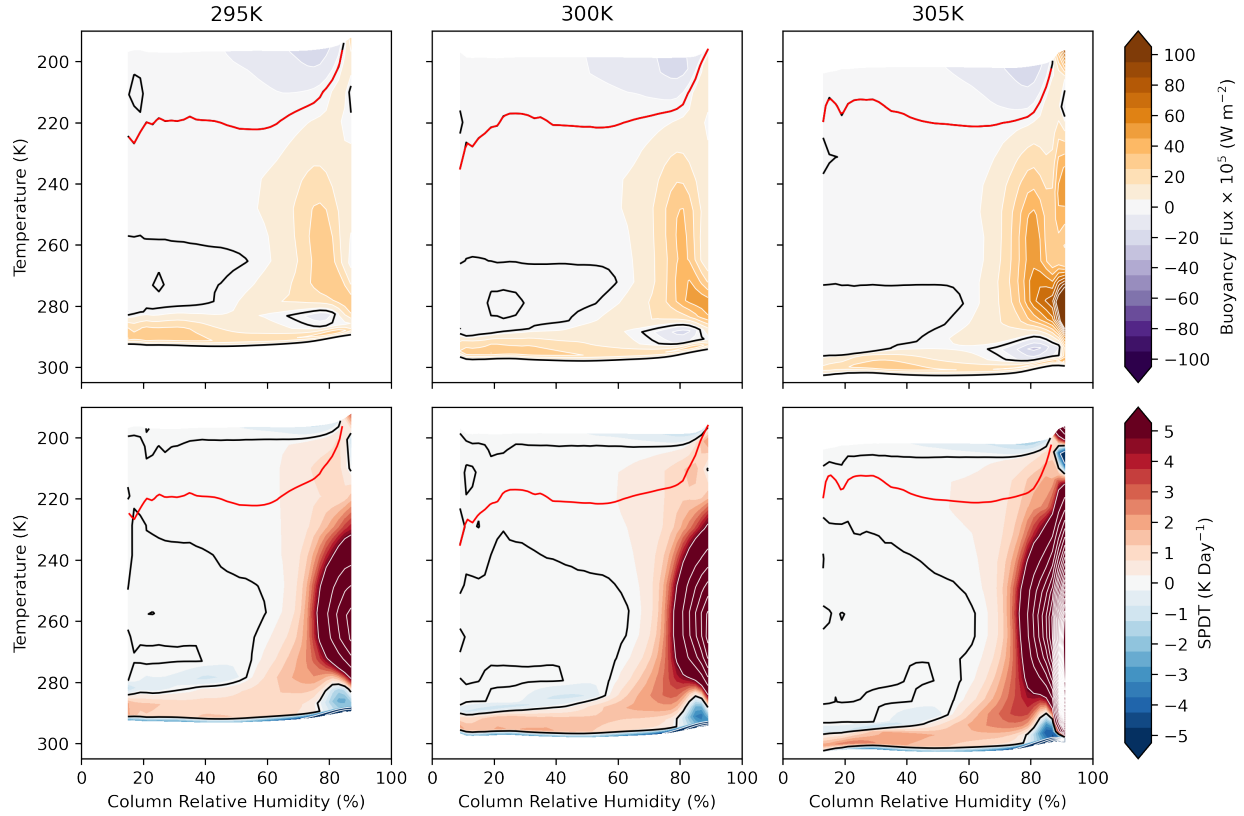


**Figure A.6: Top Row** Contours of buoyancy flux binned by the CRH. The red line shows the level where the buoyancy flux passes through zero for each CRH bin. **Bottom Row** Contours of SPDT (defined in the text) computed by the CRM. In these plots the red line again shows the level where the buoyancy flux passes through zero for each CRH bin

The bottom row of Fig. A.5 shows contours of the radiatively driven divergence, calculated using Eq. A.4 with the full-sky longwave tendency. Values near the surface for low CRH blow up and are masked because the static stability approaches zero, as seen in Fig. A.1, and the balance in Eq. A.2 cannot be expected to hold. Like the cloud fraction, the radiatively driven divergence shows a dependence on the CRH. In most of the domain the divergence is small, with a moderate peak in the upper troposphere. For regions of large CRH in the mid-to-upper troposphere, the divergence shows larger values of both positive and negative sign. The large negative values can be interpreted as enhanced divergence at the top of cloudy updrafts. The positive values, indicating convergence into cloudy regions due to radiative heating were unexpected, but may represent the effects of entrainment into the updrafts. However, later figures suggest that  $D_R$  may not be an relevant quantity in humid regions, as the non-radiative heating in Eq. A.2 becomes important.

The convergence results from a positive radiation tendency in extremely humid regions caused by strong ACRE, which was a central theme of Chapter 6. The red line shows the level of the upper-level maximum, and is near 210K for each simulation, consistent with Fig. A.4.

The top row of Fig. A.6 shows contours of the buoyancy flux. The red line in these plots shows the level where the buoyancy flux passes through zero, and is near 220 K in most of the domain for each simulation. This level, and the buoyancy flux more generally, shows a strong dependence on the CRH. The zero level occurs near 220 K between approximately 20% to 75% CRH, and then occurs at colder and colder temperatures in the extremely humid regions. In agreement with the observation from Chapter 6 that convective activity peaks near 80% CRH and declines for higher values, the buoyancy flux has a clear maximum near 80% CRH. The pocket of negative buoyancy flux just above the surface in humid regions can be interpreted as the result of convective inhibition working against deep convection. Another interesting feature of the buoyancy flux contours is the region of negative flux near the cold point. This would suggest that moist parcels overshoot their level of neutral buoyancy leading to a transport of cloud ice and a negative buoyancy flux above the neutral top of convective towers.

The bottom row of Fig. A.6 shows contours of SPDT, a field which encompasses the total non-radiative temperature tendency from the CRM (Jenney et al., 2020). SPDT includes the temperature tendency associated with phase changes of water, and is equivalent to  $\overline{C}$  in Eq. A.2. In the dry region the contours show that SPDT is small above the boundary layer. In the humid region, however, the contours show that SPDT becomes very strong, and reaches its largest values for the largest values of the CRH. As SPDT is clearly non-negligible here, the assumption leading to Eq. A.3 cannot be considered valid in the humid regions. The red line here shows where the buoyancy flux changes sign. This shows a non-negligible amount of non-radiative heating above the neutral top of convective updrafts, consistent with Kuang and Bretherton (2004).

From Figs. A.5 and A.6, the maximum in cloud fraction, in  $D_R$ , and the level where the buoyancy flux occur at similar temperatures to the corresponding quantities in Fig. A.4, although with some dependence on the CRH. This again shows evidence for the principles of the FAT

hypothesis. The following section investigates the FAT hypothesis in terms of the CRH in a more systematic way.

## **A.4 Links between SST, CRH, and Anvil Clouds**

Figs. A.7, A.8, and A.9 each show a similar set of plots, so it is worthwhile to take the time to explain them in full. The sets of contours for the cloud fraction, for  $D_R$  or for the buoyancy flux shown above in Figs. A.5 or A.6 contain a red line near 220 K representing the level of maximum cloud fraction, of maximum  $D_R$ , or the level where the buoyancy flux equals zero for each CRH bin. These lines directly correspond to three of the quantities shown in Fig. A.4. Each panel in the left column of Figs. A.7, A.8, and A.9 can then be understood as an extension to Fig. A.4. Where A.4 showed a single value for the temperature of the maximum cloud fraction for each SST, panel A of Fig. A.7 shows a single curve for the same quantity as a function of CRH for each of the RCEMIP simulations. Similar statements can be made about the level of maximum  $D_R$  and the level where the buoyancy flux passes through zero. In addition, complimentary plots are included to show the high cloud weighted temperature, and terms related to the effective emission temperature.

The center and right columns of Figs. A.7, A.8, and A.9 show the change in the quantity in the left column as the SST increases, in two different but related ways. For the panels in the center column the absolute change is shown, found by simply subtracting two of the curves from the panel in the left column. For the panels in the right column, the absolute change in the center column is divided by the change in SST between the two experiments to give the relative change. For example, the curve representing the change from 295 K to 300 K is found by subtracting the 295 K and 300 K curves in the first panel, and then dividing by 5 K to give the change in temperature per change in sea surface temperature.

### **A.4.1 Temperature changes in the upper troposphere**

Panel A of Fig. A.7 shows how the temperature of the maximum in cloud fraction depends on the SST for each CRH bin. The curves confirm that this level is near 220 K for each simulation,

although the level for the 305 K simulation is somewhat warmer than the other two. In the dry region (to the left of the vertical line at 70% CRH), the temperature of maximum cloud fraction is nearly independent of the CRH. In humid region of the domain the temperature shows more complicated behavior, reaching a maximum near 80% CRH before rapidly decreasing with CRH.

Panels B and C show the absolute and relative change in the temperature of maximum cloud fraction as the SST increases. The panels show that in the dry regions, the temperature of the maximum cloud fraction increases by less than 2 K from 295 K to 300 K, less than 3 K from 300 K to 305 K, and by less than 4 K for the larger change from 295 K to 305 K. This corresponds to an increase in the temperature of the maximum level of cloud fraction by less than 60% of the change in surface temperature across the three simulations. In the case of the shift from 295 K to 300 K, this relative change is less than 20% in most of the clear domain.

It is interesting to note that the temperature change is larger in the humid regions than in the dry regions. As seen in Fig. A.5, the cloud fraction in the humid regions is nearly independent of height, so the concept of a maximum in cloud fraction becomes less meaningful. Additionally, the large non-radiative heating (shown in Fig. A.6 with the contours of SPDT) indicates that the assumptions leading to FAT are not valid in the humid region. Then, an alternative mechanism is required to determine what controls the temperature of upper-level clouds.

Panels D-F of Fig. A.7 show the temperature at the level where  $D_R$  is largest. Like the maximum in cloud fraction, the  $D_R$  curves show some dependence on CRH, occurring near 210 K in the dry regions. The curves then shift to cooler temperatures as CRH increases in the humid regions. The absolute and relative temperature changes are more complicated for  $D_R$  than for the cloud fraction. From 295 K to 300 K (yellow) and from 295 K to 305 K (purple), the temperature of the maximum of  $D_R$  increases more in the humid regions, following the pattern of the maximum in cloud fraction. From 300 K to 305 K the largest increase in temperature occurs near the 70% line that separates the dry and humid regions.

Next, Eq. A.5 was used with the contours of  $D_R$  to calculate the divergence weighted high cloud temperature of Zelinka and Hartmann (2010). As this value is meant to be a measure of the temperature of anvil clouds formed through divergence from cloudy updrafts, positive values of

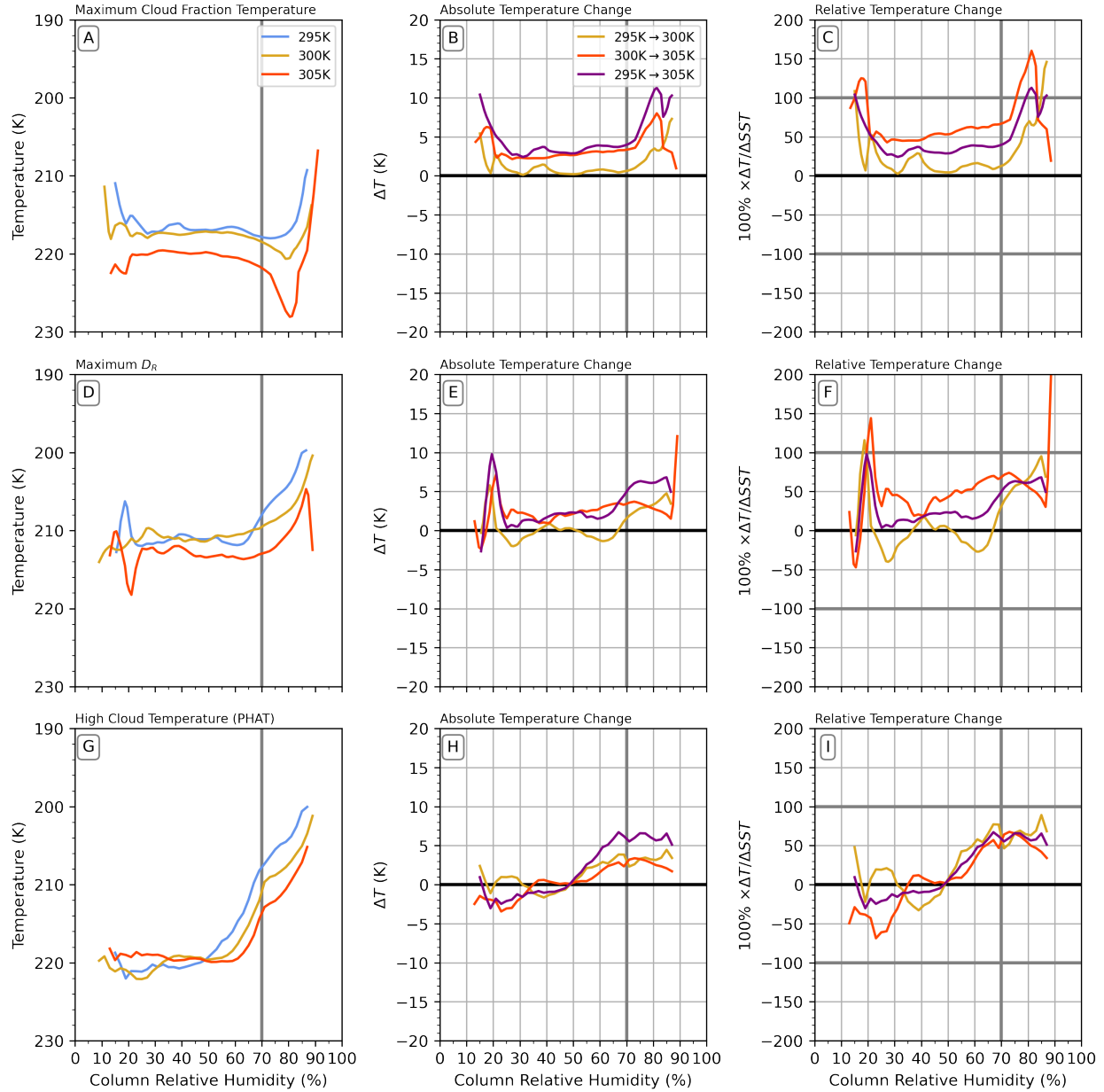


**Figure A.7:** **Panel A** The temperature of the level of maximum cloud fraction in each CRH bin for each RCEMIP simulation. **Panel B** The change in temperature of the maximum cloud level for each set of simulations. **Panel C** Same as **Panel B**, but divided by the change in SST between simulations. **Panels D-F** and **G-I** same as **Panels A-C**, but for the temperature of the maximum of  $D_R$ , and the high cloud temperature (defined in the text), respectively.

$D_R$  (representing convergence) are omitted by setting their values to zero for the calculation. The curves of the high cloud temperature are shown in the bottom row of Fig. A.7.

Like the temperature of the maximum in cloud fraction, the divergence weighted temperature is near 220 K in most of the domain. However, the curves shift to cooler temperatures as the CRH

increases, to coincide with the peak in  $D_R$  in these regions. When looking at the difference plots, the relative change shows some dependence on CRH in the dry regions, increasing approximately linearly from 50% to 70% CRH. In the humid region, the relative change is approximately 60% of the change in SST for each set of simulations. Interestingly, the difference plots are fairly consistent between the three simulations, if somewhat noisy.

Taken together, the increase in the temperature of the maximum cloud fraction, the temperature of the maximum of  $D_R$ , and the divergence-weighted temperature show support for PHAT, rather than FAT. Fig. A.7 illustrates that changes in high clouds (and related changes such as cloud feedbacks) will not be spatially uniform in a warmer climate. Instead, these changes will have different impacts in humid regions and in dry regions. To better understand how changes in these quantities impact the radiation balance at the top of the atmosphere, the next section performs a similar analysis to that seen in Fig. A.7 for the top of atmosphere brightness temperature.

#### A.4.2 Changes in the TOA Brightness Temperature

A main conclusion of Chapter 3 was that cloud radiative effects showed a strong dependence on CRH and were largely, but not completely, independent of the surface temperature. In the context of the FAT hypothesis, we now revisit the longwave CRE in terms of the brightness temperature.

Fig. A.8 shows the effective emission temperature at the TOA, with the temperature axis oriented to show temperature as a vertical coordinate, as in Figs. A.3. The emission temperature was computed using the Stefan-Boltzmann relation as

$$T_B = \left( \frac{\text{OLR}}{\sigma_B} \right)^{\frac{1}{4}}, \quad (\text{A.6})$$

where  $\sigma_B = 5.67 \times 10^{-8} \text{ Wm}^{-2}\text{K}^{-4}$  is the Stefan-Boltzmann constant, and OLR is the outgoing longwave radiation at the top of the atmosphere. Also shown in Fig. A.8 are the clear-sky emission temperature, calculated as in Eq. A.6, and the difference in clear-sky and full-sky emission temperatures. This final term is called the cloud temperature effect (CTE), in direct analogy to the cloud radiative effect, which is calculated using a nearly identical procedure. The CTE can be

thought of as a form of the cloud radiative effect expressed in terms of a temperature rather than a radiative forcing.

The two brightness temperatures and the CTE increase approximately linearly with CRH in the drier part of the domain. As the CTE is small here, this is mostly caused by decreases in the clear-sky temperature, which shifts upwards with CRH due to an increase in water vapor. In the humid region, the effective emission temperature begins to increase rapidly with CRH, while the clear-sky emission temperature continues to increase with approximately the same slope. In the dry region, both the full-sky and clear-sky emission temperatures correspond to levels in the middle troposphere. In the humid region, the clear-sky temperature remains in the mid troposphere while the full-sky temperature rapidly shifts to the upper troposphere. As seen in Fig. A.5, the cloud fraction becomes large in the humid region, so the effective emission temperature is increasingly determined by clouds.

When looking at the difference plots, the contrast between the dry and humid regions is pronounced. In the dry region, the full-sky emission temperature changes by less than 4 K or about 40% of the change in SST for all of the simulations, with slightly larger values for the clear-sky emission temperature. In the humid region, the full-sky emission temperature increases by more than double the increase in the SST. This is in contrast to the differences in the clear-sky temperatures, which show a kink at 70% CRH and change by less than 50% of the change in SST.

The full-sky and clear-sky emission temperatures correspond to temperature levels in the troposphere, so the CTE can be thought of as a distance in temperature space between the two emission temperatures. In dry regions the CTE is small, while it is large in humid regions. The reasons for this were discussed in the main text in Chapter 3, which found that the CRE was small in the dry region and large in the humid region.

Like the full-sky emission temperature, the difference plots for the CTE show qualitatively different behavior in the dry and saturated regions. In the dry region the change in CTE is near zero or positive. This indicates that as the SST increases, the full-sky and clear-sky emission temperatures are moving further apart. The difference curves for the CTE change sign near the threshold between dry and humid regions, and become strongly negative in the humid regions.

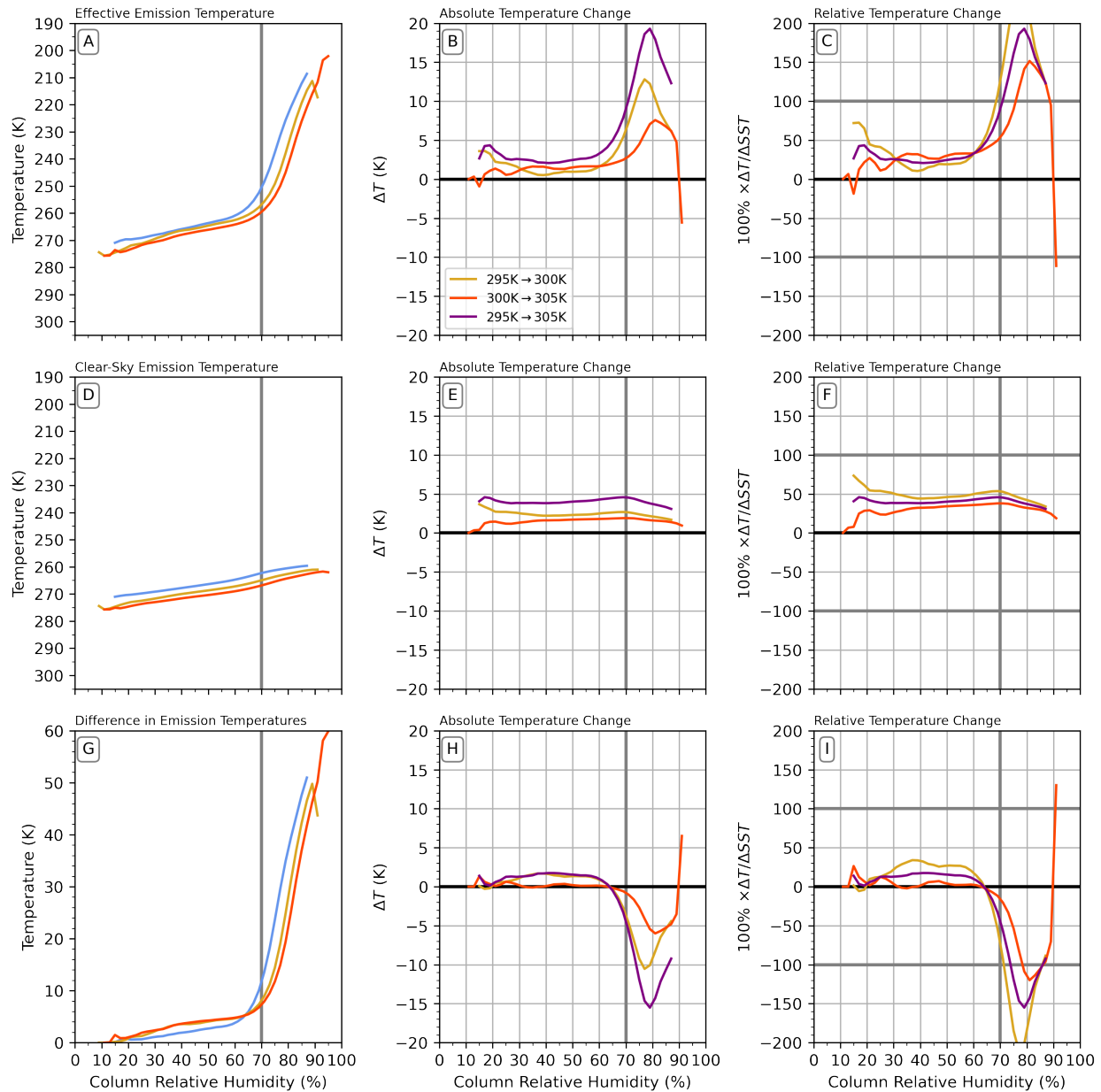


**Figure A.8:** Same as Fig. A.7, but for the **Top Row** full-sky emission temperature, **Middle Row** clear-sky emission temperature, and **Bottom Row** the CTE (defined in the text).

The negative change can be interpreted as the full-sky and clear-sky emission temperature moving closer together as the surface warms.

As the SST increases and the troposphere expands to adjust to a more stable adiabat, the clear-sky and full-sky emission temperatures move at different rates. In the dry region, the clear-sky emission temperature warms faster than the full-sky temperature, increasing the distance between

the two. However in the saturated region the opposite occurs. The full-sky emission temperature warms faster than the clear-sky temperature, working to decrease the distance between the two levels.

In the next section, the FiTT hypothesis of Seeley et al. (2019) is investigated briefly using the same analysis framework as earlier sections of this Appendix.

### **A.4.3 The Temperature of the Tropopause**

Lastly, Fig. A.9 shows the temperature at the full-sky and clear-sky “radiative tropopause,” the level where the longwave cooling passes through zero. In idealized simulations of RCE, Seeley et al. (2019) found that the radiative tropopause was nearly isothermal over the range of surface temperatures they investigated.

In these simulations of RCE, Fig. A.9 shows that the temperature of the radiative tropopause is largely independent of CRH in the dry region, before shifting to cooler temperatures in the humid region. The temperature of the radiative tropopause does show a noticeable change with SST for most values of the CRH, of a similar magnitude to the change in the temperature of the maximum cloud fraction. The radiative tropopause calculated with the full-sky longwave tendency is included for completeness although it behaves nearly identical to the clear-sky value. The full-sky curves stop abruptly at 75% CRH because the full-sky tendency does not pass through zero aloft in the saturated region.

FiTT was proposed as part of a larger critique of the FAT hypothesis, so it is worth evaluating the empirical evidence for both hypotheses in these simulations. In contrast to Seeley et al. (2019), the tropopause temperature increases as the surface warms in the RCEMIP simulations, at a similar rate as many of the other fields investigated. As Seeley et al. (2019) did not provide a mechanism to account for a FiTT, the results here suggest that the isothermal radiative tropopause found in their simulations may be attributed to the particular model configuration, rather than to some underlying physics. This is in contrast to FAT, which relies on a stronger theoretical foundation.

Additionally, the existence of a FiTT would not necessarily disprove a PHAT. In fact, there is no *a priori* reason to believe a FiTT and a PHAT are mutually exclusive. In the absence of

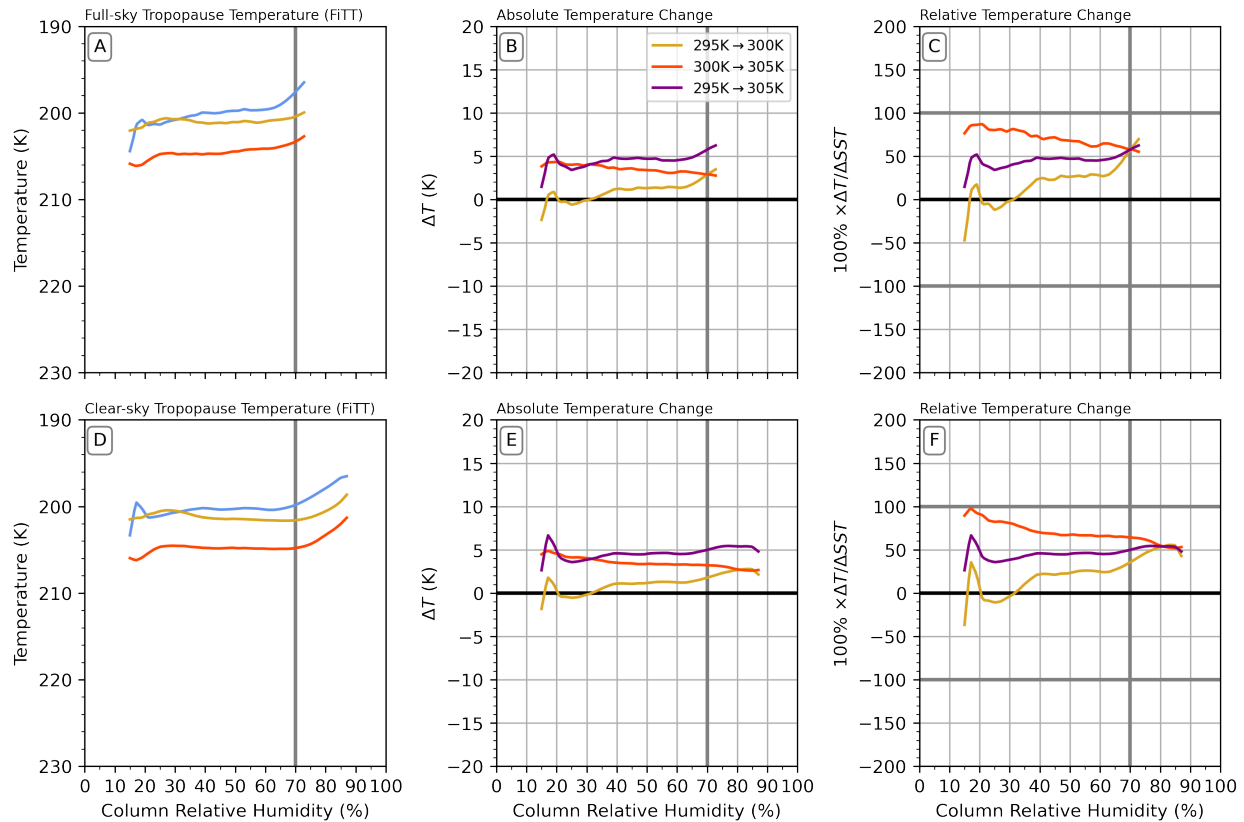


**Figure A.9:** Same as Fig. A.7, but for the **Top Row** full-sky radiative tropopause, and **Bottom Row** the clear-sky radiative tropopause.

a physical mechanism for a FiTT, the analysis here supports previous conclusions that the FAT hypothesis is still a useful conceptual tool for understanding the vertical structure of convective clouds in a warmer climate. Even so, the necessity of PHAT to account for the changes in stability indicate that the FAT hypothesis alone is not enough to fully predict future changes.

## A.5 Conclusions

In this appendix, various aspects of the FAT and PHAT hypotheses were investigated in the RCEMIP simulations used throughout the main text. Averaged over the entire domain, the temperature at the level of maximum cloud fraction, at the level of radiatively driven divergence, and the level where the buoyancy flux passed through zero each increased as the surface warmed. This increase was smaller than the magnitude of the SST, consistent with PHAT rather than FAT. The divergence weighted high cloud temperature increased from approximately 207 K in the 295 K

simulation to 210 K and 213 K in the 300 K and 305 K simulations, respectively. However the clearest argument for PHAT comes from a simple look at Fig. A.2, or the cloud fraction contours in Fig. A.5. As the surface warms, the buoyancy flux, cloud fraction, and  $D_R$  all shift to higher altitudes, but in such a way that the profiles are nearly on top of one-another. This is a change that is difficult to capture in a single metric, but is evident from a simple visual investigation of the plots. A shift to slightly warmer temperatures is evident from comparing the 295 K and 305 K curves, but the profiles are very similar across simulations.

Next, the CRH framework was used to investigate empirically how FAT and PHAT performed in dry and humid regions. Consistent with the main text, there was a qualitative difference between the dry and humid regions. In general, the relevant quantities changed by a larger magnitude in the humid region than in the dry region, suggesting that the principles of FAT are only relevant in regions with CRH less than 70%. In the dry regions, the temperature of maximum cloud fraction increased by less than 60% as the surface warmed. However the cloud temperature effect, a measure of the cloud radiative effect in terms of temperature, increased by a smaller value of 20% to 40% as the surface warmed.

Contour plots showing the dependence of non-radiative heating (SPDT) on CRH provide an explanation for the different behavior of the CTE in humid and dry regions. This is because a large amount of non-radiative heating in humid regions suggests that the theoretical arguments leading to FAT may no longer apply. Lastly, the FiTT hypothesis of Seeley et al. (2019) was investigated using the CRH framework. Contrary to results from their paper, the level where radiative heating passed through zero was no more fixed than any of the other fields investigated.

## Appendix B

### Influence of ENSO on the CRE estimated from CRH

The ENSO composite analysis of Chapter 4 found evidence for a relationship between ENSO phase and the shortwave CRE estimated from the CRH in the east Pacific. Specifically, the CRH method was found to more skillfully estimate the shortwave CRE during an El Niño event compared to a La Niña. This Appendix repeats the ENSO analysis of the main text for the longwave and shortwave CRE in the east Pacific (150°W-90°W), west Pacific (150°E-150°W), and Indian Ocean (50°E-110°E) regions. Results show that the correlation for the longwave and shortwave CRE is largest for the east Pacific during El Niño, while it is largest for the west Pacific during La Niña. The analysis shows no obvious link between ENSO phase and estimation accuracy for the Indian Ocean region, but is included for completeness.

The procedure here is identical to the procedure in §4.3.2. First, the CRE estimated from CRH was spatially averaged over each of the three subset regions to give a time series of monthly mean values. This time series was then compared to the time series of the regionally averaged CRE calculated from satellite observations, with the comparison evaluated using Pearson's  $R^2$  correlation. Next, the two time series were sorted into three categories representing the El Niño, neutral, or La Niña phase of the El Niño-Southern Oscillation (ENSO, see §2.1.4). The sorting was achieved by mapping the two time series onto the time series of the Oceanic Niño Index (ONI). Then, the correlation was evaluated for subsets of each time series. The subsets were collected by taking only the values that occurred during a particular phase or phases of ENSO. The collections included one set representing the entire record, two subsets that joined the neutral and Niño or neutral and Niña phases, and then each of the three phases alone.

#### B.1 East Pacific

Fig. B.1 shows the correlation between the actual and estimated shortwave CRE in the east Pacific region for each of the six ENSO subsets. The figure was originally included in Chapter 4 as

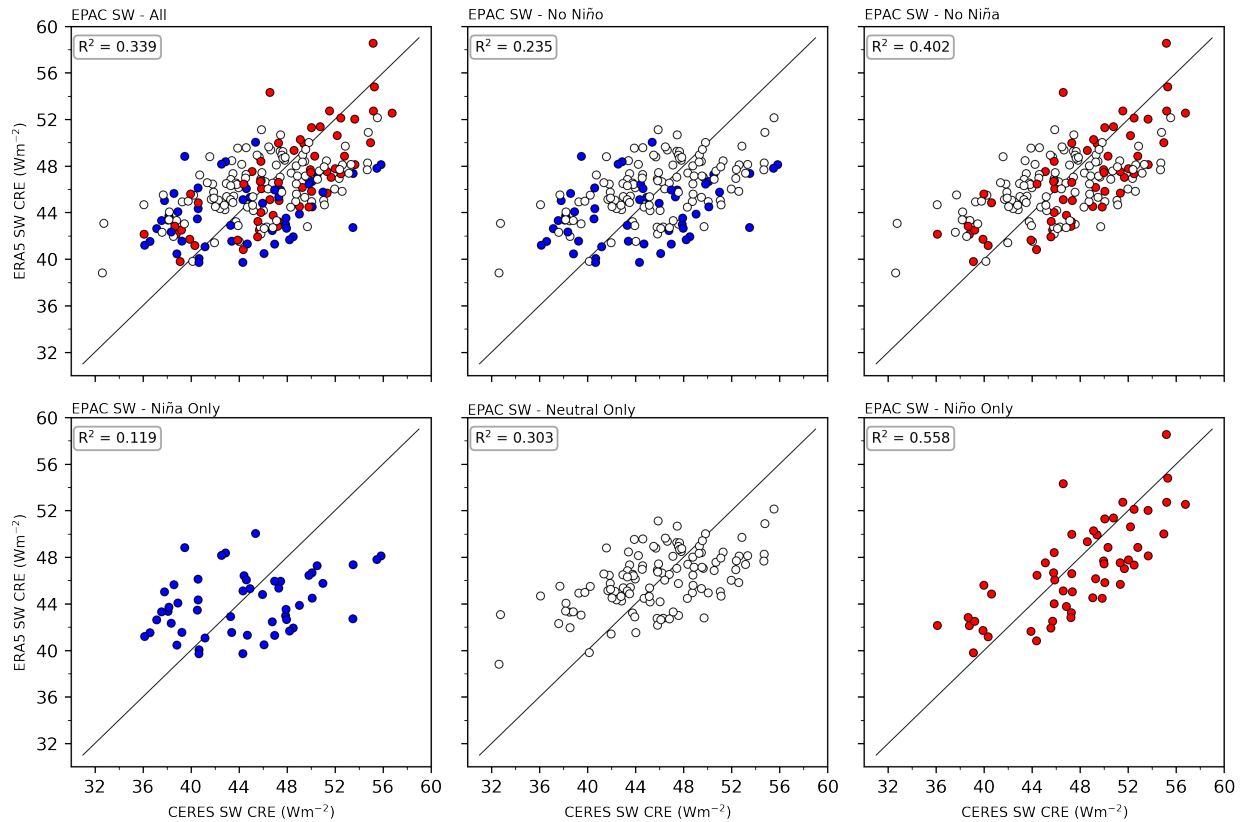


**Figure B.1:** Scatter plot composite analysis comparing actual and estimated shortwave CRE in the EPAC region, for different ENSO states. Figure repeated from Fig. 4.11

Fig. 4.11, but is repeated here for easier comparison with later figures. As mentioned in the main text, the figure shows that the correlation between estimated and actual shortwave CRE in the east Pacific is largest during El Niño and is smallest during La Niña. This was attributed to an increase in deep convection in the east Pacific associated with the warmer SSTs of El Niño. Conversely, the cooler SSTs associated with La Niña lead to an increase in the low stratus clouds that have been identified repeatedly as problematic for estimating the CRE from the CRH (see Chapter 4 and especially Fig. 4.4). The difference in the correlation for the shortwave CRE in the east Pacific is the largest of the six cases examined in this Appendix, which is why it was the only case included in the main text.

Next, the correlation between actual and estimated longwave CRE is shown in Fig. B.2 for the east Pacific. During El Niño the correlation is very good ( $R^2 > 0.85$ ). This again is likely due to an increase in deep convection during El Niño, as deep convective clouds with large CRE are

represented well by the CRH estimation method. The correlation is lower for the neutral phase ( $R^2 = 0.586$ ) and Niña phase ( $R^2 = 0.562$ ) but still represents a skillful estimation of the CRE from the CRH.

Interestingly, Fig. B.2 shows that the CRH method systematically overestimates the longwave CRE when the CRE is low in the east Pacific. The agreement becomes better when the observed CRE is larger, but still shows an overestimation. As mentioned in the main text, this may be related to the work of Kubar et al. (2007), who showed that anvil clouds are systematically warmer in the east Pacific than in the west Pacific by about 5 K. All else equal, this would lead to a lower CRE in the east Pacific than in the west Pacific as anvils would emit to space at a warmer temperature in the east Pacific. The CRH method was developed using data averaged over the entire belt from 30°S-30°N, and is thus unable to account for these type of regional differences. Perhaps the method could be improved if it were more localized and took into account regional differences in the curves of CRE versus CRH.

## B.2 West Pacific

Figures corresponding to Figs. B.1 and B.2 are shown in Figs. B.3 and B.4 for the west Pacific region. Broadly, the opposite conclusions can be drawn for the west Pacific than those for the east Pacific. While the correlation in both the longwave and shortwave was largest in the east Pacific during El Niño, the correlation was smallest in the west Pacific during El Niño.

In the shortwave, Fig. B.3 shows that the correlation during the Niño phase ( $R^2 = 0.381$ ) is lower than for the neutral phase ( $R^2 = 0.625$ ) or the Niña phase ( $R^2 = 0.619$ ). Similarly, the longwave CRE in Fig. B.3 shows a lower correlation during Niño months ( $R^2 = 0.265$ ) than during either neutral or Niña months ( $R^2 = 0.58$  and  $R^2 = 0.596$ , respectively). Compared to the explanation in the east Pacific that focused on stratus clouds, the physical explanation for this difference remains unclear in the west Pacific.

Comparing Figs. B.1-B.4 reveals that the CRH estimation method behaves differently during El Niño than during the neutral and Niña phases in both the east and west Pacific. In the east

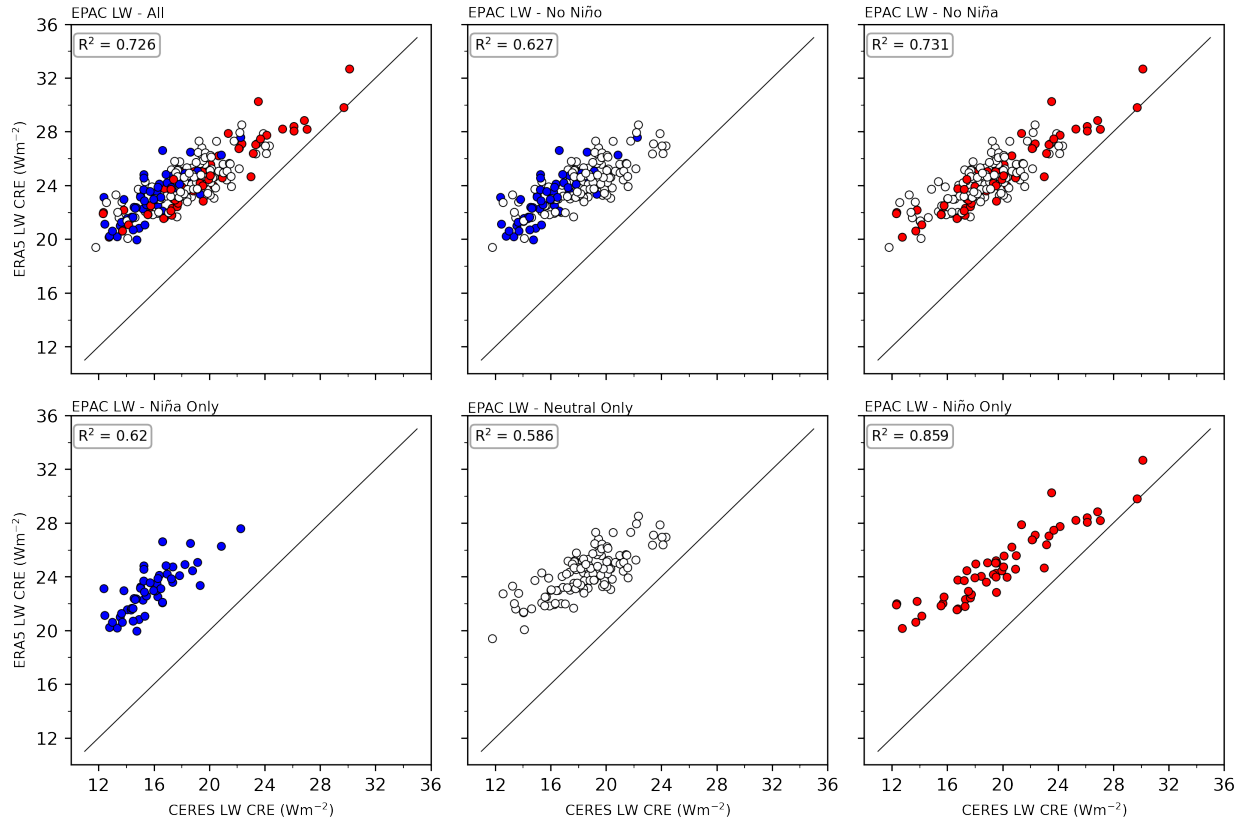


**Figure B.2:** Same as Fig. B.1, but for the longwave CRE in the EPAC region.

Pacific, El Niño increases the accuracy of the estimation compared to mediocre results during the other phases. In the west Pacific, El Niño decreases the accuracy of the estimation instead.

### B.3 Indian Ocean

Figs. B.5 and B.6 show the correlation between estimated and actual CRE in the Indian Ocean region, calculated in the same way as the previous figures. The figures show similar values for the  $R^2$  correlation for El Niño and La Niña months. In both figures the neutral phase has a somewhat lower  $R^2$  value than either of the other two phases. This may simply be a result of sampling bias, but other explanations cannot be ruled out.

In contrast to the east and west Pacific regions, there is no apparent link between the ENSO phase and the accuracy of the CRE estimation in the Indian Ocean. This is not altogether surprising, as the Indian Ocean is removed spatially from the Pacific cold tongue region, and is dominated

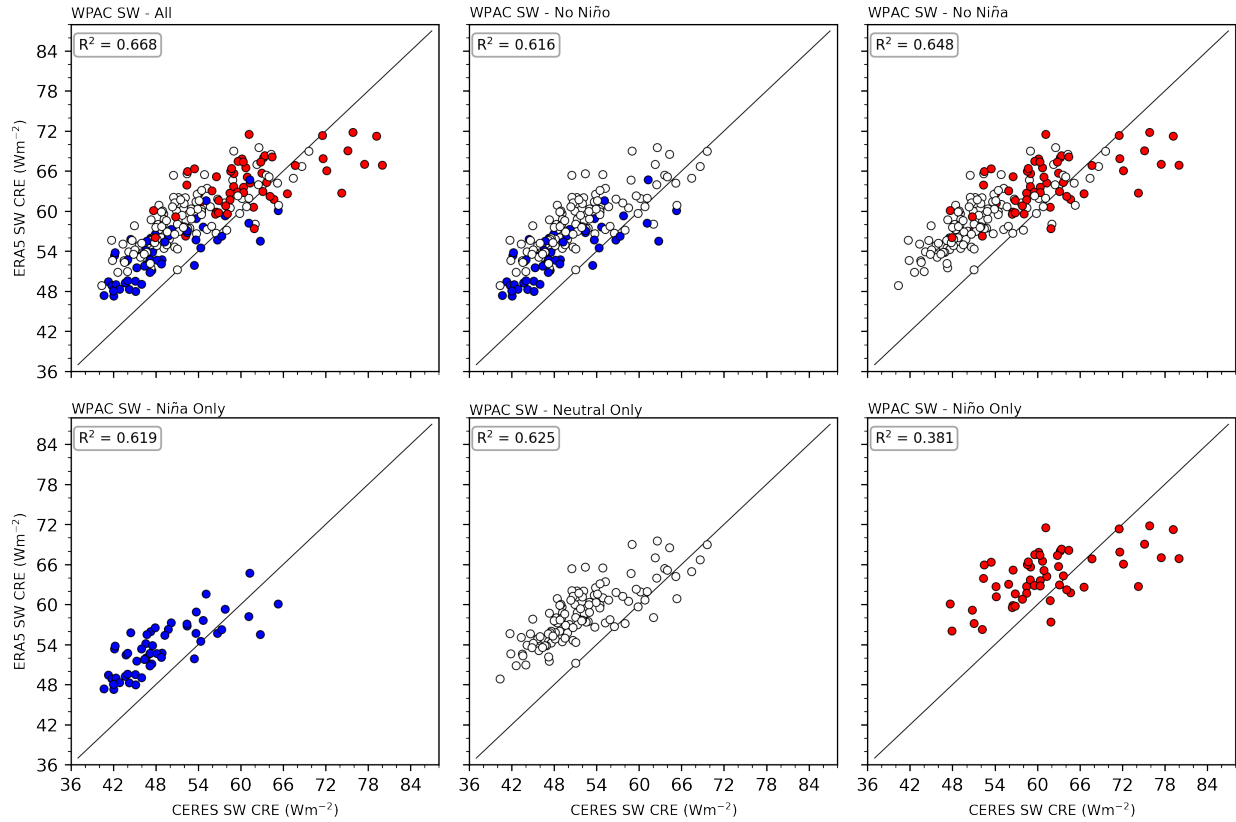


**Figure B.3:** Correlation between actual and estimated shortwave CRE in the WPAC region, as in Fig. B.1

instead by the Madden-Julian Oscillation (MJO, Madden and Julian (1971)). However, as the MJO is associated with alternating phases of enhanced and suppressed convection over the Indian Ocean and other regions, it seems plausible that a composite analysis like the ENSO analysis investigated here may uncover a link between the MJO and the estimation of CRE in the Indian Ocean. This is left for future work.

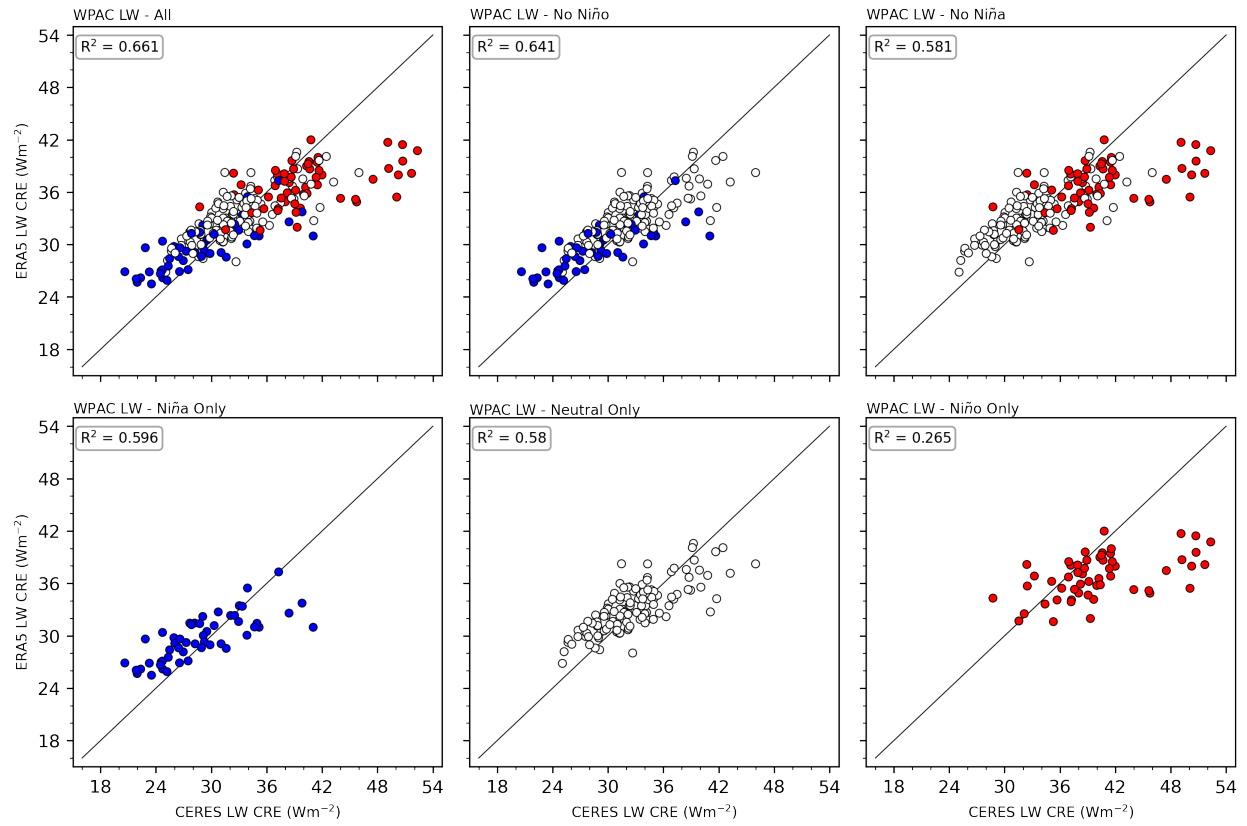


**Figure B.4:** Same as Fig. B.2, but for the longwave CRE in the WPAC region.

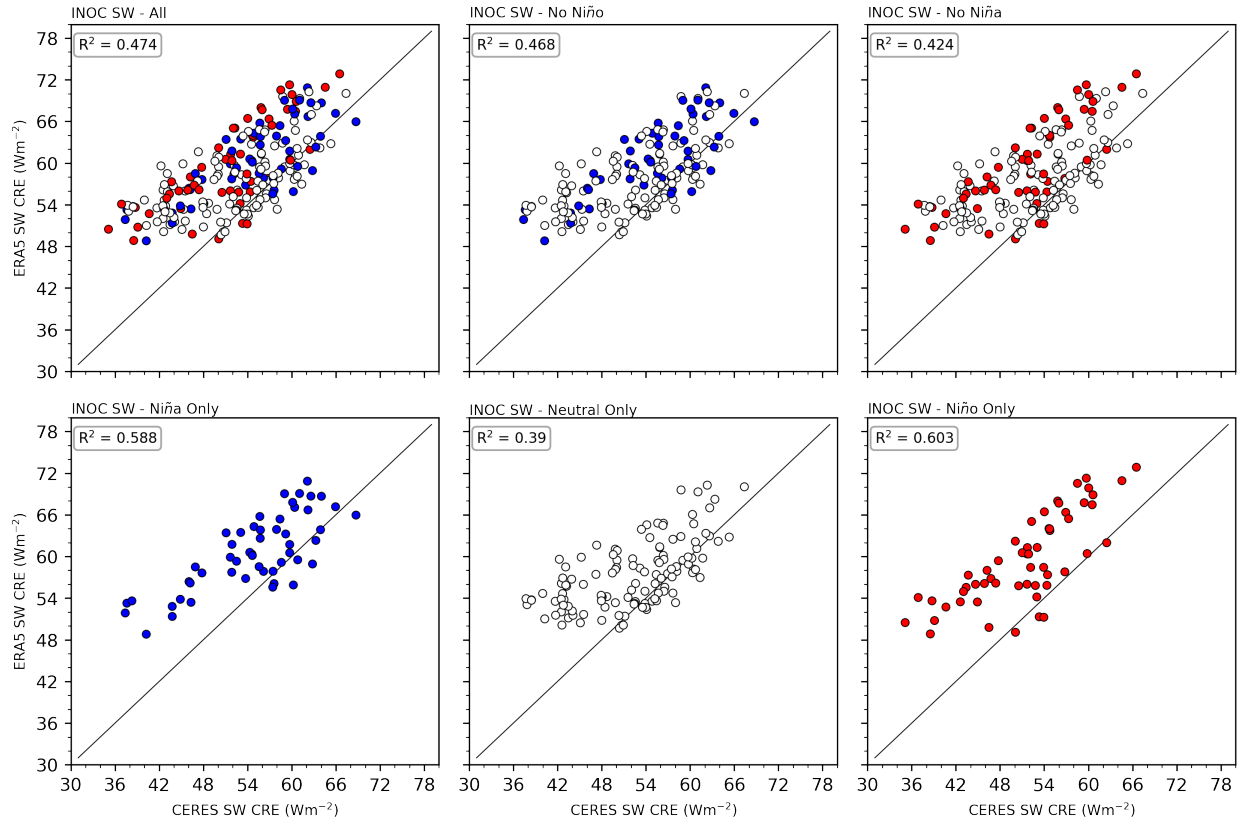


**Figure B.5:** Same as Fig. B.2, but for the shortwave CRE in the INOC region.

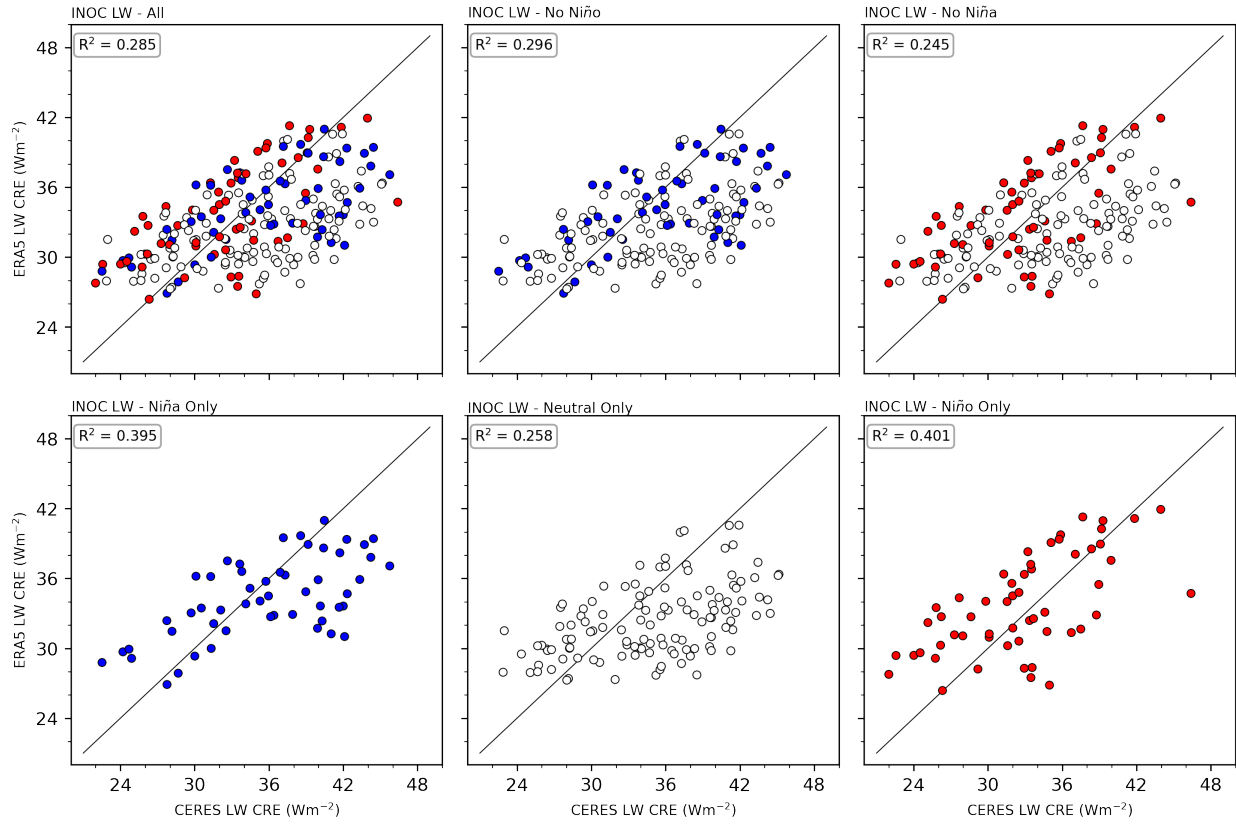


**Figure B.6:** Same as Fig. B.2, but for the longwave CRE in the INOC region.

# Appendix C

## Comparison of latitude limits for AQPJAN

### experiments

In Chapter 7, calculations from previous chapters were repeated using model output from a set of three simulations that were more realistic than the idealized RCEMIP simulations. These aquaplanet simulations (AQPJAN, described in §2.1.2) were forced by idealized SST distributions derived from ERA5 reanalyses of 2 meter temperatures for the month of January. As part of the analysis in Chapter 7, only the equatorial region (10°S-10°N) was used. The 10° cutoff was chosen to isolate the extremely humid regions associated with the ITCZ, but was ultimately an arbitrary threshold. Here, a few calculations from Chapter 7 are repeated after extending the AQPJAN region to 30°S-30°N. These are included to show that the results from the AQPJAN simulations are not overly sensitive to the choice of the latitude threshold.

First, Fig. C.1 shows the CRH distributions for each of the three RCEMIP simulations, and for each of the AQPJAN simulations with 10° and 30° cutoffs. In general, the AQPJAN simulations bounded by 30° (hereafter AQPJAN30) are more similar to the corresponding RCEMIP simulation

**Table C.1:** Summary statistics as in Tbl. 7.1, but also comparing the 10° and 30° latitude limits for both the AQPJAN experiments and for the ERA5 distribution.

	<b>Mean</b>	<b>Standard Deviation</b>	<b>Skewness</b>	<b>Mode</b>
<b>295 K AQPJAN 10°</b>	70.58%	8.64	-0.63	74.25%
<b>295 K AQPJAN 30°</b>	60.58%	13.71	-0.28	69.25%
<b>295 K RCEMIP</b>	60.75%	11.95	-0.49	64.75%
<b>300 K AQPJAN 10°</b>	71.92%	9.08	-0.63	75.25%
<b>300 K AQPJAN 30°</b>	61.29%	14.11	-0.27	70.75%
<b>300 K RCEMIP</b>	59.91%	15.08	-0.45	69.25%
<b>305 K AQPJAN 10°</b>	73.36%	10.04	-0.71	77.75%
<b>305 K AQPJAN 30°</b>	60.99%	14.9	-0.14	57.25%
<b>305 K RCEMIP</b>	59.38%	15.13	-0.26	71.25%
<b>ERA5 10°</b>	65.03%	14.96	-0.56	76.75%
<b>ERA5 30°</b>	54.29%	19.3	-0.17	75.25%

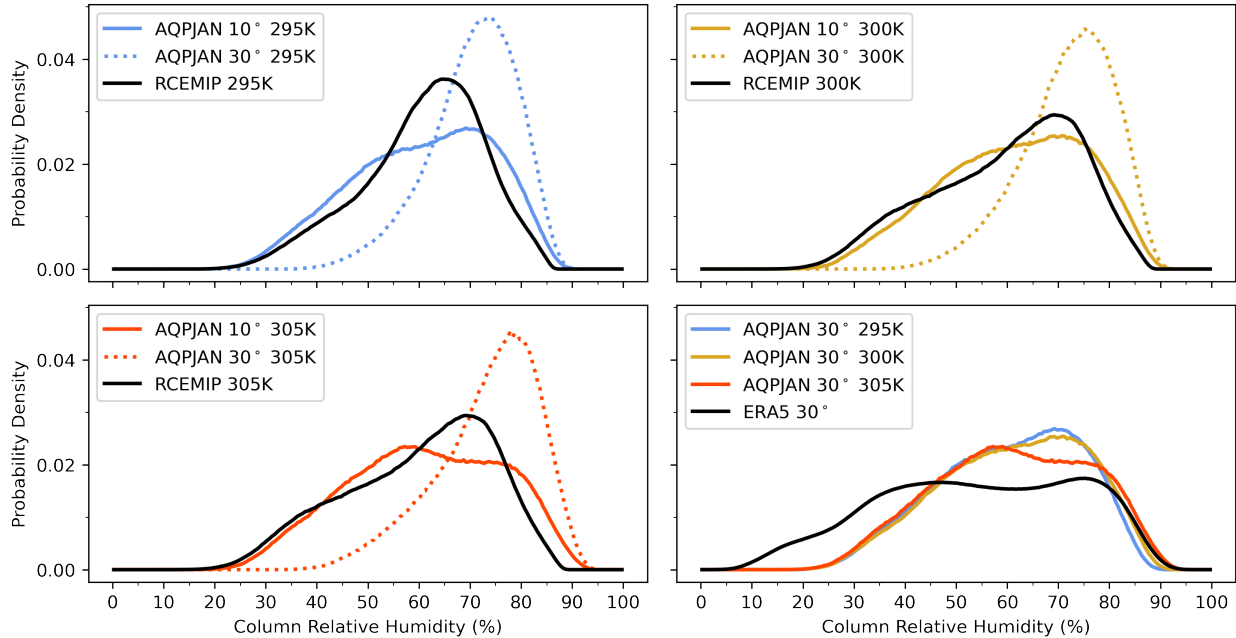


**Figure C.1:** CRH distributions for each set of RCEMIP, AQPJAN10, and AQPJAN30 data. The bottom right panel compares the AQPJAN30 data to the ERA5 CRH distribution bounded by 30°S-30°N.

than to the AQPJAN simulations bounded by 10° (AQPJAN10). The distributions for the AQPJAN10 data are dominated by the effects of the ITCZ and do not include the subtropical dry regions associated with the subsiding branches of the Hadley cells (see Chapter 7, and especially Fig. 7.3). The distributions for the AQPJAN30 data, by contrast, include a wider range of SSTs and dynamic conditions, leading to the wider range of CRH values shown in the figure. Tbl. C.1 shows summary statistics for the distributions in Fig. C.1. In addition, summary statistics are shown for the CRH distribution calculated from ERA5 reanalyses, using the same 10° and 30° cutoffs.

## C.1 Cloud radiative effects versus column relative humidity

Cloud radiative effects for the AQPJAN30 data were binned by CRH following the method in §2.2 to give Fig. C.2, which shows the CRE at TOA and surface, as well as ACRE as a function of CRH. Like earlier results shown in Figs. 3.3, 3.7, and 7.6, Fig. C.2 further supports the result that the CRE as a function of CRH is largely independent of the SST. In addition, the now-familiar “kink” at 70% CRH is an obvious feature of several of the curves, separating dry regions with small CRE from humid regions with large CRE.

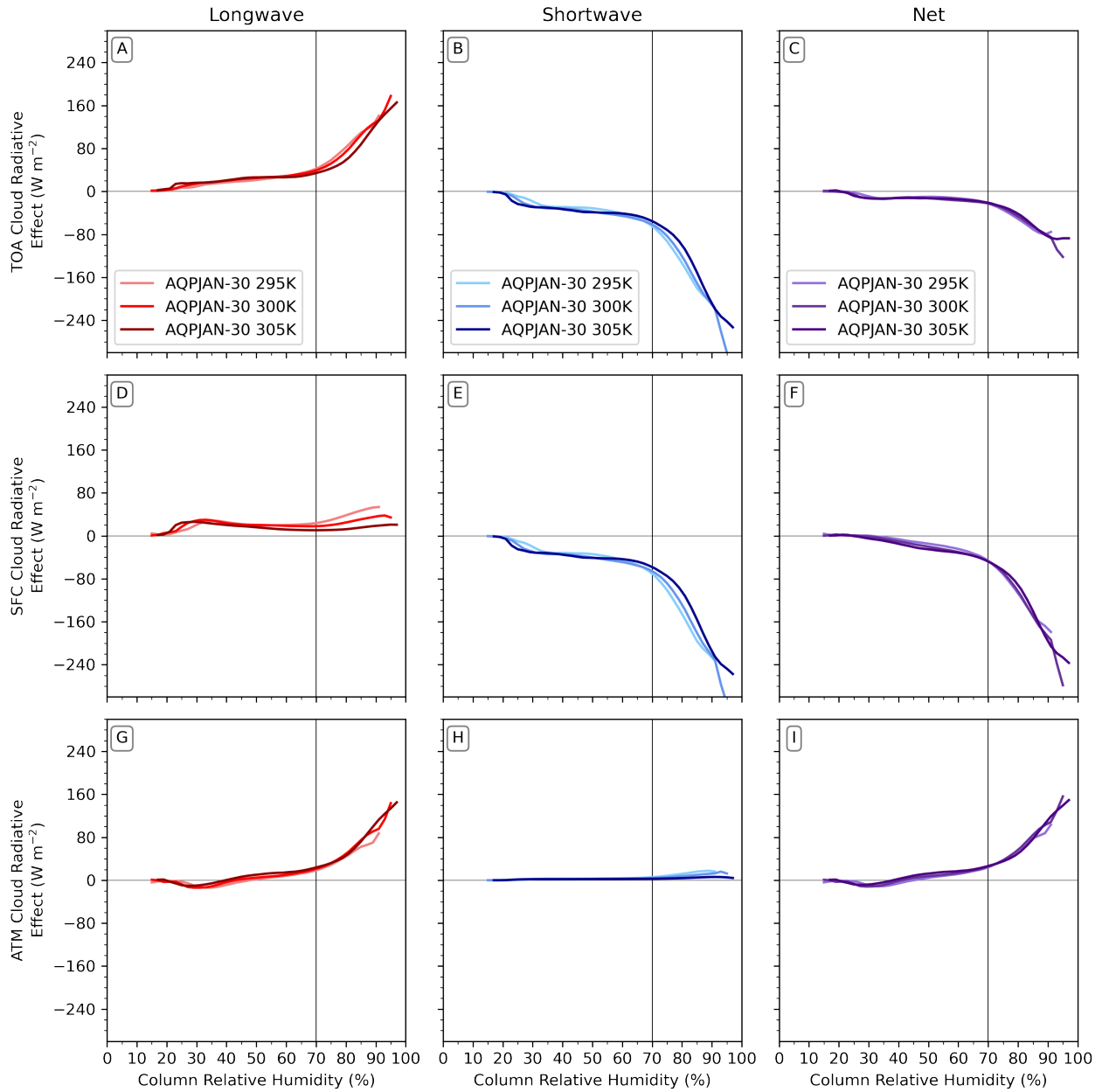


**Figure C.2:** TOA and surface CRE and ACRE binned by CRH for each of the three AQPJAN simulations ranging from 30°S to 30°N. Compare with Figs. 3.3, 3.7, and 7.6.

There are slight differences between the curves in Fig. C.2 and those of previous figures. For example, the longwave and net ACRE achieve small negative values near 30% CRH while the corresponding curves in Fig. 7.6 were uniformly positive. But these differences are minor and do not change the overall shape of the curves, and do not change one of the key conclusions of this thesis that the CRE as a function of CRH is largely independent of the SST.

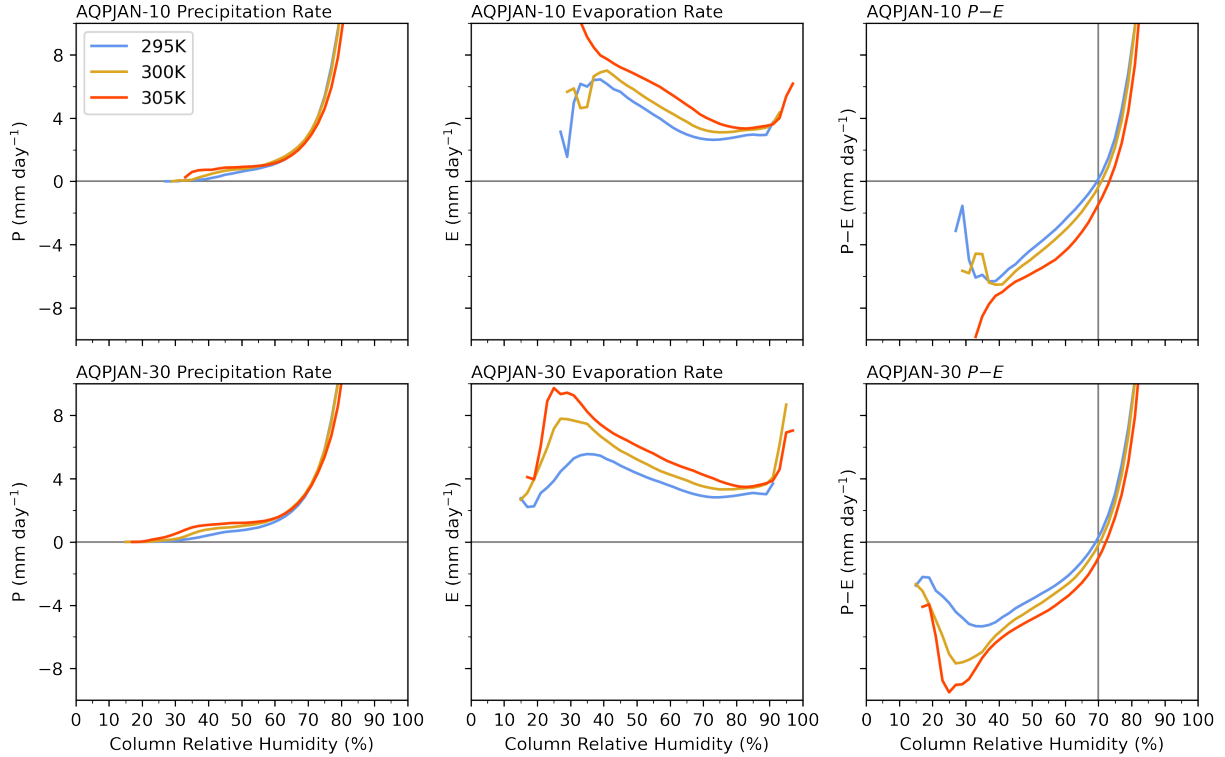


**Figure C.3:** Precipitation and Evaporation rates for the AQPJAN10 region and AQPJAN30 region. Compare with Fig. 7.7

## C.2 Budgets of energy and moisture

### C.2.1 Moisture budget

The moisture budget was then investigated in the AQPJAN30 data, following the method of Chapter 5. The top row of Fig. C.3 shows the precipitation and evaporation rates and their difference as a function of the CRH for the AQPJAN10 simulations, as presented previously in Fig. 7.7. The bottom row repeats the calculations for the AQPJAN30 data. The two rows are similar and show key features that have been identified previously. Specifically, the precipitation rate appears to follow a universal curve at high CRH, and the difference  $P - E$  passes through zero near 70% CRH. Importantly, this supports another key conclusion of this thesis, that dry and humid regions are separated by a CRH of approximately 70% and that moisture tends to flow against the gradient from dry to humid regions (Neelin and Held, 1987; Riehl and Malkus, 1958).

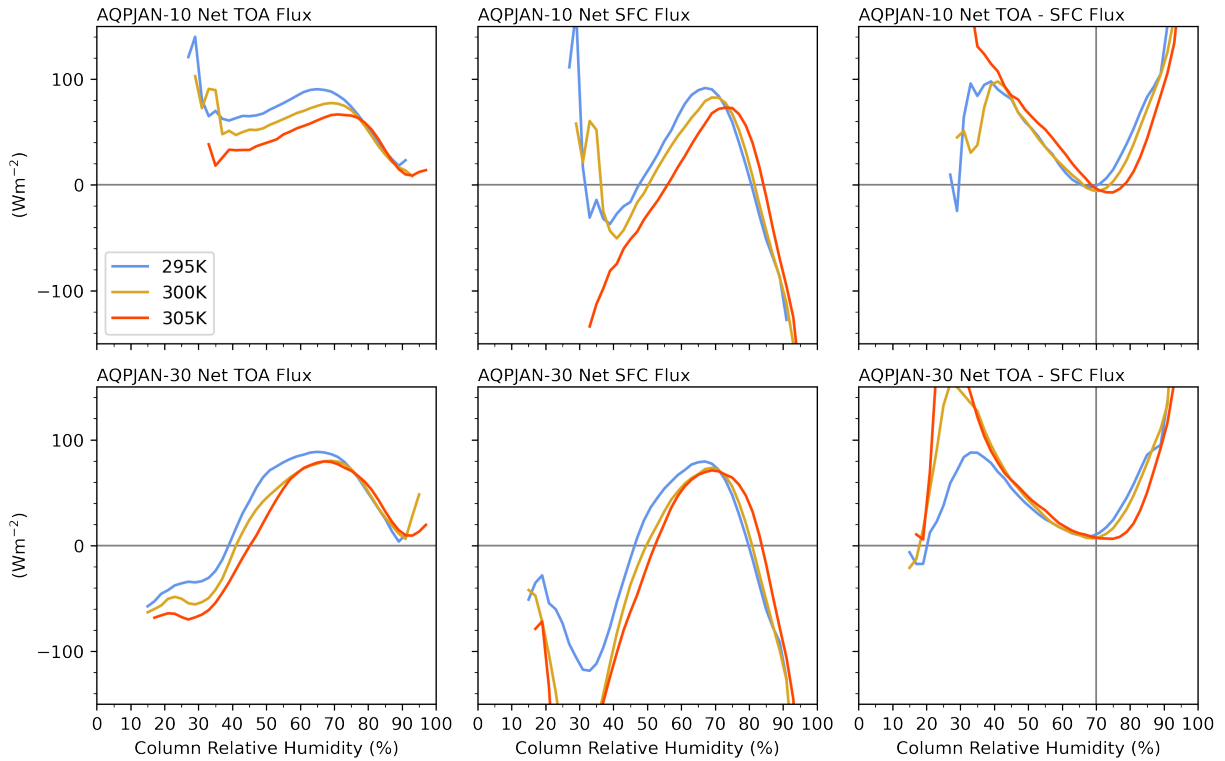


**Figure C.4:** TOA, surface, and net energy budget for the AQPJAN10 and AQPJAN30 regions. Compare with Fig. 7.8

## C.2.2 Energy budget

Next, the energy budget was investigated for the AQPJAN data. The analysis in previous chapters showed the separate components of the budget at the top of atmosphere and at the surface, but only the final result is shown in Fig. C.4. The curves are largely similar, with the exception of the net flux at the TOA, which becomes negative at low CRH in the AQPJAN30 data. The reason for this difference has not been investigated fully, but it is likely a result of the extra regions included in the AQPJAN30 data that were not in the AQPJAN10 data. The reasoning is as follows.

It is well known that the deep tropics (within  $10^\circ$  of the equator) are an energy source for the rest of the planet as the difference between shortwave radiation in minus longwave radiation out is positive. At higher latitudes this difference is negative, representing a radiation deficit where the local longwave cooling to space exceeds solar heating. In the annual mean the latitude where the local radiation surplus becomes a deficit occurs between  $30^\circ$ - $40^\circ$  in each hemisphere (Trenberth and Caron, 2001; Vonder Haar and Oort, 1973), but this latitude migrates with the seasons.

Latitudes near  $30^\circ$  receive a large amount of solar radiation in the summer months, but during the winter months the solar radiation is reduced so that the local difference in shortwave in minus longwave out may change sign.

Then, the AQPJAN30 region likely contains some areas near  $30^\circ\text{N}$  with a local radiation deficit. As these areas also correspond to dry regions where the local balance of  $P - E$  is strongly negative (see Fig. 7.3) they also are likely areas of low CRH. This may explain the negative TOA flux seen at low CRH in Fig. C.4. Further support for this explanation may be found by noticing that the extremely low CRH values do not exist in the curves for the AQPJAN10 data and only exist in the curves for the AQPJAN30 data, showing that the data leading to the negative values must have come from latitudes greater than  $10^\circ$  from the equator.

Other than this difference, the curves in Fig. 7.3 are similar between the two AQPJAN regions. In particular, both show a minimum in the difference between TOA and surface fluxes near the 70% CRH threshold. In Chapter 7, it was noted that the corresponding curves for the RCEMIP simulations became negative near this threshold instead of reaching a minimum. It was suggested that this was because the analysis of the RCEMIP simulations covered the entire planet, while the AQPJAN simulations stopped at a latitude limit where there was an export of energy (see Fig. 7.4). Regardless, Fig. 7.3 shows that the results in Chapter 7 are not sensitive to the choice of a latitude limit, with the exception of the change in sign of the TOA energy flux mentioned above.

### **C.3 The radiatively driven moisture feedback**

Another key conclusion of this thesis relates to the radiatively driven moisture feedback described in Chapter 6. In that chapter, it was found that in extremely humid regions of the RCEMIP simulations, the ACRE is strong enough to change the sign of the net radiation tendency. The resulting radiative heating then drives large-scale rising motion, consistent with the findings of recent work by Jenney et al. (2020). When the moisture tendency equation is formulated following Chikira (2014), the rising motion is found to moisten the troposphere, leading to more clouds

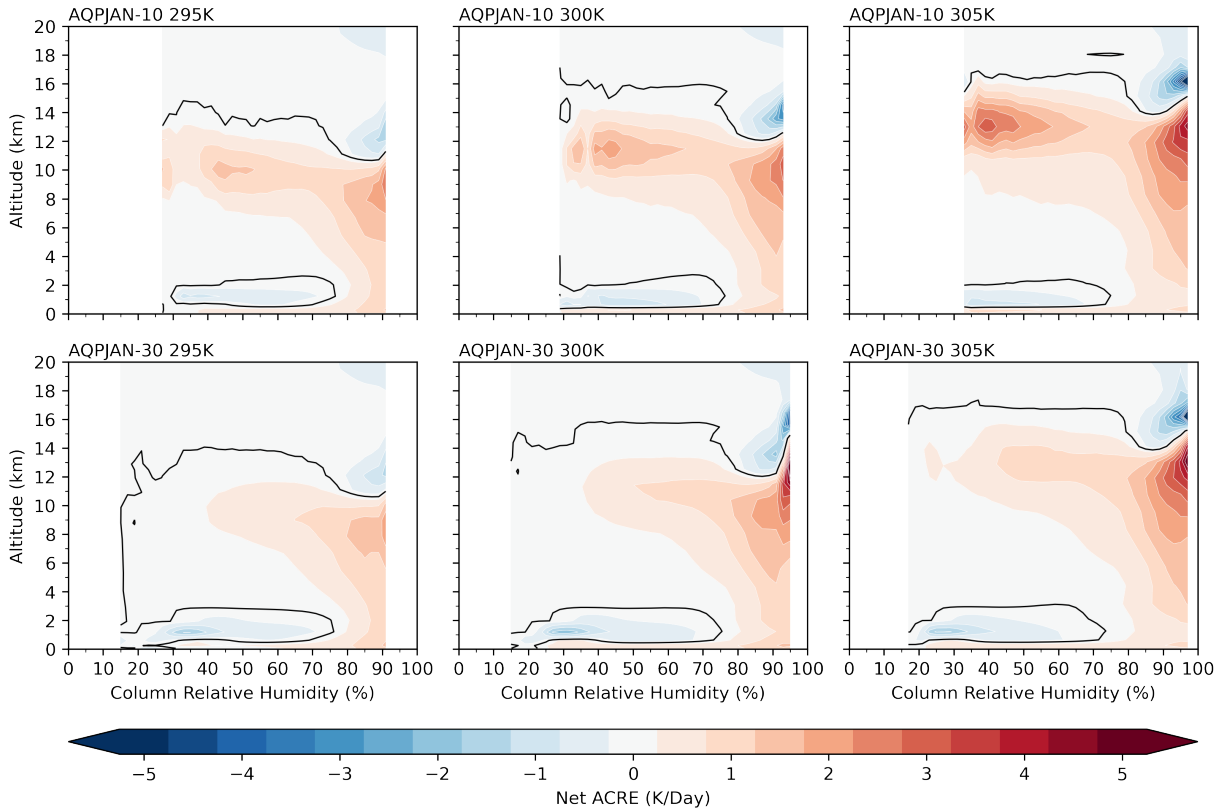


**Figure C.5:** Comparison of net ACRE for the AQPJAN10 and AQPJAN30 regions. Compare with Fig. 6.3

which then continue to moisten the environment. This feedback was then observed in the AQPJAN simulations in Chapter 7.

Here, Figs. C.5 and C.6 are included to show that the feedback is found in the AQPJAN simulations in both the AQPJAN10 and AQPJAN30 regions. Fig. C.5 shows the ACRE binned by the CRH for the AQPJAN10 and AQPJAN30 data. Both sets of data show the dependence of the ACRE on the CRH, with strong ACRE observed in extremely humid regions. The ACRE is strong enough to lead to a net positive radiation tendency (not shown). Fig. C.6 shows the moistening of the troposphere due to large-scale rising motion induced by radiative heating, following Chikira (2014). Both the AQPJAN10 and AQPJAN30 data show a region of net moistening in the extremely humid regions that extends through much of the troposphere. There are slight differences between the top and bottom rows of Figs. C.5 and C.6, but they are minor and do not change the general conclusions.

Lastly, Tbl. C.2 shows the percentage of the domain with CRH values less than 70% and 80%, respectively. The 70% value was identified in Chapter 3 as an important threshold separating regions with small and large CRE, and roughly corresponds to the boundary between dry and humid regions (see Chapter 5). As mentioned in relation to Fig. C.1 and Tbl. C.1, the AQPJAN30 distributions of CRH are more similar to the RCEMIP distributions than to the AQPJAN10 distributions. The AQPJAN10 distributions are dominated by a large amount of moisture convergence associated with the ITCZ, leading to much higher values of CRH and a large fraction of the domain exceeding the 70% threshold. The AQPJAN30 distributions in contrast include drier regions as well. These regions are associated with enhanced evaporation under the subsiding branches of the Hadley cells, leading to lower values of CRH and a smaller fraction of the domain exceeding the 70% threshold.

The 80% value was found to be approximately the threshold where the radiative heating became positive (and by extension the large-scale motion acted to moisten the environment) in the RCEMIP simulations. From Fig. C.5, the radiatively driven feedback appears to become relevant for CRH greater than 85% or 90% in the AQPJAN simulations. This suggests that the feedback may initiate above a particular CRH percentile (e.g. in the most humid 5% of the domain) rather than above an absolute CRH value (e.g. all regions with  $CRH \geq 80\%$ ), although further study is warranted to see exactly where the feedback is important.

**Table C.2:** Extension of Tbl. 6.1, showing the fraction of the domain with CRH below a given level for the AQPJAN simulations using both latitude limits the RCEMIP simulations, as well as the ERA5 reanalyses.

	CRH $\leq$ 70%	CRH $\leq$ 80%
<b>295 K AQPJAN 10°</b>	42.81%	87.08%
<b>295 K AQPJAN 30°</b>	71.75%	94.11%
<b>295 K RCEMIP</b>	78.99%	97.35%
<b>300 K AQPJAN 10°</b>	37.41%	80.51
<b>300 K AQPJAN 30°</b>	69.51%	91.87%
<b>300 K RCEMIP</b>	71.94%	94.83%
<b>305 K AQPJAN 10°</b>	32.05%	71.49%
<b>305 K AQPJAN 30°</b>	69.69%	89.27%
<b>305 K RCEMIP</b>	74.95%	94.79%
<b>ERA5 10°</b>	54.93%	83.55%
<b>ERA5 30°</b>	74.39%	90.99%

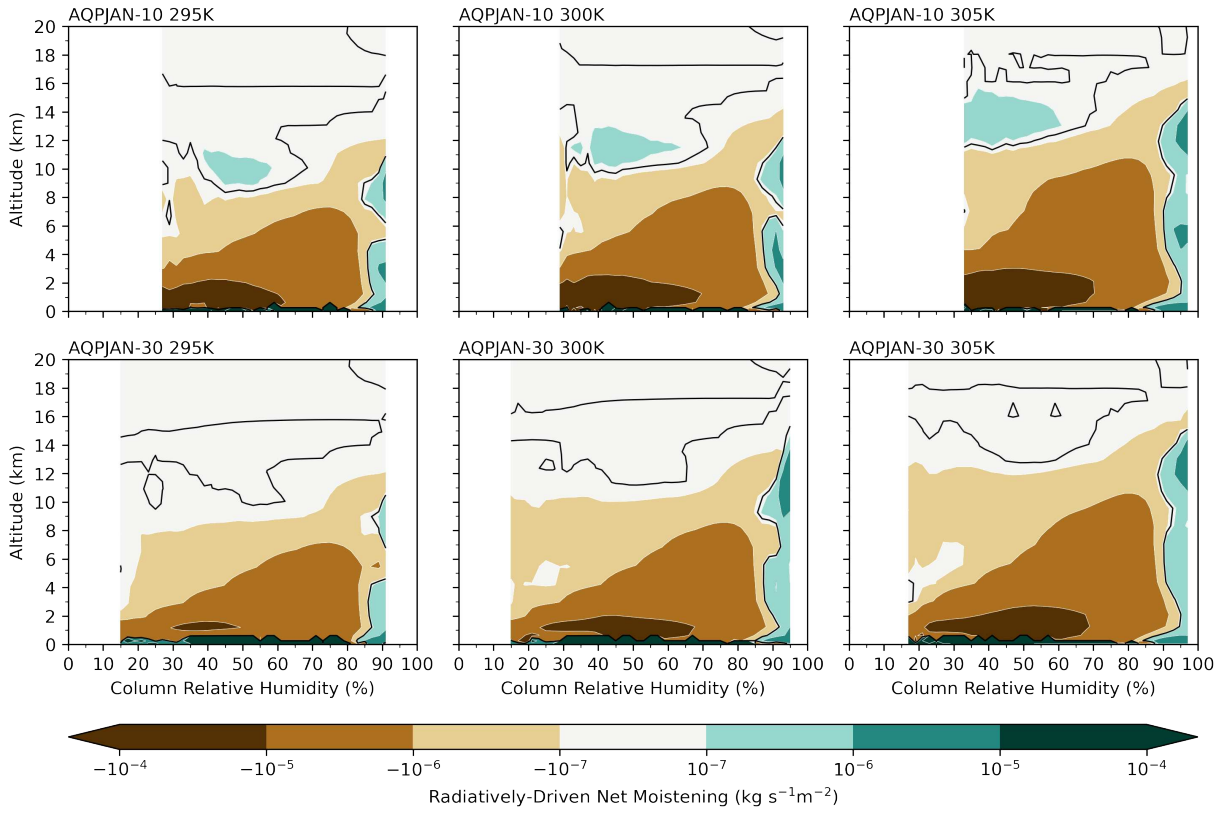


**Figure C.6:** Comparison of tropospheric moistening by net radiation for the AQPJAN10 and AQPJAN30 regions.